Process development and characterisation of (Ta,Hf)C ultra-high temperature ceramics

Omar Cedillos Barraza

A thesis submitted in partial fulfilment of the requirements for the degree of Doctor of Philosophy

Department of Materials

Imperial College London

London, UK, SW7 2AZ

May 2015

Declaration

I declare that all the work contained herein is my own and any work of others included in this work is appropriately referenced and acknowledged.

Omar Cedillos Barraza

Abstract

Tantalum carbide (TaC), hafnium carbide (HfC) and compounds in the TaC-HfC system have extremely high melting points (>3700 °C) making them potential candidates for thermal protection structures in hypersonic space vehicles. Information regarding mechanical and thermal properties of these compounds and their solid solutions is scarce. Synthesis and sintering of 4TaC-1HfC compounds was conducted using efficient reactive routes using self-propagating high temperature synthesis (SHS) and a spark plasma sintering (SPS) furnace. Reactive one-step reactive spark plasma sintering (RSPS) and a combination of SHS+SPS were used as the processing routes to produce TaC-HfC ceramics. Relative density >98% was achieved by the SHS+SPS method without sintering aids at 2100 °C for 20 min and 60 MPa. Product conversion of the reactants after SHS and after sintering was characterised by XRD. Analysis of microstructures was conducted by SEM and EDS. TaC, HfC and different TaC-HfC compounds were sintered using SPS at temperatures up to 2450 °C using commercial powders of TaC and HfC. Microstructural evolution and solid solution formation was analysed in 4TaC-1HfC ceramics fabricated using SPS from 2050-2450 °C. XRD, SEM and EDS were used to analyse the formation of (Ta,Hf)C solid solutions. TEM was conducted and the diffusion mechanisms during sintering were analysed. Single-phase solid solutions were formed at sintering temperatures ≥2350 °C for 20 min and 30 MPa. In addition, TaC, HfC, 1TaC-1HfC and 1TaC-4HfC ceramics were sintered by SPS at 2350 °C. Measurements of mechanical properties (hardness, elastic modulus and fracture toughness) and thermal properties (thermal diffusivity, thermal conductivity and coefficient of thermal expansion) are reported. Melting temperatures (T_m) were reassessed using a laser melting technique with a 4.5 kW, 1064 nm Nd:YAG CW laser programmed to deliver pulses with time ranging from 100 to 1000 ms and power up to 3980 W. HfC showed the highest melting temperature at 3959 ± 50 °C, and the highest melting temperature for any known compound. T_m for TaC was measured at 3768 ± 40 °C and the solid solutions fall in between the single member carbide values with 4TaC-1HfC at 3905 ± 40 °C. Microstructural characterisation using SEM and TEM on samples after the laser testing experiments is reported.

This work is dedicated to *Leticia*,

Thanks for all your motivation and support through these years and for sharing this adventure with me.

Acknowledgements

First of all, I would like to thank my parents Dagoberto and Esperanza for their unconditional support. Thanks for being my guidance and my inspiration. To all my family, for always being there, without you this degree would not have been possible.

Thanks to my supervisor Prof. Bill Lee for all your support and guidance throughout this PhD and to Dr. Luc Vandeperre for his valuable discussions and help.

Thanks to all the technical staff at Imperial College, Dr. Mahmoud Ardakani for all the training and technical support with SEM and TEM, Mrs. Ecaterina Ware for helping me with the preparation of FIB samples, Mr. Richard Sweeney for all the help with XRD, Mr. Gary Stakalls for all the countless times he helped me by cutting and preparing samples and with equipment training and Dr. Richard Chater.

Thanks to Dr. Doni Daniel Jayaseelan for his ideas and input on this project and his help with the TEM work, to Dr. Salvatore Grasso at Queen Mary University London for helping me in the fabrication of samples by SPS and all his valuable recommendations, discussions and feedback and Dr. Dario Manara at the Institute for Transuranium Elements (ITU) for all his attentions during my visit to Germany, his invaluable help with the laser experiments and useful feedback.

Thanks to all my colleagues at CASC for always helping me, all their constructive discussions and having those words of support in the good and the bad days.

Finally, I would like to thank CONACyT (Consejo Nacional de Ciencia y Tecnología, México) for the financial support of this PhD.

Publications

- *"Enhanced oxidation resistance of ZrB_2/SiC composite through in situ reaction of gadolinium oxide in patterned surface cavities",* Jesus Gonzalez-Julian, Omar Cedillos-Barraza, Sven Doering, Stefan Nolte, Olivier Guillon, and William E. Lee, Journal of the European Ceramic Society. 34, 4157-4166 **(2014)**

- *"Flash Spark Plasma Sintering (FSPS) of Pure ZrB_2",* Salvatore Grasso, Theo Saunders, Harshit Porwal, Omar Cedillos-Barraza, Daniel Doni Jayaseelan, William E. Lee, and Mike John Reece, Journal of the American Ceramic Society, 97 [8] 2405–2408 **(2014).**

Presentations

- *Microstructure and mechanical properties of (Ta,Hf)C ultra-high temperature ceramics,* 38th International Conference and Exposition on Advanced Ceramics and Composites, Daytona Beach, FL, USA. **(2014)**

- *Process development and microstructural characterisation of (Ta,Hf)C ultra-high temperature ceramics,* 13th Conference of the European Ceramics Society, Limoges, France. **(2013)**

- *Synthesis and sintering of TaC-HfC ceramics by SHS and RSPS techniques,* 37th International Conference and Exposition on Advanced Ceramics and Composites, Daytona Beach, FL, USA. **(2013)**

- *Fabrication of TaC-HfC for ultra-high temperature applications,* Poster presentation at Ultra-High Temperature Ceramics: Materials for Extreme Environment Applications II. Schloss Hernstein, Austria. **(2012)**. Best poster prize winner.

Table of Contents

List of figures

List of tables

Abbreviations

ASTM – ASTM International formerly known as American Society for Testing and Materials

BF – Bright field

BFP – Back focal plane

BSE – Backscattered electron

BSEI – Backscattered electron image

CCD – Charge coupled device

CIF – Crystallographic information file

CIP – Cold isostatic press

CNT – Carbon nanotubes

CTE – Coefficient of thermal expansion

DC – Direct current

DF – Dark field

DP – Diffraction pattern

EDM – Electric discharge machining

EDS – Energy dispersive X-ray spectroscopy

EMIA – Elemental mass induction analyser

EMGA – Elemental mass gas analyser

FIB – Focused ion beam

GF – Gaseous flame

GNP – Graphene nanoplatelets

HIP – Hot isostatic press

HK – Knoop hardness

HP – Hot press

HRTEM – High resolution transmission electron microscopy

HV – Vickers hardness

ICDD – International Center for Diffraction Data

ICSD - Inorganic Crystal Structure Database

IR – Infrared

LFA – Laser flash analysis

MGS – Mean grain size

NSE – Normal spectral emissivity

PID – Proportional-integral-derivative controller

PDF - Powder diffraction files

RD – Relative density

RSPS – Reactive spark plasma sintering

RT – Room temperature

RT – Room temperature

SAED – Selected area electron diffraction

SEI – Secondary electron image

SEM – Scanning electron microscopy

SF – Solid flame

SHS – Self-propagating high-temperature synthesis

SPS – Spark plasma sintering

SSS – Solid state sintering

TD – Theoretical density

TEM – Transmission electron microscopy

TPS – Thermal protection systems

UHTCs – Ultra-high temperature ceramics

VPS – Vacuum plasma spray

XRD – X-ray diffraction

1 Introduction

The design of next generation hypersonic flight vehicles has raised interest in the development of materials that can operate in extreme environments. Hypersonic vehicles are equipped with sharp nose tips and leading edges to maximize flight performance, however very high temperatures and heating rates are produced at the vehicles surface due to extreme velocities (>5 Mach). Thermal protection structures are required to operate in air at temperatures that can exceed 2000 °C, thus components are not only are required to have very high melting points, but also oxidation and ablation resistance.

The extreme conditions required for hypersonic application has introduced the motivation for research and development of high temperature materials. From the vast array of materials that an engineer can choose there is a limited number of materials (compounds and elements) that have melting temperatures above 3000 °C and in which the so-called ultra-high temperature ceramics (UHTCs) are included. UHTCs are a family of refractory materials with extremely high melting points (>3000 °C) and are typically Group IVB and VB carbides, nitrides and borides. High hardness, chemical stability, low vapour pressures, good thermal shock resistance and high elastic modulus are characteristic properties of UHTCs.

Tantalum carbide (TaC) and hafnium carbide (HfC) are of particular interest due to their high melting temperatures (TaC: 3985 °C and HfC: 3950 °C [1]) and are the highest among all inorganic materials, also TaC and HfC form a continuous solid solution over the whole range of compositions. A melting point maximum between the two was reported by Agte and Moers [2], however work conducted by Rudy [1] did not confirm this. This makes (Ta,Hf)C solid solutions of such interest since little is known regarding processing and their physical, mechanical and thermal properties.

In addition to very high melting temperatures, TaC and HfC show other interesting properties such as high hardness (TaC: 16.7 GPa; HfC: 26 GPa), high modulus of elasticity (TaC: 285-560 GPa; HfC: 350-510) and good thermal conductivity (TaC: 22.1 W/m·K; HfC: 20.0 W/m·K) [3] which make them promising materials for military and space applications. Furthermore, these carbides have very strong

chemical bonds, a complex combination of metallic, covalent and ionic bonds; this gives these carbides a combination of the physical properties of ceramics (high hardness and strength) with the electronic properties of metals (high thermal and electrical conductivities). However, this strong bonding makes TaC and HfC difficult to fabricate and process due to their refractoriness, thus limiting their commercial applications [4, 5].

The interest of defence industry in the research into transition metal carbides, especially TaC and HfC, often makes publication of research difficult due to the sensitive nature of much of the information. The majority of work in these transition metal carbides has been focused on the fabrication of monolithic TaC and HfC to improve density (processing methods, sintering additives) and with the microstructural relationship to mechanical properties. (Ta,Hf)C have been less explored, hence publications regarding these solid solutions are limited. Here lies the motivation of this work to find efficient methods to fabricate (Ta,Hf)C single phase ceramics and to measure mechanical and thermal properties which are not known and reassessing the melting temperatures in the TaC-HfC system.

This works starts with a literature review in Chapter 2, with aims and objectives presented at the end of the chapter. Chapter 3 is dedicated to experimental methods. Chapter 4 is focused on reactive methods to synthesise (Ta,Hf)C solid solutions using a combination of self-propagating high-temperature synthesis (SHS) and spark plasma sintering (SPS) techniques. Chapter 5 examines the fabrication of (Ta,Hf)C by SPS, followed by microstructural characterisation and results of mechanical and thermal properties. A comparison of mechanical and thermal properties with monolithic TaC and HfC is presented.

Melting point determination in the TaC-HfC system using a laser melting technique is presented in Chapter 6. Finally, Chapter 7 includes final conclusions and suggestions for future work.

2 Literature review

2.1 Background

Recent developments in the design of next generation hypersonic vehicles have sparked a renewed interest in the research of materials for extreme environments. Early space vehicles had blunt body designs to reduce aerodynamic heating and maintain moderate temperature limits on the vehicle surfaces. To improve performance, hypersonic vehicle designs have been proposed with slender aerodynamic shapes and profiles equipped with sharp leading edges to reduce drag. By increasing the lift/thrust to drag ratio with sharp leading edges, the vehicle could be improved in terms of manoeuvrability and safety. However, the use of sharp leading edges causes an increase in surface temperature since the temperature of the leading edge is inversely proportional to the leading edge radius [5]. Therefore improved materials are needed that can withstand the extreme conditions associated with atmospheric re-entry and propulsion system components in hypersonic vehicles. These conditions include extreme temperature, chemical reactivity, mechanical stress, radiation and wear. Leading edges and nose caps have projected operating temperatures above 2000 °C, such as those illustrated in Figure 2.1, and propulsion systems in excess of 3000 °C [6].

Figure 2.1 Conceptual hypersonic vehicle [7].

The capabilities of current engineering ceramics do not fulfil those needed by the combination of extreme temperatures, chemically aggressive environments and rapid cooling and heating regimes. Hence the interest in the development and improvement of a group of ceramics commonly known as ultra-high temperature ceramics or UHTCs [8]. A common definition of a UHTC is a material that has a melting temperature above 3000 °C; from a wide selection of materials that an engineer can choose only a limited number of materials have melting points above this criterion (Figure 2.2). These include a selected group of boride, carbides and nitrides of transition metals of Groups IV and V of the Periodic Table, as a result most of the research in UHTCs is focused on compounds such as TaC, HfC, ZrB_2, HfB_2, ZrC and TaB_2 [8, 9].

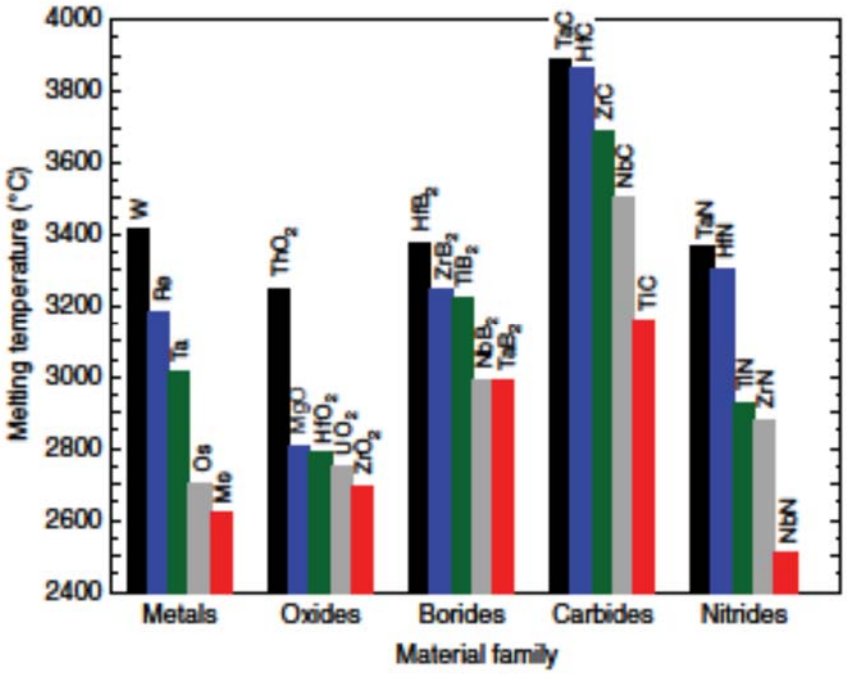

Figure 2.2 Melting temperatures of selected materials grouped by material family [9].

The second most important property required for UHTC applications is the capacity of the material to work in air (i.e. oxidation resistance). Alumina, magnesia, silicon carbide and silicon nitride are materials that can be used at temperatures up to 1600 °C in air, hence the ultra-high temperature regime should be above this temperature. Some authors have cited 2000 °C as the cutoff temperature of the

ultra-high temperature regime, then it is required that these materials can operate with minimum or no oxidation or ablation at temperatures greater than this [8]. High temperature oxidation test have been conducted in both furnace studies and simulated re-entry environments (arc jet, acetylene torch [10-14]. Because of the large temperature gradients produced in hypersonic environments, UHTCs are susceptible to high tensile stresses, in other words these materials are subjected to thermal shock. Hence, UHTCs materials are required to high thermal conductivity and the highest emmisivity possible in order to dissipate and re-radiate the heat fluxes from the leading edges [5].

2.2 Historic research

During the 1960's the US Air Force commissioned a series of studies of phase equilibria in transition metal-based systems to analyse their potential for aerospace applications. The work was performed by Aerojet-General Corporation and lead by Dr. E. Rudy. A series of extensive technical reports were produced during the programme in different research areas distributed in five parts: I. Binary systems, II. Ternary systems, III. Experimental Techniques, IV. Thermochemical calculations and V. Phase equilibria diagrams. Parallel to these studies, additional work was conducted by ManLabs which mostly consisted in processing, microstructure, properties and oxidation of ZrB_2- HfB_2-based ceramics [5, 8].

Also during the 1960's and 1970's much research into refractory carbides was conducted by Russian research institutions. The most well-known Russian scientist of that time in this field was Professor G.V. Samsonov. His research was extensive and after studying the synthesis of inorganic compounds he then realized that further studies were needed into structure, properties, processing and performance of materials. His research covered electronic configuration, phase stability and mechanical properties and contributed to the study of sintering of crystalline refractory compounds. Electrical and magnetic properties were also studied and correlated with their electronic bonding. By the end of his career, Samsonov contributed to the field of refractory compounds with more than 1500 co-authored papers [15].

2.3 Bonding and crystal structure of tantalum and hafnium carbide phases

Ceramic carbides, borides and nitrides have strong chemical bonds that give them high temperature structural stability. The bonds in refractory carbides can be ionic, metallic, covalent or a combination of these [16]. Carbides can be separated into four main categories: interstitial carbides, covalent carbides, intermediate carbides and ionic carbides.

Silicon carbide and boron carbide are the only two covalent carbides that meet the refractory criteria of T_m >1800 °C and chemical stability. In these carbides the carbon atom is slightly smaller than the other atom. The bonding in these materials is essentially covalent. Transition metals of Groups VII and VII such as manganese, iron, cobalt and nickel and chromium of Group VI form the so-called intermediate carbides. The atomic radii of the metal is too small to accommodate the carbon atom in the interstitial position without severe distortion of the lattice. In general, these carbides are not chemically stable. Ionic carbides have the characteristics of a salt such as fixed composition, physical properties different to those of their constituent elements, are in general transparent to optical radiation and are good electrical insulators. Ionic carbides are formed with carbon and the most electropositive elements found in Groups I, II and III of the Periodic Table. They decompose easily by water and acids. However, Al_4C_3 and Be_2C and three actinide carbides: ThC, UC and PuC are important industrial materials for applications such as atomic energy [3].

In interstitial carbides, the largest class of carbides that includes carbides of the metals Ta, Hf, Zr and Ti, the carbon atom has a much smaller size than the metallic atom, allowing it to be located in the interstices of the lattice. The bonding is a mixture of covalent, ionic and mostly metallic which is why interstitial carbides closely resemble metals [3]. In general, interstitial carbides have some characteristics in common: they are mainly non-stoichiometric phases and ordering of carbon is common, they combine the physical properties of ceramics and the electronic properties of metals (high hardness and strength with high thermal and electrical conductivities), have the highest melting points of known materials and also have high thermal and chemical stability [17, 18].

Compounds of carbon and nitrogen with transition metals have close packed structures in arrangements of metal atoms with smaller non-metal atoms inserted into interstitial sites. Carbon and nitrogen are located in an octahedral interstitial site or in the centre of a trigonal prism [18]. Figure 2.3 shows a cubic NaCl crystal structure of HfC and TaC. Hägg [19] proposed empirical rules for constructing crystal structures of interstitial compounds. Some exceptions to these rules have been found, but in general interstitial compounds are formed if the atomic radii of the metal R_M and non-metal R_X meet the conditions $0.41 < R_X/R_M < 0.59$, under this condition non-metal atoms are located at the largest interstitial site of the metallic lattice. The interstitial site is smaller than the interstitial atom, the change of symmetry and expansion of the metallic lattice in carbides ensures stability of the structure. The atomic radius of C is 0.0772 nm, 0.1585 for Hf and 0.1457 for Ta, and the radius ratios (R_X/R_M) are 0.486 and 0.529 for R_C/R_{Hf} and R_C/R_{Tam} respectively which meet the Hägg conditions.

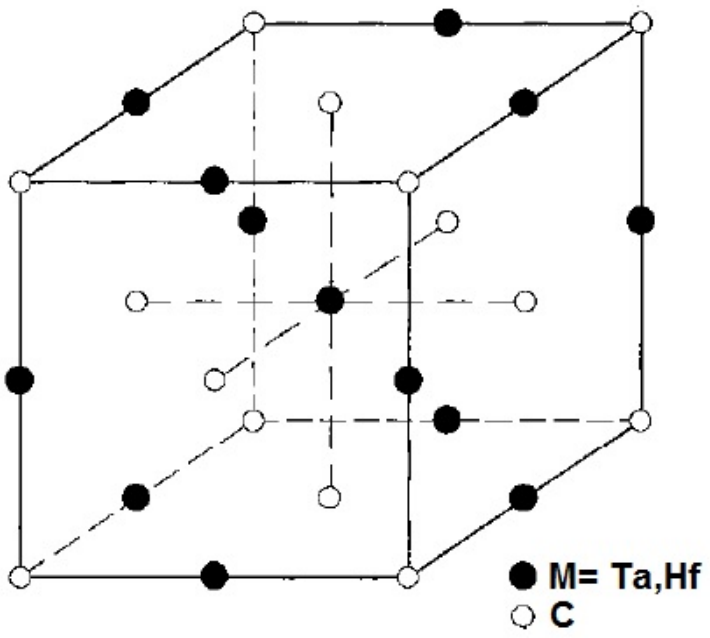

Figure 2.3 Cubic B1 (NaCl) crystal structure of TaC and HfC [20].

Group IV transition metals (titanium, zirconium and hafnium) form only monocarbides with the *B1* (NaCl) structure. The Hf-C binary phase diagram is characterised by only one carbide phase, a

monocarbide with a cubic *B1* structure with a wide homogeneity range $HfC_{1.00}$ to $HfC_{0.6}$, i.e. the carbon sublattice contains 40 at% of structural vacancies in the lower boundary of the homogeneity interval. Group V transition metals (vanadium, niobium and tantalum) form besides the monocarbides VC, NbC and TaC, lower carbides in the form of V_2C, Nb_2C and Ta_2C with an hcp crystal structure of L'3 (W_2C) type (Figure 2.4). The homogeneity intervals of monocarbides of Group V transition metals are narrower than those of Group IV metals, TaC shows a homogeneity range of $TaC_{1.00}$ to $TaC_{0.71}$ [18, 20].

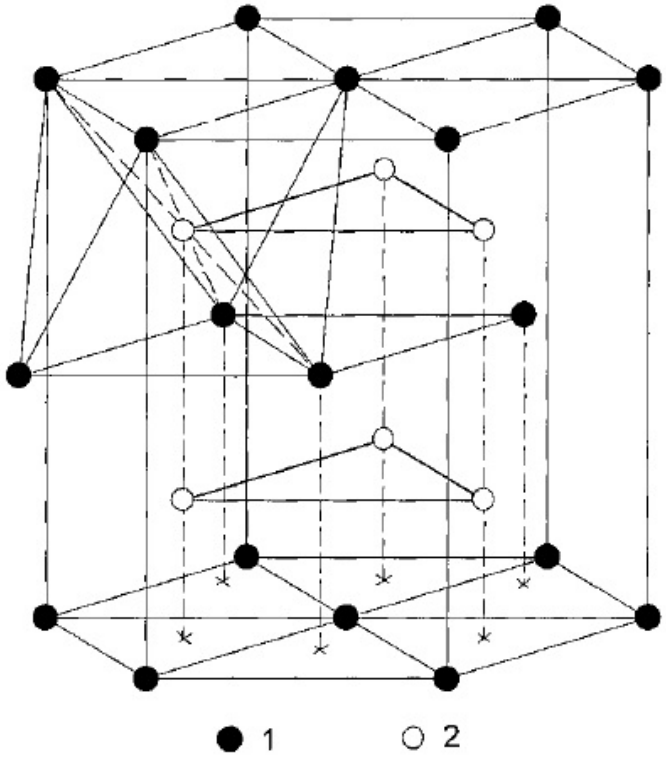

Figure 2.4 Hexagonal close-packed structure type *L'3* (W_2C) of Ta_2C: 1) metal atoms (Ta) and 2) non-metallic sublattice sites [20].

Rhombohedral ζ-phase M_4C_{3-x} is present in the Ta-C system in addition to Ta_2C and TaC [21]. It should be noted that ζ-Ta_4C_3 is not an ordered phase of cubic TaC, since it has a trigonal and not cubic metal sublattice. It has a narrow homogeneity interval from $TaC_{0.65}$ to $TaC_{0.68}$ and exists in the temperature range from 25 to ~2130 °C [22].

A summary of the crystal systems, lattice parameters and densities of the tantalum and hafnium carbide phases is shown in Table 2.1.

Phase	Crystal system	Lattice parameter (Å)	Density (g/cm^3)
HfC	fcc (B1)	a = 4.641 at $HfC_{1.00}$ [20] a = 4.462 at $HfC_{0.60}$ [20]	12.67 [18]
TaC	fcc (B1)	a = 4.456 at $TaC_{0.99}$ [20] a = 4.406 at $TaC_{0.71}$ [20]	14.50 [18]
β-Ta_2C	hcp (L$'$3)	a = 3.106, c = 4.945 at $TaC_{0.50}$ [20]	14.80 [3]
ζ-Ta_4C_3	Trigonal	a = 3.121, b = 3.121 and c = 30.058 [22]	14.84 [22]

Table 2.1 Crystal systems, lattice parameters and densities of hafnium and tantalum carbide phases.

2.4 Phase equilibria of TaC and HfC

The Hf-C system binary phase diagram (Figure 2.5) shows only one compound, HfC with a broad homogeneity interval and a *B1* structure. A phase of the Hf_2C type is not formed in this system, because its carbon content is lower than the content of HfC at the lower boundary of the homogeneity interval. It has been reported by Gusev et al. [20] that Hf_3C_2 and Hf_6C_5 phases appear under equilibrium conditions. These phases of hafnium carbide are formed at temperatures below 530 °C and at these temperatures the diffusion rates are low, therefore it is difficult to achieve equilibrium in the Hf-C system using long-time annealing experiments. Experimental evidence of these phases is still unavailable. A phase diagram constructed by Rudy [23] shows that the highest melting point in the Hf-C system is 3928 °C at a composition of $HfC_{0.94}$. Also reported is the eutectic point of HfC+C at 3180 °C at a carbon content of 65 atomic %.

The binary phase diagram of Ta-C constructed by Gusev et al. [22] shown in Figure 2.6 is characterised by the presence of a Ta_2C phase in addition to the monocarbide. The system includes a lower hexagonal carbide α-Ta_2C with a narrow homogeneity interval, and α-β transition ~1530 °C. The trigonal ζ-Ta_4C_3 phase has a narrow homogeneity interval from $TaC_{0.65}$ to $TaC_{0.68}$ and exists at a temperature from ~2130 to 25 °C. Experimentally, Ta_6C_5 has been synthesised by annealing at 1330 °C followed by slow cooling to 480 °C at a rate of 0.15-0.25 °C/min [24]. A phase diagram constructed after a Storms [17] evaluation from experimental data from Rudy and Harmon [25] and Sara et al. [26] shows the highest melting temperature in the Ta-C of 3983 °C for the cubic $TaC_{0.88}$.

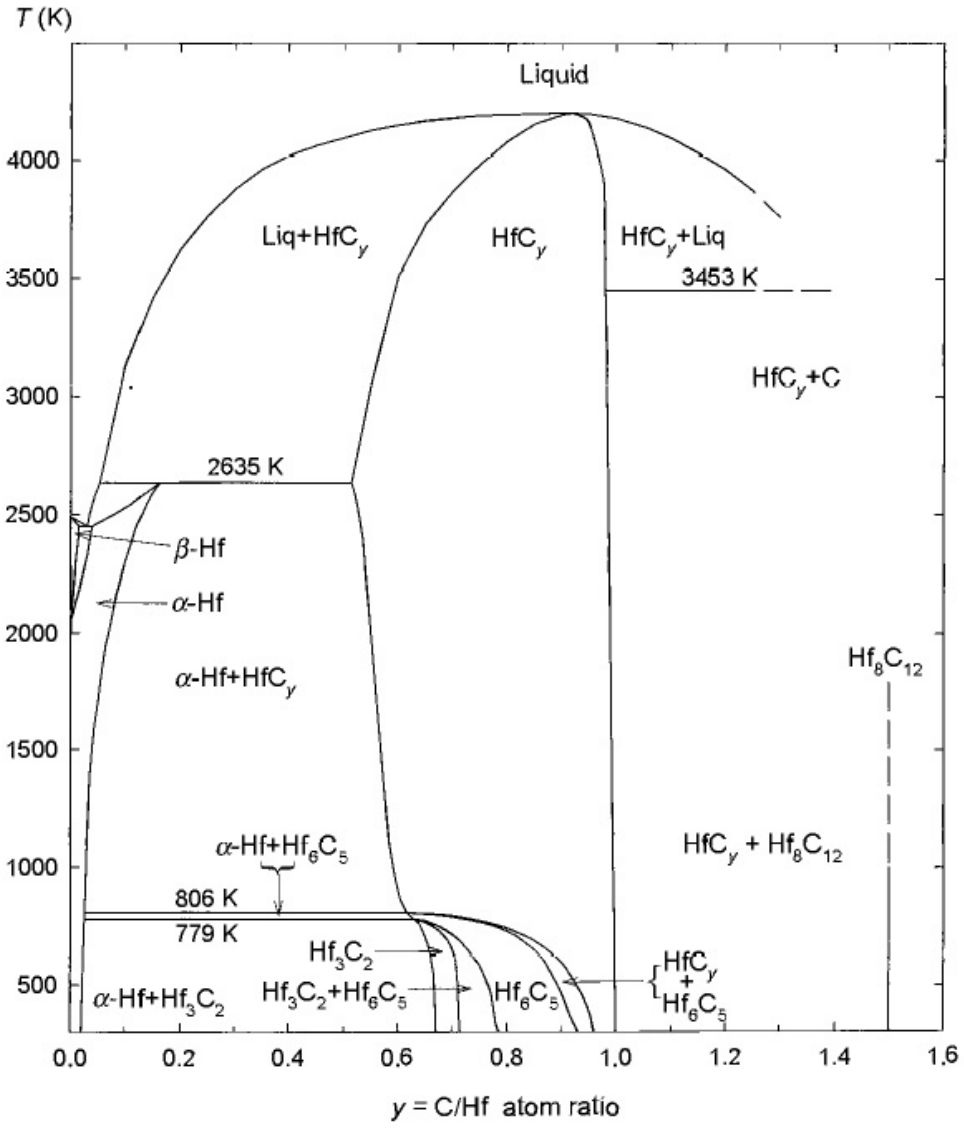

Figure 2.5 Equilibrium phase diagram of the Hf-C system proposed by Gusev et al. [20]

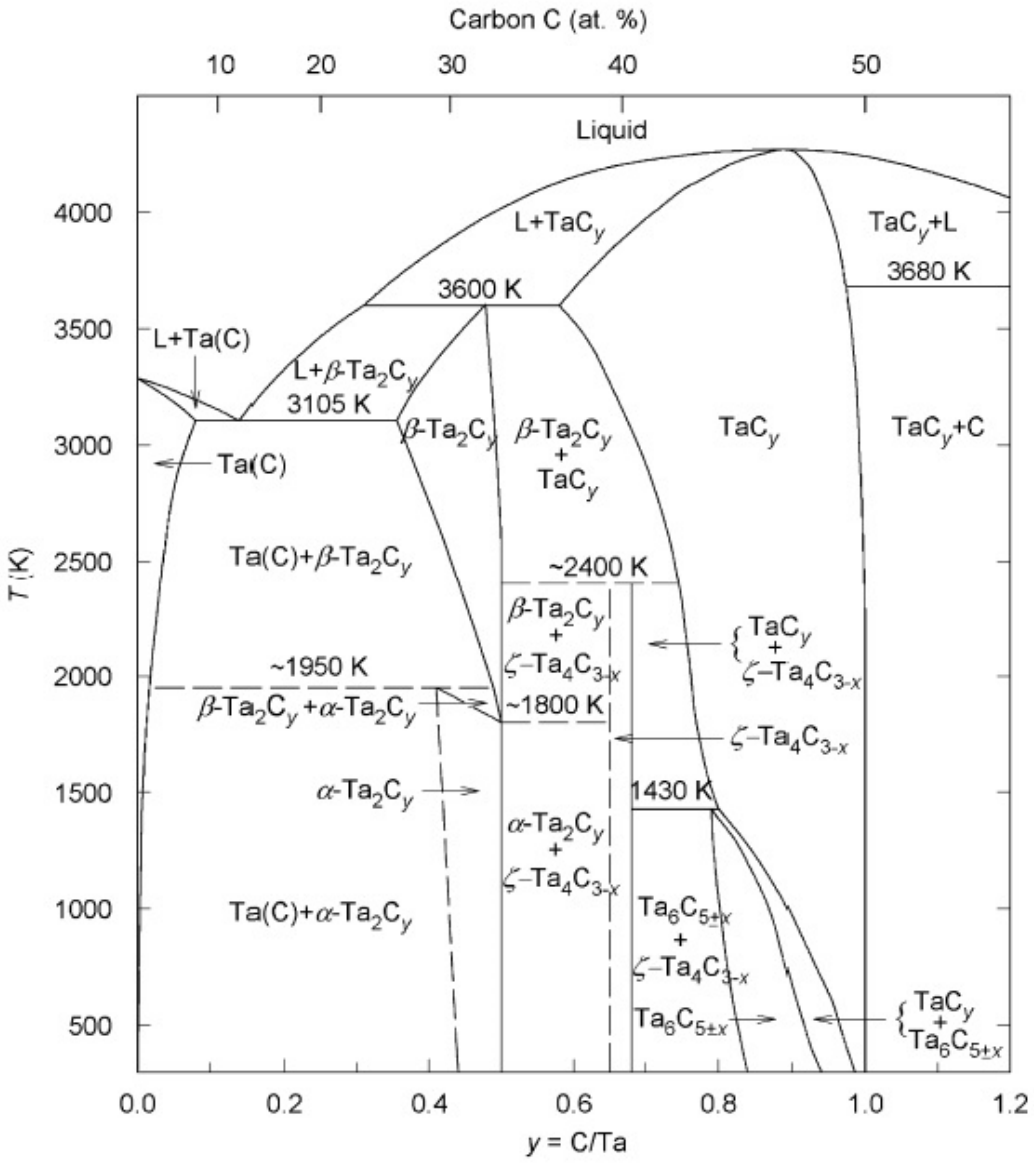

Figure 2.6 Equilibrium phase diagram of the Ta-C system [22].

2.5 The TaC-HfC system

TaC and HfC form a continuous series of solid solutions over the whole range of compositions. The lattice parameters of the solid solutions show a nearly linear variation between parameters of the binary compounds at the respective carbon concentrations (Figure 2.7) [27].

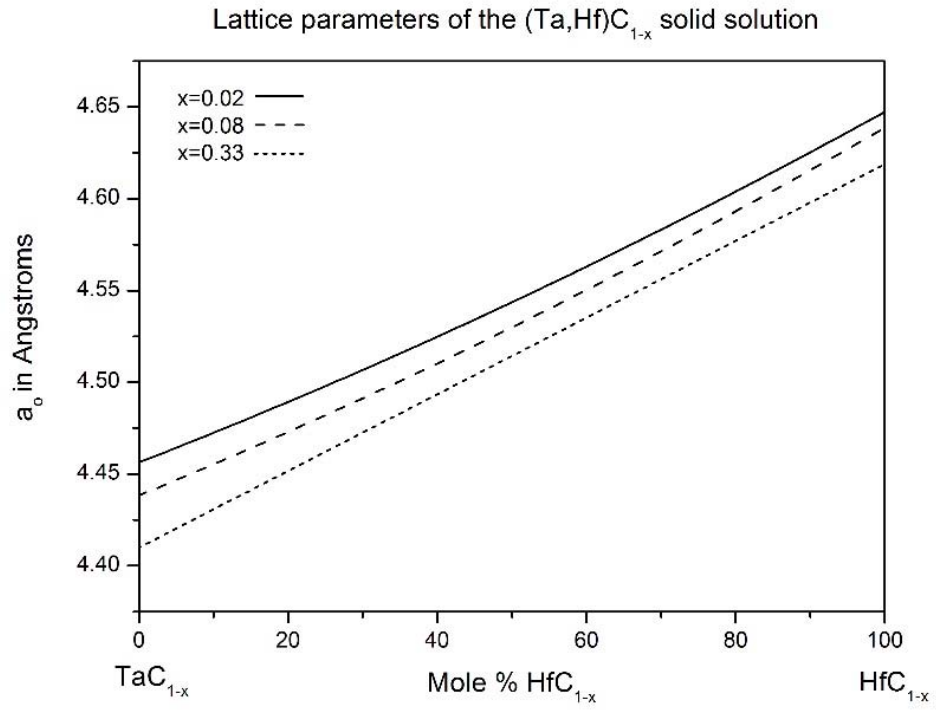

Figure 2.7 Lattice parameters of the (Ta,Hf)C_{1-x} solid solution as a function of the carbon defect [27].

Because of the extreme melting temperatures (T_m's) of both TaC and HfC, there has been considerable interest in the study and clarification of high temperature phase relationships in the TaC-HfC system. In 1930, Agte and Alterthum [28] reported melting points of compounds in the TaC-HfC system. Their results show a maximum melting temperature for 4TaC-1HfC at 3940 °C, higher than the melting temperature of the monocarbides, with T_m of HfC higher than TaC. This trend was later confirmed by the work of Andrievskii et al. [29], with specimens prepared by hot pressing (HP) at 2200 °C for 15 min and 20 MPa and then annealed 1 h at 2500 °C, from powders prepared by carbothermal reduction at 2000 °C. A maximum T_m of 3990 °C was reported for 4TaC-1HfC, with lower temperatures for $HfC_{0.97}$ at 3750 °C, and 3840 °C for $TaC_{0.98}$. Furthermore, the extensive work conducted by Rudy [27] on ternary phase equilibria in metal-carbon systems did not confirm this trend, his results show a maximum T_m for $TaC_{0.88}$ of 3983 °C and a decreasing trend in T_m as the HfC concentration is increased to 3928 °C for $HfC_{0.94}$ (Figure 2.8). Samples were prepared from commercial monocarbides, mixed, cold-compacted and melted in an electron beam furnace then an additional homogenisation step by

annealing the specimens under vacuum at 1500 °C for 69 h ($2.7x10^4$ Pa), at 2000 °C for 15-25 h ($6.7x10^{-4}$ Pa) and 2200 °C for 15 h ($6.7x10^{-4}$ Pa). Specific equilibria with temperature were studied by quenching specimens in a preheated tin bath at 300 °C. Melting temperatures were determined using the Pirani-Alterthum technique, which will be described in detail in section 2.10.

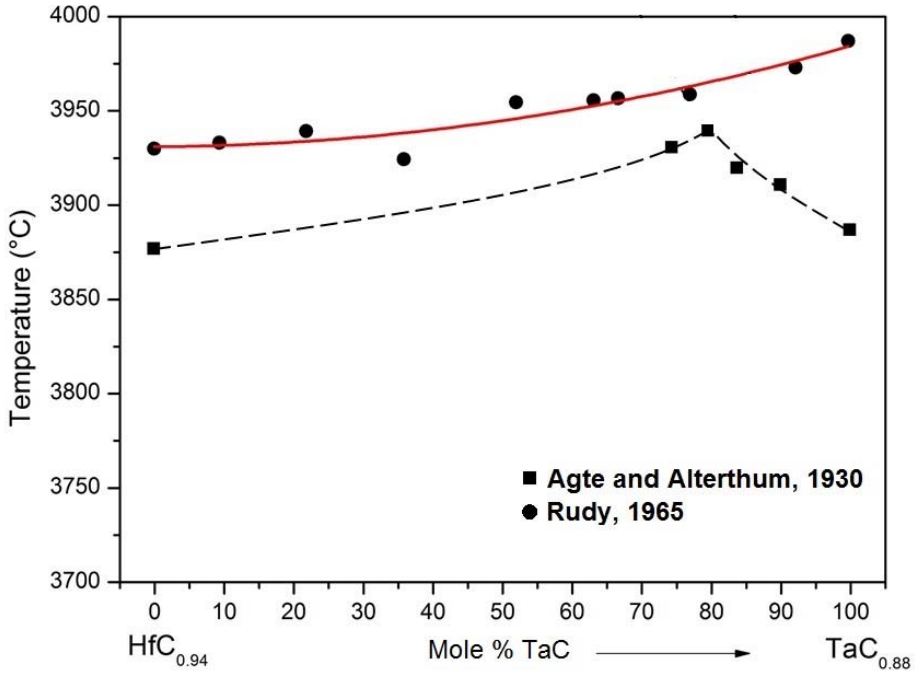

Figure 2.8 Comparison of melting temperatures in the TaC-HfC system as a function of composition as reported by Agte and Alterthum [28] and Rudy [27]. Redrawn from [1].

An interesting melting behaviour is observed when both of the monocarbides are at fixed carbon content of carbon/metal C/M= 0.96 (Figure 2.9), which shows a melting temperature maximum as proposed by Agte and Altherthum [28] and in this case it is at ~30 mole % HfC, with monocarbide melting temperatures higher for HfC (3900 °C) than TaC (3750 °C).

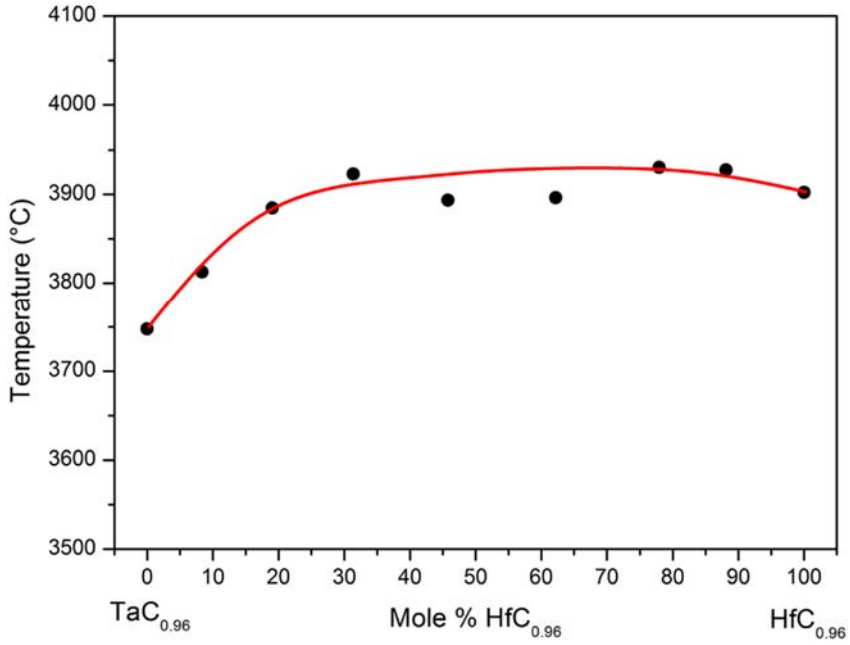

Figure 2.9 Melting temperatures of (Ta,Hf)C solid solutions at a C/M of 0.96. Redrawn from [27].

In addition, a total of 91 compositions in the Ta-Hf-C ternary system were investigated by Rudy [27]. From the melting behaviour of these specimens the liquidus projections were estimated (Figure 2.10). The dotted lines show the highest liquidus line belonging to TaC-HfC. To facilitate the reading on the Ta-Hf-C phase diagram a series of temperature sections from 1000-3980 °C divided in 22 diagrams are included in Rudy's reports [1, 27]. This is the most complete work in experimental phase equilibria to date in the Ta-Hf-C system, the isothermal sections are widely referenced in handbooks [3] and phase equilibria databases [30].

Later work by Gusev [31] reports a calculated phase diagram of the TaC-HfC system (Figure 2.11), in which the melting temperatures of the single member carbides are higher than those of the solid solutions. The different trends and contradictory results of published works raises a debate whether the monocarbides have melting temperatures higher than the solid solutions or if there is a maximum melting temperature within the system between the end members.

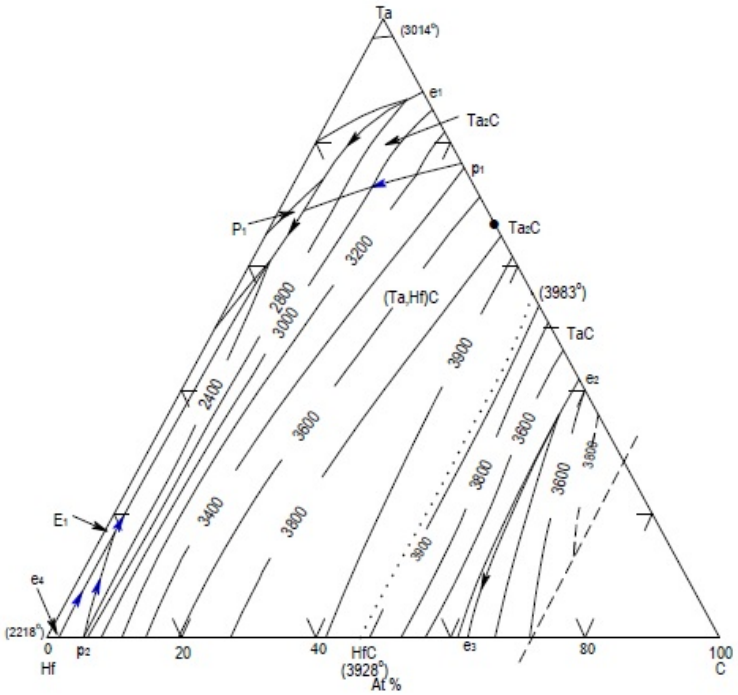

Figure 2.10 Liquidus projections in the Ta-Hf-C system [27].

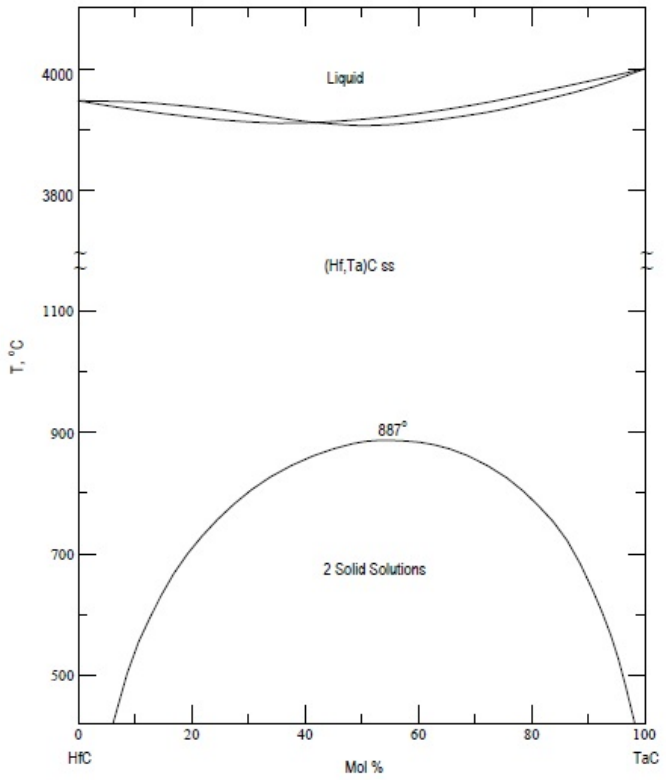

Figure 2.11 Calculated phase diagram of TaC-HfC system [31].

2.6 Powder preparation techniques

Carbides can be synthesised by direct reaction either by melting or solid-state sintering (SSS) under vacuum:

$$M + C \rightarrow MC \qquad \text{Equation 2.1}$$

This method has been widely used for producing carbides for research purposes, since it has the flexibility to produce carbides with a desired stoichiometry or to produce different phases. Many papers, reports and books from the 1960's and 70's used this technique for sample preparation [23, 25-27, 32-35].

Carbothermal reduction of transition metal oxides in a reducing or inert atmosphere is the most common and cheapest commercial method for producing carbides with a near stoichiometric composition [18, 20].

$$MO + C \rightarrow MC + CO\uparrow \qquad \text{Equation 2.2}$$

The reduction temperature and the temperature of carbide formation decreases on passing from oxides of Group IV to those of Group V. The formation temperatures of carbides of Group IV metals are in the range 1900-2200 °C while those of carbides of Group V metals are from 1800-1900 °C [36]. Samsonov and Paderno [37] reported that at 1000-1200 °C a reduction started from HfO_2, at 1300-1800 °C a solid solution was formed (HfC-HfO) and between 1900-2000 °C HfC formed with a carbon deficient lattice, further 1h repeated annealing cycles at 1900 °C resulted in near $HfC_{1.00}$. Liu et al. [38] produced HfC from HfO_2 (100 nm) and carbon black (42 nm). The powder mixtures were heat-treated to 1600 °C for 1 h and 1800 °C for 0.5h. Synthesised powders were of 225 nm size with major impurities of 0.74 wt% O and 0.80 wt% Zr.

Tantalum carbide was first prepared by Joly in 1876 when Ta_2O_5 and carbon were heated at about 1500 °C [18]. Since then Ta_2O_5 has been a common starting material for the production of TaC. Silvestroni et al. [39] synthesised TaC powders from Ta_2O_5 (100 nm) and carbon black (42 nm) with a two stage heating process, 1200 °C for 3 h and 1400 °C for 0.5 h. The purity of the synthesised powder was 99.5 wt%, oxygen content was <0.49 wt% and particle size ~250 nm.

Carbides can be also be synthesised by sintering of metal hydrides and carbon:

$$MH + C \rightarrow MC + H_2 \uparrow \qquad \text{Equation 2.3}$$

or by reaction between metal and a carburising gas:

$$M + C_nM_m \rightarrow MC + H_2 \uparrow \qquad \text{Equation 2.4}$$

$$M + CO \rightarrow MC + CO_2 \uparrow \qquad \text{Equation 2.5}$$

Synthesis of carbides by precipitation reactions from a gas phase is based on the interaction of chlorides of the transition metals with a hydrogen-hydrocarbon (Equation 2.6). Crayton and Gridly [40] used this method to synthesise submicron (35 nm), crystalline TaC by reacting a mixture of methane and tantalum pentachloride vapour in a tube furnace at 1400 °C.

$$MCl_{4,5} + C_nH_m + H_2 \rightarrow MC + HCL \uparrow + C_xH_y \qquad \text{Equation 2.6}$$

The method termed self-propagating high-temperature synthesis (SHS) has been used frequently to synthesise refractory carbides and other UHTCs. Section 2.6.1 reviews SHS since part of the work of this thesis is focused on fabrication of TaC-HfC ceramics via reaction routes which include the use of the SHS technique.

Alternative synthesis routes have been developed to produce sub-micron sized UHTC powders. Venugopal et al. [41] used a sol-gel synthesis route to produce nanosized HfB_2 powders from hafnium chloride and boric acid and using different carbon sources including sucrose, graphite carbon black, carbon nanotubes and liquid and powder phenolic resin. The finest powder was obtained using powder phenolic resin as the carbon source and the particle size was between 30 and 150 nm. Patra et al. [42] synthesised nanosized HfC (~50 nm) using a hybrid polymer precursor consisting of pectin and hafnium tetrachloride. The complete conversion to HfC during carbothermal reduction was achieved at ~1300 °C.

2.6.1 Self-propagating high-temperature synthesis (SHS)

SHS is a process in which the initial reagents, compressed as a powder mixture, are ignited producing a chemical reaction with sufficient heat release that it becomes self-sustaining. This process evolved from the initial studies from Merzhanov et al. [43] on combustion of solid compacts, at the Institute of Chemical Physics in Chernogolovka, Russia. Russian researchers lead by Merzhanov produced more than 500 materials using the SHS method, including refractory materials, composites, intermetallics, abrasives, electronic materials and metallic and ceramics superconductors [44, 45].

Conventional production of refractory materials is both energy and time consuming, because high-temperature furnaces and long processing times (on the order of hours or days) are required. Because in SHS high-temperature equipment is not necessarily required and the processing times are on the order of seconds there are advantages with respect to energy and time [44]. Another advantage is that because of the high processing temperatures involved, products are usually of high purity due to the vaporisation of volatile contaminants [46].

SHS takes place in one of two general forms. One called “propagating” in which the SHS reactions occur when the powder reactants are ignited followed by the propagation of the combustion wave through the compact. Secondly, a “bulk” mode in which the powder compact is heated rapidly (usually in a furnace) until the synthesis occurs simultaneously thought the whole sample. This is also called a

thermal explosion and combustion temperatures during this process are in excess of 2000 °C [44, 45]. All SHS processes are initiated by a rapid input of energy from an external source. A wide variety of ignition techniques are used, including but not limited to electric arc, electrically heated W/Mo filament, magnesium ribbon, laser pulse and rapid heating in a furnace.

Once the compact has been ignited, very high temperatures are achieved in significantly short times (several seconds) due to the exothermic nature of the reactions. Since there is little time for the heat to dissipate to the surroundings, the maximum temperature to which the product is raised can be assumed to be the adiabatic temperature T_{ad} [43, 47]. Merzhanov et al. [43] suggested that if T_{ad} <1230 °C combustion does not occur and if T_{ad} >2230 °C the system is self-sustaining. If T_{ad} is in the range of 1230-2230 °C the combustion wave does not propagate but this could be achieved by initial heating of the reactants. In systems where high T_{ad} is achieved (i.e. Ta-C and Hf-C) the products can be consolidated after synthesis. A combination of synthesis and sintering, like reactive spark plasma sintering (RSPS) used in this work, is an ideal condition for SHS since the available exothermic heat is used to achieve a high degree of consolidation.

A physico-chemical classification of SHS mechanisms for binary systems was made by Merzhanov [48] and is based on the adiabatic temperatures (T_{ad}) and melting and boiling points of the reactants. If the adiabatic temperature is less than the boiling point of both elements in the reaction, no vapour phase is present in the reaction. Reactions occur in liquid phase when the adiabatic temperature is greater than the melting point but lower than the boiling point of the reactants. If the adiabatic temperature is between the melting points of the components, the molten component spreads at a higher rate in the compact, resulting in the highest rate of combustion. In solid-state combustion, also known as solid flame (SF) the reactants and products are in the solid state, and this occurs when the adiabatic temperature is less than the melting temperature of the product [45]. The melting temperatures of reactants and products and the adiabatic combustion temperatures of the Ta-C and Hf-C are shown in Table 2.2.

Reaction	Melting point (°C)	Sublimation point (°C)	Melting point (°C)	Adiabatic combustion temperature, T_{ad} (°C)
X+Y → Z	X	Y	Z	
Hf + C → HfC	2200	3550	3960	3940
Ta + C → TaC	2996	3550	3985	2461

Table 2.2 Combustion data of binary element reactions of Ta-C and Hf-C.

In solid-solid reactions only a diffusion mechanism is possible. Once the product layer forms between the reactants, further reaction occurs by diffusion of reactant atoms across the product layer leading to slow reaction kinetics. The lowest combustion velocities are found in solid-solid reactions. Particle size is another factor that influences the combustion because the kinetics of solid state reactions are dependent on the dispersion and the effective contact area of the reactants. In experimental studies in the Ta-C system Shkiro et al. [49], showed that a change in the particle size of the metallic Ta component can have a significant influence on the product conversion and combustion rate. Ta mixtures (2 and 45 μm) of various ratios were used. The increase in content of the coarse fraction in the mixture had a negative effect on the combustion rate and the unreacted carbon content increased; while the fine fraction is totally burned up the coarse is only partially so the heat liberation decreases and the heat loss lead to significant lack of conversion.

The term solid flame (SF) indicates that no liquid or gaseous phases are involved in the combustion; however, starting powders always contain a certain amount of absorbed and dissolved gases that are released upon heating. Reports reveal that H_2, CO, CO_2 and N_2 are liberated during combustion in the Ta-C system [49-51]. Benck [52] also observed in Hf-C compacts, after the completion of the reaction while the products are still at high temperature, that HfC oxidises and forms CO and HfO_2. In addition, the evolution of gas may have an effect on the SF and can lead to elongation of burning samples and a

pressure dependence of the combustion velocity. The gas phase may be formed from the reduction of the oxide films at the surface of metal particles. The gaseous impurities in SF act as a gas transporting agent for reactants increasing the effective contact surface between particles [53]. Borovinskaya quoted in [53] reported that contaminated powders (of a technical pure grade) in the Mo-B system reacted in the SF mode, where the high purity grade powders did not react, it was assumed that the impurities acted as activators by promoting the gas transport of reactants.

In addition, it has been observed that the density of the starting compact and preheating temperature of the powders have an effect on the final composition of the reaction products. Also the combustion behaviour varies with starting stoichiometry of the sample compact [50, 54]. Experiments by Yeh and Liu [54] show that the flame propagation velocity increased with sample density and also improves the efficiency of product conversion. Significant amounts of unreacted Ta were found on TaC samples obtained from a 30% theoretical density (TD) compact preheated at 100 °C. However, complete conversion was achieved on a compact with 45% TD. This was also observed on compacts with a stoichiometry of Ta:C=2:1 where at 30% TD incomplete conversion was also observed. By increasing the density of the compact to 45% a single phase Ta_2C was identified.

Several authors have used a gas phase to assist in the solid state combustion as gas transporting agents. Experiments in [55] show that the ignition of Ta:C=2:1 was not possible without a transport agent being present. Combustion was made possible only after iodine was introduced. Kim and Wooldridge [56] used iodine and carbon dioxide as transport agents in Ta-C powders which resulted in an overall increase in the efficiency of the conversion of the products. Higher stoichiometry ratios were obtained, 0.96 for I_2- and 0.94 for CO_2-assisted systems, compared to a maximum of 0.90 for unassisted SHS systems.

2.7 Densification

Because of the nature of their atomic bonding, low-self diffusion coefficients, oxygen impurities on particle surfaces and the micrometre size of powders, the sinterability of UHTC powder is low.

Conventional consolidation methods like hot-pressing (HP) have been widely used for the densification of TaC, HfC and other UHTCs, since high processing temperatures (>1800 °C) and mechanical pressures are required for achieving high densification in UHTCs. Other methods such as pressureless sintering (PS) and hot isostatic pressing (HIP) are also common sintering techniques used for UHTCs. Recent developments in spark plasma sintering (SPS) technology have increased the ease of processing of materials and UHTCs by this technology. An exponential increase in papers published related to this technique and its applications has been observed since the commercial availability of SPS equipment from the 1990's. Special attention is made in this thesis to the SPS technique since it has been used for all processing routes in this work.

In polycrystalline ceramic materials there are several mechanisms of sintering that can be identified. Surface diffusion, lattice diffusion from the particles to the neck and vapour transport, are the sintering mechanisms that lead to neck grow without densification. Grain boundary diffusion and lattice diffusion from the grain boundary to the pore are the most important mechanisms for densification in ceramics. The latter permits neck grow and also densification. Plastic flow by dislocation motion is another sintering mechanism but it is more common in sintering of metal powders [57].

Also worth mentioning that for analytical purposes sintering is commonly divided in three stages. The initial stage features rapid inter-particle neck growth by diffusion, vapour transport, plastic flow or viscous flow. Shrinkage or densification accompanies neck growth for the densifying mechanisms with a relative density up to ~65%. The second or intermediate stage begins when the pore phase has reached their equilibrium shapes dictated by surface and interfacial tensions with a continuous pore phase. The intermediate stage normally ends when the relative density is ~90%. The final stage is when the microstructural features consist of an equilibrium pore shape with isolated pores at the grain corners and it is assumed that the pores shrink continuously [57].

2.7.1 Hot pressing (HP)

In hot pressing temperature and pressure are applied simultaneously to a powder compact. The pressure applied during sintering accelerates the kinetics of densification by increasing the contact stress between particles and improves packing by rearranging particle positions. The energy available for densification is increased by the application of pressure during sintering [58].

The source of pressure is usually a hydraulic press with a water-cooled platen attached to the ram. To extend the ram into the furnace blocks of graphite or refractory material are used. One of the most important elements in the hot press is the die material. It needs to be capable of withstanding temperature, transient thermal stresses and high hot-pressing loads. Graphite is the most widely used die and piston material because it is relatively inexpensive, is easily machined and has excellent creep resistance at high temperatures. A common problem is the reactivity of graphite towards other ceramics, which can lead to deterioration of the contact surfaces of the die or bonding of the sample to the die wall. To minimize this problem, the die surfaces can be coated with boron nitride if the temperature remains below 1350 °C. Another common solution is lining the graphite die with graphite foil, this prolongs the life of the die and reduces substantially bonding between the die and the sample [57].

In historic studies, Fischer [59] hot-pressed 4TaC-1HfC powders and studied the effect of hot-pressing variables, temperature, pressure and time on the density and grain size. The initial particle size was 1.5 μm. 100% TD was achieved on specimens hot-pressed at 2530 °C and 50 MPa for 15 min. Grain size after hot pressing was 28 μm. Specimens hot-pressed at 2730 °C had a grain size of 13.5 μm. The author suggests that recrystallization may have occurred at or about 2600 °C. Andrievskii et al. [29] consolidated 4TaC-1HfC, 3TaC-1HfC and 5TaC-HfC powders by hot pressing at 2200 °C for 15 min and 20MPa with an additional annealing step at 2500 °C for 1 h, the specimens did not exceed 5% porosity. In more recent studies by Gaballa et al. [60], 4TaC-1HfC powders were subjected to high energy milling for 9 h to mechanically alloy the powders and reduce the sintering temperature. After milling the powders were hot-pressed at 1500 °C for 60 min and 100 MPa, the relative density obtained was 98.6%.

Scholz [61] showed that even small additions of Fe (30 ppm) in hot-pressed TaC strongly affect the sintering due to formation of liquid phase. Roeder and Clerk [62] hot-pressed TaC with 1 wt% additions of Mo and Ni in the temperature range of 1400-2600 °C and 30 MPa. The metals were used as sintering aids, however the metal additions concentrated at grain boundaries causing rapid grain growth leading to lower densities, with similar relative density (~94%) for both compositions TaC-Mo and TaC-Ni at 2600 °C. Ramqvist [63] obtained a relative density of 93% for monolithic TaC at 2760 °C for 15 min and 40 MPa and 99% for HfC at 2900 °C for 20 min and 40 MPa. No marked differences were observed in sintering properties of mixed carbides of TaC-NbC (35 mol% - 65 mol%) compared to the sintering behaviour of pure TaC.

Commercial powder of TaC was hot-pressed from 1900-2400 °C by Zhang et al. [64], achieving 96% relative density at 2400 °C and 30 MPa without the use of sintering aids (Figure 2.12). Analysis by SEM revealed that grain growth occurred ≥2300 °C. Several studies by the same authors [64, 65] were conducted by adding B_4C and C and a combination of the two as sintering aids with the purpose of reacting with the oxide impurities on the surface of the TaC powders to enhance densification. The higher relative density was achieved with a combination of B_4C (0.43 wt%) plus C (0.13 wt%) to a >96% relative density at 2300 °C and 30 MPa and a hold time of 45 min (Figure 2.13). Furthermore, by adding 2 wt% B_4C to TaC [65] a fully dense ceramic (>99%) was consolidated at 2100 °C. The presence of TaB_2 suggests that a reaction occurred between TaC and B_4C, that enhanced the densification and suppressed the grain growth. The addition of 10 wt% TaB_2 to TaC [66] resulted in a relative density of ~99% at 2100 °C which was higher than the relative density of monolithic TaC (85% TD) hot pressed at the same temperature.

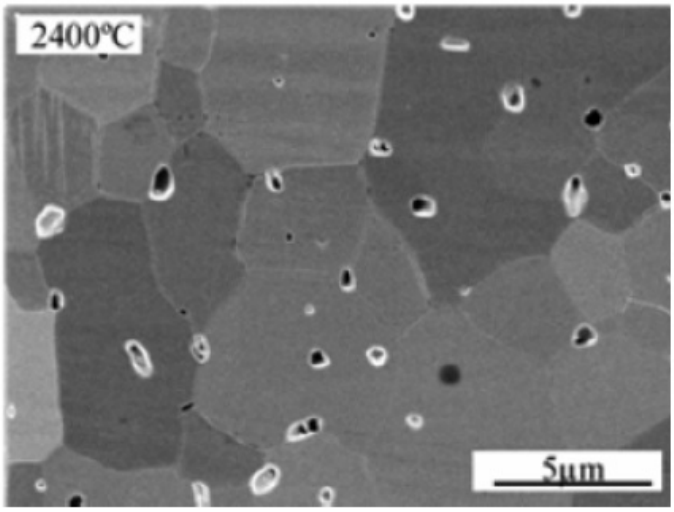

Figure 2.12 BSE image of the microstructure of TaC hot pressed without additives at 2400 °C [64].

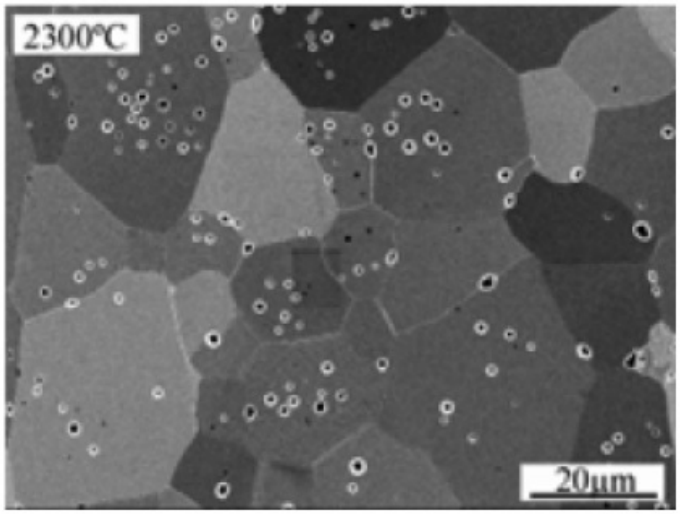

Figure 2.13 BSE image of the microstructure of TaC hot pressed at 2300 °C with 0.43 wt% B_4C + 0.13 wt% C added [64].

Sciti et al. [67] achieved high relative density in TaC- and HfC-based ceramics by adding 15 vol% of $TaSi_2$ and $MoSi_2$ as sintering aids. Hot pressed specimens were densified to 98-99% TD in the temperature range of 1750-1900 °C. The addition of $TaSi_2$ lowered the maximum sintering temperature by ~100 °C for TaC- and 140 °C for HfC-based composites compared to addition of $MoSi_2$.

2.7.2 Pressureless sintering (PS)

One advantage of pressureless sintering of UHTCs over hot pressing is that it would enable the fabrication of components to a near-net shape with complex shapes. The major limitation of hot pressing is the shape capability. Flat plates, blocks or cylinders are relatively easy to hot press, while long cylinders, non-uniform cross sections and intricate shapes are difficult by conventional uniaxial techniques. To enhance densification during PS, sintering aids are used to form a liquid phase, reactive liquid phase or to form a solid solution. In liquid-phase sintering the liquid thoroughly wets the solid particles at the sintering temperature. The capillary pressure from the liquid between the particles, enhances the densification by several mechanisms: rearranges particles to achieve better packing, increases the contact pressure between particles which increases the rate of materials transfer, by solution and precipitation, creep and plastic deformation, vapour transport and grain growth. During reactive liquid sintering, the densification forces are similar to those of liquid-phase sintering, but the liquid changes in composition or disappears during the sintering process or after it is completed [58].

Monolithic HfC showed poor sinterability in experiments conducted by Sciti et al. [68], the specimens were initially cold isostatically pressed (CIP) at 350 MPa and sintered at 1950 °C for 1 h in flowing Ar. Pure HfC was ~70% dense. Adding $MoSi_2$ to 5 vol% as sintering aid increased the relative density to 98% and the mean grain size was ~4 μm. Higher contents of $MoSi_2$ did not show any improvement in final density of the specimens which decreased to 96.5% TD and a mean grain size, MGS of ~3 μm with 20 vol% $MoSi_2$. Furthermore, the sintering behaviour of nanosized HfC powders was studied by Liu et al. [38]. Ultrafine 225 nm powders of HfC were synthesised by carbothermal reduction of HfO_2 with carbon black. The powders were PS'd at 2400 °C and a relative density as high as 98.4% and a MGS of 4 μm was achieved for monolithic HfC. In addition, commercial TaC powders (0.6 μm in size) were PS'd at 2300 °C without sintering aids also by Liu et al. [69]. A 97.5% relative density with a MGS of ~2 μm was achieved.

Silvestroni et al. [70] studied sintering behaviour of commercial powders of ZrC, HfC and TaC with and without sintering aids. Specimens were sintered at 1950 °C for 1 h in flowing Ar. Monolithic TaC

showed better sinterability (~91% TD) compared to that of pure HfC (~70% TD). Addition of 5 vol% of $MoSi_2$ was enough to achieve almost full density (~98% TD) in HfC while 10 vol% was required for TaC to reach a similar relative density. A coarser MGS was observed in TaC-based specimens (5-7 μm) than in the HfC-based ceramics (2-4 μm).

Gaffhari et al. [71] consolidated 4TaC-1HfC powders with addition of 4-30 vol% of $MoSi_2$ as sintering aid. Specimens were sintered at 2000 °C for 1 h. 24 vol% $MoSi_2$ was found as the optimum amount in these experiments since the relative density at this concentration was 94.2%. Above 24 vol% did not increase noticeably the density of the samples.

2.7.3 Spark plasma sintering

Spark plasma sintering (SPS) is a low voltage, pulsed direct current (DC) activated, pressure assisted synthesis technique [72]. This technique can also be used to synthesise and densify materials in the same step [73], as in this thesis with reactive spark plasma sintering (RSPS). SPS is similar to HP with the main difference being the way in which the heat is produced and transmitted to the material. If the initial powder compact is conductive, the energy is dissipated within the sample and the conductive punch and die tooling. For non-conductive materials electrically-conductive tools must be used and the heat produced by Joule heating is transmitted by conduction to the sample. This technique is also known as field-assisted sintering technology (FAST) but commercially and in most journal publications the name of SPS is more widely used, although the existence of a plasma during sintering is still the subject of much debate [74, 75].

In the 1960's Inoue invented the spark sintering method based on pulsed current, but commercialisation of this technology was not a success. After Inoue's patents rights came to an end in the 1990's, several companies started industrial production of spark plasma sintering machines, in particular the Japanese company Sumitomo Coal Mining Co. Ltd., this explains the predominance of patents and publications from far eastern countries in this field. Later, FTC Systeme GmbH in Germany and Thermal Technology LLC, Inc. in the USA started producing SPS equipment on an industrial scale [72, 76].

The SPS system consists of a mechanical system that also acts as a high power electrical circuit, placed in a controlled atmosphere. A schematic of an SPS apparatus is shown in Figure 2.14. Because of the good electrical conductivity of the tooling used (typical graphite) low voltage can be used (typically below 10 V) and high currents can be produced (1-10 kA) leading to the Joule heating effect. The pulse durations are on the order of milliseconds. One of the advantages of SPS are the high heating rates that can be achieved, as high as 1000 °C/min, thus significantly reducing the processing times [77]. Also the application of mechanical pressure enhances densification with maximum loads as high as 250 kN [76].

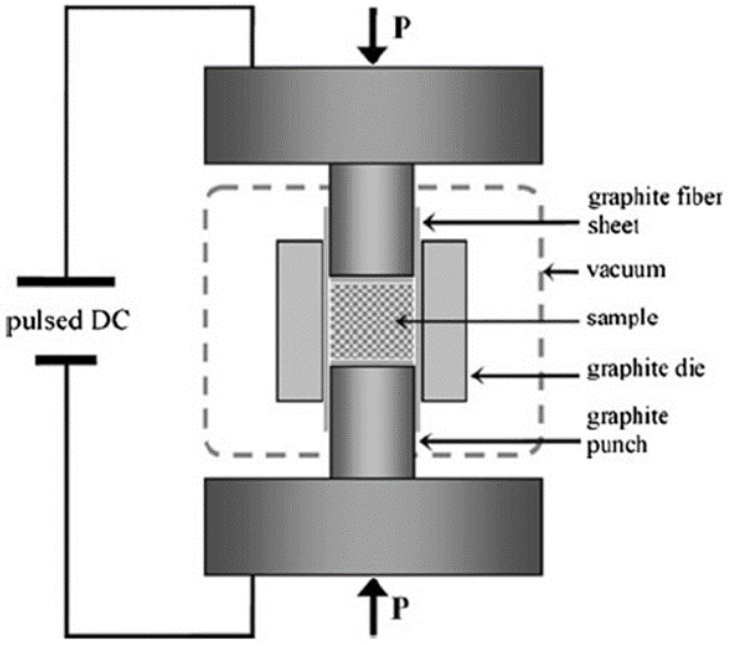

Figure 2.14 Schematic of an SPS apparatus [78].

The mechanical pressure applied in SPS has a direct effect on particle re-arrangement and destruction of agglomerates, particularly in the case of nanometre scale powders. This leads to better contact between particles and enhances the existing densification mechanisms found in pressureless sintering (grain boundary diffusion, lattice diffusion and viscous flow) and activates new mechanisms such as plastic deformation and grain boundary sliding. The permissible amount of stress is limited by the high-temperature fracture strength of the pressing tools; in the case of graphite this is 100-150 MPa [72, 76].

Grain growth is delayed and reduced with mechanical pressure, but not totally suppressed. Reports on several oxides show that the final grain size can be several times larger than the initial particle, and in agglomerated nanopowders this is more evident, a finer starting particle size may lead to even larger grain size than a coarser particle size powder at full density [79].

Another advantage of SPS besides pressure is the availability of high heating rates. When the dominant densification mechanism has higher activation energy than the coarsening mechanism, reaching rapidly high-sintering temperature can be beneficial to enhance densification while retarding microstructure coarsening [76]. Work by Quach et al. [80] and Shen et al. [81] shows that independent of the sintering method, for all heating rates from a fraction of a degree up to several hundreds of °C/min, almost fully dense samples heated at a high rate possessed a reduced grain size compared to those heated at slower rates. Because grain growth requires time at high temperature to enhance grain boundary mobility, the shorter the time the sample is held at maximum temperature, the more coarsening should be suppressed.

When an electrically-conducting powder (such as most UHTCs) is processed by SPS, high electric current flows through the green compact rather than the surrounding graphite die. Since the powder compact is not completely homogeneous and dense, the electric current cannot flow through the material homogeneously. Instead a complicated network of percolating current paths will form, which is a consequence of the initial packing structure of the powder compact. The Joule heating, fundamental to the SPS process, occurs along the percolating current paths [76].

Common atmospheres present in SPS are vacuum (10^{-4} to 10^{-5} bar), inert gas (argon, nitrogen, up to 1.3 bar) or reducing hydrogen gas mixture, which are recommended atmospheres for sintering metals and non-oxide ceramics. Furthermore, as the sample is enclosed in the pressing die, pressure and compositions inside the die can strongly differ from the atmosphere outside. Graphite starts to react with oxygen present in the sample at 600 °C, and oxygen partial pressure decreases within the furnace and especially in the pressing tool. CO forms due to reaction of moisture, oxygen forms oxides in the material with the graphite die, this produces a reducing atmosphere and intensive gas transport between

the die and the sample as long as open porosity exists. This can result in precipitation of carbides and carbon in the sample or a reduction of the oxides [76].

Sciti et al. [82] densified HfC powders (1.5 μm size) with and without $MoSi_2$ as sintering aid using SPS. The addition of 1 vol% $MoSi_2$ enhanced the densification by reducing the sintering temperature by 300 °C, from 2200 °C to 1900 °C, with a relative density of 98%. A small amount of a secondary SiC phase was detected on specimens sintered with additional $MoSi_2$. MGS was limited to 2.2 μm by 1 vol% $MoSi_2$ addition and SPS at 1900 °C for 3 min and 65 MPa compared to MGS of 19 μm for pure HfC sintered at 2200 °C for 3 min and 100 MPa. Ghaffari et al. [83] used $TaSi_2$ and $MoSi_2$ as sintering aids to enhance the densification of 4TaC-1HfC powder mixtures of commercial TaC and HfC. Full density was achieved for both compositions with additional 12 vol% $TaSi_2$ or $MoSi_2$ at a sintering temperature of 1650 °C for 5 min and 30 MPa. MGS of ~6 μm was similar for both sintered products.

Commercial powders of TaC (<44 μm) were consolidated by SPS up to 2400 °C by Khalegui et al. [84]. By adding 0.77 vol% of carbon nanotubes (CNT) at a sintering schedule of 2300 °C for 20 min and 30 MPa, TD increased from 92% for pure TaC to 96% with additional CNT's. MGS was similar for both specimens (~4 μm) suggesting that this form of carbon does not limit grain growth. However, work by Bakshi et al. [85] shows that the addition of 4 vol% of CNT's to TaC limits the grain growth at very high mechanical pressures (255 MPa) and using SiC tooling, from 4.96 μm to 1.64 μm. Full density was achieved for both specimens. Other types of carbon have also been used as sintering aids, Nieto et al. [86] reported the use of graphene nanoplatelets (GNP) improved the relative density of TaC by 4% by adding 5 vol% of GNP's, from 94% TD of monolithic TaC to 98% with GNP's at a thermal schedule of 1850 °C for 10 min and 80 MPa. Grain size was also limited to 1.4 μm compared to 4.5 μm of pure TaC sintered at the same conditions.

The role of B_4C as a sintering aid and grain growth inhibitor has been studied [87]. 1 wt% nanosize B_4C (50 nm) was added to TaC. Fully dense materials were obtained in specimens SPS'd at 1850 °C for 10 min and 255 MPa. MGS was reduced with B_4C addition from 4.9 to 0.7 μm. TEM analysis shows that

TaC reacted with B_4C leading to a formation of a TaB_2/C phase at grain boundaries, suggesting that this phase leads to grain boundary pinning, thus limiting the grain growth.

Substoichiometric $TaC_{0.7}$ was consolidated by SPS at 1600-1900 °C using TaC and Ta as the starting powders [88]. A TD of 95% was achieved at 1600 °C for 5 min and 30 MPa. The addition of Ta resulted in formation of Ta_2C intermediate phase. Further increase in sintering temperature to 1900 °C resulted in the formation of a plate-like ζ-Ta_4C_{3-x} (~21 wt%) dispersed in a TaC_{1-x} matrix.

2.7.4 Reactive sintering

In-situ reaction synthesis and densification of UHTC diborides has been explored using reactive hot pressing. ZrB_2-based composites were fabricated from starting powders of Zr, SiB_4 and C [89] or Zr, B_4C and Si [90]. The objective of these experiments was to produce dense ZrB_2-ZrC-SiC ceramics. The HP route is characterized by relatively long processing times (on the order of hours) due to the low heating rates. Compared to HP, high heating rates can be applied in SPS, accelerating the processing times and leading to reduction in energy cost. As mentioned in Section 2.7.3, the SPS furnace can be used as both a powder synthesis and ceramic sintering instrument. The fast application of thermal energy by SPS can be applied to ignite powder compacts of reactants to produce a SHS exothermic reaction. Reactive routes by SPS can be conducted using two methods: a one-step route in which synthesis and sintering are conducted in a single step, this known as reactive spark plasma sintering (RSPS) and a two-step route in which powders are synthesised by SHS using an SPS furnace, then the powders are ground and sieved then subsequently consolidated also using SPS, this technique is known as SHS+SPS.

These reactive routes have been successfully applied to UHTCs, mostly on hafnium and zirconium diborides. The development of other UHTCs like TaC and HfC and their binary systems has not been as extensively explored, and the literature on TaC-HfC fabricated by reactive routes is non-existent. Extensive work has been conducted by a research group in the University of Caglari in Italy on the development of UHTC composites and other refractory materials using reactive routes. TiC-TiB_2

composites were produced from initial powder mixtures of Ti, B_4C and C [91, 92]. The effect of high energy ball milling was reported and as the milling time was increased the final product density increased. Full density was achieved with powders milled for 6 h at 1700 °C and 20 MPa. In addition, RSPS was conducted on WC-6Co composites from starting elemental W, C, and Co, a relative density of 99% was achieved by the application of 800 A of current with mechanical pressure of 40 MPa for 4 min [93].

ZrB_2-SiC composites were fabricated by Licheri et al. [94] from commercial powders of Zr, B_4C and Si using the RSPS processing route. The sintering temperature was 1800 °C and a completely dense product was obtained after 20 min of sintering time and 20 MPa of applied pressure. It was observed that heating rates >210 °C/min and mechanical pressures >30 MPa resulted in damaged die/plungers during RSPS due to the highly exothermic reaction during the combustion.

Orrù et al. [95] studied different monolithic (HfB_2 and TaB_2) and binary composite (ZrB_2-SiC, HfB_2-SiC and TaB_2-SiC) systems prepared by RSPS and SHS+SPS. For monolithic systems RSPS is preferable for achieving higher density, while for binary composite systems a SHS+SPS route is more beneficial, since the solid-state diffusion mechanism is present during the formation of the UHTC composite, accompanied by a more gradual and slower sample consolidation.

2.8 Mechanical properties

Beside high melting temperatures, the strength of UHTCs at high temperature makes them attractive for structural applications. Measurement of mechanical properties requires the fabrication of dense samples, which is difficult with UHTCs due to the extremely high sintering temperatures. In some cases, the high temperatures and mechanical pressures used during sintering limit the size of the tooling, resulting in size limitation of the final sample, which makes strength measurements difficult to conduct [4, 9].

Room temperature flexural strength for HfC was reported in the range of 352-467 MPa [39, 82], however for fully dense HfC + 3 vol% $MoSi_2$ with a grain size of 0.9 μm strength was reported at 868

MPa [82] consolidated by SPS. TaC specimens with >94% relative density have strengths of 585-690 MPa with and without sintering additives [39, 64], although a value of 376 MPa was reported for a porous sample (15% porosity). Reports on high temperature strength of TaC- and HfC-based ceramics are scarce; strength at 1500 °C for pure HfC was reported at 301 MPa [39] and with $MoSi_2$ in the range of 241-406 MPa [39, 68]. In addition, pure TaC strength at 1500 °C was measured at 257 MPa and with 5 vol% $MoSi_2$ at 308 MPa both values reported by Silvestroni et al. [39].

Room temperature elastic modulus (*E*), Vickers indentation (HV_1) and fracture toughness values for TaC and HfC, pure or with or without sintering additives are summarised in Table 2.3. Also for comparison purposes the fabrication method and thermal schedule, relative density and grain size are included. The elastic modulus for monolithic HfC (~450 GPa) [82] is consistent with historical data reported by Toth [18]. Elastic moduli of HfC with disilicides range from 415-489 GPa. Also the elastic modulus of TaC (547 GPa) [86] is similar to that reported in [18].

Hardness of polycrystalline HfC is reported at 18.3 GPa [39], while an addition of 3 vol% $MoSi_2$ consolidated by SPS result in an increase in hardness to 22.2 GPa [82], but higher additions do not show a trend of increasing hardness. For other UHTCs, $MoSi_2$ has been reported to decrease hardness in ZrB_2- and HfB_2-based ceramics. In general, HfC hardness with and without sintering aids is in the range of 16.1-22.2 GPa. Values of TaC hardness for >94% theoretical density have been reported between 14.1-18.9 GPa. TaC with additions of different types of carbon (CNTs and GNPs) shows lower hardness than pure TaC [84-86]. Also the addition of $MoSi_2$ [39, 67, 70] and $TaSi_2$ [67] decreases the hardness of TaC. An increase in hardness (~20 GPa) of a TaC-20 vol% SiC composite is reported by Liu et al. [96].

Composition (vol%)	Sintering (°C, min, MPa)	Rel. density (%)	MGS (μm)	*E* (GPa)	HV_1 (GPa)	K_{IC} (MPa·m$^{1/2}$)	Reference
HfC	HP, 1900, 20, 30	89	0.33	-	5.79 ± 0.6	1.88 ± 0.15	[39]
HfC	SPS, 2200, 3, 65	98	19	~450	18.3 ± 0.5	-	[82]
HfC + 3% $MoSi_2$	SPS, 1750, 5, 100	99.7	0.9	~480	22.2 ± 0.7	~2.5	[82]
HfC + 5% $MoSi_2$	PS, 1950, 60	98.1	~4	434 ± 4	15.6 ± 0.6	3.62 ± 0.13	[68]
HfC + 5% $MoSi_2$	HP, 1900, 20, 30	93	1.9	-	17.8 ± 1.4	2.94 ± 0.15	[39]
HfC + 10% $MoSi_2$	PS, 1950, 60	97.8	3	415 ± 4	16.1 ± 0.4	3.53 ± 0.29	[70]
HfC + 15% $MoSi_2$	HP,1900, 10, 30	99.9	1.2	451 ± 5	19.6 ± 0.5	3.80 ± 0.03	[67]
HfC + 20% $MoSi_2$	PS, 1950, 60	96.5	~3	385 ± 4	15.6 ± 0.9	3.43 ± 0.13	[68]
HfC + 15% $TaSi_2$	HP,1900, 10, 30	98.6	0.8	489 ± 5	18.4 ± 0.9	3.58 ± 0.03	[67]
TaC	SPS, 1850, 10, 100	94.6	4.5	547 ± 25	18.9 ± 3.4	5.6 ± 1.8	[86]
TaC	SPS, 1850, 10, 255	100	4.93	469 ± 46	-	-	[85]
TaC	HP, 1900, 5, 30	85	0.8	-	11.1 ± 0.7	2.60 ±0.1	[39]
TaC	HP, 2300, 60, 30	94	-	472 ± 7	14.1 ± 0.2	3.5 ± 0.2	[66]
TaC + 1% B_4C	SPS, 1850, 10, 255	100	0.71	364 ± 38	-	-	[87]
TaC + 2% B_4C	HP, 2100, 60, 30	>99		468 ± 7	16.3 ± 0.2	3.4 ± 0.1	[65]
TaC + 0.77% CNT	SPS, 2300, 20, 30	96	3.81	-	11	-	[84]
TaC + 4% CNT	SPS, 1850, 10, 255	100	1.64	313 ± 37	-	-	[85]
TaC + 5% GNP	SPS, 1850, 10, 100	98.8	1.4	490 ± 38	12.9 ± 1.4	11.1 ± 2.4	[86]
TaC + 5% $MoSi_2$	HP, 1900, 5, 30	94	2.8	-	13.6 ± 0.3	3.45 ± 0.2	[39]
TaC + 15% $MoSi_2$	HP, 1900, 10, 30	96.3	1.2	490 ± 5	14.5 ± 0.3	4.7 ± 0.1	[67]
TaC + 20% $MoSi_2$	PS, 1950, 60	95.8	7	476 ± 4	12.1 ± 0.7	3.83 ± 0.14	[70]
TaC + 10% TaB_2	HP, 2100, 60, 30	98.6	-	543 ± 7	19.4 ± 0.6	3.4 ± 0.1	[66]
TaC + 15% $TaSi_2$	HP, 1900, 10, 30	97.3	2.5	486 ± 5	14.6 ± 0.4	4.7 ± 0.1	[67]
TaC + 20% SiC	SPS, 1900, 5, 40	100	-	537 ± 16	20.3 ± 0.6	6.7 ± 0.9	[96]
4TaC-1HfC + 12% $MoSi_2$	SPS, 1650, 5, 30	100	6.2	-	15.2 ± 0.3	3.9 ± 0.2	[83]
4TaC-1HfC + 12% $TaSi_2$	SPS, 1650, 5, 30	100	6.1	-	17.7 ± 0.5	3.19 ± 0.1	[83]

Table 2.3 Composition, fabrication method, relative density, grain size, elastic modulus, Vickers hardness at 1kg load unless specified and fracture toughness of HfC- and TaC-based ceramics reported in the literature (CNT, carbon nanotubes; GNP, graphene nanoplatelets).

Predicted hardness values using calculated elastic constants for HfC are ~33 GPa and for TaC ~25 GPa [97, 98]. In general, HfC-based materials show higher hardness than their TaC-based counterparts processed under the same sintering conditions and with same amounts of additives or without additives.

The fracture toughness of HfC is in the range 2.5-3.8 MPa·$m^{1/2}$ with and without sintering aids, and for TaC 3.5-5.6 MPa·$m^{1/2}$. The values shown in Table 2.3 were obtained using a variety of measurement techniques which makes direct comparison difficult.

2.9 Thermal properties

2.9.1 Thermal conductivity

Thermal conductivity of transition metal carbides is lower compared to those of transition metal diborides. At room temperature, the thermal conductivities of TaC and HfC (20-22 W/m·K) can be two or three times lower than those of ZrB_2 and HfB_2 (~80 W/m·K). However, at higher temperatures (>1000 °C) this difference is smaller since a reduction in thermal conductivity by increasing temperature is observed in diborides [5, 99, 100] while in carbides it increases with temperature [3].

For leading edge applications, high thermal conductivity reduces thermal stresses within the material and also allows thermal energy to be conducted away from the tip, and be radiated or conducted to other surfaces of the component with lower heat fluxes, thus reducing the surface temperature for a given heat flux. Current leading edges of space vehicles have relatively blunt profiles, and are typically SiC-based materials that are limited to operating temperatures ~1700 °C. To achieve maximum performance, new designs in leading edges require materials that can withstand operating temperatures above 2000 °C and have a high thermal conductivity that can direct the energy away from the tip of the leading edge. Figure 2.15 illustrates how the surface temperature for a UHTC sharp leading edge is determined by an energy balance of incident heat-flux, and how the energy is re-irradiated and pulled away from the tip to the sides of the component where the heat flux is lower [5].

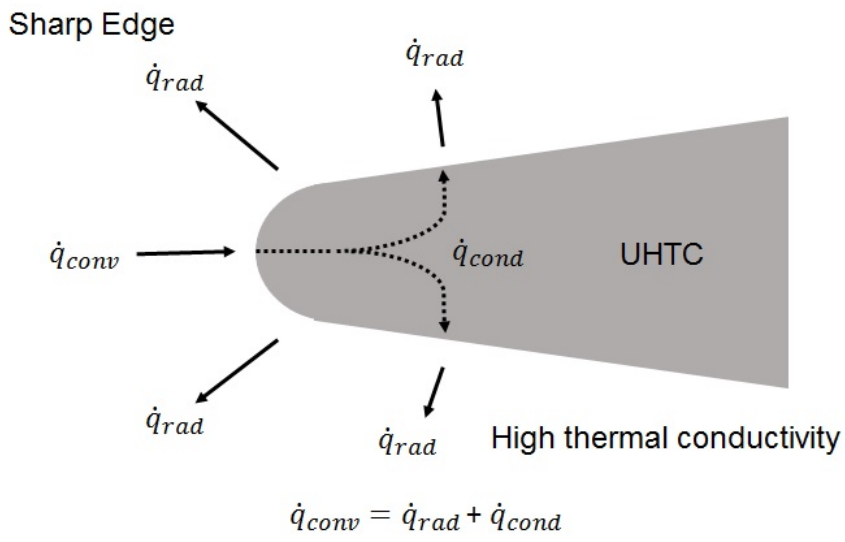

Figure 2.15 Heat conducted and radiated on a sharp UHTC leading edge with high thermal conductivity (q_{conv}: convection heat, q_{rad}: radiated heat and q_{cond}: conducted heat) [5].

The thermal conductivity or K in carbides increases with increasing temperature. The mechanism of thermal conductivity involves two components: K_e that is the conductivity due to electrons and K_p that is the phonon (lattice) conductivity. The total thermal conductivity K is the sum of the conductivities of electrons and phonons [3, 18].

$$K = K_e + K_p \qquad \text{Equation 2.7}$$

In transition metal carbides the K_e increases markedly with temperature, this behaviour is believed to be a result of strong scattering of electrons by carbon vacancies or defects. The scattering of phonons by defects and by conduction electrons reduces the lattice conductivity, K_p, and lessens its temperature dependence. Thus the total thermal conductivity K is controlled by the K_e, while the phonon contribution K_p is small [101].

In a study on cemented transition metal carbides (WC-Co) [102], increase of Co concentration was reported to lower the thermal conductivity due to a formation of a Co-W-C solid solution of lower thermal conductivity, and the overall thermal conductivity of the cemented carbide is lowered, since the

thermal conductivity of Co is lower than that of WC. The higher the percent of Co, the larger the amount of the solid solution and the lower will be the overall thermal conductivity.

Thermal conductivity of $HfC_{0.98}$ up to 800 °C was reported by Opeka et al. [89] and the values are 20, 23 and 30 W/m·K at 20, 400 and 800 °C respectively. Room temperature thermal conductivity was reported by Pierson [3] and the values are 20 W/m·K for HfC and 22.1 W/m·K for TaC.

2.9.2 Thermal expansion

The interatomic spacing between atoms of a carbide, as with any other material, is a function of temperature. The increased energy by increasing temperature causes the atoms to vibrate and move farther apart, meaning that the interatomic spacing increases as a result of thermal expansion. In strongly bonded solids such as transition metal carbides, the amplitude of the vibrations is small and the dimensional changes remain small [3]. The higher the bond energy, the lower is the expansion. Table 2.4 compares the bond energy and the coefficient of thermal expansion of carbides of group IV and V, revealing that the higher the bond energy the lower the CTE.

Carbide	Bond energy (eV)	Thermal expansion at 20 °C ($x10^{-6}$)
TiC	14.20	7.4
ZrC	15.58	6.7
HfC	16.45	6.6
VC	14.63	7.2
NbC	16.62	6.6
TaC	16.92	6.3

Table 2.4 Bond energy and thermal expansion of group IV and V carbides [3].

A decrease in the coefficient of thermal expansion (CTE) of the solid solutions as compared with the individual carbides was observed in a study conducted by Barantseva and Paderno [103]. $Ta_{0.7}Hf_{0.3}C$ showed the lowest CTE in the TaC-HfC system at ~$5.5x10^{-6}$ /K.

2.10 Oxidation

Another feature that is required in UHTCs is the ability to operate in air at high temperatures. Since components made of UHTCs are required to work in air, besides high melting temperatures, oxidation and ablation resistance are important properties needed for material selection to sustain optimum vehicle aerodynamic performance.

The formation of a solid and ablation-resistant high temperature oxide scale is the aim in Zr- and Hf-based UHTCs research. ZrO_2 has a melting temperature of 2710 °C and HfO_2 is 2774 °C. However, one limitation in Ta-based materials is the oxidation product Ta_2O_5 has a relatively low melting point (1882 °C). The oxidation of transition metal carbides is typically more rapid than their corresponding borides; based on their favourable oxidation resistance, the oxidation behaviour of HfB_2 and ZrB_2 has been extensively studied, while the oxidation of transition metal carbides and nitrides has been much less studied [4, 5, 104].

The oxidation of HfC was studied by Berkowitz-Mattuck [105] between 1500-1730 °C and oxygen pressures near 10 Torr. Linear oxidation kinetics were observed with preferential oxidation along grain boundaries. Shimada et al. [106] conducted oxidation studies of HfC at low temperatures (480-600 °C) and oxidation was observed by two processes; a diffusion-controlled process that operates up to about 50% oxidation and a phase-boundary controlled above 50% oxidation. The change in the oxidation process was also associated with the generation of cracks on the grains, resulting from stresses due to the formation of monoclinic HfO_2. In additional work on oxidation of single crystals of HfC at higher temperatures 600-900 °C, also by Shimada et al. [107], linear oxidation rates were also observed. BSE images and EDS showed that the oxide scale was divided into two regions: zone one consisted of a

compact, pore-free oxide phase with high carbon concentration and the second zone was HfO_2 containing many pores and cracks and with a carbon concentration less than half that of zone one.

Bargeron et al. [108] observed three defined layers present on cross sections of HfC specimens oxidised at 1400-1600 °C (Figure 2.16). The layers consisted of a residual carbide layer with dissolved oxygen, a dense oxide interlayer containing carbon and a porous outer layer of HfO_2. The oxidation mechanisms were similar to those reported by Shimada [106, 107], but Bargeron reported the formation of an intermediate oxycarbide layer instead of a layer consisting of HfO_2 and carbon.

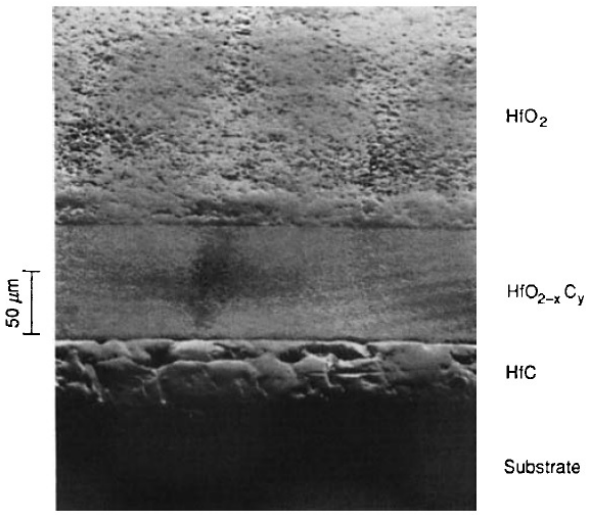

Figure 2.16 SE image of a cross sections of oxidised HfC showing a multilayered structure with defined interfaces. Oxidation was for 600 s at 1875 °C in an atmosphere of 93% argon and 7% oxygen [108].

Oxidation behaviour of hot pressed HfC, HfC-25 wt% TaC and HfC- 7wt% PrC_2 was studied by Courtright et al. [109] between 1200-2200 °C. Parabolic oxide growth was observed on HfC and HfC-25 wt% TaC. Below 1600 °C, the kinetics were dominated by gaseous diffusion across the oxide layer through the pores, and above 1800 °C the kinetics were controlled by diffusion of oxygen through the oxide layer. Furthermore, it was observed that HfC carbides produce CO gas which causes the formation of pores that provide the path for outward diffusion of gaseous CO and inward transport of oxygen though the porous oxide to the bulk material. Cracks and spallation of the oxide layer was found to be

a problem in HfC-based ceramics. The authors [101] reported that additions of TaC and PrC_2 did not improve the oxidation resistance of HfC.

Hot pressed TaC and HfC with 15 vol% additions of $MoSi_2$ and $TaSi_2$ were subjected to oxidation at 1600 °C in air for 15 min [67]. Tests showed that HfC-based composites have higher oxidation resistance than TaC-based composites. Weight gain data for TaC-based materials was higher than HfC-based materials. A "Maltese cross" oxide layer is typically observed on oxidised bulk samples of these carbides [67, 110, 111]. Oxidation of $TaC_{1-x}N_X$ crushed powders from SPS'd samples was carried out at 700-800 °C [112]. $TaC_{0.5}N_{0.5}$ showed the slowest oxidation rate, while the end members TaC and TaN showed the most rapid oxidation rates. Investigations showed that early stages of oxidation N_2 rapidly evolved before CO_2. Wuchina et al. [113] conducted an investigation into oxidation of substoichiometric HfC_x (x=0.67, 0.82 and 0.98) in air at 1500 °C. The oxidation weight and oxide thickness were found to increase with carbon content. The weight gains were 1, 21 and 14 mg/cm^2 for $HfC_{0.67}$, $HfC_{0.82}$ and $HfC_{0.97}$ respectively. The oxide scale in $HfC_{0.67}$ was less porous and contained fewer cracks, this was due to a reduced generation of CO species. An intermediate layer containing graphitic and amorphous carbon was found similar to that reported by Shimada et al. [106, 107, 114].

Opeka [115] showed that in some applications such as rocket engine systems, the formation of TaO_2 can be suppressed by lowering the partial pressure of O_2. This was conducted using an aluminium-containing propellant, and the high temperature capability was demonstrated with exposures of TaC and Ta_2C to an aluminized flame at 3370 °C, much higher than the melting point of Ta_2O_5.

The major challenges for improving oxidation resistance in UHTCs are: to lower the oxidation rates and to ensure that the oxide phases that form remain adherent, with minimal dimensional change to assure structural stability and prolong the life of the component [104]. A significant effort in current research is dedicated to the optimization of UHTC compositions to minimise oxidation rates [116].

2.11 Melting temperature measurements

Measurement of high-temperature phase transitions in refractory materials entails major experimental difficulties due to the extreme conditions produced during the experiments. At temperatures >2200 °C thermal, thermodynamic and thermochemical equilibrium conditions are difficult to obtain. Measurements of phase transitions are affected by disturbances that can originate from the equipment (for example the instability of the heat source) and also from the sample behaviour (chemical interactions with the crucible material, vaporisation, and chemical composition instability) and can lead to measurement inaccuracies and large errors [117, 118] .

In 1923, Pirani and Alterthum [119] developed a melting furnace in which the problems of the chemical interactions with the crucible material were eliminated. The experimental set-up consisted in a bar-shaped specimen clamped between two water-cooled electrodes, then the sample is heated resistively to the temperature of a phase transition. A small black body hole in the centre of the specimen serves as the reference point for optical temperature measurements. Melting temperatures of refractory carbides were measured in subsequent years by Agte and Alterthum [2, 28] using this instrument.

Later Kieffer et al. [120] described an apparatus in which the sample test is positioned in a tantalum cup, supported in a thin tungsten rod. The specimen was heated inside a thin-walled tungsten tube using water-cooled copper electrodes. Sample temperatures were measured in a quartz port in the furnace wall. This technique was well suited for metals and metal alloys, however the melting points of carbides, silicides and borides exceeded the temperature capability of the furnace (~3100 °C).

Graphite was also used frequently as a sample container material for investigation of carbide systems. Melting formation was analysed by post-melting metallographic inspection of the materials after exposure at a series of temperatures [121, 122] or by direct pyrometric observations [123, 124]. Other melting methods include heating of the sample in folded tungsten ribbon [125], in tungsten wire baskets [126] or suspending the specimen with a wire within the tubular heating element of a high temperature furnace [127].

Around 30 years after the Agte and Alterthum work, in 1964 a refined version of a Pirani-type furnace (Figure 2.17), which operates on a "containerless" principle was built at the Aerojet Materials Research facility lead by Rudy [117]. A great number of phase diagrams were determined using this technique, TaC-HfC being one of the first systems to be studied. Furthermore, at the end of the project a compendium was obtained consisting of more than 700 pages that included phase equilibria for over 50 binary and 25 ternary systems. The work also includes liquidus projections, three-dimensional views of ternary systems, vertical and isothermal sections. After 50 years, the phase diagrams and data from this project are still used by researchers working in these materials. The phase diagrams have been reproduced in papers and are still included in phase equilibria electronic databases [30].

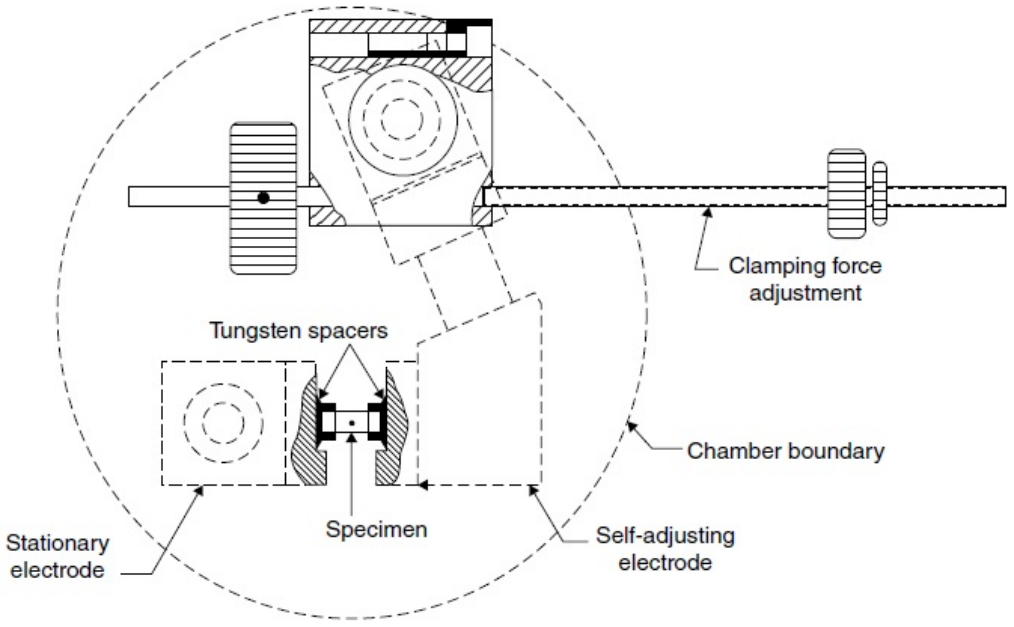

Figure 2.17 Schematic of a Pirani-type melting furnace [117].

More recently, laser heating techniques have been developed to characterise and measure high-temperature phase transitions. Laser heating can be conducted under containerless conditions by levitation techniques [128] or surface heating [129]. For the experimental study of materials with strong vaporisation, such as nonstoichiometric oxides, carbides, nitrides and graphite, the only applicable

technique is laser heating of the sample surface under high pressure inert gas in order to suppress evaporation [118].

A laser heating technique developed at the Institute for Transuranium Elements (ITU) of the European Commission's Joint Research Centre (Karslruhe, Germany) has been successfully used to measure melting points in several refractory materials such as such as uranium carbides [130], uranium oxides [131], plutonium oxides [132, 133], uranium nitrides [134] and zirconium carbides [135, 136]. The results of these studies are in good agreement with literature data. The reduction of the duration of the experiments (on the order of milliseconds) helps in the control of kinetics of undesired phenomena by limiting the time at which the materials are subjected to very high temperatures. In addition, measurements can be performed under containerless conditions with the use of an autoclave with inert gas at high pressure that can keep the evaporation rate within acceptable margins [118]. The laser heating technique and experimental set-up is described in detail by Manara et al. [118] and in Section 3.8 and Section 6.2 of this thesis.

Jackson et al. [135, 136] conducted laser melting experiments in ZrC samples. Samples were fabricated by SPS from commercial powders of ZrC, powders of different stoichiometry synthesised by carbothermal reduction of ZrO_2 and mixtures of commercial powders and carbon black. Phase transition temperatures in the Zr-C system were measured at temperatures >3000 °C. The main source of uncertainty in the reported temperatures was the ZrC emissivity. The liquidus, solidus and eutectic transitions detected for ZrC and ZrC+graphite were consistent with published phase diagrams.

2.12 Aims and objectives

The aim of this work is the development of efficient routes for the synthesis and sintering of TaC-HfC solid solutions and the measurement of the thermo-physical properties of different compounds in the TaC-HfC system.

To achieve this several objectives were defined:

- To develop efficient routes to synthesise and sinter TaC-HfC compounds using a combination of self-propagating high-temperature synthesis (SHS) and spark plasma sintering (SPS) techniques.
- To develop efficient routes to synthesise and sinter single phase (Ta,Hf)C solid solutions using SPS and evaluate the effect of sintering temperature, mechanical pressure and time in the solid solution formation.
- To evaluate phase formation and characterise microstructures using state-of-the-art characterisation equipment such as XRD, SEM, EDS and TEM.
- To measure room temperature mechanical properties such as hardness, elastic modulus and fracture toughness of TaC, HfC and TaC-HfC solid solutions using Vickers and nanoindentation techniques.
- To measure thermal properties at high temperatures (up to 2000 °C) such as thermal diffusivity, thermal conductivity and coefficient of thermal expansion (CTE) using laser flash and dilatometer techniques.
- To evaluate the oxidation behaviour of several compounds in the TaC-HfC system using thermogravimetric analysis (TGA).
- To reassess the high melting temperatures of TaC, HfC and TaC-HfC solid solutions with an accurate laser heating technique and evaluate and compare the results with historical data.

3 Experimental methods

3.1 Starting materials and powder processing

In this chapter the methods and materials used in the processing and fabrication of TaC-HfC ceramics are presented. Table 3.1 shows the starting materials used, materials grade, particle size measured and manufacturer.

Material	Grade/purity	Particle size d_{50} (μm)	Source
Ta	-325 mesh, 99.9%	4.80 ± 0.09	ABCR (Karlsruhe, Germany)
Hf	-325 mesh, 99.6%	8.88 ± 2.42	ABCR (Karlsruhe, Germany)
C	Acetylene carbon	0.04 ± 0.02	ABCR (Karlsruhe, Germany)
TaC	-325 mesh, 99.5%	3.44 ± 0.07	ABCR (Karlsruhe, Germany)
HfC	-325 mesh, 99%	8.4 ± 0.10	ABCR (Karlsruhe, Germany)
HfC	99.5% purity	2.82 ± 0.02	Alfa Aesar (Ward Hill, MA, USA)

Table 3.1 Characteristics of as-received materials used in the present investigation.

Particle size was measured using a particle analyser (Mastersizer 2000, Malvern, Worchestershire UK). Laser diffraction was used to measure particle size distribution by measuring the angular variation in intensity of light scattered as the laser beam passes through a dispersed particulate sample, in this case distilled water was used as dispersant. Large particles scatter light at small angles relative to the laser beam and small particles scatter light at large angles as illustrated in Figure 3.1. Using the Mie theory of light scattering, the angular scattering intensity data is then analysed to calculate the size of the particles responsible for the scattering pattern [137]. The Mie theory assumes the volume of the particle as opposed to Fraunhofer which is a projected area prediction. The penalty or source of error for complete accuracy is that refractive indices for the material and medium need to be known [138]. The

particle size is reported as volume equivalent sphere diameter. Five measurements were conducted on each sample, the average value of the median particle size d_{50} is reported with standard deviations.

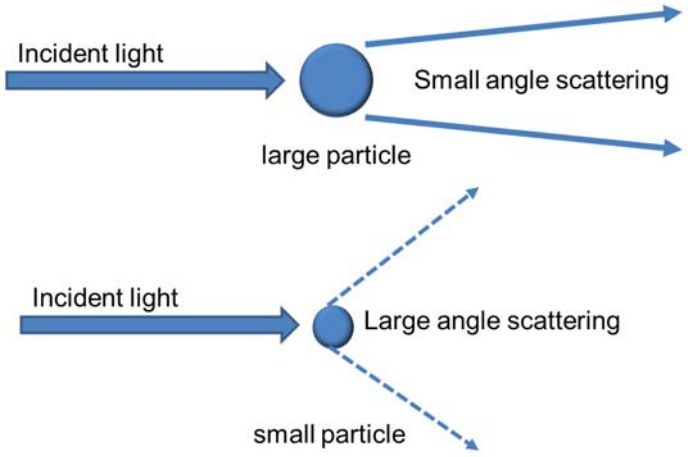

Figure 3.1 Light scattering from large and small particles

Different processing routes were used in this work in to produce TaC-HfC ceramics, two types of reactive routes and a solid state sintering route were used. Reactive routes involving self-propagating high temperature synthesis (SHS) were chosen because SHS is a rapid and economical preparation route, with synthesis of powders in the order of seconds and the products usually of high purity [44]. The use of a spark plasma sintering (SPS) furnace gives a more accurate control of the parameters applied during processing (heating rate, temperature, mechanical pressure). A reactive route consisting of synthesis of TaC-HfC powders by SHS and sintering using SPS in one step was conducted. This method will be referred as reactive spark plasma sintering (RSPS), and the block diagram of Figure 3.2 describe the processing steps for this route. Metallic powders of Ta and Hf were mixed with carbon black (Table 3.1) in the appropriate amounts to make 4TaC-1HfC powders. Then were dry milled using a rotary milling machine (CAPCO Test Equipment 12VS, Ipswich,UK) for 24 h with 10 mm SiC media at room temperature.

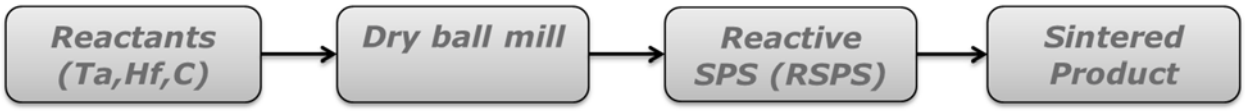

Figure 3.2 Block diagram of processing steps of the RSPS technique.

A second reactive route consisting of a two-step process of SHS and subsecuently sintering of the SHS powders by SPS. The difference with RSPS is that heating was stopped after the SHS reaction took place, powders were taken out of the graphite die then ground and sieved in a mortar with a pestle and further consolidated by SPS. In this work this method will be referred onwards as SHS+SPS. The block diagram of Figure 3.3 shows the processing steps of the SHS+SPS method.

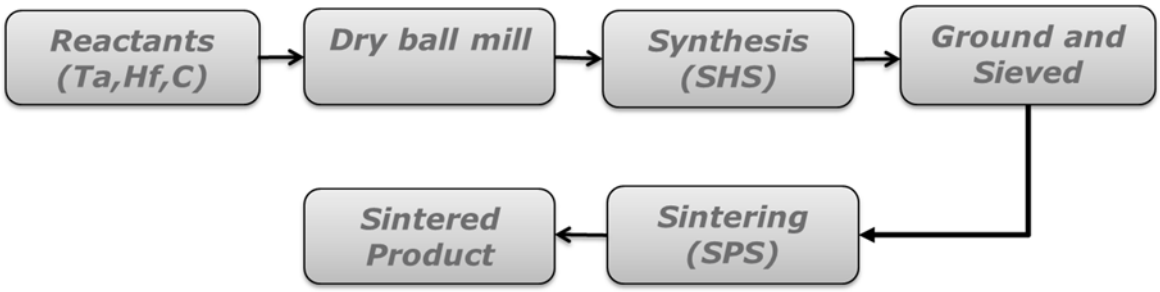

Figure 3.3 Block diagram of the processing steps of the SHS+SPS method.

For the reactive process techniques, the starting mixtures of powders were prepared by mixing reactants according to the following reaction:

$$4Ta + Hf + 5C \rightarrow Ta_4HfC_5 \qquad \text{Equation 3.1}$$

Commercial TaC and HfC (Table 3.1) were used as starting materials for a processing route using SPS. This processing route will be referred as solid state sintering (SSS); further TEM analysis shows that grain boundaries were clean with no liquid or secondary phases formed showing evidence of solid state diffusion. This route was selected since starting powders showed high purity and homogeneity and

consolidation of powders and final products desired (high density and solid solution formation) were achieved with shorter processing times. Mixtures were prepared by mixing the appropriate amounts of powders and subsequently rotary milling (CAPCO Test Equipment 12VS, Ipswich,UK) in ethanol with 10 mm diameter SiC media for 24 h at room temperature. After milling, the slurry was dried in a rotary evaporator (Rotavapor R124, Buchi; Flawil, Germany) in a 60 °C bath under vacuum. The powders were then left for 12 h in a drying oven at 110 °C to completely remove any solvent. Finally, the powders were lightly ground in a mortar with a pestle and then sieved to a final mesh size of 50 μm. The processing steps can be observed graphically in the block diagram of Figure 3.4.

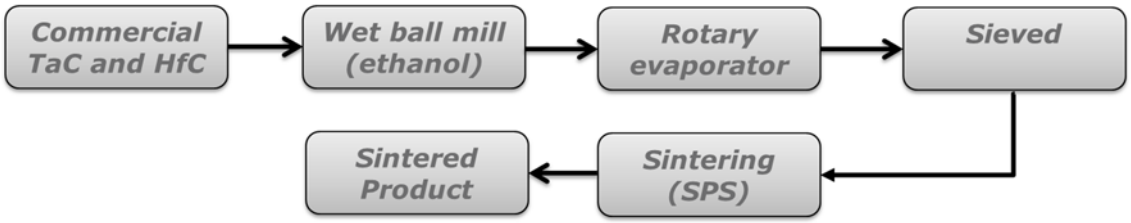

Figure 3.4 Processing steps used for the solid state sintering (SSS) route.

3.2 Elemental analysis

Carbon analysis of carbides relies on the ignition and combustion of the carbide sample in flowing oxygen and the subsequent measuring of the thermal conductivity of the emitted CO_2-O_2 gas mixture. Carbon analysis was conducted using a carbon-sulfur elemental mass induction analyser (EMIA) (Horiba, Longjumeau, France). Accelerants (tungsten and/or iron) are added to promote a fast combustion and achieve the release of the C. Non-dispersive IR sensors are used for the detection of CO and high and low concentrations of CO_2. This setup allows for relatively rapid analyses between 30-60 s [139].

Oxygen, nitrogen and hydrogen chemical analysis was conducted using an elemental mass gas analyser (EMGA) (Horiba, Longjumeau, France). This technique consists in the combustion of the sample in flowing helium, allowing the CO_2 released to be used for oxygen quantification and the H_2O as

hydrogen quantification. The sample is dropped into an impulse furnace and nickel is added as combustion accelerant. CO is firstly measured, secondly the gas is oxidised, then it is passed through a CO_2 and H_2O detector and finally the CO_2 and H_2O are absorbed and the N_2 is measured by a thermal conductivity detector. One common source of error in combustion analysers is the inhomogeneity of the sample [139].

3.3 Sintering and Densification

Sintering of TaC-HfC powders was conducted using an SPS furnace at Queen Mary University London (FTC HP D20; FCT Systeme GmbH, Rauenstein, Germany) (Figure 3.5). The SPS process utilizes pulsed high DC current along with uniaxial pressure to consolidate powders. The instrument has integrated computer software to create, save and upload sintering recipes and to download the sintering data after sintering for further analysis.

Figure 3.5 SPS facility at Queen Mary University London used in this work.

A cylindrical 20 mm graphite die was used along with a one-piece tapered cross-section design of the punch-support assembly. Figure 3.6a) shows the graphite die and punch kit design all its components, while Figure 3.6b) shows the kit after its assembly where on top of the upper punch a hole can be observed which is used for pyrometer temperature measurements. With this design it is possible to achieve sintering temperatures as high as 2450 °C without cracking and/or damaging the graphite dies.

The stress concentration is reduced with a tapered design compared to conventional design where sublimation of graphite can be produced at high temperature and pressure at the point where the cross section has an abrupt change.

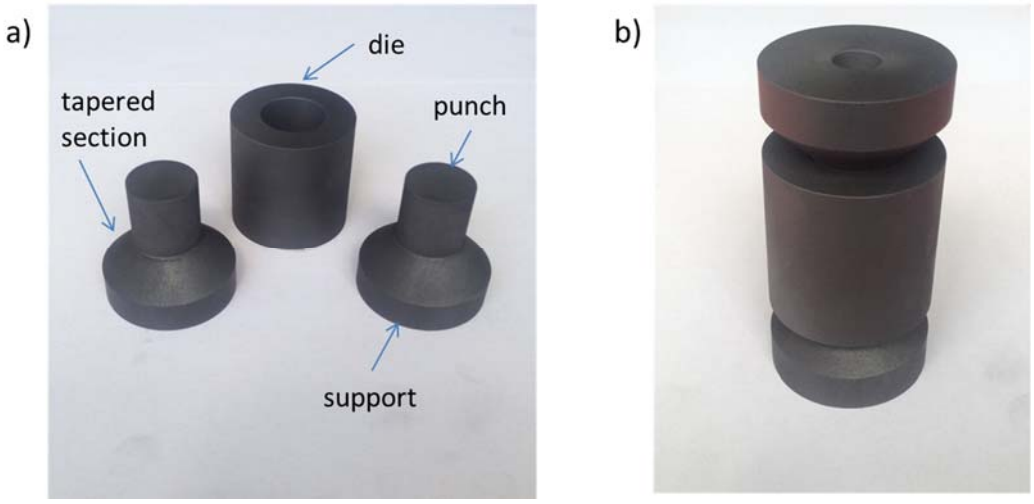

Figure 3.6 Graphite dies and punches used for sintering, a) Unassembled tooling including die and punches b) assembled tooling kit.

The graphite dies and the interface between the punch and powder are lined with a 0.3 mm thick graphite foil with a double purpose, to maximise electrical and heat conduction between the punches and the die and to prevent bonding between the sample and graphite tooling.

Powder mixtures (~15 gm) were poured into the die and uniaxially pressed at 3 MPa. For reactive processing routes (RSPS and SHS+SPS) a heating rate of 200 °C/min was used and for SSS route 100 °C/min. A minimal initial pressure of 20 MPa was applied to the samples and, depending on the experiment requirement, the pressure was increased and maintained at the desired sintering temperature. After cooling the sintered sample was removed from the die. The thickness of sintered discs was ~4-5 mm.

Sintering schedule of 4TaC-1HfC samples fabricated using RSPS and SHS+SPS are shown in detail in Table 3.2.

Processing route	Sintering conditions (T_s, t_s and P)	Thermal Schedule
RSPS	2100 °C, 20 min, 20 MPa	450-2100 °C, 210 °C/min, 20 MPa 2100 °C, 20 min, 20 MPa
RSPS	2100°, 20 min, 60 MPa	450-2100 °C, 210 °C/min, 20 MPa 1400-2100 °C, 210 °C/min, 60 MPa 2100 °C, 20 min, 60 MPa
RSPS	2100 °C, 10 min, 60 MPa	450-2100 °C, 210 °C/min, 20 MPa 1400-2100 °C, 210 °C/min, 60 MPa 2100 °C, 10 min, 60 MPa
SHS+SPS	2100 °C, 20 min 60 MPa	450-1400 °C, 210 °C/min, 20 MPa 450-2100 °C, 100 °C/min, 20 MPa 2100 °C, 20 min, 60 MPa

Table 3.2 SPS schedule of 4TaC-1HfC samples prepared by reactive processing, RSPS and SHS+SPS (T_s: sintering temperature, t_S: sintering time and P: pressure).

Sintering details of 4TaC-1HfC samples sintered at temperatures from 2050 to 2450 °C by SPS are shown in Table 3.3, with heating rate, sintering temperature, sintering time and mechanical pressure applied as indicated.

Sintering temperature (°C)	Thermal schedule
2050	450-2050 °C, 100 °C/min, 30 MPa 2050 °C, 20 min, 30 MPa
2150	450-2150 °C, 100 °C/min, 30 MPa 2150 °C, 20 min, 30 MPa
2250	450-2250 °C, 100 °C/min, 30 MPa 2250 °C, 20 min, 30 MPa
2350	450-2350 °C, 100 °C/min, 30 MPa 2350 °C, 20 min, 30 MPa
2450	450-2450 °C, 100 °C/min, 30 MPa 2450 °C, 20 min, 30 MPa

Table 3.3 SPS schedule of 4TaC-1HfC samples prepared by SPS (SSS route).

A two dwell sintering schedule was proposed for the sintering of TaC, HfC and TaC-HfC solid solutions. Heating was conducted with a heating rate of 100 °C/min, then an initial sintering step at a temperature of 2100 °C for 30 min and 55 MPa, heating from 2100 to 2350 °C was conducted at 50 °C/min, followed a second sintering step at 2350 °C for 20 min and 30 MPa. This schedule was used because highly dense ceramics and single-solid formation were desired on sintered products. Sintering schedules for each of the compositions are shown in Table 3.4

Composition	Thermal Schedule
TaC	450-2100 °C, 100 °C/min, 55 MPa 2100°, 30 min, 55 MPa 2100-2350°, 50 °C/min, 30 MPa 2350°, 20 min, 30 MPa
4TaC-1HfC	450-2100 °C, 100 °C/min, 55 MPa 2100°, 30 min, 55 MPa 2100-2350°, 50 °C/min, 30 MPa 2350°, 20 min, 30 MPa
1TaC-1HfC	450-2100 °C, 100 °C/min, 55 MPa 2100°, 30 min, 55 MPa 2100-2350°, 50 °C/min, 30 MPa 2350°, 20 min, 30 MPa
1TaC-4HfC	450-2100 °C, 100 °C/min, 55 MPa 2100°, 30 min, 55 MPa 2100-2350°, 50 °C/min, 30 MPa 2350°, 20 min, 30 MPa
HfC	450-2100 °C, 100 °C/min, 55 MPa 2100°, 30 min, 55 MPa 2100-2350°, 50 °C/min, 30 MPa 2350°, 20 min, 30 MPa

Table 3.4 Thermal schedule of TaC, HfC and TaC-HfC solid solutions prepared by SPS (SSS route).

3.4 Density measurements

The theoretical density (TD) of a polycrystalline ceramic assumes that the porosity is zero, but it does take into account secondary phases, solid solutions and defects. Bulk density is defined as the mass of a solid divided by the bulk volume, where the bulk volume is the volume of the space enclosed by an imaginary skin covering the external surface of the porous solid [140]. To determine the bulk density of the sintered TaC-HfC ceramics, the Archimedes' method was applied using a density determination kit (Sartorius, YDK01, Goettingen, Germany). A solid immersed in a liquid is subjected to the force of buoyancy. The value of this force is the same as that of the weight of the solid displaced by the volume of the solid. It is possible to determine the specific gravity of a solid when the density of the liquid causing buoyancy is known:

$$\rho = \frac{W_a \cdot \rho_{fl}}{W_a - W_{fl}} \qquad \text{Equation 3.2}$$

$$\rho_{fl} = \frac{G}{V} \qquad \text{Equation 3.3}$$

where ρ, specific gravity of the solid; ρ_{fl}, density of the liquid; W_a, weight of the solid in air; W_{fl}, weight of the solid in liquid; G, buoyancy of the immersed solid and V, volume of the solid.

With Equation 3.2 and Equation 3.3 the density of the sample can be calculated. For this apparatus density is given by Equation 3.4 :

$$\rho = \frac{W_a \cdot \left[\rho_{fl} - 0.0012 g/cm^3\right]}{0.99983G} + 0.0012\ g/cm^3 \qquad \text{Equation 3.4}$$

Samples after sintering were ground and polished to remove excess of carbon at the surface due to contact with the graphite foil, then introduced in distilled water and put under vacuum for 30 min to remove air trapped in pores and the samples were removed from the fluid, excess water was removed with a damp cloth then the saturated mass weight was measured. Subsequently, the sample was submerged in distilled water in a beaker and buoyancy (G) was measured. A minimum of 10 measurements were conducted on sample, the mean value with respective standard deviation are reported.

3.5 Microstructural characterisation

3.5.1 X-ray diffraction analysis (XRD)

Phase analysis and precise lattice parameter measurements were conducted using an X-ray diffractometer (PANalytical MRD; Almelo, The Netherlands) with a vertical goniometer. An X-ray diffractometer consist of a source of X-rays, an X-ray generator, a diffractometer assembly and an X-ray data collection and processing software. A schematic of a diffractometer with Bragg-Brentano geometry is shown in Figure 3.7; the sample is mounted on a goniometer while the detector travels along the focusing circle.

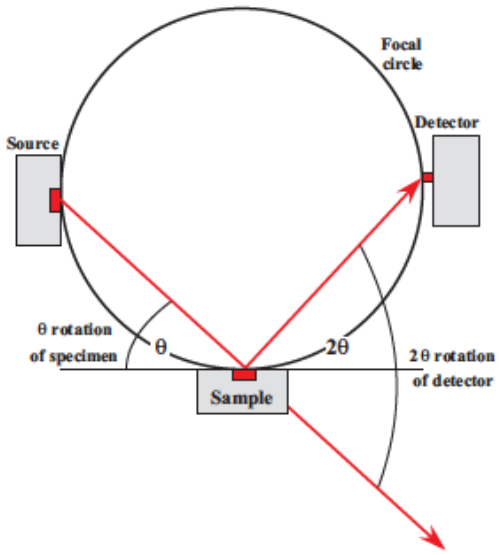

Figure 3.7 Schematic of an X-ray diffractometer with sample mounted on a goniometer. [141]

The X-rays are generated by accelerating a beam of electrons onto a pure metal target, Cu in this work, contained in a vacuum tube. This X-ray beam is directed towards the analysed sample and diffracted from atoms in the crystal lattice. Diffraction of X-rays takes place at angles of incidence that satisfy Bragg's Law, which can be written in the form:

$$\lambda = 2d\ sin\theta \qquad \text{Equation 3.5}$$

where λ is the wavelength of the radiation, d is the spacing of the crystal lattice planes of a particular diffracted beam, and θ is the diffraction angle, the angle that the incident plane makes with the lattice planes, as shown in Figure 3.8.

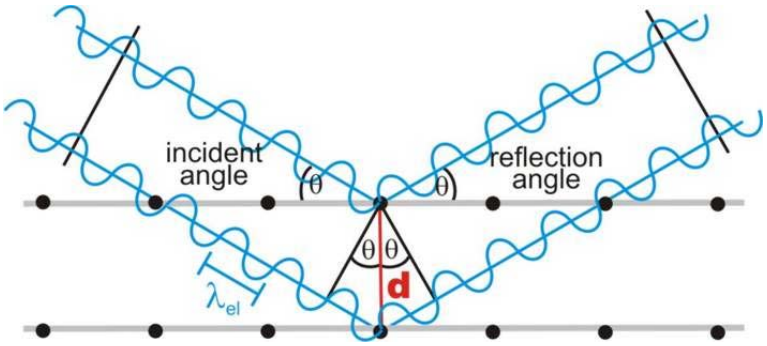

Figure 3.8 Diffraction of X-rays in a crystal.

Samples were put in the diffractometer in powder form. Sintered samples were crushed manually in a mortar with a pestle until all sintered particles were reduced to a powder form. Cu Kα radiation was used (λ=1.54178 Å) and data was collected using a 0.015° step. Diffraction peaks were indexed using ICDD (International Center for Diffraction Data) powder diffraction files (PDF), #035-0801 for TaC and #039-1491 for HfC, and using XRD analysis software (X'Pert High Score, PANalytical; Almelo, The Netherlands). PDF files for TaC-HfC solid solutions are not available.

Solid solutions can be distinguished experimentally using XRD, the formation of substitutional solid solutions may be accompanied with and increase or decrease in cell volume. Calculation and measurement of precise lattice parameters of the TaC-HfC solid solutions was conducted using the extrapolation method explained in detail by Cullity and Stock [142]. The method consists in measuring the Bragg angle θ for *hkl,* then using Bragg's Law determine d allowing calculation of a (lattice parameter). Measured values of a are plotted against $\cos^2\theta$, then values of the calculated parameters are extrapolated to a value of θ=90°. The precision of this method relies in the use of reflected beams to 2θ as close as possible to 180°. The parameter error disappears when 2θ is close to 180°, however diffracted beams cannot be measured at this angle. A practical approach to get a true value of a to plot the measured values against 2θ and a could be simply found by extrapolating to 2θ=180°. Nonetheless, this curve is nonlinear and extrapolation is inaccurate using this curve. Certain functions of θ are used, rather than θ or 2θ alone and the resulting curve is a straight line that can be extrapolated with confidence [142].

When measuring d-spacings, the most common sources of systematic errors using a diffractometer are:

1. Misalignment of the instruments. Incident beam must intersect the diffractometer axis and the 0° position of the detector slit.
2. Use of a flat specimen instead of a curve specimen to conform to the focusing circle.
3. Absorption of the specimen. Specimens with low absorption are required to be made as thin as possible. The error is minimized by decreasing the irradiated width of the specimen with an incident beam of small horizontal divergence.
4. Displacement of the specimen from the axis. This is usually the largest source of error.
5. Vertical divergence of the incident beam, can be minimized by decreasing the vertical opening of the detector slit.

From differentiation of Bragg's law, neglecting $\Delta\lambda$ and using $\Delta d/d = -\cot\theta\,\Delta\theta$, shows that to achieve a precision of ±0.0001 Å in the lattice parameter at a 2θ position of 160°, must be measured to within 0.02° [142].

3.5.2 Scanning electron microscopy (SEM)

In an SEM an electron beam passes through an electron column and strikes a solid sample within the optic axis of the column. A schematic drawing of the SEM with essential components (gun, lenses, apertures, scan coils and electron detector) is shown in Figure 3.9. The electrons interact elastically and inelastically with the sample over an interaction volume in which various types of signals are generated. Backscattered, secondary, and absorbed electrons, characteristic and Bremsstrahlung X-rays, cathodoluminescence radiation are signals produced at the interaction volume (Figure 3.10).

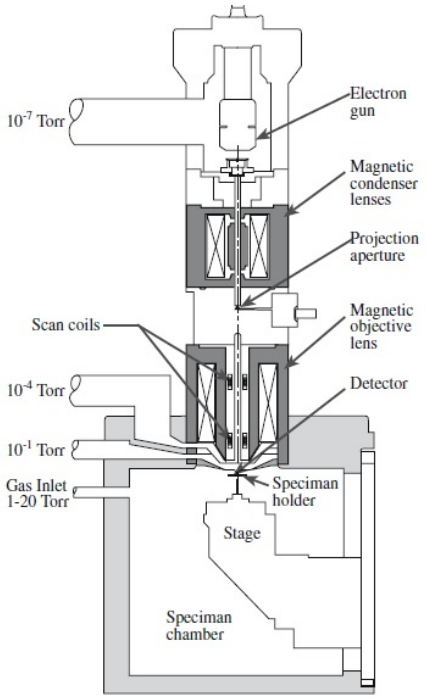

Figure 3.9 Schematic drawing of a SEM and examples of pressures used in the instrument. [143]

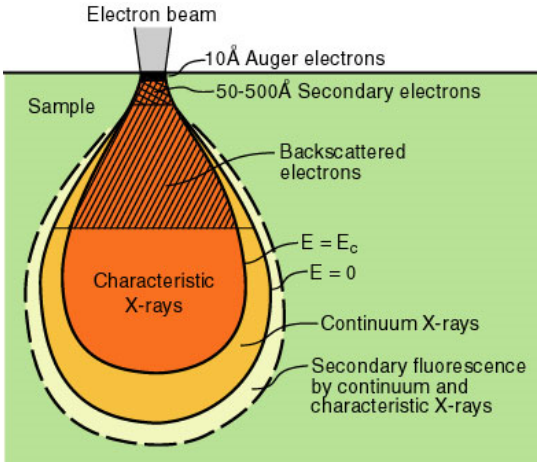

Figure 3.10 Illustration of the interaction volume and related electron-sample interactions.

Because of the different signals and detectors available in an SEM, this instrument is one of the most versatile for materials characterisation. Backscattered (high energy) electrons are sensitive to the atomic number of the scattering atom; in consequence the intensity of the backscattered electron (BSE) signal depends on the average atomic number and density of the sample. Hence, the high contrast images produced with BSE give useful compositional information. Secondary (low energy) electrons are sensitive to surface topography since they escape from the outermost region of the sample, a small region of the interaction volume. The depth of field of secondary electron images (SEI) gives important information about the surface topography of the sample [144].

Energy dispersive spectroscopy (EDS) makes use of the characteristic X-rays emitted by the sample bombarded by the electron beam to obtain a localized chemical analysis. Rapid qualitative and quantitative analysis with EDS can be achieved. Elements above atomic number 4 can be detected at currents at typical beam currents used for SEI. However, lighter elements (Z<10) and in this case carbon in TaC-HfC and single carbide ceramics are difficult for quantitative analysis [141].

Microstructural analysis was performed using a scanning electron microscope (Auriga, Carl Zeiss; Oberkochen, Germany). Backscattered electron (BSE) and secondary electron images (SEI) were taken

at an acceleration voltage of 15 kV and elemental analysis conducted using an Energy Dispersive Spectroscopy (EDS) unit (X-Max 20, Oxford Instruments; Abingdon, UK) coupled to the SEM.

Samples for SEM were prepared by cutting sintered samples with a diamond cut-off wheel, then cold mounted in an epoxy-resin. Samples were ground using resin-bonded diamond grinding discs with water as lubricant and coolant, polished using a satin woven acetate cloth with diamond slurries to a ¼ μm finish and a final polishing step with a porous neoprene cloth disc using a vibratory polisher machine (VibroMet 2, Buehler; Lake Bluff, Ill., USA) for 24 h to a ¼ μm finish with a colloidal silica suspension. A detailed polishing schedule with type of grinding and polishing discs, force applied, polishing time and suspensions used are shown in Table 3.5.

Surface / Grain Size	**Abrasive/Grit Grain**	**Time**	**Force / Power**
Resin bonded diamond 120	Water	2 min	30 N
Resin bonded diamond 1200	Water	3 min	30 N
Resin bonded diamond 2000	Water	5 min	30 N
Resin bonded diamond 4000	Water	7 min	30 N
Satin woven acetate	Diamond suspension 3 μm	9 min	20 N
Satin woven acetate	Diamond suspension 1 μm	11 min	20 N
Satin woven acetate	Diamond suspension ¼ μm	13 min	15 N
Porous neoprene	Colloidal silica suspension	24 h	80% power

Table 3.5 Polishing materials and methods for SEM sample preparation.

3.5.3 Grain and pore size measurement

BSE images were used for grain and pore size measurements. Samples were prepared as described in Table 3.5. Grain size measurements were performed using image analysis software (Simagis, Smart Imaging Technologies Co.; Houston, TX, USA) according to ASTM E112 and ASTM E1382 [145, 146] and pore size measurements were conducted using ImageJ software (open source).

3.5.3 Transmission electron microscopy (TEM)

A very thin, electron transparent sample (usually <200 nm) is required in TEM. Because of the range of signals (Figure 3.11) produced by the incident electron beam the TEM allow for full characterisation of samples at high resolution. Traditional image modes in TEM are bright-field (BF) and dark-field (DF) imaging. In BF mode the direct beam is used for image formation, diffracted electrons are excluded from the image using the objective aperture. If the diffracted electrons are used to form the image this is a DF image. Characteristic X-rays are used for chemical analysis using EDS.

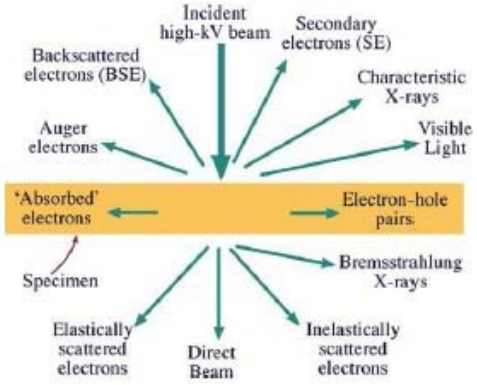

Figure 3.11 Signals generated when an electron beam interacts with a thin specimen in TEM. [147].

In diffraction mode to see a diffraction pattern (DP) the lenses in the imaging system are adjusted so that the back-focal plane (BFP) of the objective lens acts as the object plane for the intermediate lens, then the DP is projected onto the viewing screen (Figure 3.12a)). In image mode, the intermediate lens

are adjusted so that its object plane is the image plane of the objective lens and the image is projected onto the viewing screen. (Figure 3.12b)) [147].

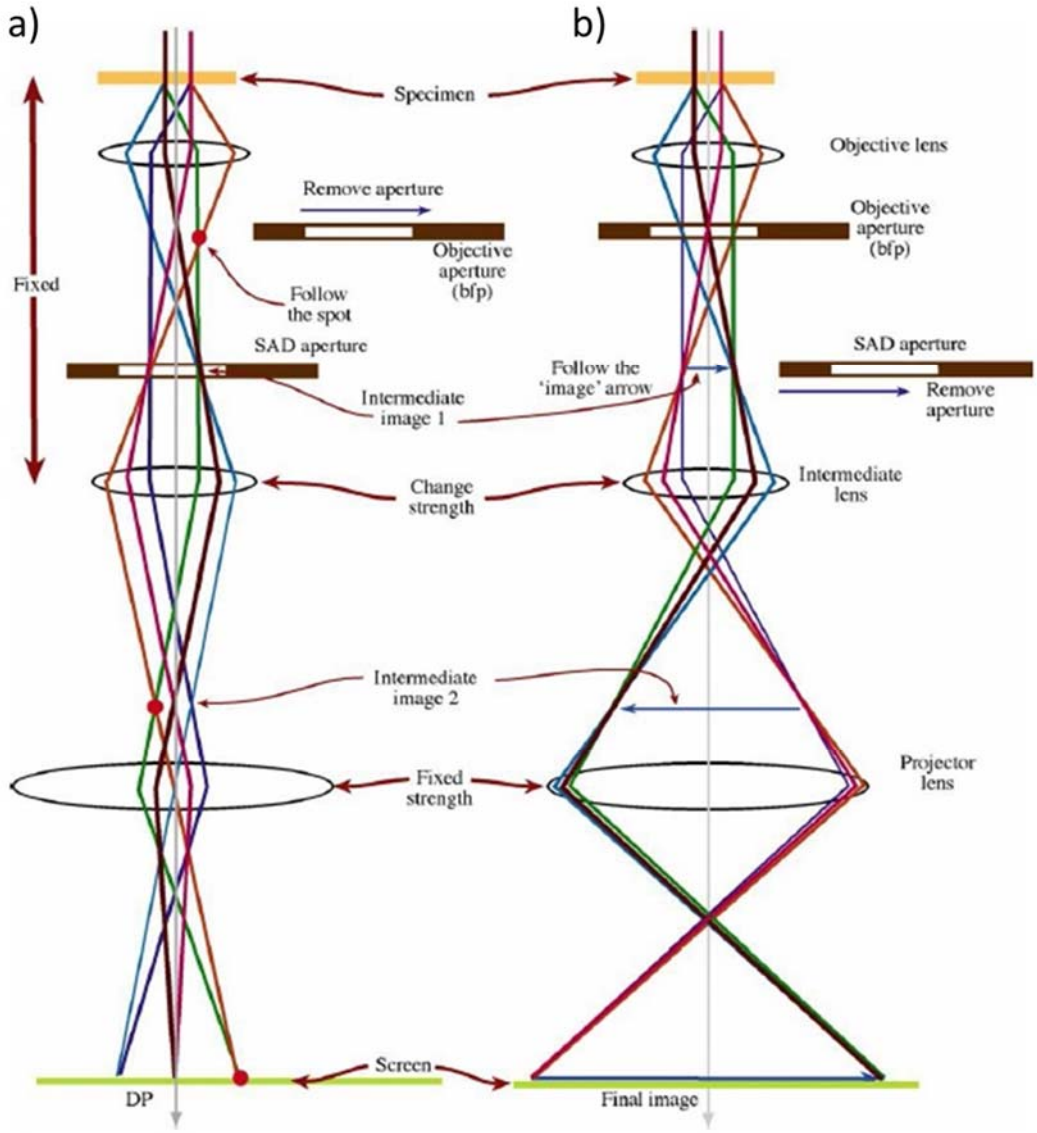

Figure 3.12 Basic TEM imaging system with two basic operations: a) diffraction mode: with a DP projected on screen and b) image mode: projecting the image on screen. [147]

The dominant image formation mechanism in thin samples of crystalline materials is that of diffraction contrast. Electron diffraction occurs at those planes orientated at or near the Bragg angle. The extent of diffraction is determined by the relationship between the electron beam, the crystal type and the crystal

orientation [140]. A zone axis is a direction common to several set of planes, composed of highly symmetrical array of diffraction spots, produced from planes at the Bragg condition (Figure 3.13a)).

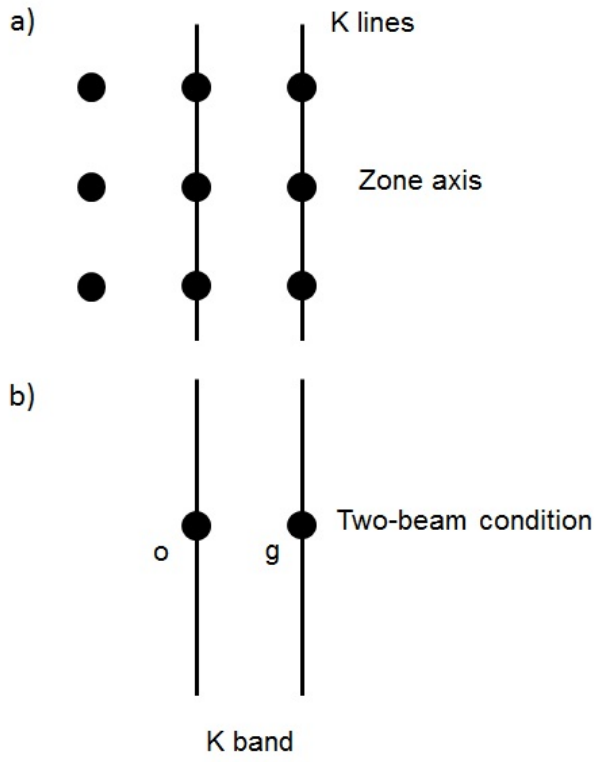

Figure 3.13 Diffraction patterns showing: a) zone axis and b) two-beam condition obtained by a small tilt in the direction of ***g***. K band is a Kikuchi band [140].

Lee and Rainforth [140] describe three conditions where image contrast is produced from diffraction. First, when the crystal is oriented in a way that the electron beam is parallel to a zone axis. Second, when the sample is oriented that the beam is close to a zone axis but tilted a few degrees away that only one plane is diffracting, known as two-beam condition in which the electron intensity in the single diffracted beam is equal to that of the transmitted beam (Figure 3.13b)). And finally, when the sample is oriented well away from a zone axis, but still diffraction from one or several planes. To interpret TEM images of defects with confidence only two conditions should be considered, where a zone axis is oriented exactly to the electron beam and a two-beam condition with a known diffraction ***g***.

Transmission electron microscopy (TEM) was conducted using a JEOL FX2100 (Tokyo, Japan) at 200 kV and elemental analysis using EDS (X-Max 80, Oxford instruments; Abingdon, UK) and TEM diffraction analysis software (SingleCrystal, CrystalMaker Software Ltd.; Begbroke, UK) was used for indexing the selected area electron diffraction (SAED) patterns. A crystallographic information file (CIF) from the Inorganic Crystal Structure Database (ICSD, FIZ Karlsruhe, Germany) is loaded to the Single Crystal software, then the experimental SAED image is loaded and compared over the simulated SAED from the CIF file and the orientation is determined and reflections are indexed. Also ratios of the principal spot spacings and angles between the principal plane normal were measured and using standard indexed diffraction patterns for FCC crystals from the literature [147] the patterns were compared and indexed.

TEM samples were prepared by cutting sintered samples into 3 mm cylinder by electric discharge machining (EDM). With a low-speed diamond cutting blade samples were cut into discs of ~1 mm, mounted with wax in a 10 mm diameter steel stub and ground and polished with diamond paste to a 1 μm finish and a thickness of <50 μm using a disc grinder (Gatan, Abingdon, UK). The polished samples were dimpled with a dimple grinder (Gatan 656 Dimple Grinder, Abingdon, UK) with 1 μm paste to a <10 μm thickness. Subsequently the samples were mounted on a copper ring (Agar Scientific, Stansted, Essex, UK) and ion-polished using a Precision Ion Polishing System (PIPS, Gatan 691, Abingdon, UK). Initially samples were milled using a voltage of 4.5 keV, and at different milling angles from 0° to 10° in increments of 2° for 60 min at each step until a hole appears at the centre of the sample. Afterwards a fine milling was conducted using 2.5 keV for 60 min at each angle.

In addition, thin sections were cut out from specimens using a focused ion beam (FIB) instrument (Helios 650 Nanolab, FEI, Hillsboro, OR, USA). FIB is a technique in which a single ion gun produces a well-controlled beam of Ga ions. A selected area of the sample surface is bombarded using the Ga ions and sputters a small amount of material, which produces secondary ions, neutral atoms and secondary electrons. By controlled sputtering, very thin electron transparent cross sections can be made at specific locations, these samples then can be transferred for analysis to a TEM.

Figure 3.14 show images of the preparation steps of a TEM sample using the lift-out technique by FIB. A selected area is milled down by making trenches alongside the section of interest, then the cross section is cut out and welded using Pt to the instrument needle in order to perform the lift-out. The sample is then attached to a TEM grid and the sample is then detached from the needle by cutting the Pt welding. A final polishing step is conducted to achieve the transparency required for analysis.

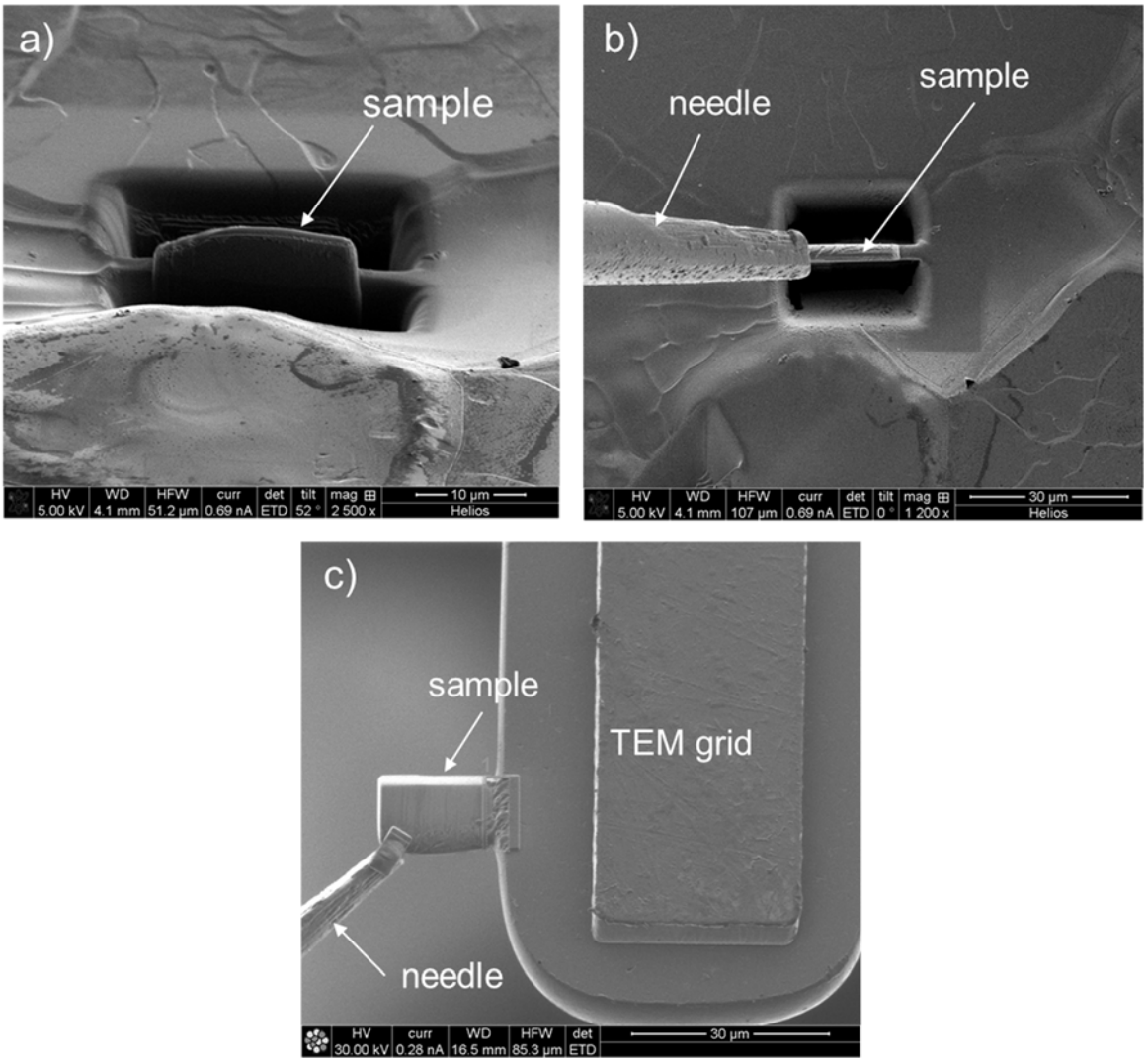

Figure 3.14 Preparation steps of an SPS'd TaC sample after laser melting experiments: a) Trenches are milled alongside the sction of interest, b) the sample is welded to the instrument needle and then cut to make the lift-out process and c) the sample welded to a TEM grid and detached from the needle for final polishing.

3.6 Mechanical characterisation

3.6.1 Hardness

Hardness was measured using a ZHU 2.0 instrumented hardness testing machine (Zwick Roell, Ulm, Germany) with a Vickers tip. Experiments were conducted in accordance with ASTM Standard C1327 [148] at a load of 1 kg (9.8 N) (unless otherwise specified) and a hold time of 15 s. A minimum of 10 indents were made for at each sample and the average value of the measurements with respective standard deviations are reported. To minimize errors due to sample surface finish the test specimens were polished to a 1 μm finish using diamond suspensions. The largest source of error or uncertainty in hardness usually arises from the error and uncertainty in the measurement of the diagonal length [148].

Vickers hardness is defined as the applied force on the indenter divided by the area of contact between the indenter and the surface. For a standard Vickers indenter the formula for hardness is given by:

$$HV = 1.8544\frac{P}{d^2} \qquad \text{Equation 3.6}$$

where P is the applied load and d is the diagonal length of the indent measured with an optical microscope integrated to the hardness machine.

3.6.2 Nanoindentation

The goal of this test is to measure the elastic modulus and hardness of the sample from experimental readings of indenter load and depth of penetration. In a conventional hardness test the impression of size the plastic deformation is measured as a function of the indenter load, however in nanoindentation the size of the impressions is often in the size of a few microns making it difficult to measure the indents with an optical microscope. In nanoindentation tests the depth of penetration is measured as the load is applied to the indenter and with the known geometry of the indenter the area of contact can be determined, thus hardness can be calculated [149].

Nanoindentation experiments were conducted using a nanoindentation instrument (Nanotest, Micro Materials Ltd, Wrexham, UK) with Berkovich tip with a face angle of 65.27°. The test loads were varied from 50 mN to 500 mN and a minimum of 30 indents were made on each specimen. The average value of hardness and E_r with standard deviation was reported. Since errors in nanoindentation can come from the specimen surface finish and the bluntness of the indenter as well, specimens were polished with diamond suspension to a 1µm finish and calibration of the indenter was loaded before each experiment to take in account the bluntness of the indenter. The Oliver and Pharr method [150, 151] was used to calculate nanohardness and reduced modulus from compliance curves of indentation experiments. A typical compliance curve from a nanoindentation experiment is shown in Figure 3.15.

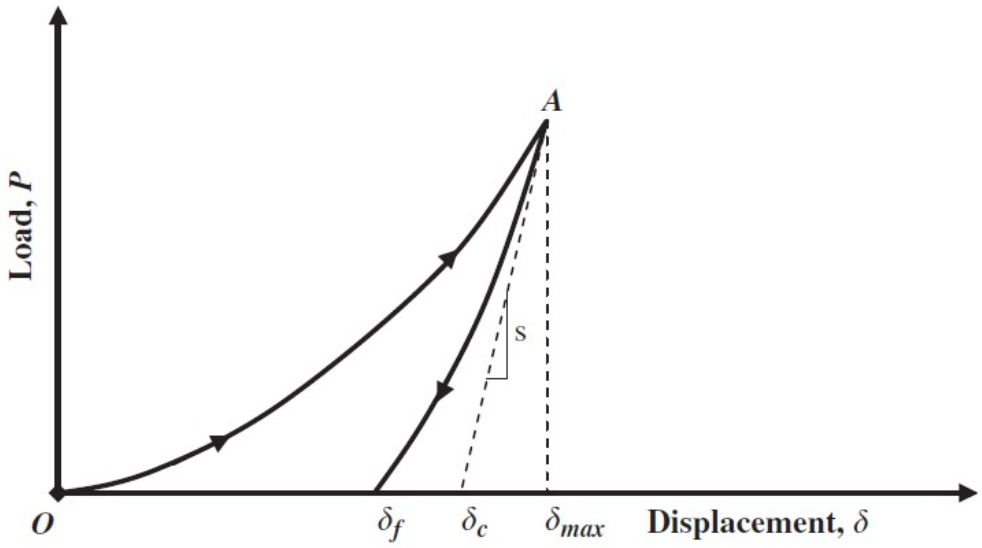

Figure 3.15 Compliance curve of a nanoindentation experiment with maximum load at point A, δ_{max} the depth beneath the specimen surface, S the slope of the elastic unloading also known as *dP/dH* and δ_f is the depth of the residual impression [152].

Indentation hardness is obtained from the indentation load divided by the contact area A_c.

$$H = \frac{P}{A_c} \qquad \text{Equation 3.7}$$

The reduced modulus E_r is determined by calculating the slope of the unloading curve at maximum load. Equation 3.8 shows the reduced modulus as a function of the slope S and the area of contact A_c.

$$E_r = \frac{S}{2}\sqrt{\frac{\pi}{A_c}} \qquad \text{Equation 3.8}$$

The reduced modulus E_r combines the elastic properties of both the indenter and the sample and can be written as [153]:

$$\frac{1}{E_r} = \frac{1-\nu^2}{E} + \frac{1-{\nu_i}^2}{E_i} \qquad \text{Equation 3.9}$$

where E and v are the elastic modulus and Poisson's ratio of the specimen and E_i and v_i are the elastic modulus and Poisson's ratio of the indenter respectively. If the elastic properties of the indenter and the specimen Poisson's ratio are known is possible to calculate the actual elastic modulus of the sample. Poisson's ratio of the indenter (ν_i) is 0.07 and the elastic modulus (E_i) 1141 GPa [154].

3.6.3 Indentation fracture toughness

The Vickers indentation test was used for determining the fracture toughness of sintered samples. The method consists in indenting the specimen in order to generate radial cracks at the indent and measure the cracks to calculate fracture toughness (K_{IC}). A typical illustration of a Vickers indentation with radial/median crack mode is shown in Figure 3.16. A Zwick Roell ZHU 2.0 (Ulm, Germany) instrumented hardness testing machine was used for producing the indentations. A minimum of 10 indents were produced at each specimen at a load of 1 kg (9.8N) for 15 sec. The average hardness value and standard deviation are reported. Radial cracks and diagonal indentation lengths were measured with and optical microscope (Axio Imager 2, Carl Zeiss, Jena, Germany) and a charged coupled device (CCD) camera and software integrated to the microscope.

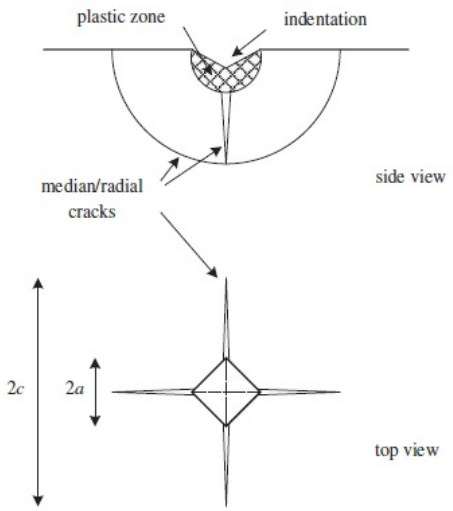

Figure 3.16 Schematic representation of Vickers indentation with radial/median cracks [152].

Fracture toughness (K_{IC}) was calculated using the model of Anstis et al. [155]

$$K_{IC} = 0.016 \cdot \left(\frac{E}{H}\right)^{1/2} \left(\frac{P}{c^{3/2}}\right) \qquad \text{Equation 3.10}$$

where E is the elastic modulus, H is Vickers hardness, P the indenter load and c the average radial crack length.

The errors in indentation fracture toughness experiments can come from surface finish of the specimen and error and uncertainty in the measurement of the crack lengths. Specimens were polished to a 1 µm finish using diamond suspensions, indents with chipping or denting were discarded and the microscope software was used to accurately measure the crack lengths.

3.7 Thermal characterisation

3.7.1 Dilatometry

The coefficient of thermal expansion (CTE) was measured using a push-rod type dilatometer (DIL 402 E, Netzsch, Selb, Germany). Experiments were carried out to 2000 °C using a 10 °C/min heating rate

and under inert atmosphere (argon) using specimens of 15 mm x 5 mm x 3.5 mm. Tests were based on standards ASTM E831 and ASTM E228 [156, 157]. The standard test method consist in the use of a thermomechanical analyser or similar device to determine the linear thermal expansion of solid materials when subjected to a constant heating rate. The change of the specimen length is electronically recorded as a function of temperature. The coefficient of linear thermal expansion can be calculated form these recorded data.

CTE (α) is defined as the degree of expansion divided by the change in temperature and can be written as in Equation 3.11. L_0 is the initial sample length, Δl change in length and ΔT change in temperature.

$$\alpha = \frac{1}{L_0}\left(\frac{\Delta l}{\Delta T}\right) \qquad \text{Equation 3.11}$$

Systematic errors can result from many sources. These include: accuracy in the length and temperature measurements; deviation of the specimen mean temperature from that indicated by the sensor; deviation from linearity of the transducer; temperature gradients between the dilatometer tube and push-rod. Systematic errors can be reduced by careful calibrations of the individual components and the total system.

3.7.2 Thermal diffusivity and thermal conductivity

Thermal diffusivity was measured by the laser flash analysis (LFA) method based on the principle introduced by Parker et al. [158]. The front surface of a plan-parallel sample is heated by a short laser pulse. The temperature rise on the rear surface is measured versus time using an infrared (IR) detector (Figure 3.17).

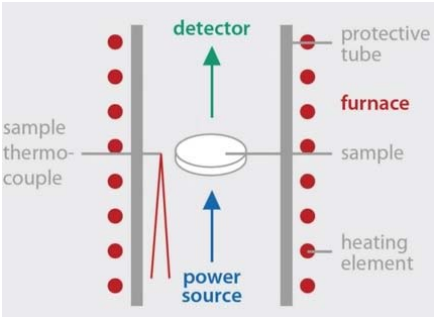

Figure 3.17 Schematic drawing of a laser flash instrument.

The analysis of the time-temperature data is conducted using the following expression:

$$a = 0.1388 \cdot \frac{d^2}{t_{1/2}} \qquad \text{Equation 3.12}$$

where a is the thermal diffusivity, d is the sample diameter and $t_{1/2}$ is the time where the increase in temperature (ΔT) is at half of the maximum. Figure 3.18 shows a typical temperature versus time curve of a LFA experiment.

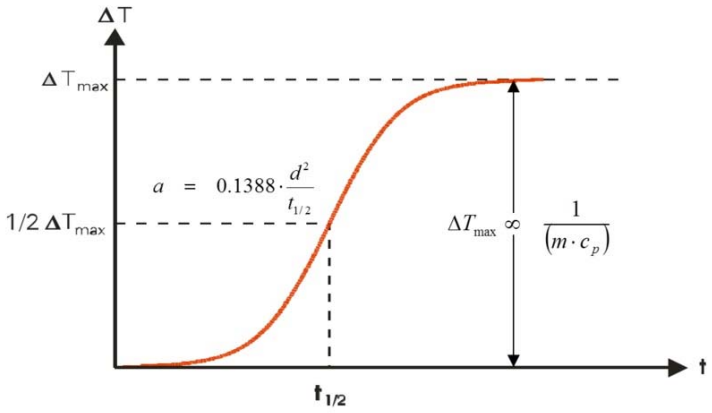

Figure 3.18 Typical graph of a LFA experiment, a is calculated at the time the increase in temperature is at half of the maximum.

The LFA experiments were conducted using a LFA 427 (Netzsch, Selb, Germany) instrument which consists of a measuring unit with furnace, sample holder and IR detector, a controller for the measuring

unit, a laser system and a data acquisition system connected to a computer. The experiments were made in accordance with ASTM E1461 [159]. The standard test method consist on the following: a small, thin disc specimen is subjected to a high intensity short duration radiant energy pulse. The energy pulse is absorbed on the front surface of the specimen and the resulting rear face temperature rise is recorded. The thermal diffusivity value is calculated from the specimen thickness and the time required for rear face temperature rise to reach a percentage of its maximum value. When the thermal diffusivity of the specimen is to be determined over a temperature range, the measurement must be repeated at each temperature of interest [159].

10 mm diameter samples were cut from the SPS'd samples using EDM (electro discharge machining) and coated with graphite emulsion to help increase the energy absorbed on the laser side and to increase the temperature signal on the detector side. Measurements were made from room temperature to 1950 °C in increments of 100 °C. Three shots and measurements were made at each temperature point; average values and standard deviations were reported. Propagation of errors can come from the errors in the thickness and density measurements.

In addition, thermal conductivity (k) was calculated using Equation 3.13.

$$k = a \cdot C_p \cdot \rho \qquad \text{Equation 3.13}$$

where a is thermal diffusivity, C_p is the specific heat capacity and ρ is the density of the specimen. C_p values of TaC and HfC were obtained from Pierson [3] and those of the TaC-HfC solid solutions were calculated by the rule of mixtures. Bulk density (ρ) at room temperature was measured by the Archimedes method described in Section 3. The temperature dependent density values were determined using Equation 3.14 [100] and linear expansion data for TaC, HfC and TaC-HfC solid solutions obtained in this work.

$$\rho = \rho_0 \left(1 + \frac{\frac{\Delta L}{L_0}}{100} \right)^3$$ Equation 3.14

3.8 Melting points

The measurement of high temperature phase transitions in TaC, HfC and their intermediate solid solutions was conducted at the Institute for Transuranium Elements (ITU) in Karlsruhe, Germany. The experiments were carried out by using a laser-heating technique described in detail by Manara et al. [118, 131] . A schematic of the laser melting instrument set-up is shown in Figure 3.19. Samples of 5 mm diameter were fitted in a stainless steel holder secured with graphite screws inside a pressure vessel filled with an inert gas (argon) at 2 bar to minimise evaporation. The pressure vessel is fitted with a sapphire window. Vapour products from the sample surface could cause interference with the optical measurement of temperature; for carbides (and less volatile materials) gas pressures of a few bar are sufficient to suppress the effect of evaporation products.

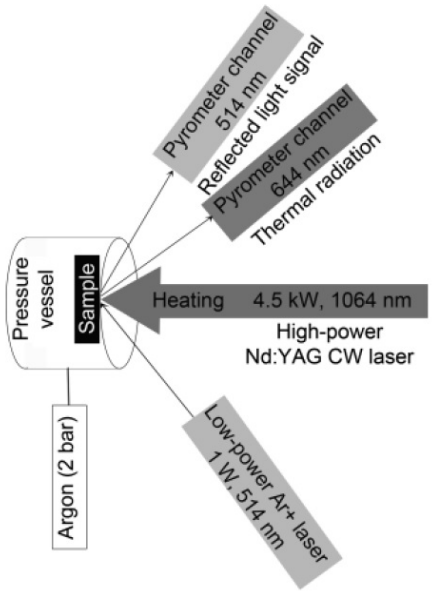

Figure 3.19 Schematic of the laser-melting apparatus employed in the present work [136].

A 4.5 kW Nd:YAG CW Laser (HLD4506, TRUMPF, Schramberg, Germany) was used for heating the sample. The laser beam was focused to the specimen surface through an optical fibre and with the help of a low-power He-Ne pilot laser, the target position was adjusted so it is assured that the beam hits the centre of the sample.

The temperature of the sample surface was measured with a fast two-channel pyrometer (10% settling time in the order of 10 μs). The first pyrometer channel used for temperature measurements operated at λ=644 nm and was calibrated against standard band lamps at 2500 K and temperature linearity was verified using a blackbody at 3400 K. The second channel was tuned at the same wavelength as the low-power (1 W) Ar^+ laser (λ=514 nm) and was used to detect the reflected light on the sample surface to determine the moment in which melting or solidification occurs on the surface, as the sample is heated the appearance of liquid in the surface causes a rapid change in the angular reflectivity signal. The vibrations of the liquid mass result in oscillations of the reflected light signal, in addition when these oscillations suddenly end the freezing point was reached.

The analog signals were transferred to a Nicolet Pro 44C (Madison, WI, USA) digital oscilloscope and the output curves were displayed in a computer in a LabVIEW (National Instruments, Austin, TX, USA) custom interface.

The functioning principles of pyrometers and the role played by ε_λ can be understood in the frame of thermal radiation theory [160]. The thermal radiation emitted by an object at absolute temperature T can be expressed in terms of spectral radiance L_λ:

$$L_\lambda = \frac{d^3\Phi}{dA \cdot cos\theta \cdot d\omega \cdot d\lambda} \qquad \text{Equation 3.15}$$

where Φ is the radiant flux or power, A is the projected area, θ the angle between surface normal and direction of the radiant flux, ω is the solid angle and λ the wavelength.

Planck's radiation law establishes a link between the spectral distribution of radiance emitted by an incandescent body and its temperature. For so-called blackbodies and in terms of the wavelength λ in a medium with refractive index n it takes the form:

$$L_{\lambda b}(T) = \frac{c_1}{n^2 \cdot \lambda^5} \cdot \left[e^{\left(\frac{c_2}{n \cdot \lambda \cdot T}\right)} - 1 \right]^{-1} \qquad \text{Equation 3.16}$$

where $c_1 = 2 \cdot h \cdot c_0^2$ is the first radiation constant (for radiance L) and $c_2 = h \cdot c_0 \cdot k_B$ is the second radiation constant, c_0 is the speed of light in vacuum, h is Planck's constant, and k_B Boltzmann's constant. For the purposes of the present work, the index of refraction is always taken to be equal to 1 (being the current medium air or an inert gas close to atmospheric pressure), whereas a value of 14388 μm·K is retained for c_2. A blackbody is a surface (material or geometrical) that absorbs all radiant flux of all wavelengths and polarizations incident upon it from all possible directions. For a prescribed temperature and wavelength, no surface can emit more thermal radiation than a blackbody. The ability of a real surface to emit thermal radiation L_λ at a given wavelength λ, as compared to that of a blackbody at the same temperature, is expressed in terms of its spectral-directional emissivity (ε_λ):

$$L_\lambda(T) = \varepsilon_\lambda(T) \cdot L_{\lambda b}(T) \qquad \text{Equation 3.17}$$

where L_λ is the thermal radiation of the real body, ε_λ is the spectral-directional emissivity and $L_{\lambda b}$ the thermal radiation of the blackbody.

Since pyrometers in the present work were always set up near normal with respect to the sample surface, the angle dependence of ε_λ was not considered and, 'emissivity' will always refer to *normal* spectral emissivity (NSE). The value of ε_λ must always be between 0 and 1, whereby $\varepsilon_\lambda = 1$ corresponds to an ideal blackbody behaviour.

The determination of the NSE is possible by doing a non-linear fit of the thermal emission spectrum (recorded, for example, by the current multi-channel pyrometers) with the equation:

$$L_{ex} = \frac{L_\lambda}{c_1} = \frac{1}{\lambda^5} \cdot \frac{\varepsilon_\lambda(T)}{e^{\frac{c_2}{\lambda \cdot T}} - 1} \qquad \text{Equation 3.18}$$

L_{ex} being the detected intensity, L_λ the radiative power, and the NSE ε_λ and temperature T are the free parameters or variables. This approach has been demonstrated to be numerically difficult and unstable in materials with metallic-like behaviour, such as the carbides of this study, in which the spectral emissivity depends on λ in a non-negligible way. NSE cannot be treated as a single parameter in such case, but all the parameters describing its dependence on wavelength should also be determined in the analysis. Nonetheless, it is sometimes the only possible way to obtain an at least approximate values for the NSE. Equation 3.18 can also be expressed in terms of radiance temperature T_λ by substituting $\varepsilon_\lambda = 1$:

$$L_{ex} = \frac{1}{\lambda^5} \cdot \frac{1}{e^{\frac{c_2}{\lambda \cdot T}} - 1} \qquad \text{Equation 3.19}$$

T_λ is thus defined as the temperature at which an ideal blackbody source would emit the same thermal radiation as the sample under investigation at a given wavelength λ. It is therefore a function of the real sample temperature T, emissivity ε_λ and the wavelength. This function can be derived analytically from equations Equation 3.18 and Equation 3.19 in the assumption (also called “Wien's approximation”) that $exp(C_2/\lambda \cdot T) >> 1$, acceptable within a 1% accuracy for $\lambda \cdot T < 3100$ µm·K:

$$\frac{1}{T_\lambda} = \frac{1}{T} - \frac{\lambda}{c_2} \ln \varepsilon_\lambda \qquad \text{Equation 3.20}$$

Radiation pyrometers, like those used in the present work and in previous investigations on the same materials, measure the sample radiance L_{ex}, which is then converted, through a calibration equation, into radiance temperature T_λ. It is then easy to understand, with the help of Equation 3.20, the important role played by the NSE, which is needed in order to convert the experimental radiance temperature into real temperature. Equation 3.20 also allows us to obtain the relative temperature change due to a relative emissivity change $\Delta\varepsilon_\lambda/\varepsilon_\lambda$:

$$\frac{\Delta T}{T} = -T\frac{\lambda}{c_2}\frac{\Delta\varepsilon_\lambda}{\varepsilon_\lambda} \qquad \text{Equation 3.21}$$

Equation 3.21 can also be used to obtain the temperature uncertainty corresponding to an emissivity error. It can be seen, that this uncertainty is higher, the higher the absolute temperature. It certainly becomes paramount in determining the melting behaviour of ultra-high melting materials like the carbides being examined here.

4 Characterisation of (Ta,Hf)C fabricated by reactive routes

Characterisation of the products of two methods of fabrication of (Ta,Hf)C are described in this chapter. The first (Section 4.1) describes synthesis of 4TaC-1HfC powders using self-propagating high temperature synthesis (SHS) and subsequent sintering by SPS in a single step. This method will be referred to from here in this thesis as reactive spark plasma sintering (RSPS). Then characterisation of the products of a two-step method are described in which synthesis of 4TaC-1HfC powders was conducted by SHS using an SPS furnace, heating was stopped after the SHS and then the synthesised powders were taken out of the graphite die, ground and sieved and finally consolidated using an SPS furnace. The latter method will be referred as SHS+SPS. Details of the processing steps were described in Section 3.1. The effect of mechanical pressure and sintering time on the final products was investigated with analysis of the SPS output profiles, XRD for phase evolution and SEM-EDS for microstructural characterisation.

Early work on the TaC-HfC system [2, 28, 29, 161] reported that the 4TaC-1HfC composition has a higher melting point than the individual constituents and the highest in the TaC-HfC system while other properties like vaporisation rate were reported to be the lowest in the system. Therefore the main interest in this chapter is on the synthesis, sintering and solid solution formation of the 4TaC-1HfC composition.

4.1 Reactive Spark Plasma Sintering (RSPS)

4.1.1 Synthesis and sintering

Powder mixtures of reactants after 24 h milling show particles of Ta and Hf coated with smaller (0.04 μm) particles of carbon black (Figure 4.1). Because carbon black particles (~0.04 μm) were smaller than the metallic powders (Ta: 4.80 ± 0.09 μm and Hf: 8.88 ± 2.42 μm), the morphology observed in the mixture after milling was larger metallic powders surrounded/coated by smaller nanosized flake-like carbon particles, as illustrated in Figure 4.1. The mixture and distribution of the particles observed by SEI was homogeneous; the long milling time provided good mixing between the particles and reduced the agglomeration between metallic particles.

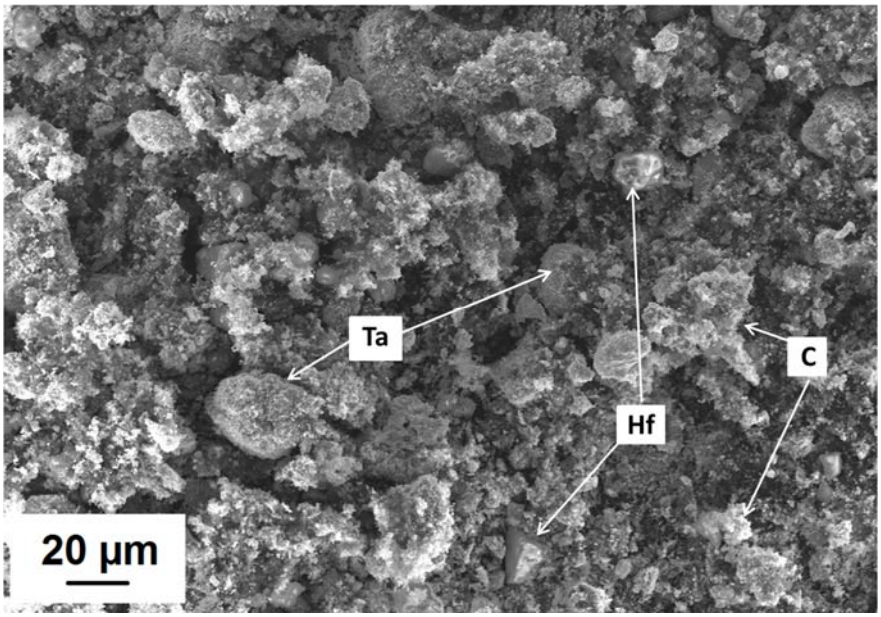

Figure 4.1 SEI of reactant powder mixture consisting of Ta, Hf and carbon black after 24 h dry milling.

Temperature, displacement (δ) and pressure (*P*) output profiles during the synthesis and sintering process are shown in Figure 4.2., the lowest temperature threshold at which the pyrometer picks up a temperature signal is 400 °C. Initial heating took ~4 min to reach 400 °C, the heating rate was 210 °C/min and pressure was kept to a minimum. The minimum load required by the SPS to have the required electrical conduction between electrodes and dies is 6 kN, which for a 20 mm diameter sample is 20 MPa. For the RSPS experiments higher heating rates (>210 °C) and mechanical pressures (>20 MPa) could damage the carbon dies [162]. Even at the minimum pressure graphite dies sometimes cracked during the experiment due to the exothermic reaction produced during the combustion stage.

After ~5 min of heating and after reaching 400 °C, the SPS furnace started to ramp up a constant rate of 210 °C/min. At 1135 °C the temperature signal suddenly increased, with a sharp change in the temperature, which indicates the start of the exothermic reaction. The actual combustion temperature could not be measured since the pyrometer was measuring the temperature on the top of the sample die. However, the change in the graphite die temperature gave a clear indication of the temperature at which the combustion regime started.

The dwell temperature (T_D) was set at 2100 °C and the sintering time (t_D) 20 min; after this sintering time was completed the pressure was kept constant at 20 MPa to reduce the risk of sample cracking until the sample was cooled at room temperature.

The displacement of the ram which indicates the sample shrinkage is shown in Figure 4.2. An initial displacement of ~0.4 mm was due to initial force applied to the graphite plungers and the compaction of powders for the initial 7.5 min of the process. At t=7.5 min there is sharp change in the displacement (from 0.4 mm to 1.8 mm) due to the reactants being converted to carbides, confirmed by XRD analysis (see later Figure 4.15b)). From 8-11.5 min there is a decrease in the displacement from 1.8 mm to 1.3 mm, this can be attributed to the thermal expansion of the sample under sintering (Figure 4.2) [95], at this stage the effect of thermal expansion overcomes that of the powder densification. Fast reaction and sample shrinkage are common phenomena observed also in other systems (such as TiC-TiB_2 and $MoSi_2$) processed by RSPS [73]. Once the sample reaches the sintering temperature at t=12 min the displacement increases from 1.3 mm until it reaches a plateau of 3.4 mm at t=27.5 min. During the remaining 5 min of sintering time there was a small and slow increase in the sample shrinkage of ~0.1 mm. Afterwards, when the sintering time was finished (t=32 min) the cooling regime started, an increase in the displacement signal was observed, this is due to the cooling and subsequent shrinkage of the graphite dies and plungers.

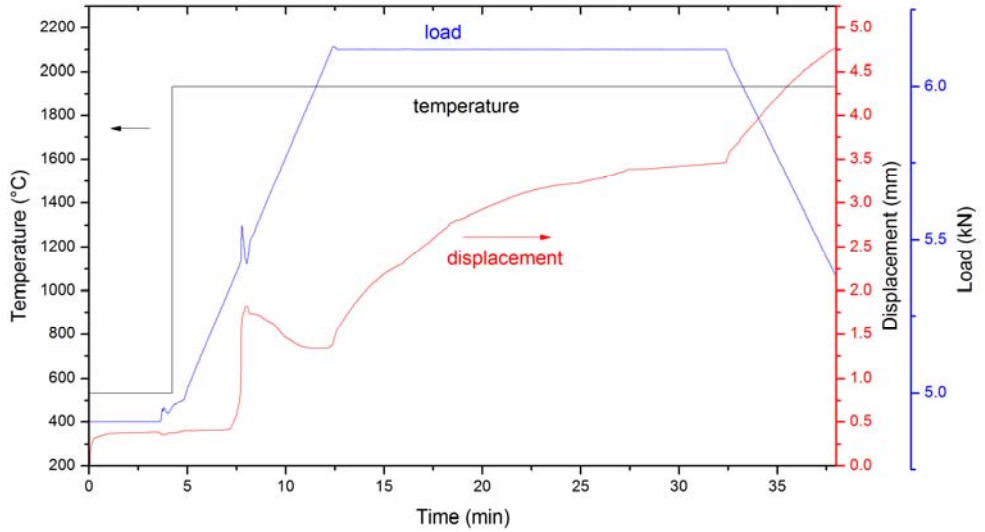

Figure 4.2 Temperature, displacement and mechanical pressure output profiles of 4TaC-1HfC prepared using RSPS, sintered at 2100 °C for 20 min and 20 MPa.

The electrical behaviour of the system was analysed using the current and voltage output profiles (Figure 4.3). Initial current was applied at the 3 min mark into the process, an overshoot in the current and voltage (1100 A, 5.3 V) can be observed, this is a result of the proportional-integral-derivative (PID) controller that needed ~2 min for the system to stabilise the current and voltage to a constant rate. Similar to the temperature and displacement profiles, there was a sudden interruption of voltage and current during the exothermic reaction, however current and voltage were stabilised by the SPS control in less than 1sec. An increase of current (1800 A) and voltage (6.3 V) can be observed until the sintering temperature was reached at t=12 min. At this point, when the sintering regime started the current and voltage were reduced to a constant value of 1500 A and 5.8 V for 20 min. After the sintering, current and voltage were reduced at a constant rate to produce controlled cooling of the sample.

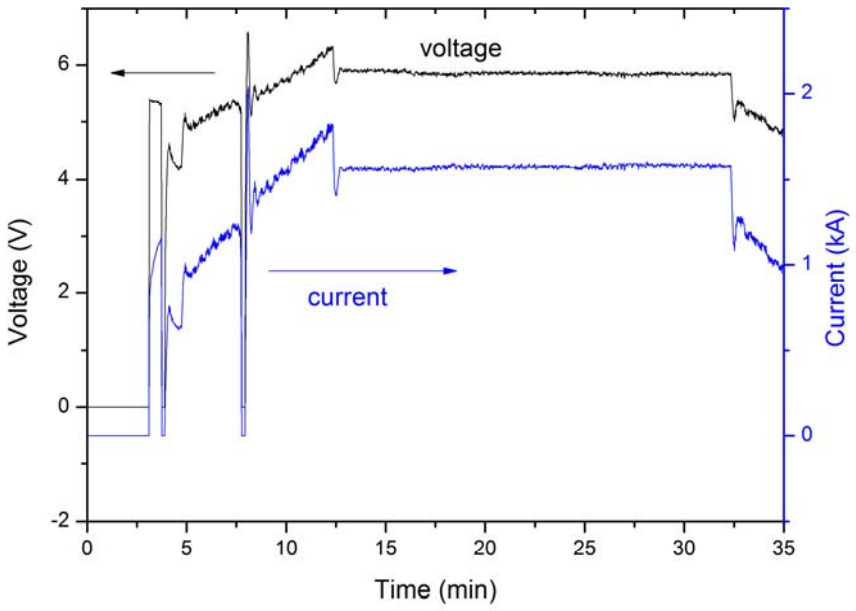

Figure 4.3 Effective electrical current and voltage profiles of RSPS'd 4TaC-1HfC at 2100 °C for 20 min and 20 MPa.

4.1.2 Effect of applied load

The effect of increasing load during the RSPS process was studied. Figure 4.4 shows the output profiles of temperature, displacement and mechanical pressure applied. The sample was heated to 400 °C at a heating rate of 210 °C/min until a temperature of 2100 °C was reached, which was held for a dwell time of 20 min. After sintering the sample was cooled under a controlled cooling rate of 180 °C/min.

The pressure was set at 20 MPa at 4-9 min into the process. An increase in mechanical pressure to 60 MPa was applied when 1500 °C was reached, and the increase in mechanical pressure was conducted in ~2 min. It was observed that the temperature range in which the SHS took place in the current experiments was 1135-1250 °C. Thus a temperature of 1500 °C was selected by which the SHS was completed and all the reactants (Ta, Hf and C) were expected to have been converted to the expected products (TaC and HfC).

For the initial 7 min, the displacement was constant at ~0.3 mm (Figure 4.4). A slight increase in the displacement to 0.6 mm was observed (t=8.5 min). Afterwards the displacement stopped momentarily due to the SHS reaction and the sample expansion. A rapid increase in the displacement can be observed after the load was increased at 9.5 minutes into the process. Sample shrinkage increased from 0.6 mm to 3 mm in less than 3 min, before the sintering temperature was reached. During the soak time the displacement increased at a slower rate to a maximum displacement of 5.3 mm. It can be observed that the densification of the SHS powders started before the sintering temperature was reached; this effect is a result of the increase in mechanical load to the sample. After the sintering stage (~32 min), the increase in the displacement was a consequence of the sample/die/plungers thermal shrinkage during the cooling stage.

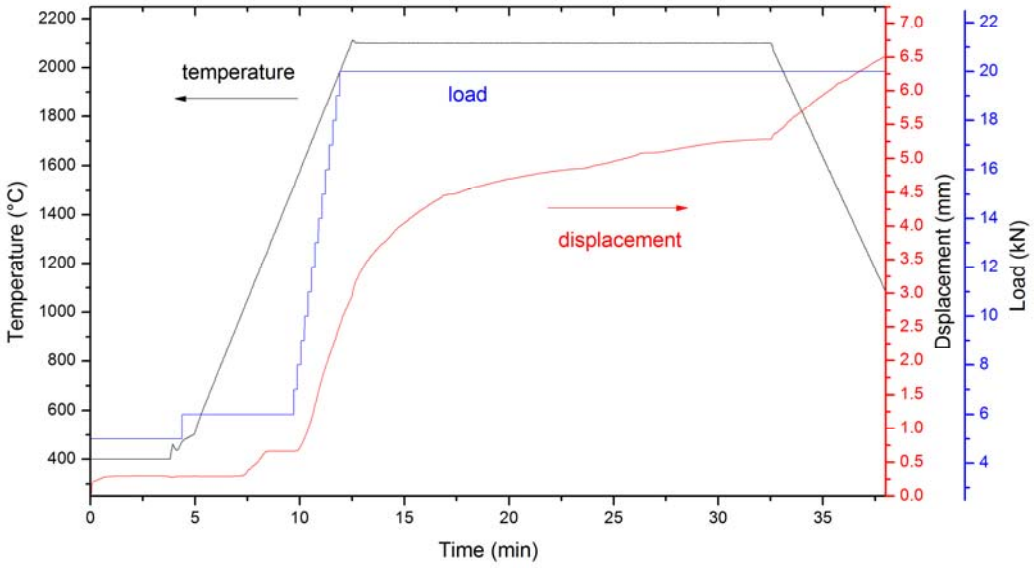

Figure 4.4 Temperature, displacement and mechanical pressure output profiles of 4TaC-1HfC prepared using RSPS, sintered at 2100 °C for 20 min and 60 MPa.

4.1.3 Effect of sintering time

The effect of the sintering time on the final products, density and microstructure was subsequently examined by studying the RSPS by applying a mechanical pressure of 60 MPa at a sintering temperature of 2100 °C and setting different sintering times (10 and 20 min).

Figure 4.5 shows the temperature, displacement and mechanical pressure output profile of 4TaC-1HfC prepared by RSPS at a sintering temperature of 2100 °C for 10 min and 60 MPa. Heating increased at a constant rate of 210 °C/min after the first 5 min of the process. The sample was constantly heated until the sintering temperature of 2100 °C was achieved at t=12.5 min. Afterwards the sintering stage started and temperature was constant for 10 min. At t=22.5 min the sintering stage ended and the sample was cooled to room temperature at a controlled rate of ~180 °C/min.

Mechanical pressure at the start of the heating cycle was 20 MPa. The pressure was constant for 5 min until the temperature reached 1500 °C, afterwards the pressure was increased in the following 2 min to 60 MPa. The pressure reached 60 MPa when the sample was at 2000 °C at t=12 min and was maintained constant for the remainder of the heating, sintering and cooling stages.

The displacement behaviour in Figure 4.5 shows an initial small displacement of ~0.3 mm from the start of the experiment to t=7 min, a small increase to 0.6 mm. Then the displacement stops increasing due to the SHS reaction and was constant for ~1 min until mechanical pressure was increased, then shrinkage of the sample reactivates afterwards. When mechanical pressure started to increase at t=10 min there was a sharp increase of displacement to 2.9 mm (t=12.5 min). The sintering stage started at t=12.5 min and the displacement increased moderately during the sintering stage (12.5-22.5 min) to 4.5 mm. Shrinkage of the sample was interrupted by the start of the cooling stage at t=22.5 min. Additional displacement during cooling was due to the thermal shrinkage of sample and dies.

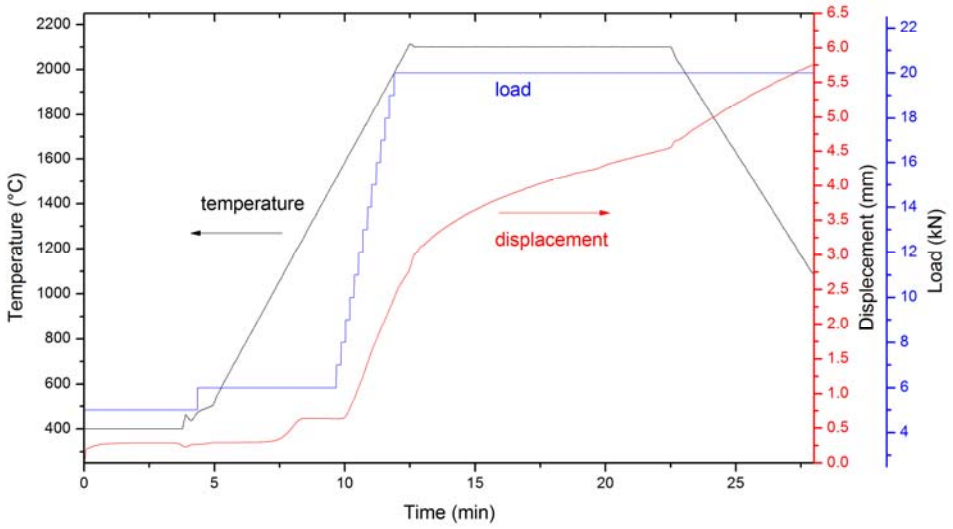

Figure 4.5 Temperature, displacement and mechanical pressure output profiles of 4TaC-1HfC prepared using RSPS, sintered at 2100 °C for 10 min and 60 MPa.

4.1.4 Density

Pellets of synthesised powder in the green state show a copper colour distinctive of TaC powder with a mixture of a HfC grey phase distributed throughout the samples. After polishing the samples had a matte finish. Dense TaC and HfC show a metallic high-gloss finish after polishing, suggesting that the dull finish was due to high level porosity after sintering and confirmed by density measurement by Archimedes method. Samples fabricated by RSPS are shown in Figure 4.6, where a) is a sample sintered at 2100 °C for 20 min at 20 MPa and b) 2100 °C for 20 min at 60 MPa.

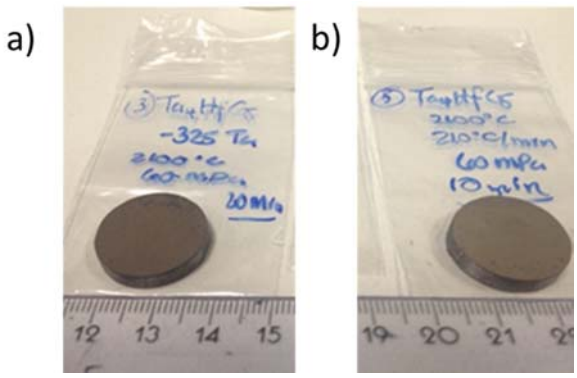

Figure 4.6 4TaC-1HfC pellets prepared by RSPS a) 2100 °C, 20 MPa, 20 min and b) 2100 °C, 60 MPa, 10 min; rule scale in cm.

Sintering conditions (t_D, P)	Density ρ (g/cm$^{3)}$	Relative density %
20 min, 20 MPa	8.7 ± 0.39	62.6 ± 0.30
20 min, 60 MPa	12.5 ± 0.38	89.6 ± 0.36
10 min, 60 MPa	11.7 ± 0.18	83.3 ± 0.13

Table 4.1 Density and relative density of 4TaC-1HfC fabricated by RSPS under different sintering conditions (sintering pressure and time).

Density and relative density of the samples prepared by RSPS with variations in pressure (20 and 60 MPa) and sintering time (10 and 20 min) are shown in Table 4.1. A highly porous material with 62.6 ± 0.30 % density was produced by keeping the mechanical pressure of 20 MPa constant throughout the experiment. An increment in density from 8.7 to 12.5 gm/cm^3 was achieved by increasing the pressure from 20 MPa to 60 MPa after the SHS reaction. A maximum 89.6 ± 0.36 % relative density was achieved with 60 MPa for 20 min. In addition, the reduction in sintering time to 10 min resulted in a reduction in relative density to 83.3 ± 0.13 %.

4.1.5 Phase evolution during RSPS

XRD analysis was conducted in the initial reactant powder mixture and RSPS'd products. XRD (Figure 4.7) reveal that only reactant signals are present after milling (Ta and Hf). No additional phases were

formed or found (by mechanical activation or reaction) by XRD in the mixed reactant powders (Figure 4.7d)). After RSPS all reactants have been converted to carbides and other products. Figure 4.7c) shows that under P=20 MPa, t_D= 20 min, TaC and HfC formed, with small reflections of an HfO_2 phase at a diffraction angle (2θ) of 28 and 31 degrees [52]. Lattice parameter was measured for the TaC phase at 4.449 Å, and using Bowman's equation [32] the stoichiometry was $TaC_{0.94}$.

In addition, similar phase formation was found for the patterns of 4TaC-1HfC RSPS'd at an increased pressure of 60 MPa and sintering times of 10 (Figure 4.7b)) and 20 min (Figure 4.7a)). The respective measured lattice parameters were 4.448 ± 0.003 Å and 4.464 ± 0.001 Å. The calculated stoichiometry was $TaC_{0.94}$ and $TaC_{1.04}$ respectively.

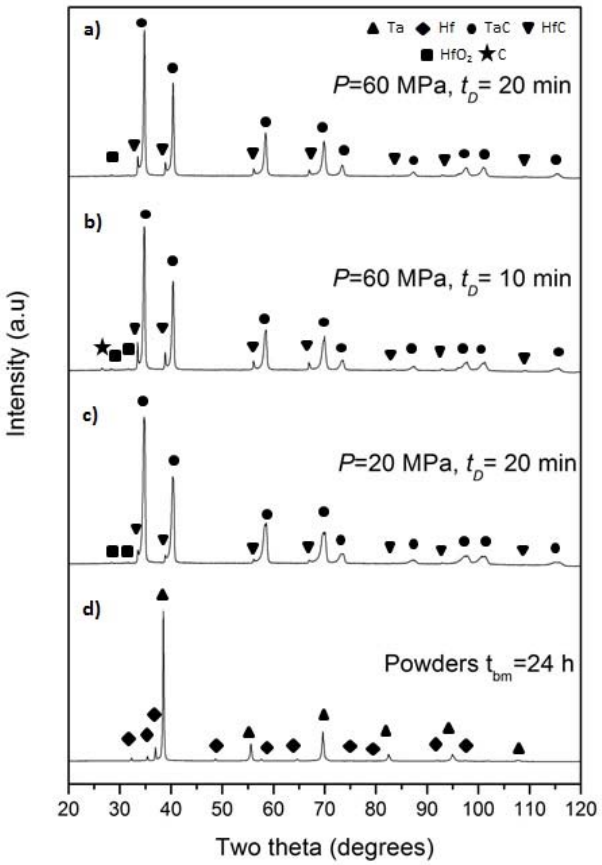

Figure 4.7 X-ray Diffraction (XRD) patterns of 4TaC-1HfC RSPS products obtained by sintering at 2100 °C and under different parameters a) P=20 MPa, t_D=20 min, b) P=20 MPa, t_D=10 min, c) P=20 MPa, t_D=20 min, and d) reactant powder mixture ball milled for 24 h (P= mechanical pressure, t_D= sintering time and t_{bm}=time of ball milling).

4.1.6 RSPS microstructures

BSE SEM images of a polished surface of 4TaC-1HfC fabricated by RSPS at 2100 °C for 20 min at 20 MPa are shown in Figure 4.8. A porous microstructure (~63% dense) was obtained with the first trial of the RSPS route. In Figure 4.8 a) two main areas can be easily identified in the microstructure; a dense area consisting of a core rim/structure containing ~15 µm diameter HfO_2 grains surrounded by a rim of ~4 µm HfC grains and porous regions containing fine <5 µm TaC phase. At higher magnification the phases can be easily identified (Figure 4.8 b)) with elongated dark grey ~15 µm HfO_2 grains with a rim consisting of smaller HfC grains of ~4 µm diameter. In addition, the porous TaC phase comprises 1.45 ± 0.26 µm grains and black contrast pores of ~2.5 µm.

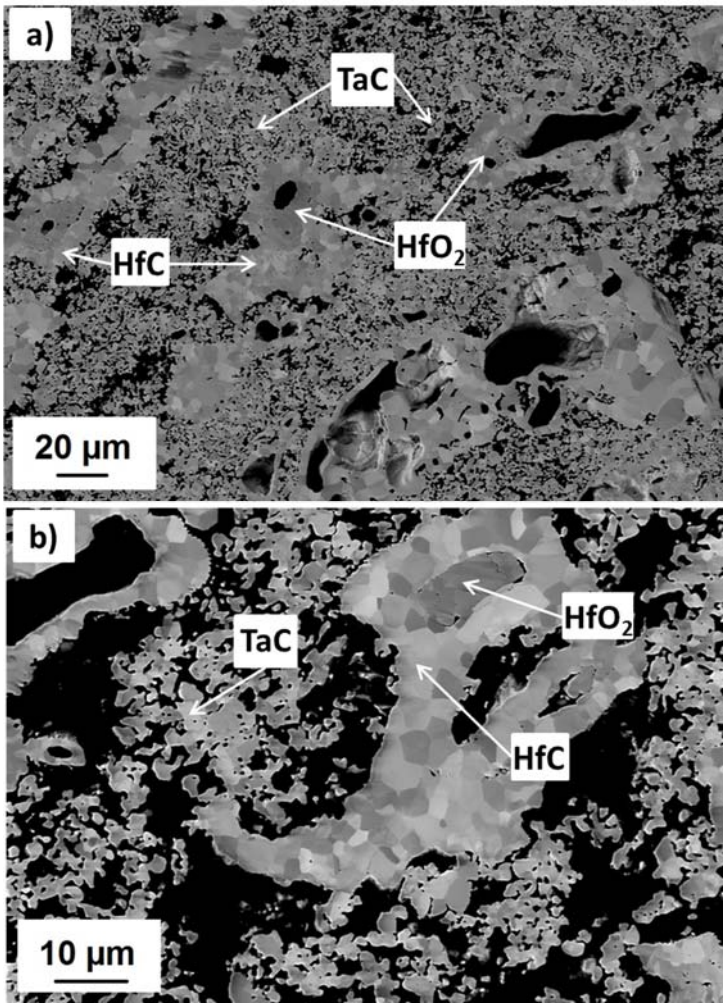

Figure 4.8 BSE images of 4TaC-1HfC fabricated by RSPS and sintered at 2100 °C for 20 min and 20 MPa a) shows the general microstructure and b) the detailed morphologies at higher magnification.

Two BSE images at different magnifications of the 4TaC-1HfC RSPS'd at 2100 °C for 20 min and 60 MPa pressure are shown in Figure 4.9a) and b). A denser microstructure in Figure 4.9a) (89.6 ± 0.36 % TD) can be observed in comparison with the micrographs of samples RSPS'd at 20 MPa (Figure 4.8a)). A core/rim structure containing an HfO_2 phase indicated by the arrow can be observed in the micrograph of Figure 4.9b) with a core size of 14.2 µm. The rim structure contains an HfC phase that encloses completely the HfO_2 phase. The remainder of the microstructure was TaC grains with enclosed porosity within the grains and at triple junctions, the micrograph reveals the early stages of sintering of TaC with necking between particles forming a connected network in a highly porous structure. In addition there was an increase in grain size in TaC to 2.7 ± 0.62 µm by increasing the mechanical pressure to 60 MPa after SHS.

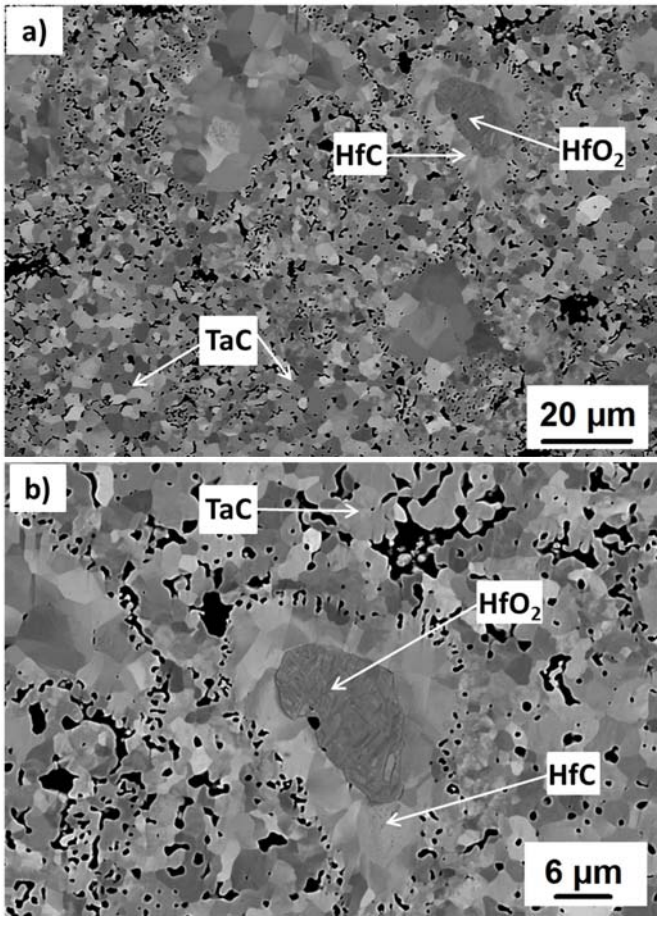

Figure 4.9 BSE images of 4TaC-1HfC fabricated by RSPS and sintered at 2100 °C for 20 min and 60 MPa a) general area and b) higher magnification showing detail of phase morphologies.

In addition to point and region EDS analysis, EDS mapping was conducted on samples to analyse the distribution of elements throughout the sample. An SEI (Figure 4.10a)) is shown to illustrate and identify the areas in the microstructure where the core/rim structures are present and in conjunction with the EDS map in Figure 4.10 b) the areas of concentration of each of the constituent elements are revealed for a 4TaC-1HfC sample prepared by RSPS at 2100 °C, P=60 MPa and t_D=20 min.

Areas of concentration of Hf can be observed as blue areas in the EDS map. Hf is concentrated in regions in the HfC phase and HfO_2 and was not homogeneously distributed throughout the sample. Also the signals from Ta (yellow) show a concentration outside the blue Hf areas, while O was found as the green regions mainly on what was HfO_2. Red signal from C could be seen mixed throughout the whole sample, mixed with the regions saturated with Hf and Ta, suggesting that these areas are formed of HfC and TaC respectively. These images suggest that the resulting microstructure of the sample is a composite consisting of a core/rim structure of HfO_2-HfC in a matrix of TaC.

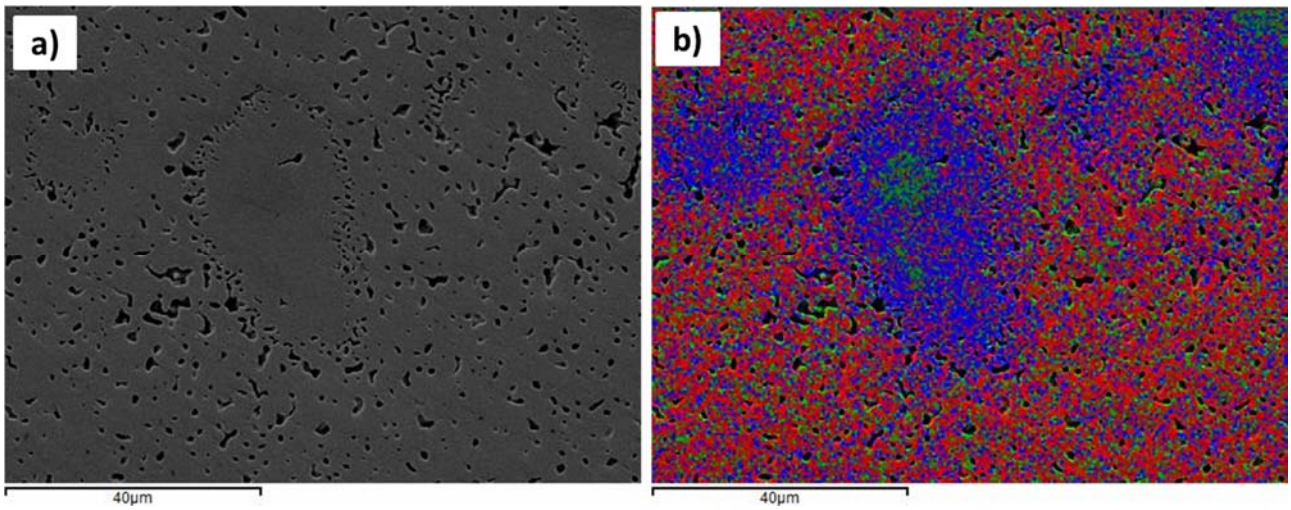

Figure 4.10 Images of 4TaC-1HfC produced by RSPS at 2100 °C for 20 min and 60 MPa a) BSE image of polished surface and b) mixed signal EDS mapping (C: red; O:green; Hf: blue; Ta: yellow)

The effect of the sintering time was observed in BSE images of 4TaC-1HfC fabricated by RSPS at 2100 °C, P=60 MPa and t_D=10 min. Typical images of samples prepared under these conditions are shown in Figure 4.11, which reveal that the grain size of the sample sintered for t_D=10 min in Figure 4.11 a)

is smaller than the one sintered for t_D=20 min of Figure 4.9a). An increase of 6.3% in residual porosity was observed by reducing the t_D by 10 min, the maximum relative density was 83.3 ± 0.13 %. In addition, the particle size of the oxide phase was ~15 μm, similar in size to oxide particles in other samples prepared by RSPS. The grain size of the HfC was 4.8 μm ± 0.9 μm and a reduction in the TaC grain to 2.1 ± 0.67 μm compared to 2.7 ± 0.62 μm from a sample sintered for 20 min was observed.

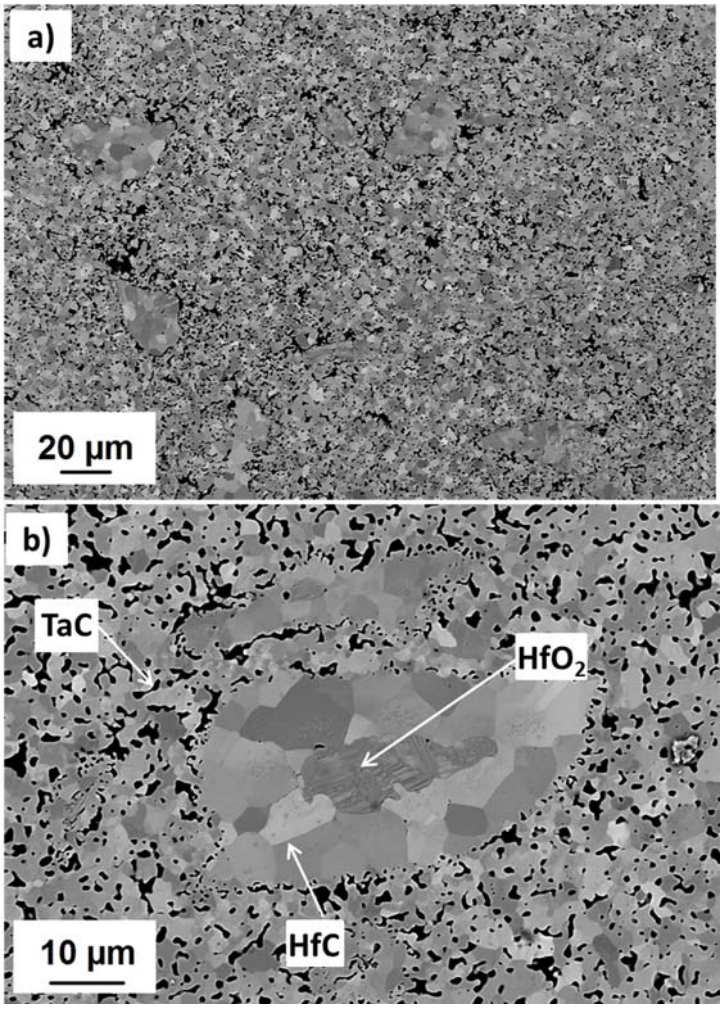

Figure 4.11 BSE images of 4TaC-1HfC fabricated by RSPS and sintered at 2100 °C for 10 min and 60 MPa a) Low magnification and b) high magnification.

4.2 Reactive two-step SHS+SPS processing

After the initial trials of synthesis and sintering of 4TaC-1HfC by RSPS, it was decided to evaluate the sintering behaviour of synthesized 4TaC-1HfC powders by a two-step synthesis and sintering route in

which first the powders were synthesised by SHS in an SPS furnace and in a separate step the reacted powders were consolidated by SPS.

4.2.1 Synthesis by SHS

Reactant powders of a 4TaC-1HfC composition were heated to 1400 °C at a heating rate of 210 °C/min. After the initial 4 minutes and a few temperature oscillations, the PID control stabilized the heating of the sample. After the sample reached 1400 °C and the SHS was conducted, the heating was stopped and the powder was cooled to room temperature. The temperature output profile of the synthesis of 4TaC-1HfC powders can be observed in Figure 4.12.

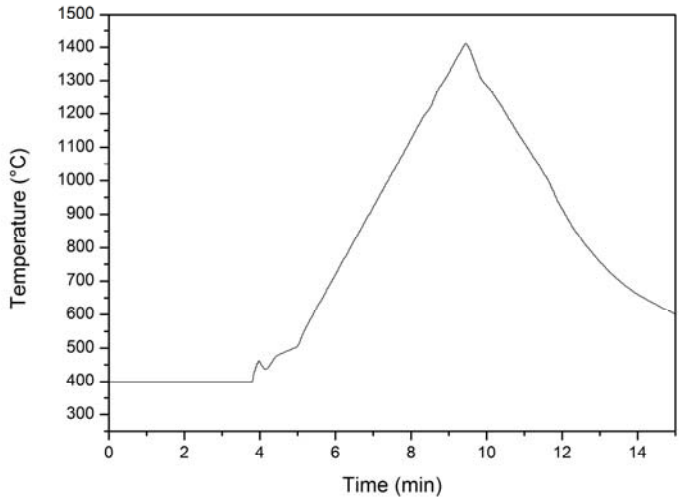

Figure 4.12 Temperature profile of 4TaC-1HfC powders synthesised by SHS using and SPS furnace.

After the SHS process and the powders being cooled the pellets from the SHS powders were taken out of the graphite die. They were of a copper/dark brown colour (Figure 4.13), typical of TaC, with a crumbly texture. Afterwards the powders were ground in a mortar with a pestle and sieved with a final mesh size of 50 μm. and subsequently the particle size was measured using a laser diffraction to be d_{50}=5.82 ± 0.11 μm.

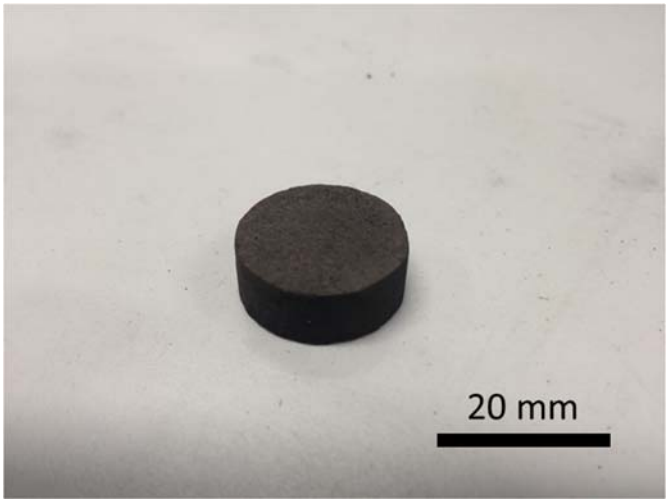

Figure 4.13 Photograph of a pellet of compacted 4TaC-1HfC powder after SHS.

An SEM SEI of the SHS powders (Figure 4.14) shows angular agglomerated particles with a particle size of d_{50}=5.82 ± 0.11 µm, with all particles <40 µm.

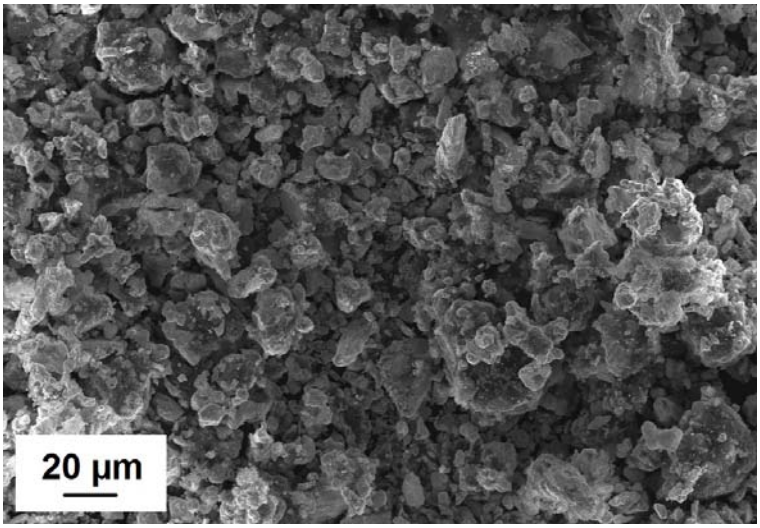

Figure 4.14 SEI of 4TaC-1HfC powders prepared by SHS after grinding and sieving.

4.2.2 Phase evolution by SHS-SPS

Phase evolution was analysed using XRD. The initial reactant powders after 24 h milling were analysed and the mixture shows reflections of pure metallic Ta and Hf (Figure 4.15c)), no other secondary phases or impurities were found. After SHS the reflections of the reacted powders (Figure 4.15b)) show high

relative intensity peaks of TaC with some small reflections identified as Ta_2C [49, 50]. Also small peaks of HfC were observed along with reflections from secondary phases of HfO_2 and Ta_2O_5, this confirms that all the reactants were converted to carbides and secondary oxide phases since no other metallic elements were found [52, 55]. The lattice parameter of the TaC in the reacted powder was 4.453 ± 0.001 Å with a calculated stoichiometry of $TaC_{0.98}$.

XRD from consolidated SHS powders by SPS (T_D=2100 °C, t_D=20 min and P=60 MPa), Figure 4.15a) shows that after sintering the main reflections observed were of TaC, with some small peaks of HfO_2 at 2θ ~28 and 32 peak locations. This suggests that the Ta_2C phase formed during SHS was converted to TaC during the sintering process by reacting with available loose C from the reacted powders. In addition, Ta_2O_5 secondary phase was not found in the final products after sintering likely due to the processing temperatures used (2100 °C) which are higher than the melting point of Ta_2O_5 (1872 °C), thus the oxide phase melted and reacted to give TaC. However, the HfO_2 phase is more difficult to remove due its high melting point of 2758 °C.

Another observation was that HfC phase reflections were not found in the XRD patterns, this suggests that HfC diffused into the TaC lattice, in the form of a solid solution of the $(Ta,Hf)C_{1-x}$ type. Also a shift of the TaC peaks to lower 2θ values was observed and was an indication that a solid solution was formed, however the peaks were not symmetrical (Figure 4.15a)), this is more evident in angles 2θ >60 degrees. The left side of the peaks is broader, this suggests that there is more than one composition of (Ta,Hf)C solid solution. The lattice parameter of TaC phase was calculated at 4.462 ± 0.001 Å and using data reported by Rudy [1] and assuming the initial composition of $TaC_{0.98}$ from the SHS powders the major phase present was a (Ta,Hf)C solid solution with a HfC mole content of 4.15%.

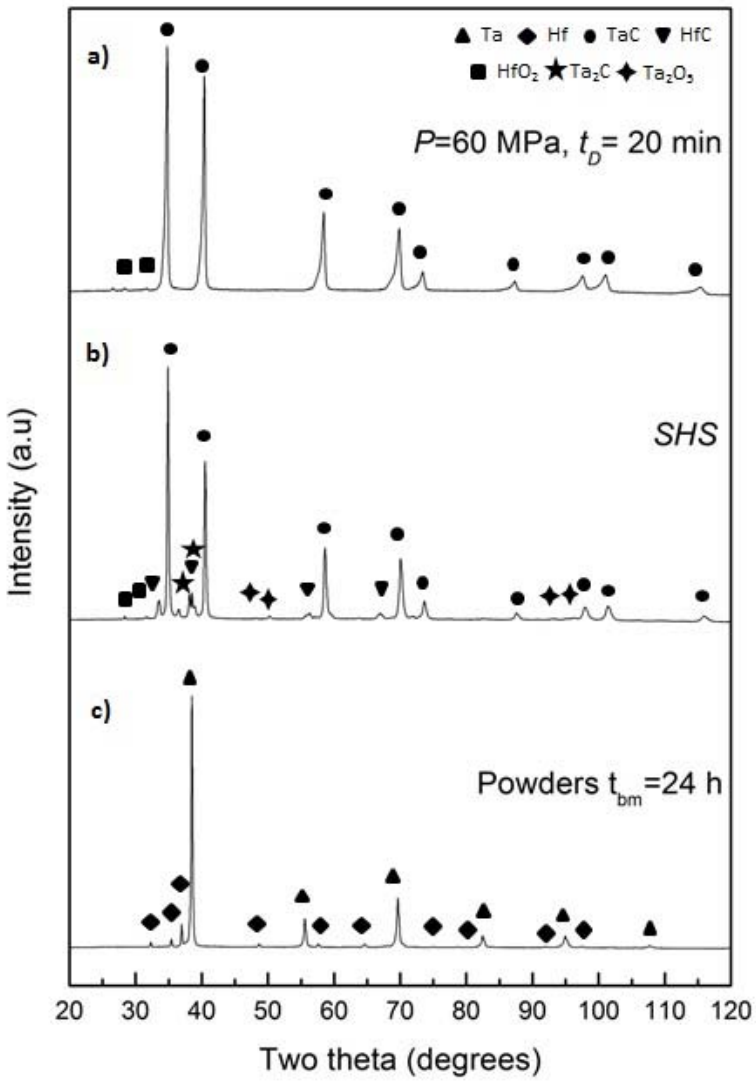

Figure 4.15 X-ray Diffraction (XRD) of a) product consolidated by SPS at 2100 °C, P=60 MPa, t_D=20 min, b) 4TaC-1HfC powders produced by SHS and c) reactant powder mixture ball milled for 24 h.

4.2.3 Microstructural characterisation of SHS powders sintered by SPS

Table 4.2 shows an overview of the thermal schedule and resulting microstructures of samples prepared by SHS+SPS. Density of the consolidated powders was 13.8 ± 0.19 g/cm^3. BSE images (Figure 4.16) show a highly dense microstructure with a 98.2 ± 0.13 % relative density, with entrapped 1.1 ± 0.5 μm size round pores mostly observed inside the grains. The microstructure consisted of a matrix of grains

of (Ta,Hf)C with a mean grain size (MGS) of 6.4 μm and with a secondary phase constituted of ~10 μm HfO_2 grains distributed throughout the sample in ~2 vol%.

Sintering conditions (T_D, t_D, P)	Density (g/cm^3)	Relative density (%)	MGS (μm)	Grain size range
2100 °C, 20 min, 60 MPa	13.8 ± 0.19	98.2 ± 0.13	6.4	1.4-20.5

Table 4.2 Sintering conditions and microstructural properties of 4TaC-1HfC powders produced by SHS and consolidated by SPS.

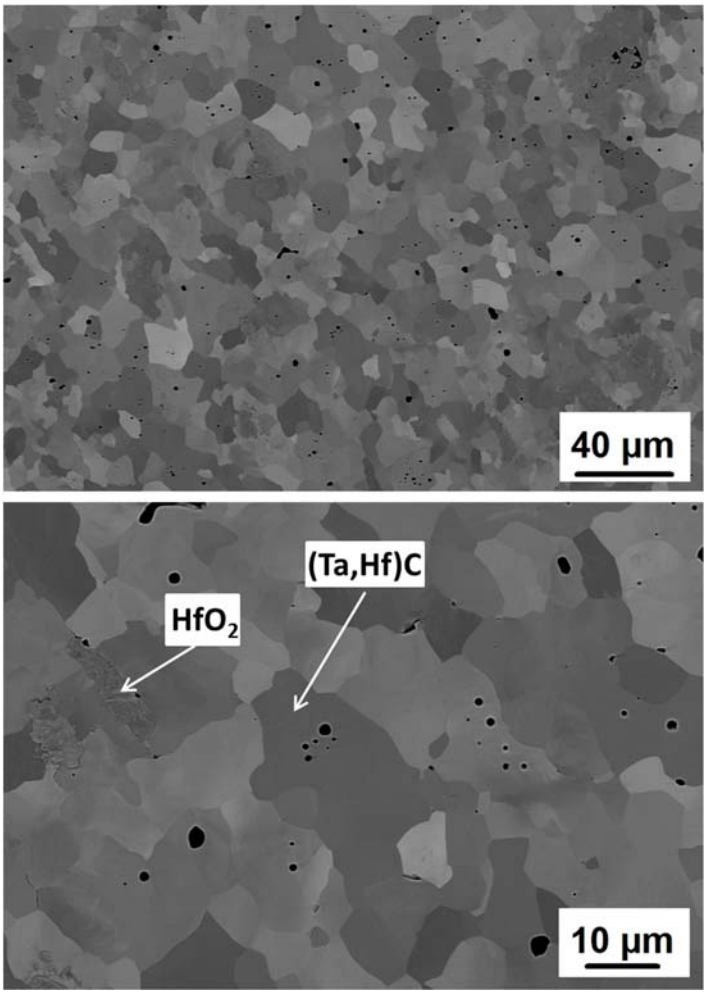

Figure 4.16 BSE images of polished sample of 4TaC-1HfC fabricated by the SHS-SPS route and sintered at 2100 °C, P=60 MPa, t_D=20 min.

EDS map analysis (Figure 4.17) shows a Hf-rich (Ta,Hf)C solid solution in the region of where the map shows a higher concentration of the blue coloured Hf signal in an area of ~10 μm around the HfO_2 grain (green and blue region). Outside this area a Ta-rich (Ta,Hf)C solid solution region with a higher concentration of the yellow-coloured Ta signal was observed. This is in agreement with the observations of section 4.2.2 of a Ta-rich (Ta,Hf)C solid solution with a 4.15% mole concentration of HfC.

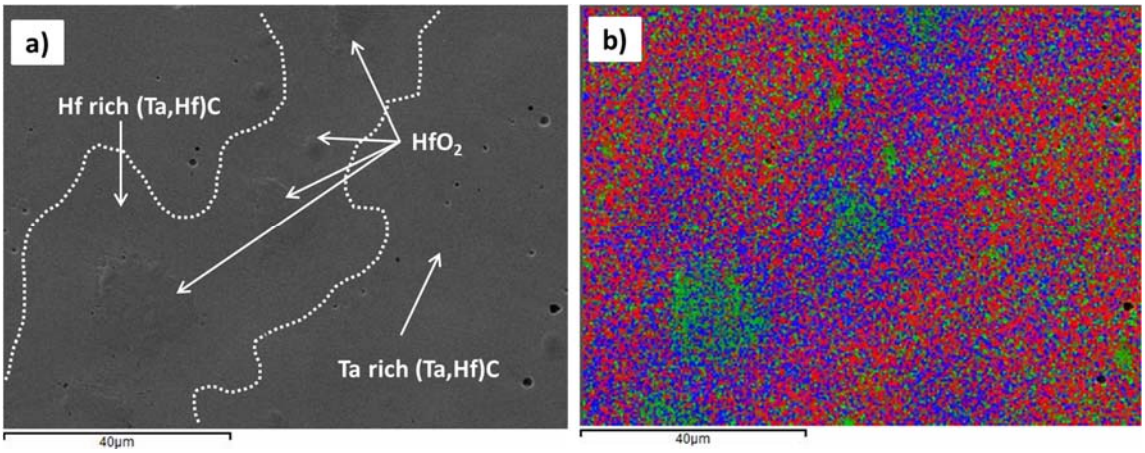

Figure 4.17 Images of 4TaC-1HfC SHS powders consolidated by SPS at 2100 °C for 20 min and 60 MPa a) BSE image of polished surface and b) mixed signal EDS mapping (C: red; O:green; Hf: blue; Ta: yellow)

The results obtained by the SHS+SPS method showed that the deagglomeration of the synthesised powders by grinding and sieving was beneficial for achieving high density (>98%) and helps in the solid state diffusion mechanisms of solid solution formation. XRD and EDS techniques showed that a single-phase solid solution was not formed at the sintering conditions of 2100 °C, 20 min and 60 MPa, however these results suggests that longer sintering times would make the (Ta,Hf)C solid solutions homogeneous.

4.3 Discussion

The viability of producing refractory carbides using combustion synthesis has been reported by several authors [43, 49, 50, 52-55] mainly on monolithic systems and fabrication of UHTC composite materials using reactive routes (RSPS and SHS+SPS) has been investigated mostly in diboride (ZrB_2/HfB_2) +

SiC systems [94, 95, 162, 163]. Synthesis and sintering of 4TaC-1HfC powders was conducted using RSPS in a single step; the samples were heated at 210 °C/min and 20 MPa of mechanical pressure was applied before the SHS reactions. Higher heating rates and pressures increase the incidence of die breakage due to the highly exothermic reaction [94]. A maximum relative density of ~90% was achieved by increasing the mechanical pressure to 60 MPa after the SHS reaction, also densification started when the pressure was increased to 1400 °C (Figure 4.4). In experiments with constant pressure applied throughout the experiment (20 MPa) and sintering temperature of 2100 °C the relative density was 62.6 ± 0.30 %. A decrease in relative density to 83.3 ± 0.13 % was observed by reducing the sintering time to 10 min.

Since the adiabatic temperatures (T_{ad}) of TaC and HfC are lower than their melting points, a solid flame combustion mechanism was expected (Table 2.2) [49, 53]. The exothermic reaction was produced at ~1135 °C, a sudden change in the temperature was observed in the pyrometer signal (Figure 4.2) but the combustion temperature could not be measured. After the SHS reaction there was a sharp change in the displacement curve (Fig 4.2), the expansion of the sample can be attributed to several factors; firstly gases formed in the combustion, from metallic oxide impurities and absorbed gases, strongly expanded the reaction mass [50]. In addition, the higher the density of the reactant mixture or in this case with the mechanical pressure applied, escape of these gases is more difficult, as a result the reaction mixture expands more. Although the combustion process is of that of a gasless type, it has been reported that during combustion H_2, CO, CO_2 and N_2 are produced [49-51] from the impurities of the starting materials. These gases increase the effective contact between particles of reactants improving the conversion of the reactants to final products. Also the milling time (24 h) increases the interfacial area between the reactants improving the combustion process [91]. XRD analysis (Figure 4.15b) confirms the conversion of the reactants (Ta, Hf and C) to carbides (Ta and HfC) and secondary phases (HfO_2).

Microstructures of RSPS samples (Figure 4.8, Figure 4.9 and Figure 4.11) revealed core/rim structures consisting of HfO_2 grains surrounded by rims of HfC in a porous matrix of TaC. The core/rim structure suggest that Hf readily oxidises during the milling process, although its detection by XRD was difficult.

Then during the SHS reaction and further sintering, the outer surface of the HfO_2 particles reacted with the available carbon to form HfC. Hence, the dense outer rim HfC structure surrounding the HfO_2 particles.

Benck et al. [52] suggest that after completion of the SHS reaction, while the HfC is still at high temperature, the product readily oxidises, forming CO and HfO_2. BSE images revealed that the core/rim structures are highly dense and closely bonded, while the surrounding areas are formed of a porous TaC matrix, this explains why it is difficult to diffuse HfC into TaC, since there is limited surface contact between HfC-TaC grains and within the TaC phase. XRD peaks do not show a single-phase solid solution of TaC-HfC, but revealed a solid solution with different compositions confirmed by peaks of both TaC and HfC (Figure 4.7)

Using a two-step SHS+SPS processing route, and by XRD analysis reacted powders revealed the formation of TaC, Ta_2C, Ta_2O_5, HfC and HfO_2 (Fig 4.15) after SHS. During the reaction, formation of both TaC and Ta_2C may occur [34, 35] and since the combustion temperature of Ta_2C is ~100 °C less than TaC (2430 °C) the appearance of Ta_2C would be expected to precede the formation of TaC [50]. However, in this study the relative intensities of Ta_2C XRD peaks compared to TaC are small, only a small amount of Ta_2C was present, and after SPS this was converted to TaC (Figure 4.15). Furthermore, after sintering Ta_2O_5 was not present, likely due to the processing temperatures used (2100 °C) being above the melting temperature of the oxides, which thus melted and reacted to give TaC. HfO_2 is more difficult to remove since its melting point is 2758 °C.

Deagglommeration of SHS powders by grinding and sieving improved the sinterability of powders; a density of 13.8 ± 0.19 g/cm^3 was obtained after SPS at 2100 °C and 60 MPa. SHS+SPS microstructures (Figure 4.16) show increased density (98.2 ± 0.13 % relative density) compared to RSPS ceramics; HfO_2/HfC core-rim structures were not found by SHS+SPS processing. XRD and EDS show that a single-phase solid solution was not formed at these sintering conditions, longer sintering time would be needed to make the solid solutions homogeneous.

5 Characterisation of (Ta,Hf)C fabricated by solid state sintering

This chapter examines the sintering behaviour of TaC-HfC ceramics fabricated by SPS at different sintering temperatures (densification and solid solution formation) and evaluates the thermal and mechanical properties of the solid solutions and how they compare with those of single member TaC and HfC. The first part of the chapter focuses on the 4TaC-1HfC composition; the evolution of microstructures, solid solution formation and mechanical and thermal properties with sintering temperature. After evaluation of optimal conditions for preparing a single phase solid solution material, the second part of the chapter examines the microstructures, thermal and mechanical properties of TaC-HfC with different compositions (4TaC-1HfC, 1TaC-HfC and 1TaC-4HfC) and evaluates and compares them with properties of single phase end member TaC and HfC sintered ceramics.

5.1 Characterisation of 4TaC-1HfC fabricated by SPS

Fabrication of 4TaC-1HfC ceramics was conducted using SPS. As described in detail in Chapter 3, for this processing route the initial materials used were commercial powders of TaC and HfC (<44 μm mesh, ABRC, Karlsruhe, Germany). Sintering behaviour and solid solution formation were studied by varying the sintering temperature from 2050 to 2450 °C in increments of 100 °C. The sintering time (t_D) and mechanical pressure (P) for the 4TaC-1HfC sintering experiments were set at 20 min and 30 MPa respectively for all samples.

5.1.1 Density

The sintering conditions, bulk density, relative density, mean grain size (MGS), open porosity and pore size of 4TaC-1HfC powders after consolidation by SPS are shown in Table 5.1. There was an increase in the relative density from 77.9 ± 0.18 to 85.5 ± 0.17 % when the temperature was increased from 2050 to 2150 °C. A sharp increase to 93.0 ± 0.16 % was observed when the temperature increased to 2250 °C. Grain boundary and lattice diffusion mechanisms were probably active at sintering temperatures between 2150-2250 °C leading to a considerable reduction in porosity from 14.5 vol% to 6.7 vol%. Higher sintering temperatures resulted in a limited increment in density, with a small increase of 1.7%

from 93.0 ± 0.16 to 94.8 ± 0.17 % relative density in the range of 2250-2450 °C and the highest relative density (94.8 ± 0.17 %) and bulk density (13.35 ± 0.02 g/cm^3) was achieved at 2450 °C.

Sintering temperature (°C)	Bulk density (g/cm^3)	Relative density (%)	Mean grain size, MGS (μm)	Pore size (μm)
2050	10.94 ± 0.02	77.7 ± 0.18	-	0.48 ± 0.37
2150	12.01 ± 0.02	85.2 ± 0.17	-	0.56 ± 0.32
2250	13.10 ± 0.02	93.0 ± 0.16	3.2	1.17 ± 0.47
2350	13.28 ± 0.05	94.5 ± 0.38	5.1	1.61 ± 0.88
2450	13.35 ± 0.02	94.8 ± 0.17	6.2	1.79 ± 0.77

Table 5.1 Sintering temperature, bulk density, relative density, mean grain size of the matrix and pore size of 4TaC-1HfC ceramics fabricated by SPS at temperatures indicated for 20 min and 30 MPa.

5.1.2 X-ray diffraction (XRD) analysis

XRD patterns of 4TaC-1HfC powders before and after consolidation are shown in Figure 5.1a) and b). The 4TaC-1HfC powder mixture show pairs of diffraction peaks corresponding to the cubic structures of TaC and HfC compounds, no other phases were detected. At a sintering temperature (T_D) of 2050 °C the XRD patterns show that the reflection peaks of TaC and HfC start to merge, both peaks were not completely separated, indicating that a solid solution was starting to form. As the sintering temperature was increased to 2150 °C, the HfC reflections were relatively small due to the diffusion of HfC into the TaC lattice, the broadening of the TaC peak on the left side shows that the (Ta,Hf)C solid solution was not monophasic, but a mixture of (Ta,Hf)C solid solutions of different compositions. In addition, as shown in Figure 5.1 b), the TaC peaks shift to lower angles as the sintering temperature increases.

As the temperature was increased to 2250 °C, no HfC peak was visible in the enlarged section of the XRD patterns (Figure 5.1b)), although the broadening of the TaC peak shows the formation of the

(Ta,Hf)C solid solution. Finally, after SPS at higher temperatures (i.e. ≥2350 °C), HfC was still not detected and the TaC peaks are further shifted. Both phenomena suggest that HfC and TaC mutually diffused into their lattices giving a solid solution indicated by a narrow single-phase peak. Formation of solid solution was confirmed by lattice parameter measurement using the Nelson-Riley function as described in Section 3.5.1. These results will be correlated and discussed with results from additional analytical techniques (EDS, TEM) later in this chapter.

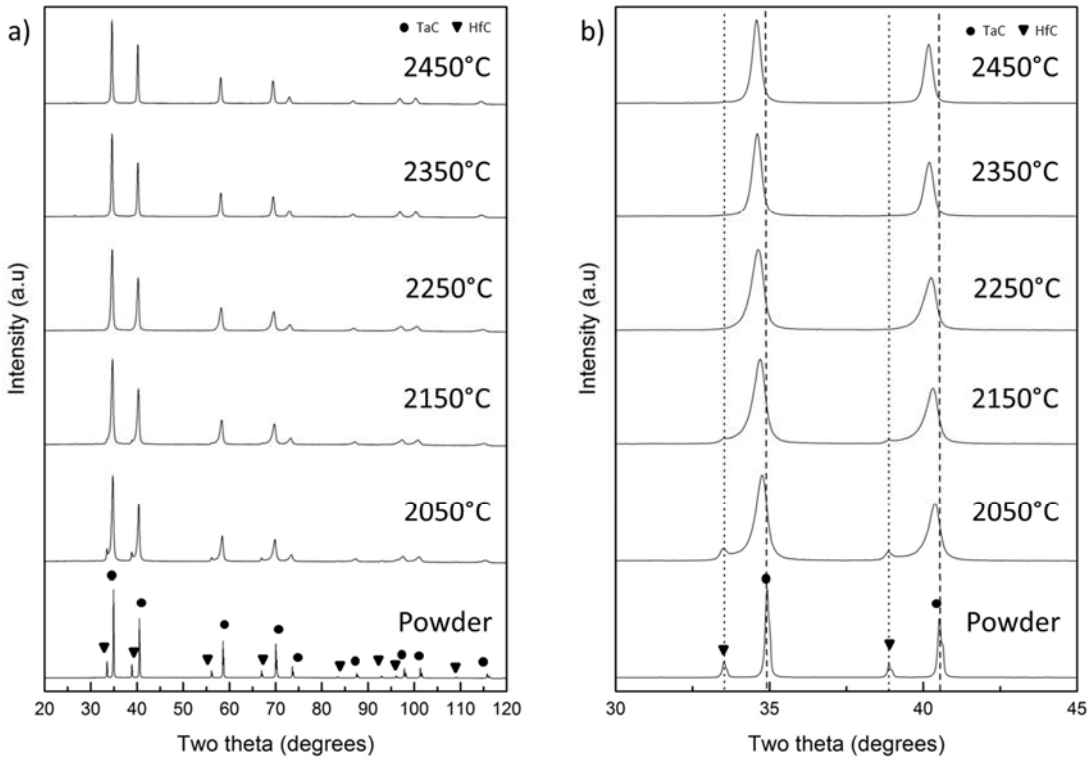

Figure 5.1 a) XRD of 4TaC-1HfC before and after SPS at the temperatures indicated for 20 min and 30 MPa b) enlarged section between 30-45 two theta degrees showing the shift of TaC peaks and formation of (Ta,Hf)C solid solution.

The lattice parameters of the TaC and HfC phase of the powder mixture were measured before sintering, being 4.459 ± 0.002 Å for TaC and 4.636 ± 0.002 Å for HfC. These measurements are in close agreement with the values reported by several authors of 4.455 Å for TaC and 4.638 Å [5, 17, 164]. Table 5.2 shows the measured lattice parameters of the TaC phase in the powder mixture and samples

after SPS. By increasing the sintering temperature the lattice parameter increases from 4.461 ± 0.001 Å at 2050 °C to 4.468 ± 0.002 Å, this is a small increase relative to the value of the initial powder mixture, but as revealed in Figure 5.1, at these sintering temperatures the solid solution was still not single phase. After SPS at 2250 °C the lattice parameter increases to 4.473 ± 0.003 Å, at this point no HfC phase is detectable and the value is close to that of a single phase solid solution. At higher sintering temperatures the lattice parameter was similar, 4.483 ± 0.001 Å at 2350 °C and 4.484 ± 0.002 Å at 2450 °C.

Sample	Lattice parameter (Å)
Starting TaC (powder)	4.459 ± 0.002
2050 °C	4.461 ± 0.001
2150 °C	4.468 ± 0.002
2250 °C	4.473 ± 0.003
2350 °C	4.483 ± 0.001
2450 °C	4.484 ± 0.002

Table 5.2 Lattice parameters of starting TaC powder and (Ta,Hf)C solid solutions after sintering for 20 min and 30 MPa at indicated temperatures using SPS.

According to Vegard's law, unit cell parameters should change linearly with solid solution composition [165, 166]. Figure 5.2 ilustrates the lattice parameter of the powder TaC and HfC phases and the line between the two is the values that are followed by Vegard's Law. Comparing this line to the actual values of the SPS'd 4TaC-1HfC solid solutions reveals the deviations to this law. At the highest sintering temperature (2450 °C) the deviation was 0.15% from the theoretical value of 4.491 Å.

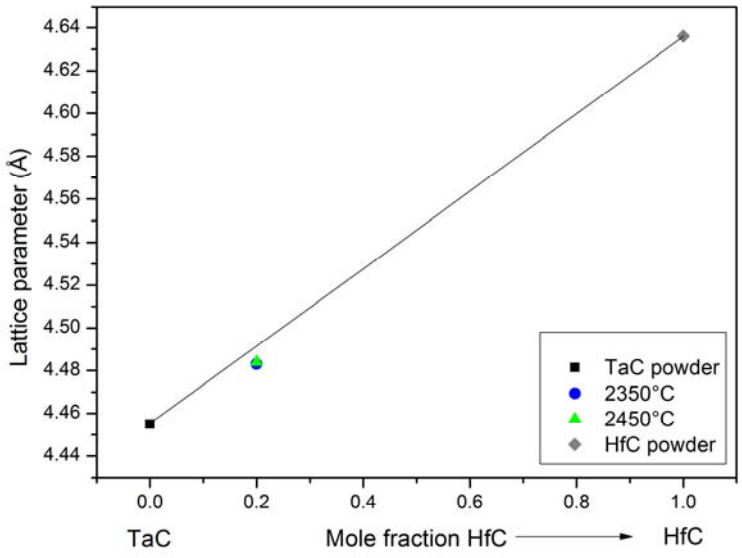

Figure 5.2 Lattice parameter of 4TaC-1HfC SPS'd at temperatures indicated and deviation comparison to Vegard's Law (straight line between TaC and HfC).

5.1.3 Microstructural evolution and solid solution formation by increasing sintering temperature.

Polished cross sections of sintered samples were studied by SEM to examine the evolution of the microstructures with sintering temperature. Figure 5.3a) shows a BSE image of a porous microstructure of a sample sintered at 2050 °C, with residual porosity of ~22 vol% (Table 5.1). Open porosity quantification using digital imaging analysis, shows that at this stage the entire porosity in the ceramic was open (Table 5.1). Furthermore, a similar microstructure is shown after SPS at 2150 °C (Figure 5.3b)) with a decrease in porosity to ~14 vol% and with closed porosity of ~1.2 vol%. It was difficult to measure the mean grain size (MGS) of samples sintered at 2050 °C and 2150 °C due to their high porosity levels and the limited contrast between the pores and grains. Residual porosity was reduced to ~7 vol% at 2250 °C, with a reduction in open porosity to 4.87 vol% and a MGS of 3.2 μm was observed after SPS at 2250 °C (Figure 5.3c)). The grain size is still comparable with that of the as-received powders, 3.44 μm. Regions of rounded and elongated closed pores located at the grain boundaries and inside grains are present after SPS at this temperature with a size of 1.17 ± 0.47 μm. The microstructure

after SPS at 2350 °C (Figure 5.3d)) shows an increase in MGS (5.1 μm) and reduction in residual porosity to ~6 vol%. In addition, pores of 1.61 ± 0.88 μm are observed at triple junctions and the shape becomes more rounded with entrapped pores within the grains while elongated pores are located at grain boundaries. A denser microstructure with a residual porosity of ~5 vol% is observed (Figure 5.3e)) after SPS at 2450 °C. Pores (black contrast) exceeding 2.5 μm are localized at triple junctions while round pores of smaller size (1.2 μm) are found inside the grains. At this temperature the grain size of the (Ta,Hf)C phase has increased to 6.2 μm, almost double the grain size after SPS at 2250 °C and 21% larger than the sample sintered at 2350 °C.

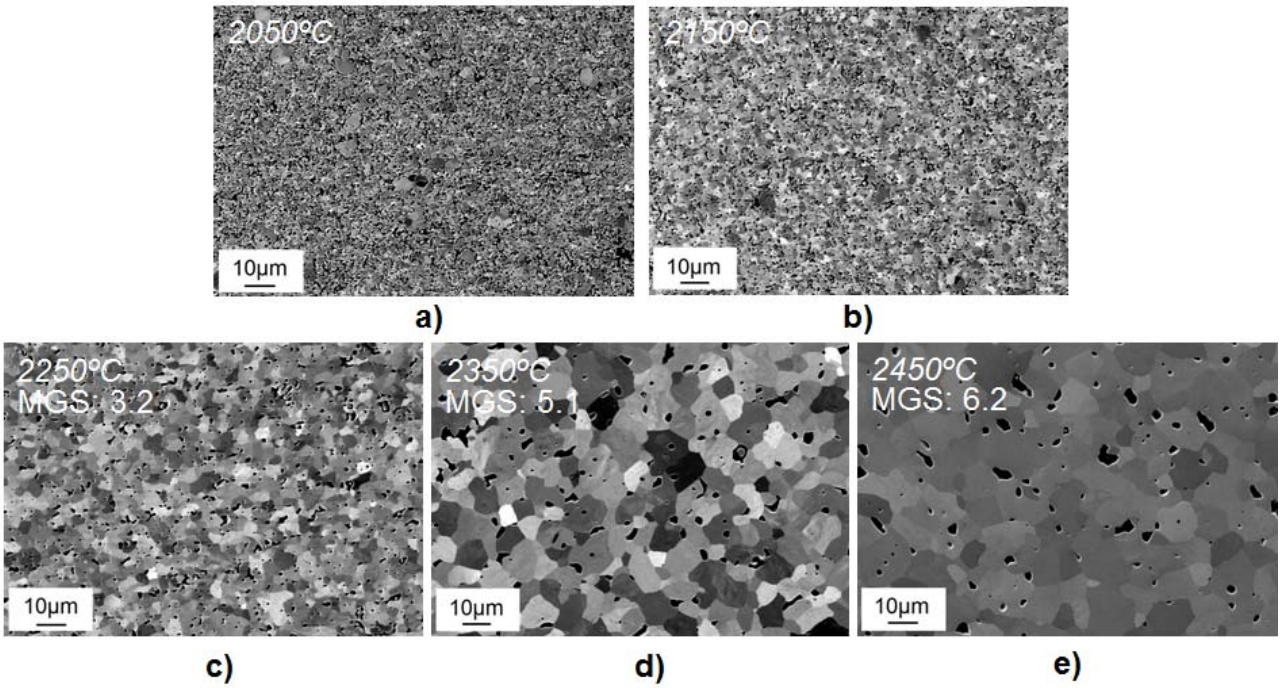

Figure 5.3 Backscattered electron images (BSE) of samples sintered using SPS at: a) 2050 °C; b) 2150 °C; c) 2250 °C; d) 2350 °C and e) 2450 °C for 20 min and 30 MPa.

Secondary electron images of fracture surfaces after SPS (e.g. Figure 5.4a) and b)) reveal the early stages of sintering with necking between particles forming a connected network in a highly porous structure. Different features were observed on the fracture surface after SPS at 2250 °C (Figure 5.4c)), where the microstructure consists of equiaxed grains of 3 μm size with inter and intragranular pores. The predominant fracture mode was intergranular. After SPS at 2350 °C (Figure 5.4d)) a denser

microstructure was observed and also transgranular fracture mode becomes significant as highlighted by the arrows. An increase in grain size to 6.2 μm was observed after SPS at 2450 °C (Figure 5.4e)); even at these high sintering temperatures it was difficult to completely remove the residual porosity (~5 vol%) in these compounds.

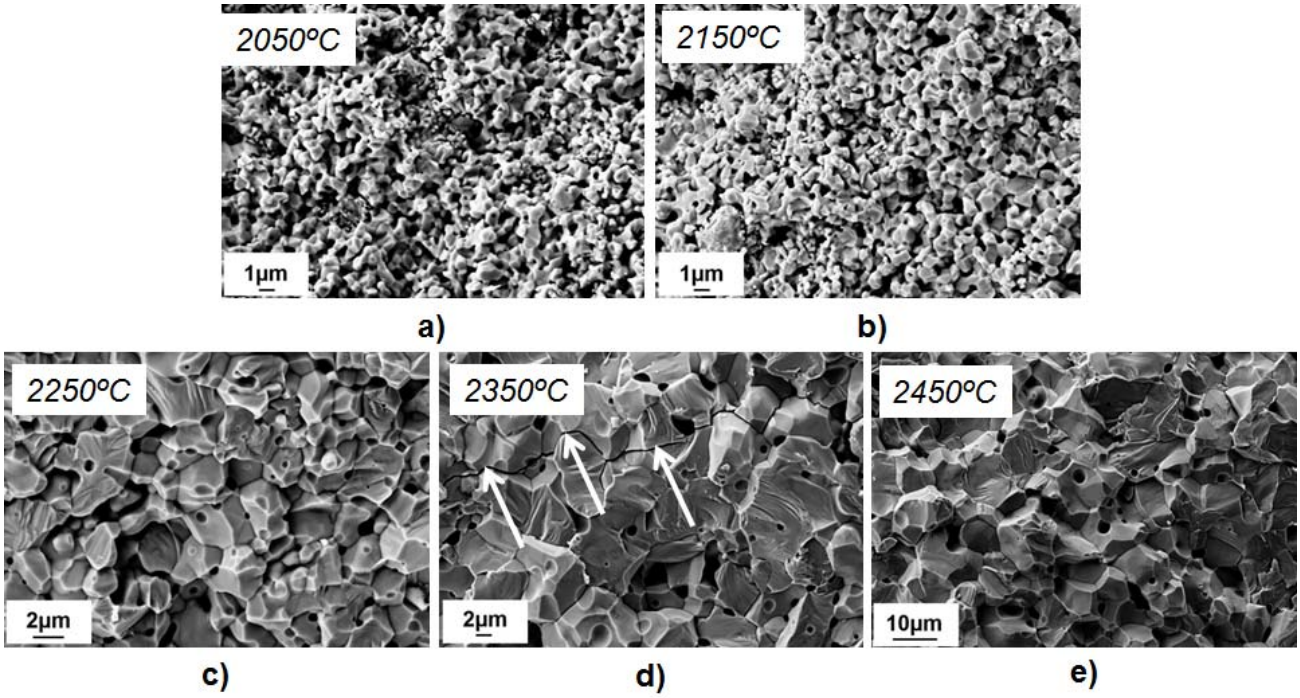

Figure 5.4 Secondary electron images (SEI) of fractured surfaces of samples sintered using SPS at a) 2050 °C, b) 2150 °C, c) 2250 °C, d) 2350 °C and e) 2450 °C for 20 min and 30 MPa.

Compositional EDS mapping was used to investigate the formation of TaC-HfC solid solutions. Figure 5.5 and Figure 5.6 show EDS mapping conducted on polished surfaces of SPS'd 4TaC-1HfC powders after sintering at 2050 and 2350 °C respectively. For comparison, a SEI of the selected area and an EDS map of mixed signals are presented, along with EDS maps of signals of C, Hf and Ta. Figure 5.5b) is a mixed signal map displaying regions of starting Hf particle (in green colour). Carbon maps (Figure 5.5c) show a homogeneous distribution of the element throughout the selected region. In comparison, areas with high concentration of Hf are present as isolated regions (Figure 5.5d)) while the Ta map (Figure 5.5e)) shows the distribution of Ta throughout the samples with regions of low concentration signal where the Hf clusters are present.

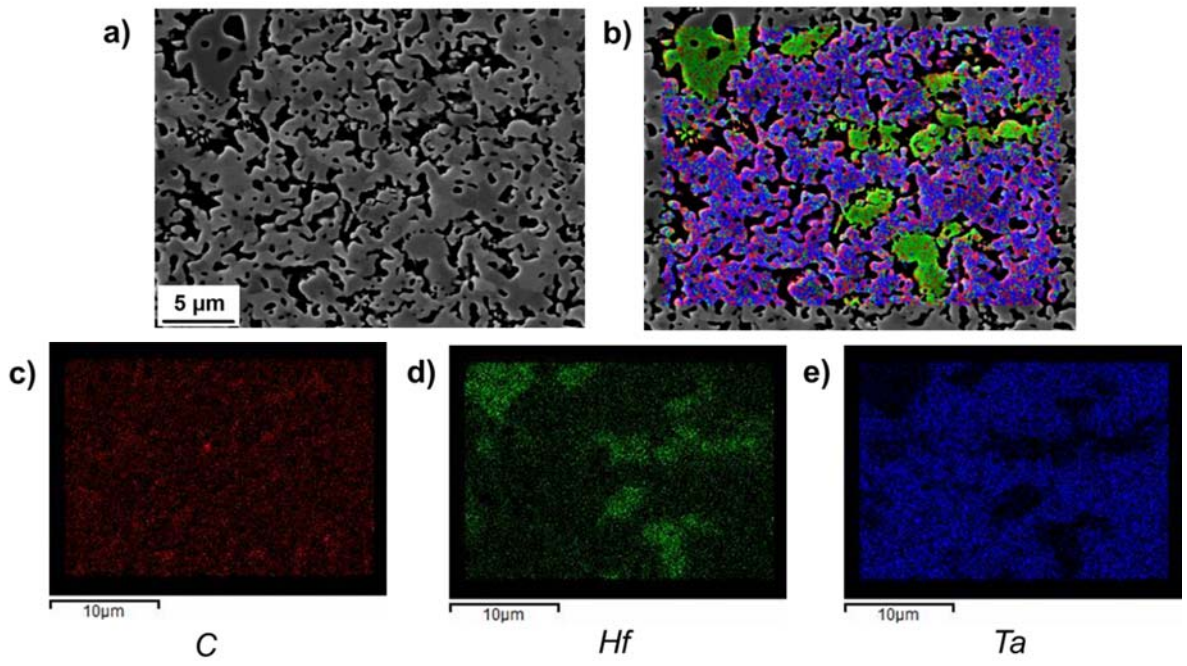

Figure 5.5 EDS mapping of sample sintered at 2050 °C for 20 min at 30 MPa, a) SE image of polished surface, b) map of mixed signals (Ta,Hf and C), c) map of C, d) map of Hf and d) map of Ta.

At a sintering temperature of 2350 °C, the EDS maps indicate that C, Hf and Ta are homogeneously distributed in the sample; no isolated regions of single elements are observed (Figure 5.6). This suggests that at this sintering temperature and above a single-phase solid solution of (Ta,Hf)C was formed. Dot map images of samples sintered at 2350 °C and above always show a homogeneous distribution of Hf in the microstructure.

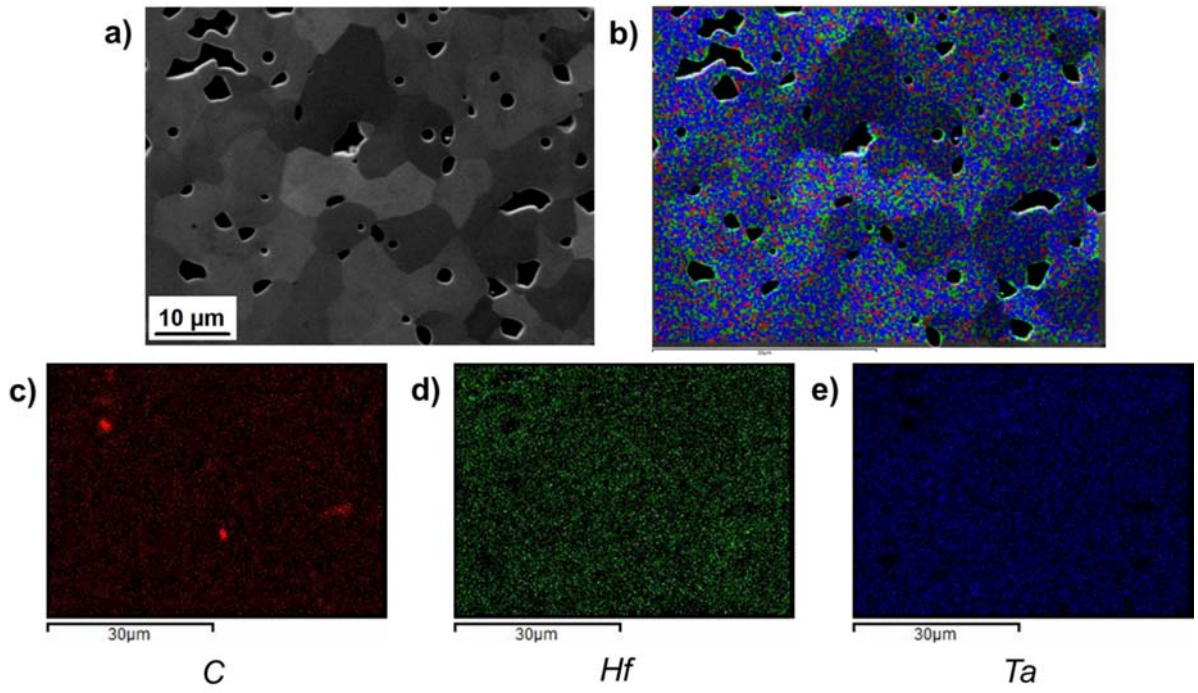

Figure 5.6 EDS mapping of sample sintered at 2350 °C for 20 min at 30 MPa, a) SE image of polished surface, b) map of mixed signals (Ta,Hf and C), c) map of C, d) map of Hf and d) map of Ta.

For comparison each stage of solid solution formation is shown in the dot map images of Figure 5.7. After sintering at 2050 °C areas of ~18 μm^2 containing Hf are present as isolated regions. After sintering at 2150 °C areas ~12 μm^2 of clustered Hf were still present. The dissimilar size of the Ta and Hf rich regions could be attributed to the size of the starting particles, which were 3.44 and 8.4 µm respectively (Section 3.1). After sintering at 2250 °C it was observed that Hf is almost completely but not entirely distributed throughout the analysed region.

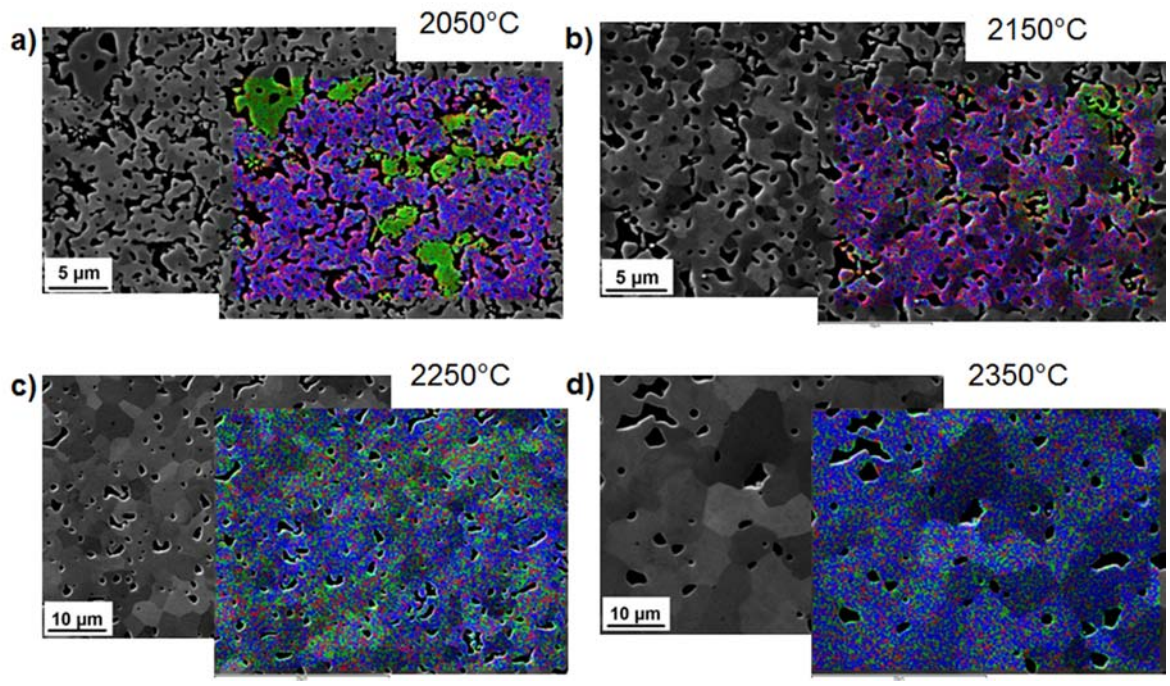

Figure 5.7 SEI and mixed signal EDS maps of samples sintered at: a) 2050 °C, b) 2150 °C, c) 2250 °C and d) 2350 °C. Green, blue and red colours correspond to hafnium, tantalum and carbon.

5.1.4 TEM and STEM analysis

Unlike previous investigations [167], TEM analysis was used here for the first time to provide a more detailed insight of the mechanism involved in the formation of the solid solution. Figure 5.8 shows a BF TEM image of a grain boundary in a sample sintered at 2450 °C. EDS chemical analysis indicates that both grains (A and B) are (Ta,Hf)C solid solutions since the spectra from A and B contain Ta, Hf and C. This suggests that mutual diffusion was the main mechanism involved in the formation of (Ta,Hf)C solid solution.

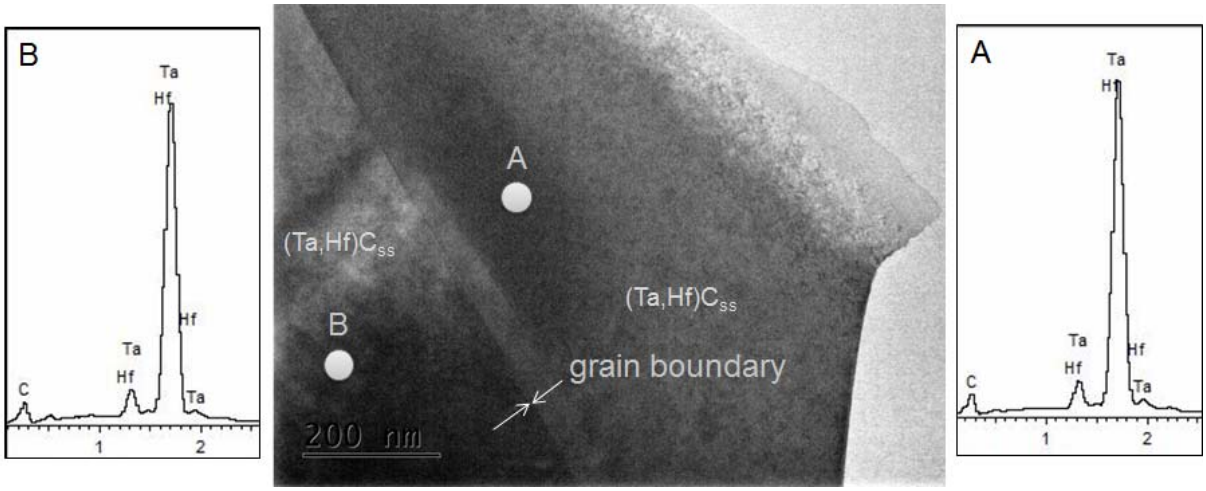

Figure 5.8 TEM Image of (Ta,Hf)C grains and EDS (taken at point A and B) of sample sintered at 2450 °C.

A clean grain boundary was observed by HRTEM imaging (Figure 5.9) with no apparent secondary or amorphous phases along the interface. The absence of any evidence of liquid phase during sintering indicates that densification occurred by solid state diffusion. The results suggest the densification was nearly completed at 2250 °C, while solid solution and significant grain growth were achieved at 2350 °C. As expected, densification and solid state diffusion (associated with grain growth) occurred in two separate steps. In fact when the densification progressed, the extended neck formed between the particles worked as an effective diffusion path.

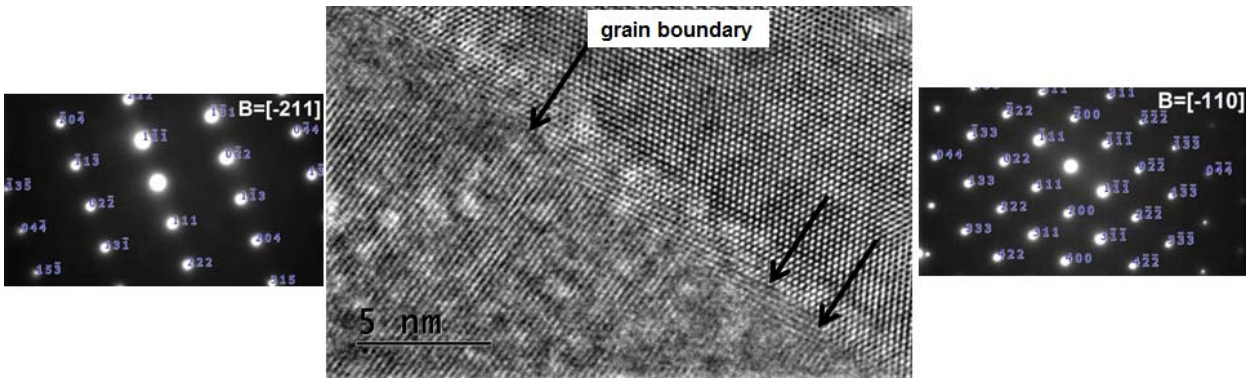

Figure 5.9 HRTEM image and interface of sample sintered at 2450 °C and corresponding SAED patterns taken along respective areas.

SAED confirms the crystal structure of the (Ta,Hf)C phase is FCC. [-211] was the zone axis found for grain A and [-110] for grain B in Figure 5.9. SAED also confirmed that there was no preferential ordering or clustering of Ta or Hf in the solid solution. Images using STEM mode were taken on a sample sintered at 2450 °C (Figure 5.10) and analysis by EDS confirms that all grains contain Ta, Hf and C. Areas analysed by EDS using STEM are easier to identify due to the scanned images obtained by this method. Quantitative analysis for lighter elements (in this case C) is difficult using EDS. However, results were consistent in both TEM and SEM, and 4:1 ratio of Ta to Hf was detected.

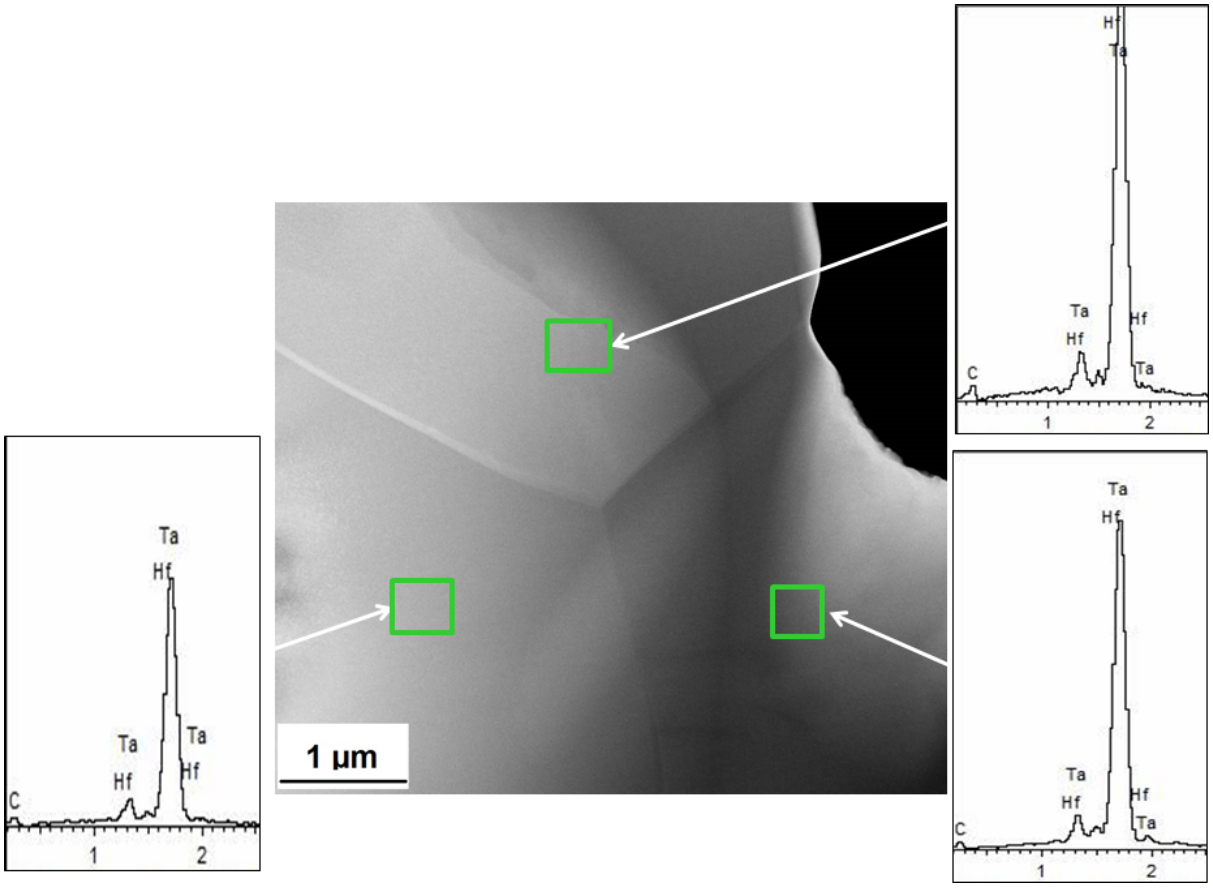

Figure 5.10 STEM Image of (Ta,Hf)C grains and corresponding EDS of sample sintered at 2450 °C.

In addition EDS linescans were made in two grains and across the grain boundary, revealing no significant change in composition through the grains or within the grain boundary. Red Ta, green Hf and blue C linescan signals can be seen in Figure 5.11.

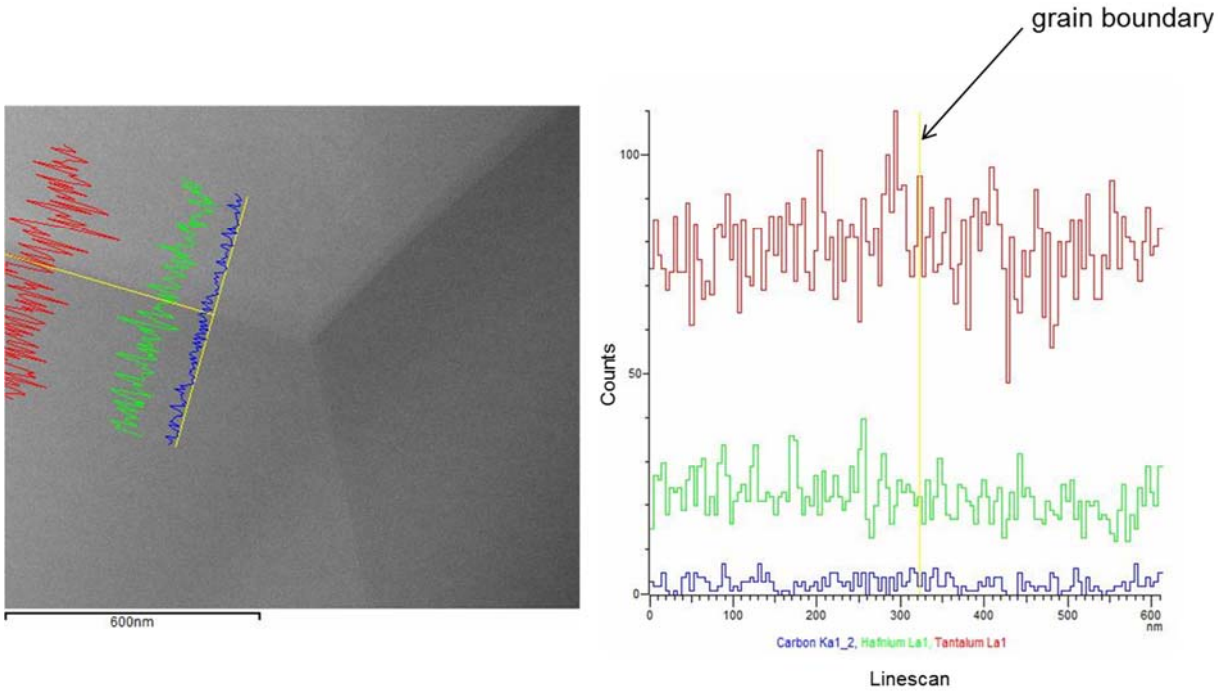

Figure 5.11 STEM Image of (Ta,Hf)C grains and corresponding EDS linescan of sample sintered at 2450 °C.

5.1.5 Mechanical properties

Figure 5.12 show the Vickers hardness (HV1) at room temperature of SPS'd 4TaC-1HfC ceramics at sintering temperatures from 2050-2450 °C. After sintering at 2050 °C the measured hardness was 6.1 ± 0.3 GPa, then by increasing the temperature to 2150 °C the hardness increased by almost double to 11.0 ± 0.6 GPa. As the sintering temperature increases to 2250 °C and densification is nearly completed at this stage the hardness was 15.7 ± 0.8 GPa. At a sintering temperature of 2350 °C and above Vickers hardness reached a plateau with 16.7 ± 1.2 GPa after SPS at 2350 °C and a minimum increment at 2450 °C with a similar value of 16.8 ± 1.1 GPa.

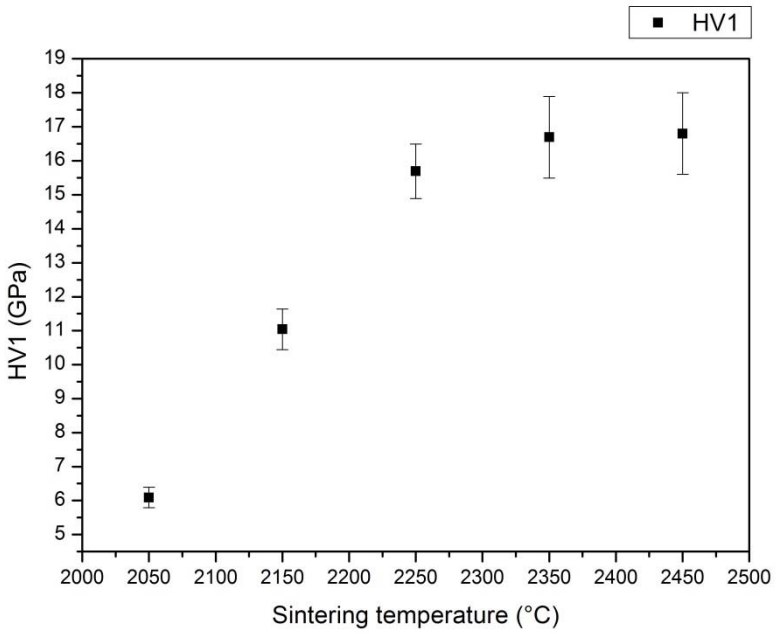

Figure 5.12 Vickers hardness (HV1) at room temperature of 4TaC-1HfC products processed by SPS at the sintering temperatures indicated for 20 min and 30 MPa.

Similarly, nanoindentation experiments at room temperature were conducted on SPS'd 4TaC-1HfC specimens. Nanoindentation test results done with a Berkovich tip are shown in Figure 5.13. After the initial sintering stage of 2050 °C the 4TaC-HfC specimen nanohardness was 6.0 ± 0.6 GPa. As the sintering temperature was increased, nanohardness increased to 10.3 ± 1.4 GPa. A sharp increase in nanohardness between 2150-2250° was observed to 16.8 ± 0.8 GPa. An increase of 10% was observed after SPS at 2350 °C. A maximum of 19.2 ± 1.2 GPa was obtained after sintering at 2450 °C.

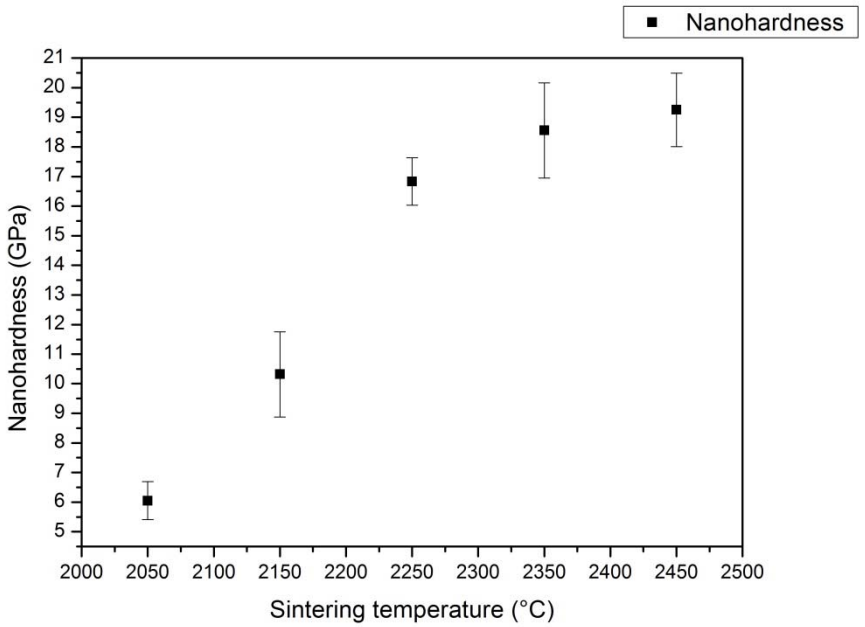

Figure 5.13 Nanoindentation hardness (Berkovich test) at room temperature of 4TaC-1HfC ceramics processed by SPS at the sintering temperatures indicated for 20 min and 30 MPa

5.1.6 Thermal properties

Thermal diffusivity and conductivity were measured using the laser flash method previously described in Section 3.7.2. Experiments were conducted from 25-1950 °C. The thermal diffusivity behaviour with temperature is shown in Figure 5.14. Thermal diffusivity was measured on samples after SPS at different sintering temperatures (2050-2450 °C). All samples show a similar trend; an increase of thermal diffusivity as the temperature increases. As expected, the lower values were measured on the sample sintered at 2050 °C, at room temperature (25 °C) was ~7 mm^2/s, which was the lowest value for all sintered samples. It slowly increased to 8.5 ± 0.07 mm^2/s at 1000 °C and 9.5 ± 0.06 mm^2/s at 1950 °C. As expected 4TaC-1HfC powders sintered at 2050 °C showed lower values due to higher levels of porosity at this sintering temperature. It can be observed that a room temperature thermal diffusivity for 4TaC-1HfC after SPS at 2150 to 2450 °C is similar with values in the range 7.7-8.0 mm^2/s.

Thermal diffusivity in samples SPS'd at temperatures ≥2250° followed the same trend up to 1000 °C. At 1000 °C values were similar in the range 10.1-10.4 mm^2/s. At low and moderate temperatures

convective and radiative heat transfer across and between the pores are insignificant, thermal diffusivity is determined by the heat flux transmission through the solid and not the pores, in the case of SPS'd 4TaC-1HfC the threshold temperature was 1000 °C. At higher temperatures the flux is dependent on both the solid and pore phases [168]. The maximum measured thermal diffusivity was 12.0 ± 0.08 mm^2/s at 1950 °C of 4TaC-1HfC sintered at 2450 °C.

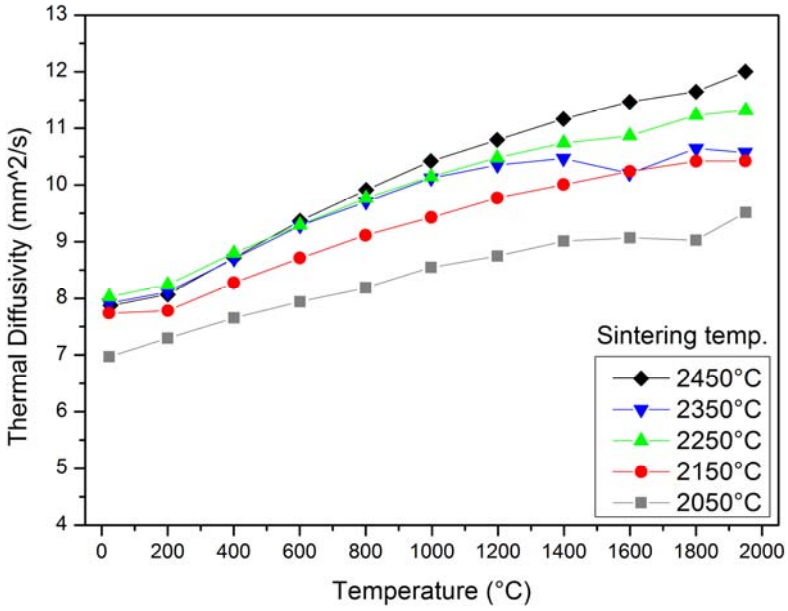

Figure 5.14 Thermal diffusivity of 4TaC-1HfC as a function of temperature for samples sintered at temperatures indicated.

Thermal conductivity was calculated as described in Section 3.7.2 and results are shown in Figure 5.15. All samples show a similar trend of increased thermal conductivity with temperature. 4TaC-1HfC sintered at 2050 °C had the lowest value of thermal conductivity, while samples after SPS at 2450 °C had the highest value. At room temperature (25 °C) the thermal conductivity was 15.5 W/m·K and 32.0 W/m·K at 1950 °C. As the sintering temperature was increased the thermal diffusivity of the sample also increases. It was observed that in samples with relative density over 93% (SPS'd ≥2250 °C) the thermal conductivity at lower temperatures is similar until 1000 °C, where a deviation between the values was observed. For a sample with single phase 4TaC-1HfC solid solution and with a relative

density of 95%, the thermal conductivity a room temperature was 21.5 W/m·K and the maximum achieved value was 49.3 W/m·K at 1950 °C.

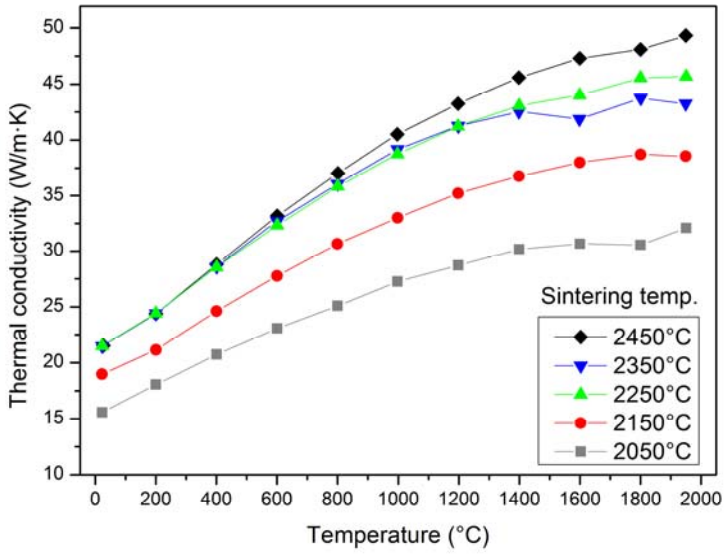

Figure 5.15 Thermal conductivity of 4TaC-1HfC of samples sintered at temperatures indicated.

The coefficient of thermal expansion (CTE) was measured in 4TaC-1HfC ceramics made from powders SPS'd at 2450 °C. Porosity has no significant effect on thermal expansion properties; CTE depends on the atomic bonding of the material [168]. Sample sintering conditions, coefficient of thermal expansion (CTE) and the temperature range in which the CTE was measured are shown in Table 5.3. After SPS at 2450 °C the CTE in the range of 25-2000 °C was 7.24 ± 0.53 x10^{-6} /K.

Sintering conditions (T_D, t_D, P)	Coefficient of thermal expansion (CTE) (10^{-6}/K)	Temperature range (°C)
2450 °C, 20 min, 30 MPa	7.24 ± 0.53	25-2000

Table 5.3 Coefficient of thermal expansion (CTE) of 4TaC-1HfC SPS'd at 2450 °C for 20 min and 30 MPa.

5.2 Characterisation of TaC, HfC and TaC-HfC solid solutions

After evaluating the sintering behaviour and solid solution formation of 4TaC-1HfC, the next chapter section describes an investigation of additional compositions (1TaC-1HfC and 1TaC-4HfC), their solid solution formation, microstructural analysis and mechanical and thermal property measurements and compares them with the properties of monolithic TaC and HfC.

5.2.1 Density

Table 5.4 shows the bulk density, relative density, MGS and pore size of TaC, HfC and TaC-HfC solid solutions after SPS. As previously explained in Section 5.1, a single-phase solid solution of 4TaC-1HfC was produced at sintering temperatures ≥2350 °C. A two-step sintering schedule was performed to achieve high density and single-phase solid solution formation and reduce the maximum sintering temperature to 2350 °C. This schedule starts with an initial dwell temperature of 2100 °C for 30 min and 55 MPa then the sintering temperature is increased to 2350 °C for an additional 20 min at an applied pressure of 30 MPa. A bulk density of 14.25 ± 0.2 g/cm^3 was achieved in ceramics made from TaC powders after SPS, this was 98.3 ± 0.14 % relative density.

The remaining TaC-HfC compositions (4TaC-1HfC, 1TaC-1HfC and 1TaC-4HfC) and HfC were also processed using this thermal schedule. 4TaC-1HfC powders were consolidated to produce a single-phase solid solution ceramic with high density, which in this case was 13.77 ± 0.2 g/cm^3 (97.7 ± 0.09 % TD). A reduction in relative density to 95.7 ± 0.29 % was achieved for 1TaC-1HfC ceramics with a bulk density of 12.94 ± 0.03 g/cm^3. A drop in relative density to 87.0 ± 0.26 % was obtained for 1TaC-4HfC ceramics with a similar grain size of 4.4 μm. Furthermore, it was observed that at higher HfC contents (≥0.8 mole fraction) achieving a relative density >90% was difficult even at high temperatures (2350 °C). Relative density for monolithic HfC was observed at 85.3 ± 0.10 % (10.81 ± 0.01 g/cm^3) the lowest value for the TaC-HfC ceramics analysed in this study. As a general trend, at higher HfC content the sintering of TaC-HfC powders was found to be more difficult. Composition analysis conducted by combustion (Section 3.2) on HfC after SPS showed that O content was 0.49 ± 0.1 wt% and 0.58 ± 0.005 wt% of N which is higher than the manufacturer data of the as-received powders of 0.32 wt% of O and

0.02 wt% of N. Suggesting that the O and N impurities on coating the particle surface hinders the sintering of HfC.

Sample	Bulk density (g/cm^3)	Relative density (%)	Mean grain size (μm)	Mean pore size (μm)
TaC	14.25 ± 0.02	98.3 ± 0.14	5.8	0.58 ± 0.13
4TaC-1HfC	13.77 ± 0.02	97.7 ± 0.09	7.1	1.27 ± 0.49
1TaC-1HfC	12.94 ± 0.03	95.7 ± 0.29	4.2	1.35 ± 0.63
1TaC-4HfC	11.31 ± 0.03	87.0 ± 0.26	4.4	1.26 ± 0.32
HfC	10.81 ± 0.01	85.3 ± 0.10	1.8	1.01 ± 0.72

Table 5.4 Bulk density, relative density, MGS of the matrix and mean pore size of TaC, HfC and TaC-1HfC ceramics fabricated by SPS.

5.2.2 XRD analysis

XRD analysis was conducted on samples after SPS to evaluate the solid solution formation. Figure 5.16 shows the XRD profiles of initial TaC and HfC and TaC-HfC solid solutions after SPS. In the XRD profiles of Figure 5.16 a) the top and bottom profiles show the reflections of HfC and TaC respectively, and for the TaC-HfC compositions mutual diffusion of TaC and HfC was ocurring, and as a result a single XRD profile was observed. The shift of the peaks in Figure 5.16 b) could be easily observed and they shift on the 2θ axis depending on the solid solution composition. At ~35 degrees the TaC peak was observed, then a single peak of a monophasic solid solution of 4TaC-1HfC with an angle shift to 34.6 degrees could be identified. Furthermore, for 1TaC-1HfC the first reflection was measured at 34.2 and for 1TaC-4HfC at 33.8 degrees. At each solid solution composition a single peak of monophasic solid solution was observed, with no other reflections of single phase TaC or HfC detected.

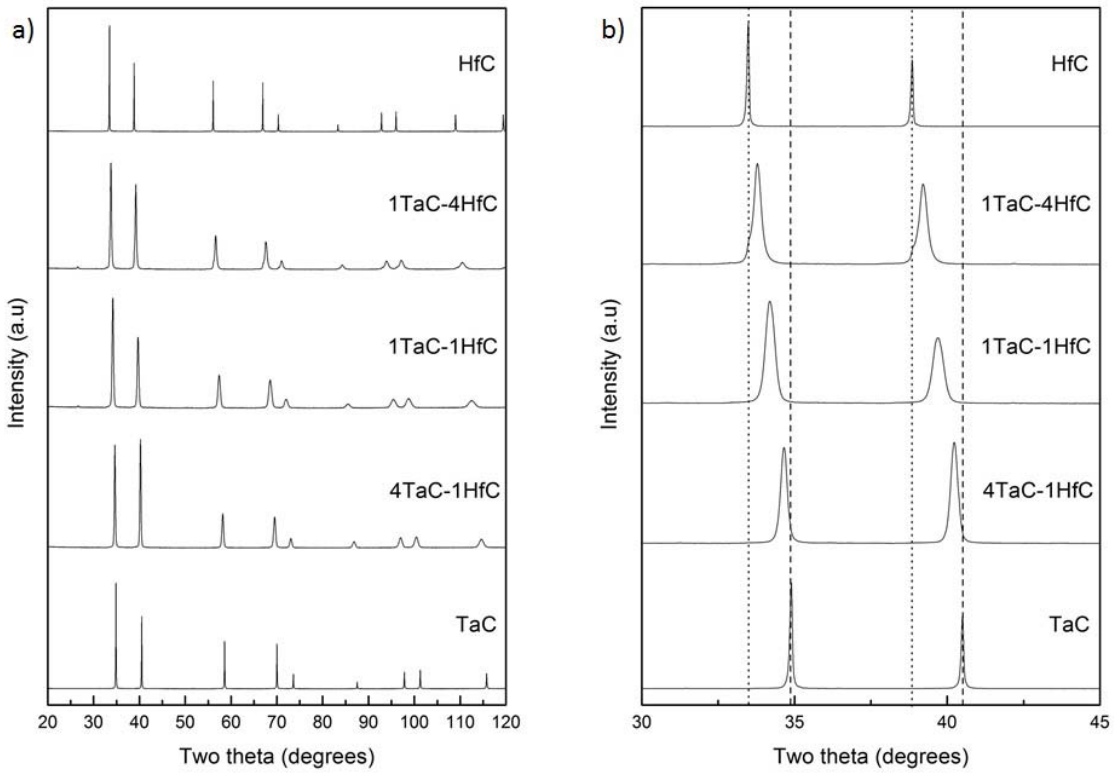

Figure 5.16 a) XRD of TaC, HfC and TaC-HfC ceramics after SPS at the temperatures indicated for 20 min and 30 MPa b) enlarged section of the diffraction patterns between 30-45 two theta degrees showing the shift of peaks and the formation of (Ta,Hf)C solid solutions.

In addition, lattice parameters for both single-phase carbides (TaC and HfC) and the solid solutions (4TaC-1HfC, 1TaC-1HfC and 1TaC-4HfC) were measured. Table 5.5 shows the measured lattice parameter for each of the TaC-HfC compositions after SPS. The lower limit was for TaC at 4.459 ± 0.002 Å, while the upper limit was HfC at 4.636 ± 0.002 Å. The solid solutions lattice parameter values fall in between those of TaC and HfC in a linear relation with respect of HfC concentration. Lattice parameter was 4.484 ± 0.001 Å for 4TaC-1HfC, 4.536 ± 0.001 Å for 1TaC-1HfC and 4.594 ± 0.001 for 1TaC-4HfC.

Sample	Lattice parameter (Å)
TaC	4.459 ± 0.002
4TaC-1HfC	4.484 ± 0.001
1TaC-1HfC	4.536 ± 0.001
1TaC-4HfC	4.594 ± 0.001
HfC	4.636 ± 0.002

Table 5.5 Lattice parameters of TaC and HfC and (Ta,Hf)C solid solutions after SPS.

The lattice parameters of the TaC-HfC solid solutions were found to follow Vegard's Law, with some deviation involved. The solid solution lattice parameter increased linearly as the HfC content was increased and could be observed graphically in Figure 5.17, which shows the close agreement of the measured with theoretical values. The deviations from Vegard's Law were 0.22% for 4TaC-1HfC, 0.24% for 1TaC-1HfC and 0.10% for 1TaC-4HfC respectively.

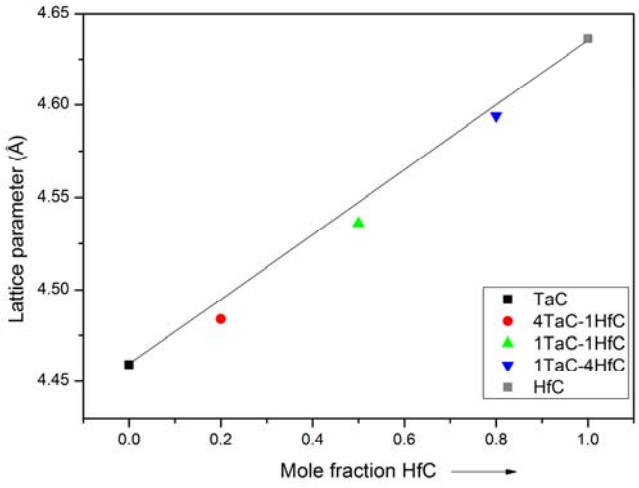

Figure 5.17 Lattice parameters of TaC, HfC and TaC-HfC solid solutions after SPS and comparison to Vegard's Law (straight line between TaC and HfC).

5.2.3 Microstuctural characterisation by SEM and EDS

BSE images were taken from polished surfaces of samples after SPS at the sintering conditions described in Table 3.4. A dense microstructure of TaC with ~1.7 vol% porosity can be observed in Figure 5.18a), with a grain size of 5.8 μm and homogeneously distributed fine pores (black contrast) of ~0.58 μm, mainly entrapped inside the grains. The images obtained from SPS'd 4TaC-1HfC (Figure 5.18 b)) show a microstructure with a residual porosity of ~2.7 vol% with a grain size of 7.1 μm. Pores are distributed throughout the sample (~1.27 μm), large pores at triple junctions and round entrapped smaller pores occur inside grains.

In addition, a dense microstructure with ~4 vol% porosity was obtained in 1TaC-1HfC specimens (Figure 5.18 c)) with a MGS of 4.2 μm and mean pore size of 1.35 ± 0.63 μm. Only grains of 1TaC-1HfC solid solution and the residual porosity were observed, no other secondary phases were found. A similar MGS of 4.4 μm was found in 1TaC-4HfC ceramics after SPS (Figure 5.18 d)), however the residual porosity increased to ~13 vol% due to the increased HfC content which is believed to be caused by oxygen impurities on particle surfaces that inhibit densification [39, 64, 65]. Pore size was measured at 1.26 ± 0.32 μm. The microstructure of single-phase HfC shown in Figure 5.18 d) reveals a porous structure (~15 vol% porosity) with regions of interconnected pores and entrapped round pores inside the grains with a MGS of 1.8 μm. Even at high temperatures it was difficult to achieve higher density (>90%) in samples with higher HfC content (≥0.8 mole fraction). As noted and reported by other authors [39, 70] monolithic HfC is difficult to densify without sintering aids due to oxygen impurities on the particle surfaces [39, 64, 65]. TaC powders showed better sinterability than HfC powders even at lower sintering temperatures (2100 °C).

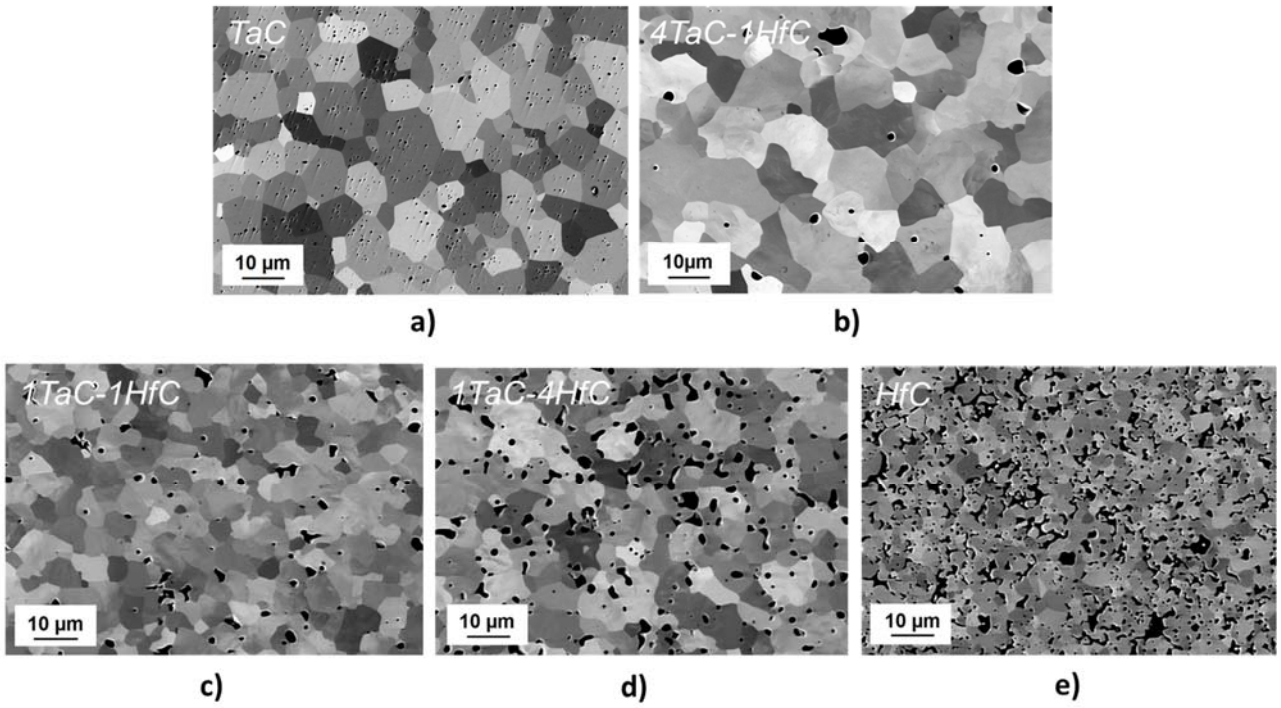

Figure 5.18 Backscattered electron images (BSE) of samples sintered using SPS at: a) TaC; b) 4TaC-1HfC; c) 1TaC-1HfC; d) 1TaC-1HfC and e) HfC all with a two-step sintering schedule of 2100/2350 °C for 20 min and 30 MPa.

EDS analysis was conducted on TaC-HfC solid solutions, Figure 5.19 shows SEI images of polished SPS'd TaC-HfC samples and their respective EDS element dot maps. The mixed signal EDS dot map shows the distribution of elements in the region selected. For these images red colour dots are from C, green signal is Hf and blue colour is Ta signal. This technique in conjunction with XRD analysis confirms the solid solution formation. Figure 5.19 a) shows the mixed signal map of 4TaC-1HfC, the map shows a strong Ta blue colour signal, this is due to higher concentration of Ta in this composition, a 4:1 molar ratio of TaC to HfC. All elements (C, Hf and Ta) showed a homogeneous distribution in the region selected. In Figure 5.19 b) a balanced mixture of element signals was observed on 1TaC-1HfC, this is due to an almost 50-50 wt% composition of TaC and HfC in this composition. Furthermore, EDS maps from 1TaC-4HfC (Figure 5.19 c)) reveal a strong green colour Hf signal, with uniform distribution of blue colour Ta signal. As opposed to of the 4TaC-1HfC, the 1TaC-4HfC map shows stronger Hf signals due to the higher HfC content. All single element signals in all three compositions show uniform distributions of elements, no clusters or agglomerations of elements were observed on these maps.

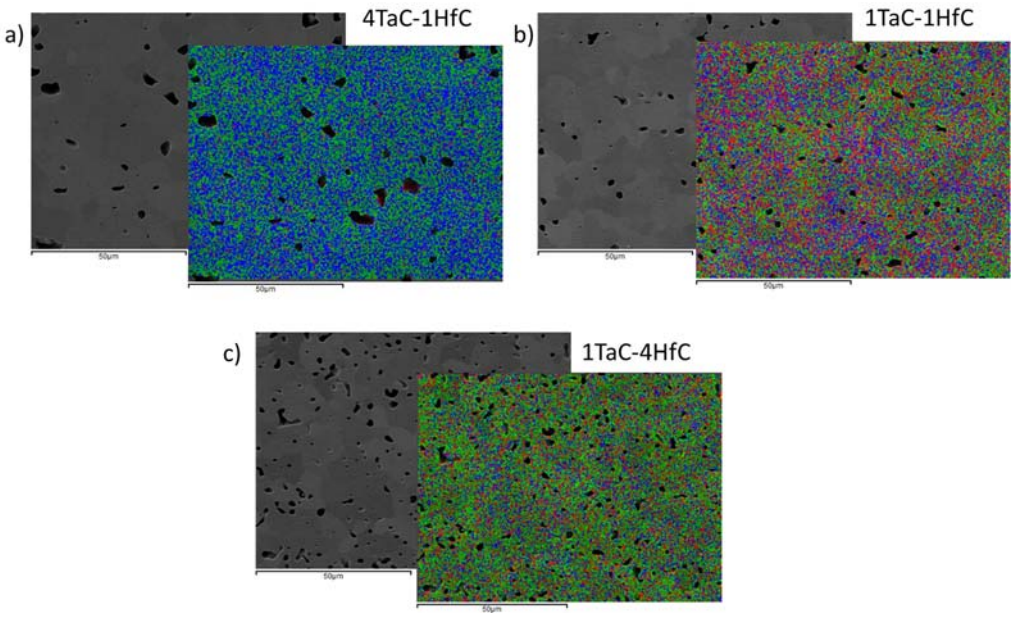

Figure 5.19 SE and images of mixed signal EDS mapping of TaC-HfC solid solutions: a) 4TaC-1HfC, b) 1TaC-1HfC, and c) 1TaC-4HfC. Green, blue and red colours correspond to hafnium, tantalum and carbon, respectively.

5.2.4 Mechanical properties

The hardness of TaC, HfC and TaC-HfC ceramics was measured at room temperature by Vickers (HV1) and Berkovich nanoindentation techniques. Vickers hardness (HV1), nanohardness, elastic modulus (*E*) and fracture toughness (K_{IC}) of TaC, HfC and TaC-HfC after SPS are shown in Table 5.6. Hardness of monolithic TaC was 13.9 ± 0.07 GPa, higher than the value reported for pure TaC of 11.14 GPa by Silvestroni et al. [39] and similar to the 14.1 GPa reported by Zhang et al. [66]. With the increase of HfC content to a 4TaC-1HfC composition the hardness increased to 17.1 ± 1.2 GPa. A maximum value of 20.4 ± 2.3 GPa was measured at a 1TaC-1HfC composition, a reduction in hardness to 15.0 ± 0.5 GPa at a composition of 1TaC-4HfC, suggesting that this reduction in hardness was related to the increase in porosity in the samples (Table 5.4). The lowest hardness was measured for HfC at 10.2 ± 0.7 GPa. This value is almost double the value of 5.79 GPa reported by Silvestroni et al. [39] for HfC fabricated by HP at 1900 °C for 20 min and 30 MPa and lower than 18.3 GPa of almost fully dense (98%) HfC consolidated by SPS at 2200° for 3 min and 65 MPa reported by Sciti et al. [82].

Nanoidentation results showed a similar trend to Vickers indentation, the lower values were for the end members, with TaC 13.3 ± 0.7 GPa and HfC 10.5 ± 1.0 GPa. An increase in nanohardness was observed for 4TaC-1HfC to 19.3 ± 1.3 GPa and a maximum value of 22.1 ± 1.8 GPa was obtained in 1TaC-1HfC. The reduction in hardness for 1TaC-4HfC was also observed, to 16.7 ± 3.0 GPa.

Elastic modulus (*E)* was measured using the method by Oliver and Pharr [150, 151], described in Section 3.6.2, with measurement data from the Berkovich nanoindentation experiments. Similar values of *E* ~460 GPa were measured for both TaC and 4TaC-1HfC. An increase of the elastic modulus with increasing HfC content was observed to a maximum value 549 ± 11.2 GPa at 1:1 molar ratio of TaC-HfC. A reduction to 438 ± 17.8 GPa at 1TaC-4HfC composition was observed. Furthermore, the elastic modulus showed the lowest value of 283 ± 9.6 GPa for HfC.

Fracture toughness (K_{IC}) on TaC-HfC ceramics was measured using the Vickers indentation fracture toughness technique by measuring the median cracks produced by indentation described in Section 3.6.3. Taking in account the errors in measurements, the fracture toughness of the specimens was found to be similar with values in the range of 2.7-3.4 $MPa \cdot m^{1/2}$.

Composition	Vickers hardness (HV1)	Nanohardness (GPa)	Elastic modulus *E* (GPa)	K_{IC} ($MPa \cdot m^{1/2}$)
TaC	13.9 ± 0.7	13.3 ± 0.7	458 ± 6.6	2.72 ± 0.30
4TaC-1HfC	17.1 ± 1.2	19.3 ± 1.3	459 ± 5.8	2.92 ± 0.91
1TaC-1HfC	20.4 ± 2.3	22.1 ± 1.8	549 ± 11.2	2.98 ± 0.77
1TaC-4HfC	15.0 ± 0.5	16.7 ± 3.0	438 ± 17.8	3.43 ± 0.63
HfC	10.2 ± 0.7	10.5 ± 1.0	283 ± 9.6	2.91 ± 0.51

Table 5.6 Mechanical properties at room temperature of TaC, HfC and selected TaC-HfC ceramics fabricated by SPS in a two-step thermal schedule (2100 °C/30 min/55 MPa-2350 °C/20 min/30 MPa)

5.2.5 Thermal properties

Thermal diffusivity and thermal conductivity were measured to 1950 °C using the laser flash technique as described in Section 3.7.2. As a general trend for the TaC-HfC ceramics the thermal diffusivity increases with increasing temperature, and the solid solution values fall in between the values of pure TaC and HfC. Figure 5.20 shows the thermal diffusivity of TaC-HfC ceramics from 25-1950 °C. Thermal diffusivity at room temperature for HfC was 7.8 ± 0.49 mm^2/s with a slow increase to 9.5 ± 0.50 mm^2/s at 1950 °C. Thermal diffusivity for TaC show a similar behaviour to HfC but with ~30% higher values at all temperatures, with 10.3 ± 0.12 mm^2/s at 25 °C and maximum in the TaC-HfC system at 12.1 ± 0.03 mm^2/s at 1950 °C. At low temperatures thermal diffusivity of 1TaC-4HfC increases at a higher rate than pure HfC, but after 1000 °C, the values of these two compositions are similar due to porosity levels, which is ~13 vol% for 1TaC-4HfC and ~15 vol% for HfC (Table 5.4). The solid solution of 4TaC-1HfC showed the maximum thermal diffusivity and was close to that of TaC (12.0 ± 0.08 mm^2/s).

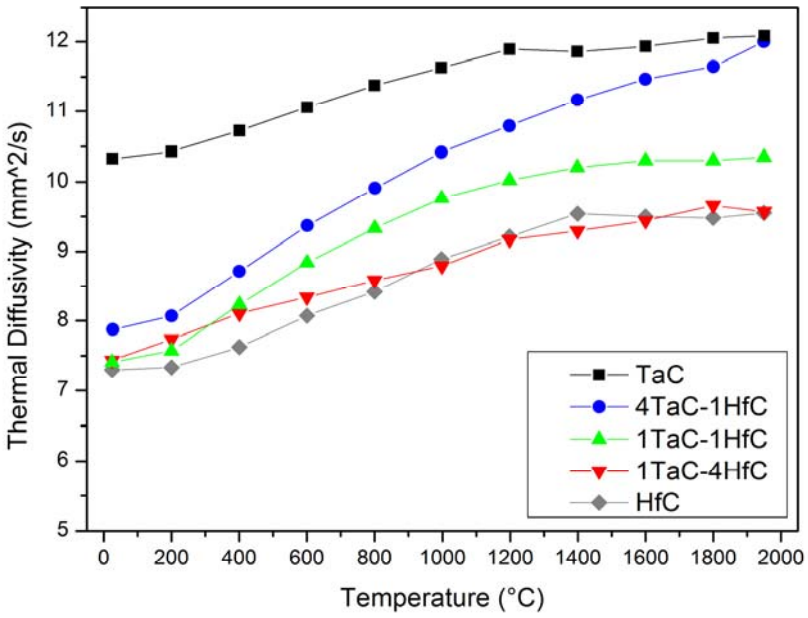

Figure 5.20 Thermal diffusivity of TaC, HfC and TaC-HfC solid solutions after SPS.

For better comparison, thermal conductivity was normalized to 100% relative density using the Maxwell-Eucken equation [169]. Similar behaviour was observed for all samples in the TaC-HfC system; as a general trend thermal conductivity increases with temperature, HfC had the lowest thermal conductivity of 16.0 W/m·K at 25 °C, steadily increasing to 40.0 W/m·K at 1950 °C. 1TaC-1HfC and 1TaC-4HfC show similar results overlapping their values at low temperatures (<600 °C), while from 800-1600 °C they were slightly higher for 1TaC-1HfC. Figure 5.21 shows that the thermal conductivity values of the TaC-HfC solid solutions were between the values of those of end member TaC and HfC. The highest thermal conductivity was observed in TaC, 32.8 W/m·K at 25 °C, steadily increasing to 52.8 W/m·K at 1200 °C, then a plateau with small increase to 54.3 W/m·K at 1950 °C.

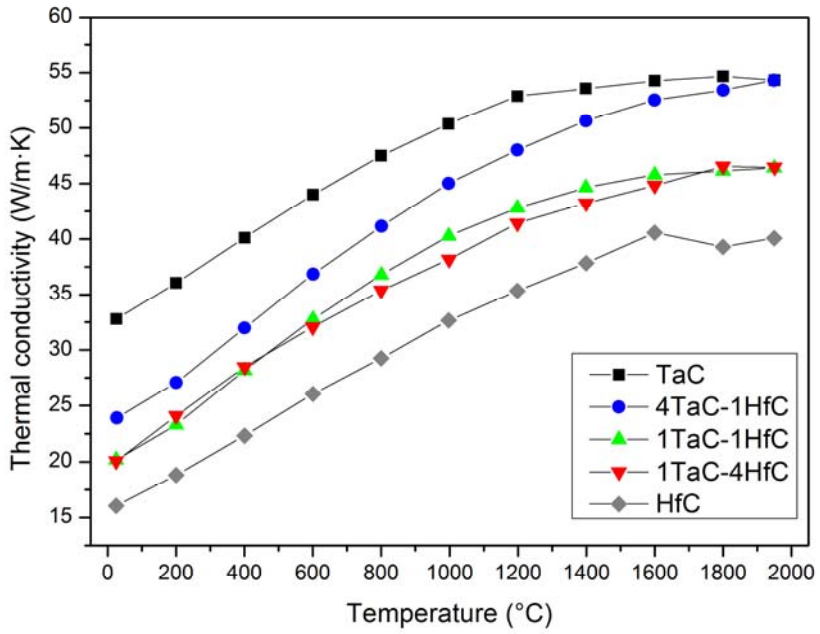

Figure 5.21 Thermal conductivity of TaC, HfC and TaC-HfC solid solutions after SPS, normalized to 100% theoretical density using the Maxwell-Eucken equation.

Table 5.7 shows the coefficient of thermal expansion (CTE) measured using a dilatometer described in Section 3.7.1 from 25-2000 °C under an argon atmosphere. An increase in CTE was observed with increasing HfC content; a linear increase was observed for the solid solutions. CTE of TaC was 7.08 ±

0.33 x10^{-6} /K, and a maximum of 7.66 ± 0.11 x10^{-6} /K for HfC. Gasch et al. [5] reported values of 6.3x10^{-6} /K for TaC and 6.6x10^{-6} /K for HfC but over a lower range of temperatures (20-1500 °C).

Composition	Coefficient of thermal expansion (CTE) (10^{-6} /K)	Temperature range (°C)
TaC	7.08 ± 0.33	25-2000
4TaC-1HfC	7.24 ± 0.53	25-2000
1TaC-1HfC	7.41 ± 0.28	25-2000
1TaC-4HfC	7.59 ± 0.30	25-2000
HfC	7.66 ± 0.11	25-2000

Table 5.7 Coefficient of thermal expansion (CTE) of TaC, HfC and TaC-HfC solid solutions SPS'd.

5.2.6 Oxidation of TaC-HfC ceramics

Oxidation of bulk specimens in the TaC-HfC system was conducted by TGA in air to 1600 °C. HfC started to oxidise at 450 °C as shown in Figure 5.22 which was the lowest oxidation temperature threshold observed, also after this point the oxidation rate abruptly increases. TaC and 1TaC-4HfC showed similar oxidation behaviour and began to oxidise at ~730 °C and after the initial oxidation both compositions oxidised at a similar rate. In addition, at ~870 °C both 4TaC-1HfC and 1TaC-1HfC, started to oxidise at a temperature that was ~220 °C higher than HfC and ~140 °C more than TaC. 1TaC-1HfC was the composition most resistant to oxidation; the oxidation rate was lower than 4TaC-1HfC even though the oxidation threshold temperature was similar, the grey dash-dot line shows the slow oxidation rate compared to the other compositions in the TaC-HfC system.

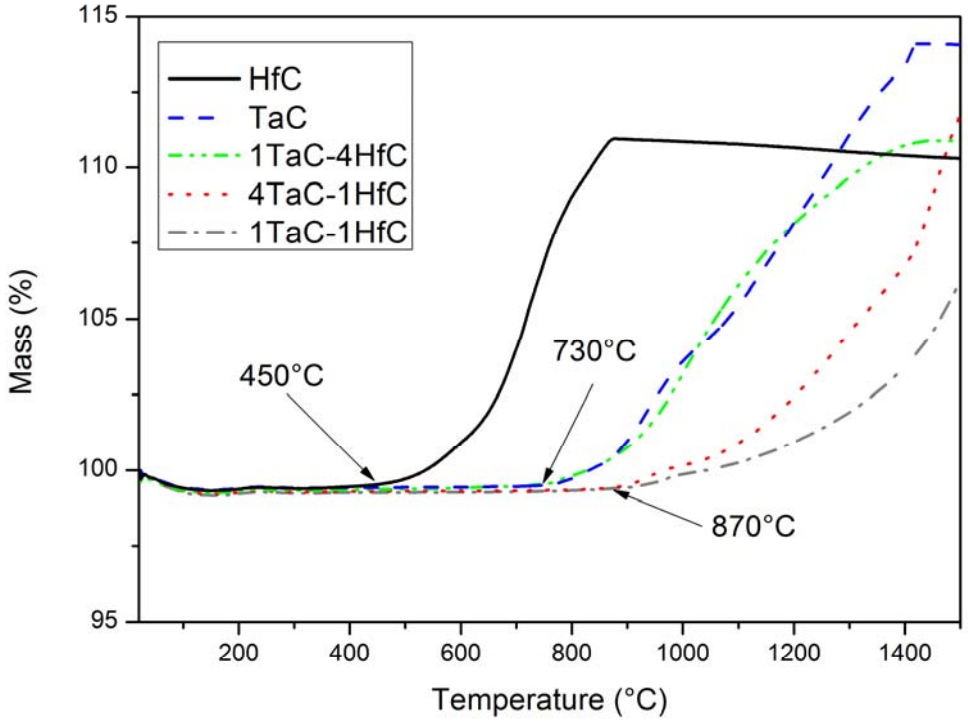

Figure 5.22 Oxidation behaviour of SPS'd TaC, HfC and TaC-HfC ceramics using TGA at a heating rate of 10K/min under air atmosphere.

5.3 Discussion

A processing method was proposed and successfully conducted to produce highly dense single-phase solid solution TaC-HfC ceramics from commercial powders of TaC and HfC using the SPS technique. A sintering study on the densification behaviour and solid solutions formation was conducted on TaC-HfC of a composition of 4TaC-1HfC. Several authors have reported phase diagrams indicating the temperatures at which the solid solution of 4TaC-1HfC is achieved. Gusev [20, 31] reported a binary phase diagram of TaC-HfC and shows that under steady state conditions the solid solution is formed at around ~800 °C, the work by Rudy [1] on phase equilibria reports in the Ta-Hf-C ternary phase diagram the solid solution of 4TaC-1HfC could be formed at a temperature as low as 1000 °C.

In recent work by Ghaffari et al. [167], 4TaC-1HfC was pressureless sintered from commercial powders of TaC and HfC at 2000 °C for 1 h in flowing argon; the author reports that a single phase solid solution was formed, however the XRD profiles shown in the paper do not show complete diffusion of HfC into TaC to form a single phase solid solution. Gaballa et al. [60] used high-energy milling, at up to 18 h of milling time to form solid solutions by mechanical means, then powders were sintered by hot press (HP) at 1500 °C for 1 h. The authors report that after HP the XRD peaks of samples after sintering correspond to a solid solution of 4TaC-1HfC but there are small HfC reflections that show that a single phase solid solution was not achieved completely. Moreover, Schulz et al. [170] used vacuum plasma spray (VPS) to fabricate 4TaC-1HfC. After VPS, the carbide materials were sintered in a graphite furnace at 2000 °C under vacuum and further hot isostatically pressed (HIP) at 2000 °C in pressurized Ar at 200 MPa. Further analysis showed that the final product contains 97 vol% of 4TaC-1HfC solid solution and 3 vol% of Ta_2C, this shows that by increasing temperature and pressure Ta_2C phase is converted to TaC.

In this work a monophasic solid solution was achieved at temperatures of 2350 °C and above and with an applied pressure of 30 MPa using SPS. A combination of techniques was used to analyse the solid solution formation with respect to sintering temperature. First XRD analysis was conducted on samples after SPS (Figure 5.1) showing that a single phase solid solution was formed on samples sintered at 2350 °C and above. This was confirmed by compositional EDS mapping (Figure 5.7) revealing a homogeneous distribution of the Hf signal was achieved in samples sintered ≥2350 °C. Also a uniform distribution of Ta and C signals was observed.

Highly porous microstructures were observed on samples sintered ≤2150 °C (Figure 5.3). At 2150 °C samples showed a relative density of 85.2 ± 0.17 %. Fracture surfaces (Figure 5.4) reveal early stages of sintering with necking between particles forming a connected network in a porous structure. Densification was nearly complete at 2250 °C, while solid solution and grain growth still occurred at 2350 °C. Highest relative density of 94.8% was achieved at a sintering temperature of 2450 °C with a MGS of 6.2 μm. In addition, fracture surfaces (Figure 5.4) of sample sintered at 2150 °C show equiaxed

grains of 3 μm with inter and intragranular pores and with predominant intergranular fracture. After sintering at 2350 °C a denser microstructure (94.5 ± 0.38 % dense) was observed and transgranular fracture becomes significant at this point. For comparison, a relative density of 97% was achieved by Gaballa et al. [60] after HP at 1500° for 1 h and 97.5% with a MGS of 2.8 after HIP by Schulz et al. [170]. Fischer [59] reported 98% relative density on specimens fabricated by HP under a range of temperatures and pressures applied with MGS of 28 μm was reported after sintering at 2500 °C for 15 min and 25 MPa and a MGS of 13.5 μm for a sample sintered at 2700 °C for 30 min and 40 MPa.

Further analysis by TEM (Figure 5.8 and Figure 5.9) showed that grains analysed were of a TaC-HfC solid solution. HRTEM images shows the absence of a liquid phase or a secondary phase during sintering suggesting that densification occurred by solid state diffusion mechanism [57].

Hardness of the 4TaC-1HfC sintered samples was measured using the Vickers and Berkovich indentation techniques. As expected, due to lower porosity [140, 152, 168], the highest Vickers hardness (HV1) was achieved on 4TaC-1HfC after SPS at 2450 °C for 20 min and 30 MPa at 16.8 ± 1.1 GPa and Berkovich nanoindentation was 19.2 ± 1.2 GPa for the same specimen. Reported hardness values of 4TaC-1HfC solid solutions are limited and the different types of tests used makes the comparison of hardness values difficult. Deadmore et al. [171] and Schulz et al. [170] measured hardness with the Knoop hardness test (HK), with reported values of 3720 HK and 1430 HK respectively. A value of 21.4 GPa is reported by Gaballa et al. [60] with a HV2 test. 15.2 GPa was reported on 4TaC-1HfC with 12 vol% $MoSi_2$ and 17.7 GPa for 4TaC-1HfC with 12 vol% $TaSi_2$ for a HV1 test [83].

An increase in thermal diffusivity was observed with increase of temperature on all samples. A small difference in thermal diffusivity value was observed at room temperature (Figure 5.14) between the sample sintered at 2050 °C and the sample sintered at 2450 °C. Room temperature thermal diffusivity was ~8 mm^2/s and increased to 12.0 ± 0.08 mm^2/s at 1950 °C. Thermal conductivity of 4TaC-1HfC show a similar trend (Figure 5.15) by increasing with temperature. At temperatures below 1000 °C, thermal diffusivity is determined by the heat flux transmission though the solid phase, while the convective and heat transfer across and between the pores at this stage is insignificant [168]. Above the

threshold temperature of 1000 °C the heat flux is dependent on both the solid and pore phase. A value of 49.3 W/m·K was achieved at 1950 °C.

After the analysis of the sintering behaviour of 4TaC-1HfC at different temperatures, a two-step sintering process was proposed to produce highly-dense single phase solid solution TaC-HfC ceramics. TaC, HfC and TaC-HfC powders were consolidated by SPS under a thermal schedule consisting of a first stage sintering at 2100 °C for 30 min and 30 MPa, then a second stage of 2350 °C for 20 min and 30 MPa. After the sintering experiments a relative density of 98.3 ± 0.14 % was achieved on TaC. As the HfC content was increased the relative density decreased to a minimum value for HfC of 85.3 ± 0.10 %. This suggests that the inhibition of sintering of HfC was due to the presence of impurities on the particle surface [39, 64]. Oxygen impurities at the particle surfaces hinder the diffusion-driven mass transport mechanisms during consolidation and can also enhance coarsening leading to entrapped pores within the microstructure [172-175]. This also suggests that HfC may be prone to increased oxygen content even on keeping the powders under ambient conditions. Even at very high temperatures (2350 °C) it was very difficult to achieve a relative density above 90% in HfC samples. Further work is suggested to analyse the hygroscopic behaviour of TaC and HfC.

Previous reports highlight the difficulty in densification of monolithic HfC and TaC by different sintering techniques (HP, SPS and presureless sintering) and most studies concentrate on consolidation of TaC and HfC with sintering aids ($MoSi_2$, $TaSi_2$, B_4C, C and graphene) [39, 64, 65, 67, 68, 86] while reports on TaC-HfC are limited [60, 71, 167]. Silvestroni et al. [39] consolidated TaC and HfC synthesised powders by HP and report a maximum density for TaC of 85% of TD and 93% for HfC at 1900 °C. For commercial powders the relative density was higher at 92% for TaC and 96.3% for HfC. At 2300 °C for 60 min and 30 MPa a relative density of 94.3% was reported by Zhang et al. [65] consolidated by HP. A highly dense HfC was consolidated using SPS by Sciti et al. [82], 98% relative density at 2200 °C for 3 min and 65 MPa. Lower relative density was achieved by pressureless sintering, 91% TD for TaC and 73% TD for HfC at 1950 °C for 60 min as reported by Silvestroni et al. [70] .

High temperatures (2350 °C) were needed to achieve a single phase solid solution materials due to the solid state mechanisms involved. As observed by XRD analysis (Fig 5.16) it was proved that in the intermediate TaC-HfC compositions a monophasic solid solution was successfully achieved. This was further proved with elemental EDS maps (Figure 5.18) revealing the homogeneous distribution of Ta, Hf and C. In addition, the behaviour of an ideal solid solution was proved by lattice parameter measurement and Vegard's law [166]. The solid solutions lattice parameters behave linearly between the lattice parameters of TaC and HfC.

Room temperature hardness of TaC-HfC was measured by Vickers indentation and Berkovich nanoindentation. HV1 of TaC was measured at 13.9 ± 0.7 GPa. However, at concentrations of 0.8 molar HfC content or higher the hardness decreases, due to higher porosity levels [168]. The lowest hardness measured was for pure HfC at 10.2 ± 0.7 GPa. Theoretical hardness of TaC is reported as 25 GPa [98] and for HfC 33 GPa [97]. The experimental hardness values were expected to increase to a maximum value for pure HfC, however as mentioned before the effect of porosity was the main factor in the decrease in hardness and nanohardness at higher HfC contents. The maximum hardness (HV1) value was 22.1 ± 1.87 GPa for 1 TaC-1HfC. Hardness values determined for pure TaC were similar to those reported by Zhang et al. [65] of 14.1 GPa, hot pressed at 2300 °C for 60 min and 30 MPa with 94% TD, and higher than the 11.14 GPa reported by Silvestroni et al. [39], hot pressed at 1900 °C for 5 min and 30 MPa with 85% TD. Hardness of HfC was almost double the value of 5.79 GPa reported for HfC (89% TD) consolidated by HP for 20 min and 30 MPa with reported by Silvestroni et al. [39] and lower than the value of 18.3 GPa by SPS at 2200 °C for 3 min and 65 MPa and a relative density of 98% by Sciti et al. [82].

The same behaviour was observed for the elastic modulus (E), values obtained from the reduced modulus (E_r) from nanoindentation experiments (Section 3.6.2). Elastic constants are an indirect measure of the interatomic bonding and the presence of carbon in the lattice promotes strong metal-nonmetal and metal-metal bonds, hence relatively high values of the elastic constants are observed in transition metal carbides [17]. A modulus of 458 ± 6.6 GPa was measured for TaC and increased to 459

± 5.8 for 4TaC-1HfC and a maximum of 549 ± 11.2 GPa at 1TaC-1HfC composition. After this point the modulus drops to 438 ± 17.8 GPa at 1TaC-4HfC and a minimum at 283 ± 9.6 GPa for pure HfC. The modulus value trend show an anomalous behaviour, since the modulus value drops at higher HfC content (≥0.8 molar content). Elastic modulus is sensitive to porosity, hence the drop in value at higher porosity contents. Values of elastic modulus for TaC (537 GPa) and HfC (461 GPa) [17] and also computed values for substoichiometric $TaC_{0.96}$ (515 GPa) and $HfC_{0.96}$ (445 GPa) have been reported. The elastic modulus for pure TaC obtained in this work (458 ± 6.6 GPa) is lower than the reported values, and the value of HfC (283 ± 9.6 GPa) was expected to be higher, however the porosity in HfC samples was responsible for the drop in elastic modulus value.

Fracture toughness similar values for all specimens taking in account the error values. Measured values were in the range of 2.7-3.4 $MPa \cdot m^{1/2}$. For comparison, previously reported values for monolithic TaC are 3.5 $MPa \cdot m^{1/2}$ prepared by HP at 2200 °C for 1 h and 30 MPa [66] and for HfC prepared by SPS at 2200 °C for 3 min and 65 MPa is 2.5 $MPa \cdot m^{1/2}$, which are in close agreement with the values obtained in this work.

Thermal conductivity showed a similar behaviour for all TaC-HfC compositions; the thermal conductivity increases with temperature, being TaC at the high end and HfC at the lower end of the graph (Figure 5.21). At room temperature HfC showed a thermal conductivity of 16 W/m·K which is lower than the 20 W/m·K reported in the literature [3, 89], and as the temperature increases is in close agreement with reported 30 W/m·K at 800 °C [5] and increased to a maximum 40 W/m·K at 1950 °C. A higher range of temperatures is reported for all compositions in this work up to 1950 °C. Similar trend for TaC starting at 32.8 W/m·K at room temperature higher than 22.1 reported by Pierson [3] and with an steady increase with temperature up to 52.8 W/m·K at 1950 °C. In TaC and HfC the phonon contribution (K_p) decreases with temperature and electron contribution of thermal conductivity (K_e) increases markedly with temperature, thus the mechanism of heat transport in TaC-HfC compounds is dominated by electrons.

Coefficient of thermal expansion (CTE) was in the range of 7.08-7.66 x10^{-6} /K in the range of 25-2000 °C. Being TaC the lowest and HfC the highest value. Solid solution values are in between those of the single member carbides. Measured CTE of TaC is ~12% higher than the value of 6.3x10^{-6} /K reported by Exner [176] and ~16% higher for HfC reported by Opeka et al.[89] a value of 6.6x10^{-6} /K. Also the results contradict the CTE behaviour of the TaC-HfC solid solutions reported by Barantseva and Paderno [103] that the CTE of the solid solutions are lower as compared to the single carbides. As expected because of the bond energy of HfC (16.45 eV) compared to TaC (16.92 eV) the CTE was higher. And the CTE of pure TaC (7.08 ± 0.33 x10^{-6} /K) was the lowest in the TaC-HfC systems. The higher the bond energy, the lower is the expansion [3].

The mechanical properties measured (HV1: 22.1 ± 1.87 GPa and *E*: 549 ± 11.2 GPa of 1TaC-1HfC) show the potential of TaC-HfC compounds for their use as structural components in aerospace applications. In addition, the high thermal conductivity (52.8 W/m·K at 1950 °C) show that these compounds have the ability to dissipate high fluxes of heat required in hypersonic flight conditions. Also TaC-HfC compounds offer exciting opportunities by tailoring of mechanical and thermal properties in applications such as thermal protection systems (TPS) and layered structures.

Oxidation conducted by TGA showed that 1TaC-1HfC was the composition most resistant to oxidation; oxidation temperature threshold was 870 °C. A study by Patterson et al. [177] on oxidation of TaC-HfC solid solutions reports oxidation resistance of several Hf-rich TaC-HfC (90 wt% HfC/ 10 wt% TaC, 80 wt% HfC / 20% TaC and 70 wt% HfC / 30% TaC) solid solutions deposited by chemical vapour deposition (CVD) on graphite substrates, coating behaviour was similar for all compositions between 1000° and 1200 °C. Courtright et al. [178] found that additions of 25 wt% TaC into HfC, do not improve oxidation resistance on a series of thermal cycles (in air) between 2000 °C and 500 °C, the TaC-HfC sample was damaged by the thermal cycles compared to the HfC sample. This study under different oxidation conditions, showed that additions of HfC up to 50 mol% increased the temperature of oxidation compared to that of single member TaC and HfC. Similar experiments were carried out in TaC-TaN solid solutions [112] and showed similar oxidation behaviour as the one in this work, the end

members showed higher oxidation rates than the solid solutions, being $TaC_{0.5}N_{0.5}$ the composition with slowest oxidation rate. This suggest that in end member carbides (TaC and HfC) the evolution of CO and CO_2 may be quicker than in the (Ta,Hf)C solid solutions. Although more studies are required for better understanding of the oxidation mechanisms of TaC-HfC compounds. Still one of the main challenges in the development of TaC-HfC compounds is the improvement of the oxidation resistance of these materials.

6 Melting point determination of TaC, HfC and TaC-HfC solid solutions by laser melting.

The objective of this chapter is to demonstrate the feasibility of using laser melting techniques for accurate calculations of thermophysical properties of TaC-HfC UHTC's at high (over 2000 °C) temperatures. The measurement of thermophysical properties at such high temperatures is difficult due to increased reactivity of the materials, heat transfer, volatility and loss of mechanical strength, particularly in the carbides of interest in this work, known to be the highest melting compounds ever studied [1, 28, 29]. Several experimental investigations of the high temperature behaviour of pure and mixed tantalum and hafnium carbides were carried out mostly between 1930 and 1969, including the early work by Agte and Althertum [28] and the comprehensive experimental campaign and literature review provided by Rudy [1]. In all these cases, high temperature melting of these carbides was studied with the help of the so-called Pirani-Alterthum approach [28]. This experimental method consists in observing the disappearance, in a sample heated by Joule effect, of a blackbody hole when this is filled by the newly formed liquid. Such an approach has been shown to be effective in many cases. However, it does involve significant uncertainty especially at temperatures above 2000 °C, where observation of liquid formation is extremely hard, in particular when using the early pyrometers which had limited time resolution.

The current laser melting technique constitutes a first alternative to the Pirani-Alterthum method for the study of melting in tantalum and hafnium carbides. It offers several advantages over traditional methods; by controlling the time at which the sample is kept at extreme temperatures, a laser pulse shape and duration can be optimised in order to produce desired heating and cooling rates and avoid or at least minimise undesired effects such as sample vaporisation and reaction with the container. Extremely high temperatures are achieved in the order of ms. A high-pressure cell filled with an inert atmosphere is used to minimize evaporation from the samples surface. The sample is held by millimetre long graphite screws, so that interaction with the container is kept to a minimum. Fast multi-channel

pyrometers (time resolution of the order of 10 μs) are used to record the sample thermal radiance at different wavelengths in the visible and near infrared range.

Measurement of melting points (T_m) was conducted using a laser heating technique developed at the Institute for Transuranium Elements (ITU) of the European Commission's Joint Research Centre (Karlsruhe, Germany) [118] with the goal of studying refractory materials at high temperature for nuclear application. The work in this chapter was conducted in collaboration with Dr. Dario Manara at ITU. This technique has been successfully used in several refractory systems such as uranium carbides [130], uranium oxides [131], plutonium oxides [132, 133], uranium nitrides [134] and zirconium carbides [135, 136]. The results obtained on already well assessed phase transition temperatures are in good agreement with literature data.

A sensitive drawback of the current approach, shared, at least partly, with the Pirani-Alterthum technique, is the emissivity dependence of the measured temperatures on the sample normal spectral emissivity ε_λ (or NSE). The role played by this parameter is extensively discussed in this chapter.

6.1 Sample composition analysis and sample preparation

Samples were prepared from commercial powders of TaC and HfC (Table 3.1) using SPS. Carbon, sulphur, nitrogen and oxygen contents in the as-received powders were reported by the manufacturer and on sintered products it was determined by combustion (Section 3.2). Elemental analysis of the powders is in Table 6.1. From the elemental analysis initial powder compositions were calculated to be sub-stoichiometric $TaC_{0.94}$ and $HfC_{0.94}$ and for products after sintering the compositions measured were $TaC_{1.00}$ and $HfC_{0.98}$.

Compound	Wt% C	Wt% O	Wt% N	Wt% S	C/M ratio (M=Ta, Hf)
TaC (as-received) †	6.24	0.13	0.01	0.001	0.94
TaC (sintered) *	6.31 ± 0.03	0.37 ± 0.01	0.016 ± 0.001	-	1.00
HfC (as-received) †	6.38	0.32	0.02	0.0051	0.94
HfC (sintered) *	6.11 ± 0.05	0.49 ± 0.01	0.58 ± 0.005	-	0.98

Table 6.1 Composition of as-received powders of TaC and HfC († manufacturers data, *combustion data).

Powders of TaC and HfC were mixed in the appropriate amounts to make 4TaC-1HfC, 1TaC-1HfC and 1TaC-4HfC compositions. Ceramic powder processing was conducted using the methods described in detail in Section 3.1. Afterwards the powders were consolidated using an SPS furnace under the sintering conditions described in Table 6.2.

Composition	Sintering conditions (T_D, t_D, P)	Bulk density (g/cm^3)	Relative density (%)
TaC	2100 °C, 20min, 60 MPa	14.01 ± 0.03	96.7 ± 0.24
4TaC-1HfC	2100 °C, 30 min, 55 MPa 2350 °C, 20 min, 30 MPa	13.77 ± 0.02	97.7 ± 0.09
1TaC-1HfC	2100 °C, 30 min, 55 MPa 2350 °C, 20 min, 30 MPa	12.94 ± 0.03	95.7 ± 0.29
1TaC-4HfC	2100 °C, 30 min, 55 MPa 2350 °C, 20 min, 30 MPa	11.31 ± 0.03	87.0 ± 0.26
HfC	2100 °C, 20 min, 60 MPa	10.42 ± 0.01	82.2 ± 0.04

Table 6.2 Sintering conditions, bulk density and relative density of TaC, HfC and TaC-HfC solid solutions fabricated by SPS.

Samples were characterised after sintering using several techniques. XRD analysis (Section 5.2.2) was conducted on the samples after sintering. XRD patterns of TaC and HfC show only peaks of their respective single end member carbide, no other phases were detected. Also the diffraction patterns of the solid solution show a single-phase solid solution for the 4TaC-1HfC, 1TaC-1HfC and 1TaC-4HfC compositions. Microstructural characterisation by SEM and EDS (Section 5.2.3) showed that only single phase TaC and HfC was detected on end member carbide samples and analysis by EDS confirmed a single-phase solid solution on 4TaC-1HfC, 1TaC-1HfC and 1TaC-4HfC specimens.

For the laser melting experiments, samples of 5 mm diameter were cut by EDM (Electrical Discharge Machining) from the 20 mm sintered pellets. Samples were held in a graphite fixture inside the pressure cell fitted with a sapphire window. One advantage of the graphite fixture is where possible, samples could be melted several times on the same surface. For each experiment the cell was evacuated using a vacuum pump and backfilled with argon at a 0.2 MPa pressure.

6.2 Laser melting thermal analysis

6.2.1 Heating technique

The specimen surface was heated using a 4.5 kW, 1064.5 nm Nd:YAG CW laser (HDLS, TRUMPF, Ditzingen, Germany) with a 3 mm focal spot. The laser heating experiment consisted of four consecutive laser pulses, starting with a low-power and long hold time, and then subsequent pulses were increased in power but shortened in hold time. Initial pulse was 1000 ms and maximum power 1810-2480 W, then a long-intermediate pulse of 500 ms and 2400-2980 W of power. A third shorter intermediate pulse of 250 ms and 2980-3480 W was applied and finally a short pulse of 100 ms with a maximum peak power of 3200-3980 W was used. A summary of the laser pulse profiles and power density is shown in Table 6.3.

Timescale	Hold time (ms)	Peak power (W)	Power density (MW/m^2)
Long	1000	1810-2480	256-350
Intermediate-long	500	2400-2980	339-421
Intermediate-short	250	2980-3480	421-492
Short	100	3200-3980	452-563

Table 6.3 Laser pulse profiles of melting experiments of TaC-HfC ceramics.

6.2.2 Temperature measurements

The specimen brightness temperature was detected using a fast two-channel pyrometer, using the first channel at λ = 655 nm and calibrated against standard lamps at 2500 K. Calibration linearity was also verified using a graphite blackbody to 3400 K. An additional, slower 256-channel radiance spectro-pyrometer operating between 515 nm and 900 nm was employed for the study of the NSE (ε_λ) in the current samples.

Section 3.8 describes in detail the setup of the instrument, theory on principles of pyrometers and limitations of using this approach on carbides. Thermal radiation intensity (L_{ex}) was recorded using the muti-channel pyrometer and analysis of the NSE (ε_λ) was conducted by a non-linear fit of the thermal emission spectrum with equation Equation 3.18. The radiance temperature T_λ at wavelength λ was converted to true temperature T using Wien's approximation given in Equation 3.20.

Since little data exist on optical properties of tantalum and hafnium carbides, in the current work first approximation true temperature versus time curves (thermograms) were estimated using ε_λ values reported by Deadmore [179]. He measured emissivity data at 650 nm for the following compositions up to approximately 2800 °C: $TaC_{0.97}$, $HfC_{0.98}$, $Ta_{0.8}Hf_{0.2}C_{0.93}$, $Ta_{0.5}Hf_{0.5}C_{0.96}$ and $Ta_{0.25}Hf_{0.75}C_{0.97}$ (Figure 6.1). Although these measurements are likely to be accurate, extrapolation to the melting temperatures studied in this work (3750 °C and more) is far from straightforward. In addition to the large temperature extrapolation range, the NSE temperature dependencies measured in [179] are not the same at different

compositions. NSE slightly increases with temperature in tantalum carbide, whereas it sharply decreases in hafnium carbide and in mixed compositions, although no uniform evolution of the ε_λ vs T slope can be observed. Shaffer [180] and Coffman et al. [181] showed that in these compounds, abrupt changes in NSE can occur between 1800-2500 °C, while the NSE remains approximately constant at >2500 °C and up to the melting point. Also the values measured by Deadmore seem to stabilise around 2800 °C. Taking this observation into account, the highest temperature NSE values proposed by Deadmore are retained here as first-approximation values to obtain true temperature from the measured radiance temperature through Equation 3.20: an emissivity of 0.52 was used for TaC, 0.47 for 4TaC-1HfC, 0.55 for 1TaC-1HfC, 0.56 for 1TaC-4HfC and 0.5 for HfC.

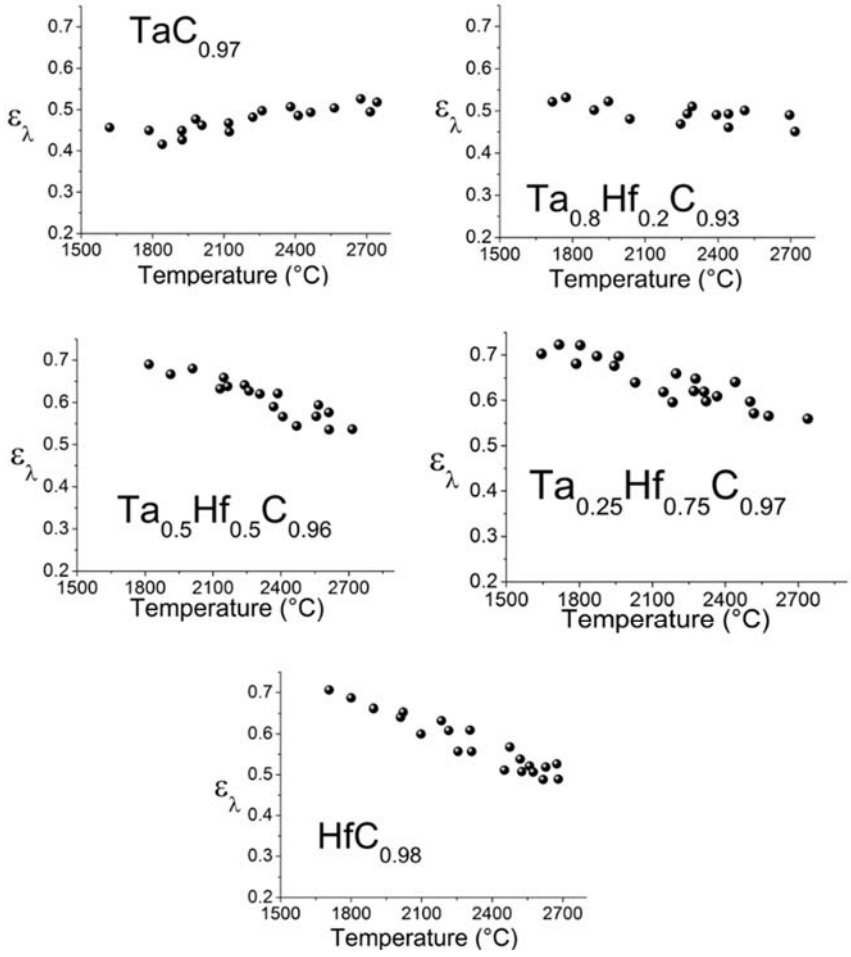

Figure 6.1 Deadmore's emissivity data as a function of temperature at 650 nm for the compositions $TaC_{0.97}$, $HfC_{0.98}$, $Ta_{0.8}Hf_{0.2}C_{0.93}$, $Ta_{0.5}Hf_{0.5}C_{0.96}$, $Ta_{0.25}Hf_{0.75}C_{0.97}$ [179].

These values can be used also as the starting point for fitting the thermal emission curves recorded in the current research by the multi-channel spectro-pyrometer between 515 nm and 900 nm. However, without further information on the high-temperature emissivity of the studied materials, the current radiance spectra can only be used for a qualitative study of the NSE trends across the melting/solidification transition, without yielding any accurate absolute value for this parameter.

6.2.3 Thermal analysis

Inflections or thermal arrest in the time-temperature thermograms give information related to phase transitions (solidus, liquidus and isothermal phase transformations). An additional technique called reflected light signal (RLS) analysis was used to confirm phase transitions (melting/freezing) and was conducted using the second channel of the pyrometer tuned to a low-power (1W) Ar^+ laser (λ=514 nm). A constant RLS signal indicates a solid surface while random oscillations appear after melting due to vibrations on the sample liquid surface. The oscillations are easier to analyse using the time derivative of the RLS.

The output signals of the laser melting experiment of TaC are shown in Figure 6.2. The thermogram (black line) shows the sample temperature during the laser heating and cooling cycle. Combining the thermogram with the RLS technique enables identification of the phase transformation. In these experiments the time derivative of the RLS was used to identify the melting transition. The first derivative RLS signal (green) shows that melting occurred on the first three laser pulses, while heating/cooling without any phase transformation was observed on the last pulse. A longer or more powerful laser pulse was needed to produce a pronounced freezing arrest. This observation, combined with visual observation of the samples after lower power laser shots, confirmed that the recorded thermal arrests and the corresponding RLS oscillations correspond to melting of the sample surface freezing.

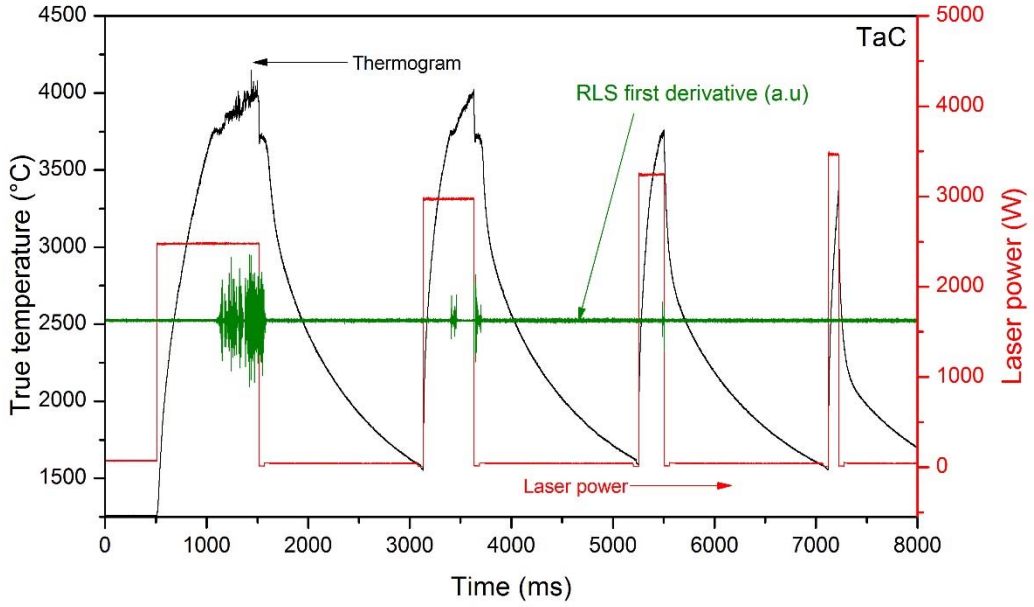

Figure 6.2 Thermogram, laser pulse profile and derivative of RLS of laser melted TaC.

A detailed view of a thermogram and RLS signal of a laser melted TaC is shown in Figure 6.3. A thermal arrest at the cooling section and oscillations in the RLS confirm that the sample melted. Melting of the sample is difficult to identify using only the thermogram, since there was no thermal arrest or inflection during heating, with the RLS technique the initiation of melting is easy to identify with the initiation of the noise-like signal. Also during the cooling it is easy to spot the solidification point when the oscillations in the RLS signal stop. The time lapse where liquid was present can be easily observed with the RLS signal. During heating and after melting, noise at the maximum point of the thermogram was observed, this is believed to be boiling from the sample surface [130].

Since no further inflections were observed during heating or cooling it can be inferred that, within the current experimental uncertainties. TaC melts congruently and does not show further phase changes below the melting temperature [130]. Further analysis of the thermal arrest showed that T_m of TaC was 3768 ± 40 °C, with the emissivity value chosen above. In addition, during melting a significant volume of vapour production was observed visually, which is related to the disturbed shape of the thermogram

at the highest temperatures [134]. However, vaporisation was not a concern since the experiments showed satisfactory reproducibility with at least 12 laser shots performed on each sample pellet.

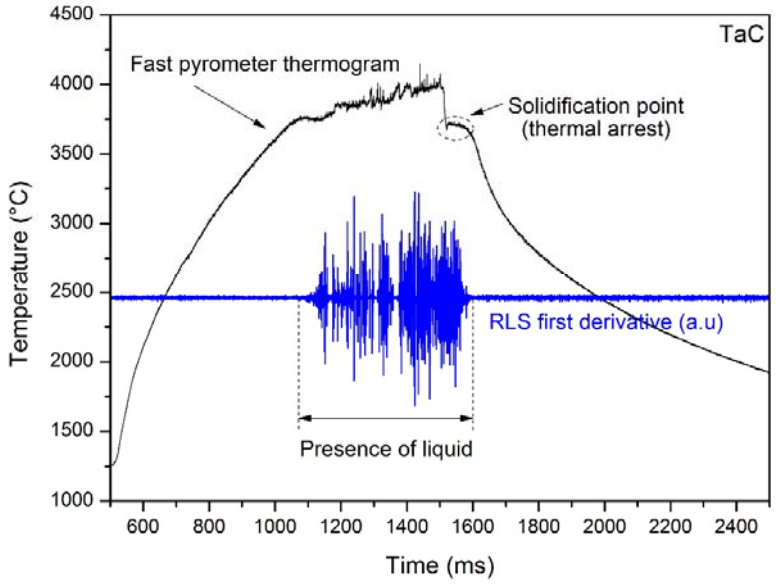

Figure 6.3 Thermogram and time derivative of RLS of laser melted TaC.

Similarly 4TaC-1HfC powders sintered by SPS were tested under the same laser profiles as TaC. Melting on the four pulses was observed with a clear thermal arrest on the first three pulses (Figure 6.4). Comparing the profiles of TaC (Figure 6.2) and 4TaC-1HfC (Figure 6.4) it was observed that at the same thermal conditions 4TaC-1HfC melted more quickly than TaC, ~300 ms before, at 3905 °C. Also the RLS signal during melting was consistent without interruptions.

Similar experiments were conducted on 1TaC-1HfC and 1TaC-4HfC samples. The melting temperatures recorded for 1TaC-1HfC at emissivity of 0.55 was 3803 ± 40 °C and for 1TaC-4HfC with an emissivity of 0.56 was 3847 ± 40 °C.

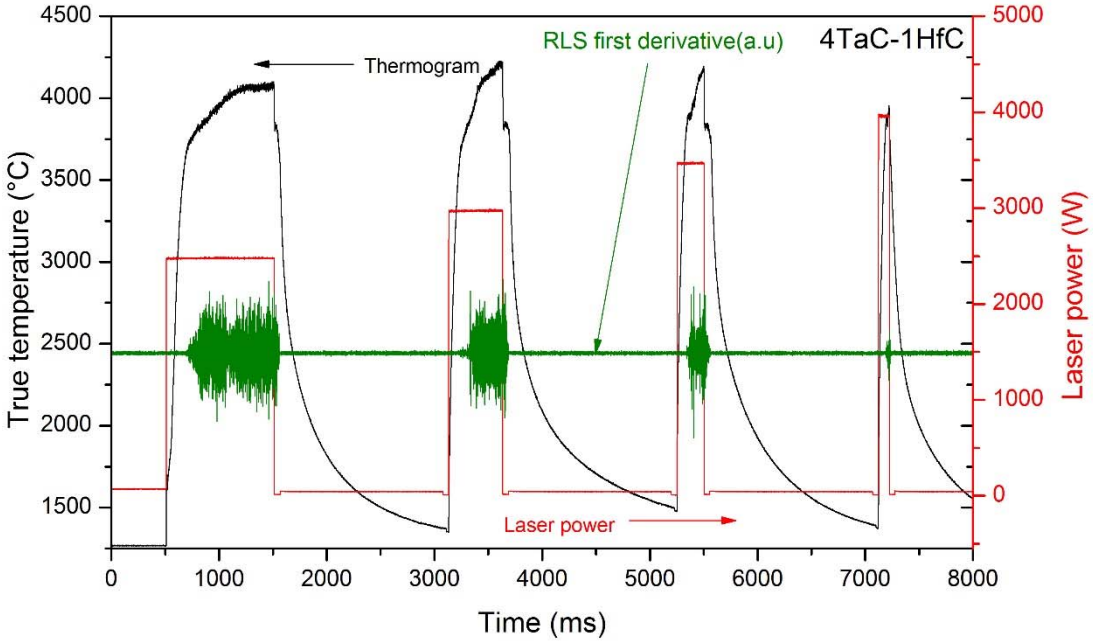

Figure 6.4 Thermogram, laser pulse profile and derivative of RLS of laser melted 4TaC-1HfC.

One of the thermograms recorded in the 4TaC-1HfC melting experiments is reported in Figure 6.5. The melting point was clearly visible during the heating stage when the slope of the thermogram changes and the disturbance in the RLS is present. At higher temperatures there was less disruption in the signal and subsequent less vaporisation during melting. After the end of the laser pulse the sample was cooled naturally then a slight undercooling effect was produced during the thermal arrest, this effect is common during fast freezing conditions and is related with the solidification kinetics (nucleation and growth) [134]. The samples were successfully subjected to repeated laser cycles with consistent results achieved. A melting temperature of 3905 ± 40 °C was achieved after consecutive melting cycles.

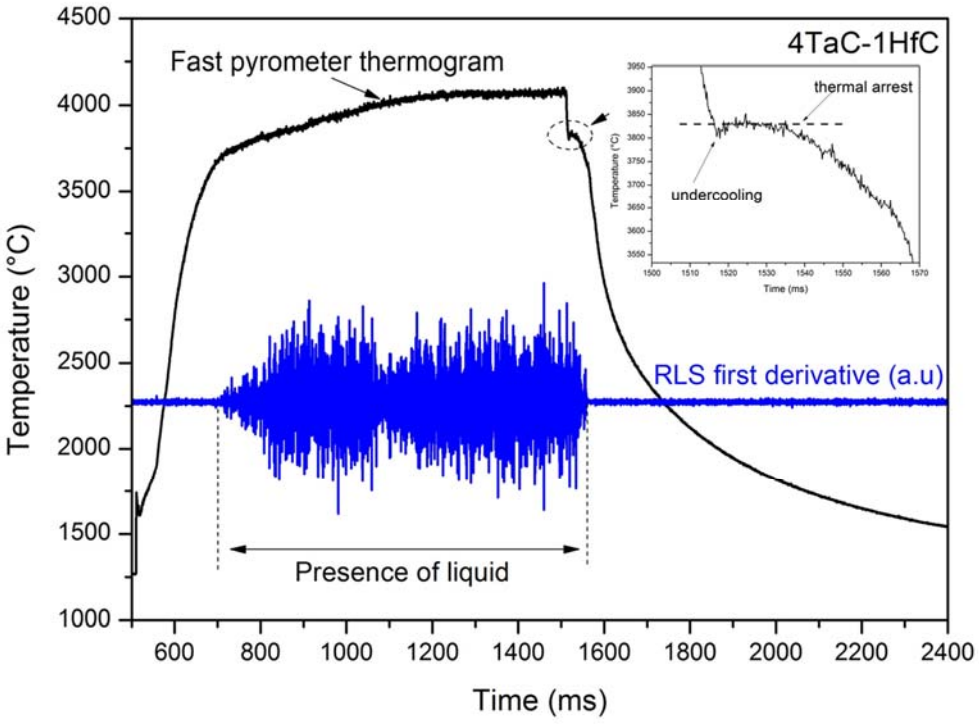

Figure 6.5 Thermogram and time derivative of RLS of laser melted 4TaC-1HfC.

During the initial pulse of the HfC melting experiments it was observed that less laser power was required to melt a hafnium carbide sample than all the previous specimens of similar shape and volume. An initial laser pulse with an output power of 1810 W was required to melt the sample, compared to 2480 W required to melt TaC. As shown in Figure 6.6, melting of samples was also achieved on intermediate and short pulses. The lower thermal conductivity (Section 5.2.5) and emissivity of HfC induces higher heat concentration in the sample surface, producing higher temperatures at lower applied power. Furthermore, much less vaporisation (thickness of the vapour plume formed on top of the sample) was observed in pure hafnium carbide compared with all the other compositions. Most probably the excess power needed to heat the other compositions was largely dissipated in the sample vaporisation. However, higher temperatures were necessary to melt the HfC samples.

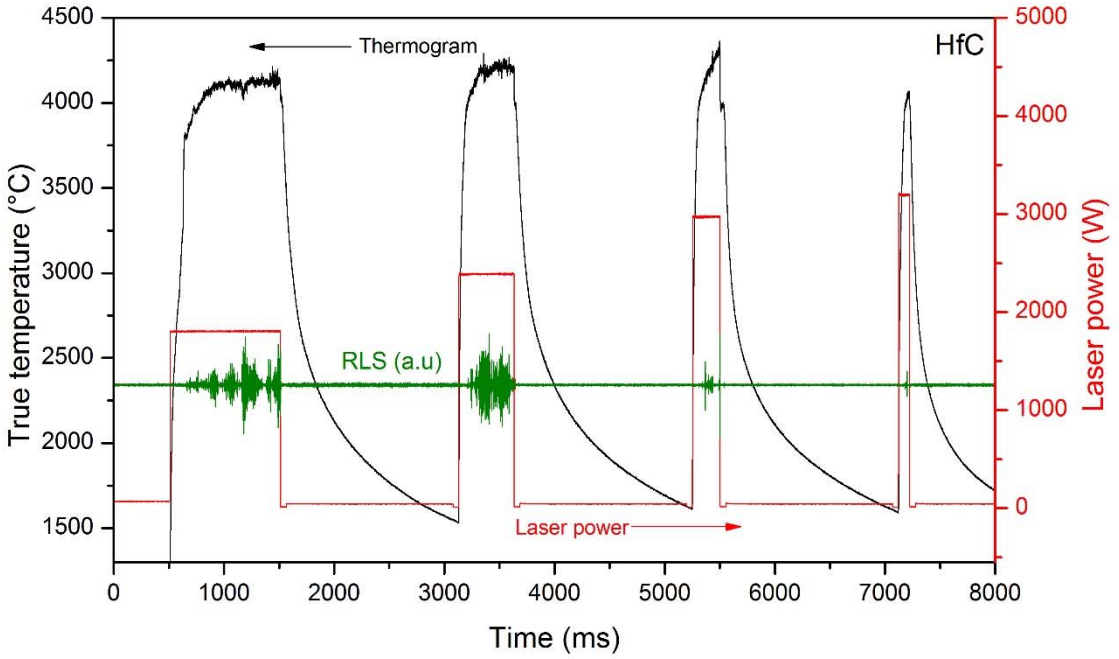

Figure 6.6 Thermogram, laser pulse profile and derivative of RLS of laser melted HfC.

As shown in detail in the thermogram of Figure 6.7, a similar behaviour to that of the TaC-HfC solid solutions during the heating stage was observed. A change in slope of the thermogram profile was observed as the sample started to melt, with less vaporisation observed visually during the melting stage, and with a clear thermal arrest upon the cooling stage. With the selected emissivity value of 0.5, the melting temperature value measured for HfC was 3959 ± 50 °C, the highest value measured in the TaC-HfC system.

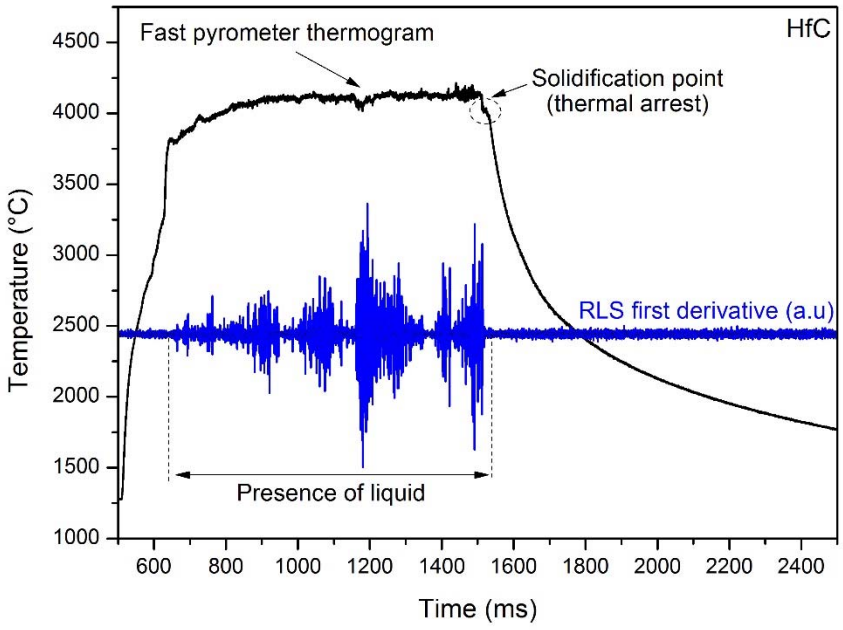

Figure 6.7 Thermogram and time derivative of RLS of laser melted HfC.

6.3 Post-melting characterisation

Samples were characterised after melting experiments. A digital photograph of post-melted samples is shown in Figure 6.8. After 8 laser pulses the TaC sample (Figure 6.8a)) showed separation of material from the bulk material around the molten pool, revealing unmelted bulk material, easily identifiable as a rough matte finish region in the sample surface. A bright melted and refrozen pool at the centre of the sample was observed.

Furthermore the 4TaC-1HfC pellet (Figure 6.8b)) showed better structural integrity than the other compositions, the sample retained its shape even after consecutive laser shot cycles of 12 laser pulses in total. A rounded region of a molten pool of ~3 mm with a swollen region at the centre of the sample was observed. In addition, radial cracks initiating at the focal spot of the laser and propagating to the edge of the sample were produced.

Massive damage was produced on the HfC sample during the laser melting experiments. A molten pool covering the whole surface with a crater-like shape is shown in Figure 6.8c). During laser heating, parts

of the sample separated and fell off the sample, due to the high porosity (~18%) of the sample. In some experiments, the thermogram showed disruptions due to bulk material falling off the sample surface. This was stabilized after a few laser shots, when a denser surface was produced after melting and freezing of the material.

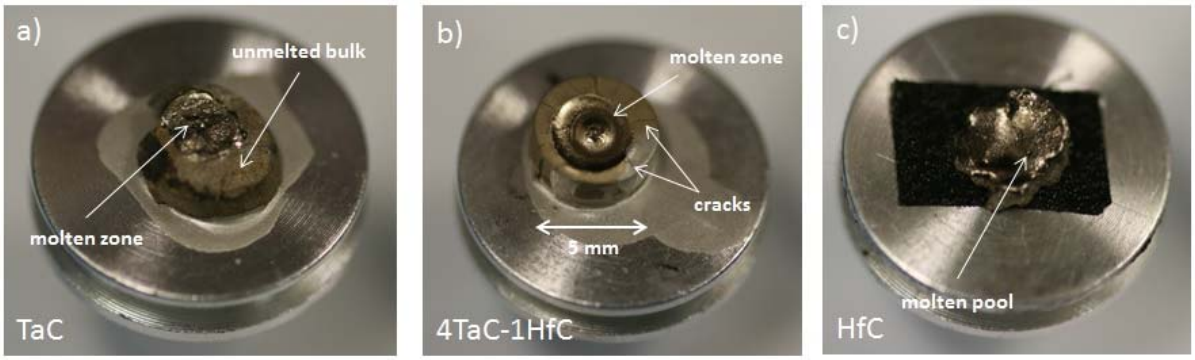

Figure 6.8 Digital photograph images of laser melted samples: a)TaC, b) 4TaC-1HfC and c) HfC.

In addition, SEM analysis was conducted on post-melted samples. A BSE image in Figure 6.9a) shows a melted sample of TaC after laser heating experiments. The centre of the sample consists of a molten pool surrounded by unmelted bulk material. At the centre of the molten pool a crater can be observed where the focal point of the laser was targeted. A region surrounding the void or crater (Figure 6.9b)) shows the recrystallised grains after freezing. The morphology of the grains shows a rippled surface after freezing. This morphology is consistent through the molten pool and a single grain can be observed at higher magnification in Figure 6.9c).

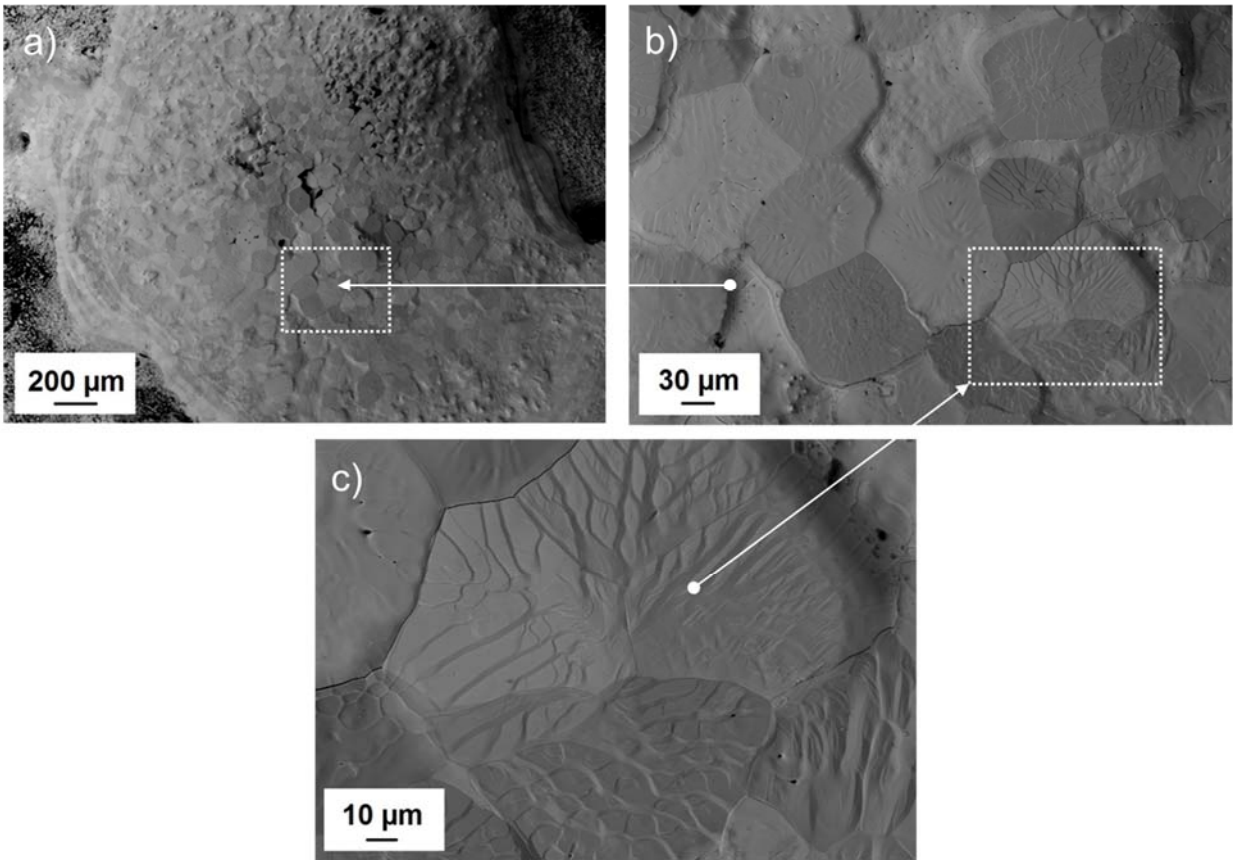

Figure 6.9 BSI of TaC after laser induced melting showing a) molten pool, b) morphology of grains after melting and c) higher magnification of a grain after melting.

The molten region of a 4TaC-1HfC sample is shown in Figure 6.10 revealing a circular region of molten material with a swollen area at the centre was observed. Cracks were observed starting from the focal point of the laser, radially propagating to the outer regions of the sample. A dendritic structure was formed after consecutive melting of the same spot. In Figure 6.10b) next to the dendritic structure cracks have formed. As the material surrounding the dendrites freezes, ripples formed on the surface of recrystallised grains (Figure 6.10c)). Also revealed is a change in grain morphology from the swollen to a heat affected zone, with three different areas; elongated grains with rippled surface, then a transition zone with equiaxed grains and finally a region with grains with lumps or peaks at each grain (Figure 6.10d)).

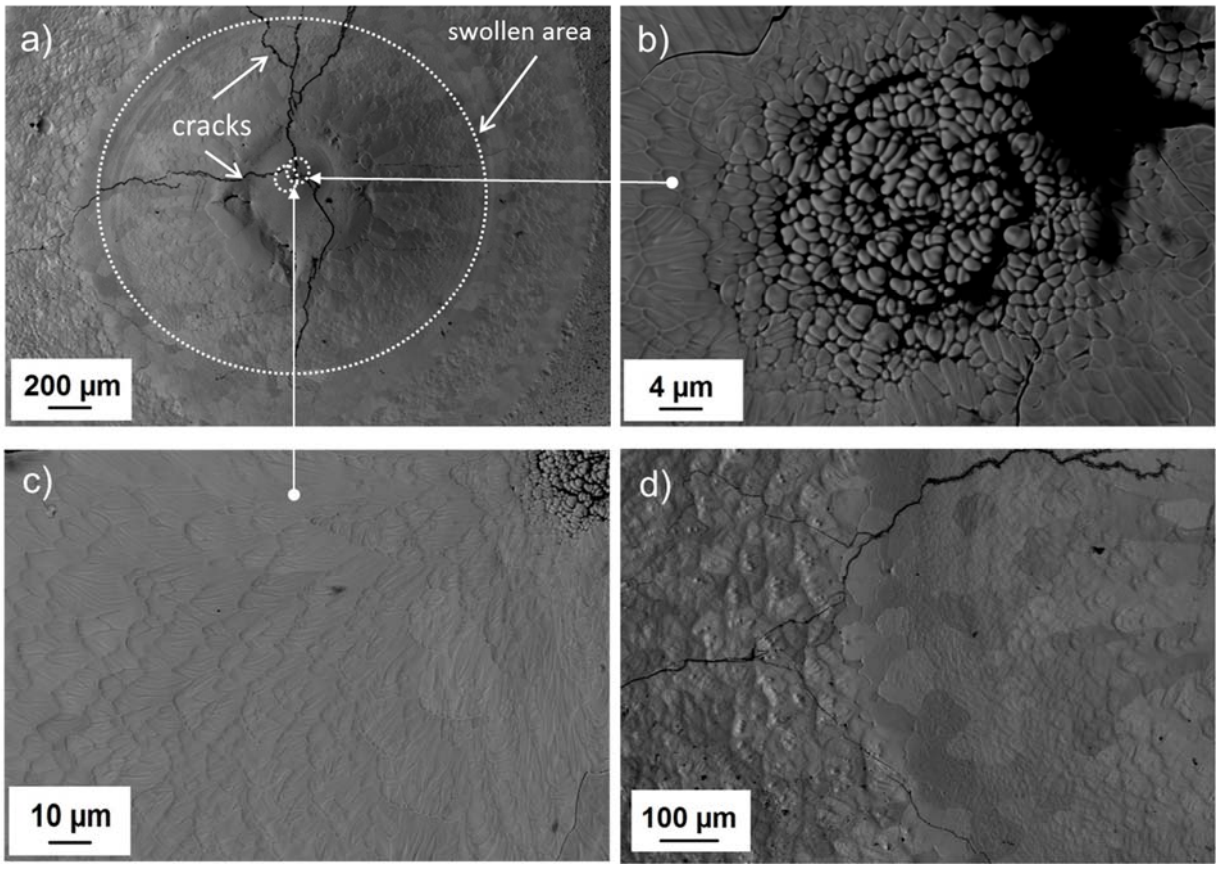

Figure 6.10 BSI of the solidified molten pool of 4TaC-1HfC a) swollen area near the centre of the laser focal point with cracks in the surface, b) dendritic microstructure after repeated melting, c) ripples at the surface near the laser focal point and d) change in grain morphology from the swollen area to a heat affected zone.

BSI of melted HfC shows in Figure 6.11a) the molten pool of the sample which constitutes the whole top surface of the sample after severe damage caused by repeated melting experiments. The area indicated by a white oval (Figure 6.11a)) shows the beam focal point where the highest thermal load was concentrated and is formed of a dendritic structure formed after consecutive melting and freezing of the same spot. An enlarged image (Figure 6.11b)) shows the formed dendrite structures with interdendritic voids shown in black contrast. The square indicated in Figure 6.11a) and enlarged in Figure 6.11c) shows the melted surface outside the dendritic region in which recrystallised equiaxed grains formed after freezing of the melted surface. This morphology is uniform throughout the molten pool surrounding the dendritic region.

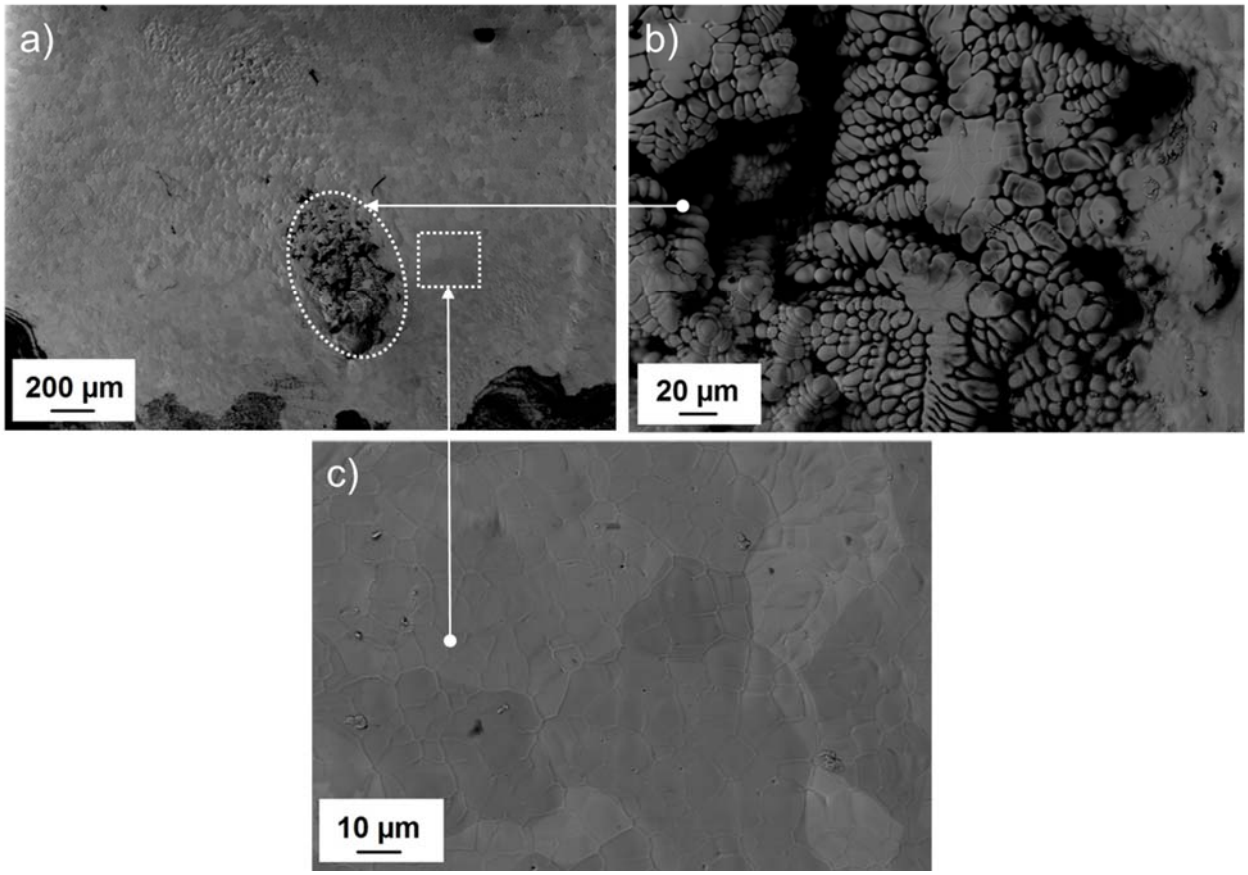

Figure 6.11 BSI of molten pool of HfC, a) molten pool, b) formed dendrites after repeated melting and c) grain morphology around dendritic structure.

An important concern in melting experiments is the occurrence of phase transformations during and after melting. Due to vaporisation of carbon products and a possible reduction in carbon content it is possible that hexagonal Ta_2C or other Ta-C phases formed. This situation is not a concern in HfC where the carbide has a wide range of homogeneity at high temperatures and does not form higher order carbides (Section 2.4). Additional TEM analysis conducted on FIB prepared section showed that in a melted TaC sample (Figure 6.12) only TaC grains were observed. SAED patterns were indexed and only cubic [1 1 0], [1 2 -1] and [1 4 -1] zone axes were identified, confirming that the grains analysed are cubic TaC. No lower temperature thermal arrests have been observed in the thermograms of the present study. Such thermal arrests would have been expected, according to the phase diagram proposed by Rudy [1] if new phases, such as Ta_2C, had been produced as a result of a hypothetical massive vaporisation of carbon-rich species.

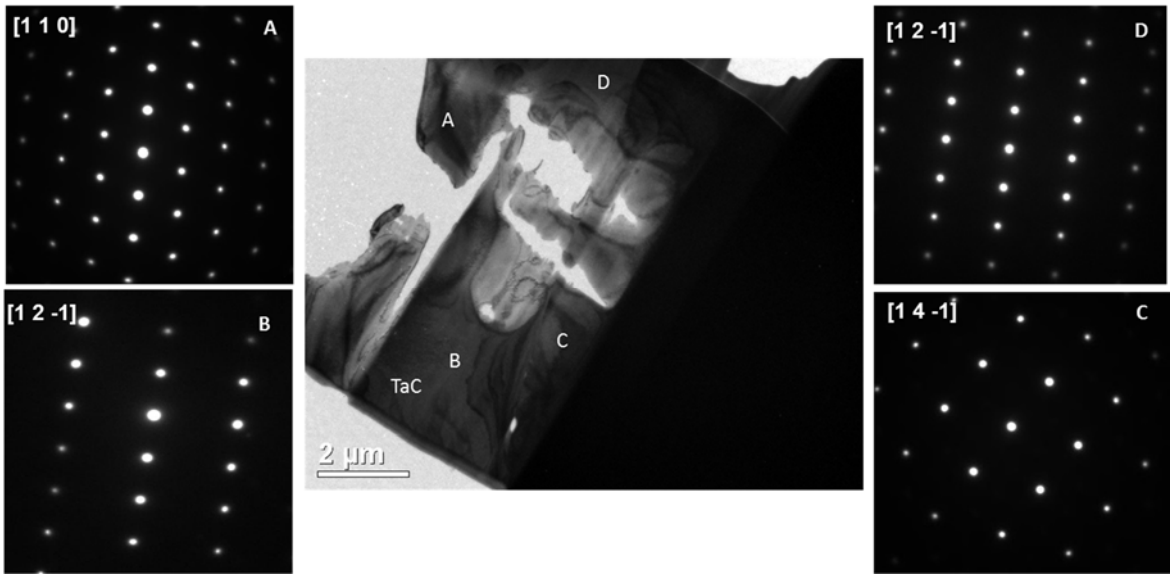

Figure 6.12 BF TEM image of FIB section of laser melted TaC and respective SAED indexed patterns showing cubic grains.

A statistical limitation of FIB is that the samples prepared by this method contain only a few grains for analysis. However, with the size and condition of post melted samples FIB was the only option for TEM sample preparation. Also an advantage with FIB is that samples can be made out of specific features or regions of interest within the melted samples. Samples prepared by FIB were made from recrystallised grain regions and can be taken as representative of the molten pool region.

Similar results were observed on FIB sections of laser melted 4TaC-1HfC (Figure 6.13) and HfC (Figure 6.14). Only grains consisting of a solid solution of TaC-HfC were observed with SAED patterns in the [1 1 0] beam direction were observed. For the HfC FIB section, TEM analysis showed that only HfC grains are present and SAED of cubic crystal indexed as the [1 2 -1] zone axis for both of the grains analysed in Figure 6.14.

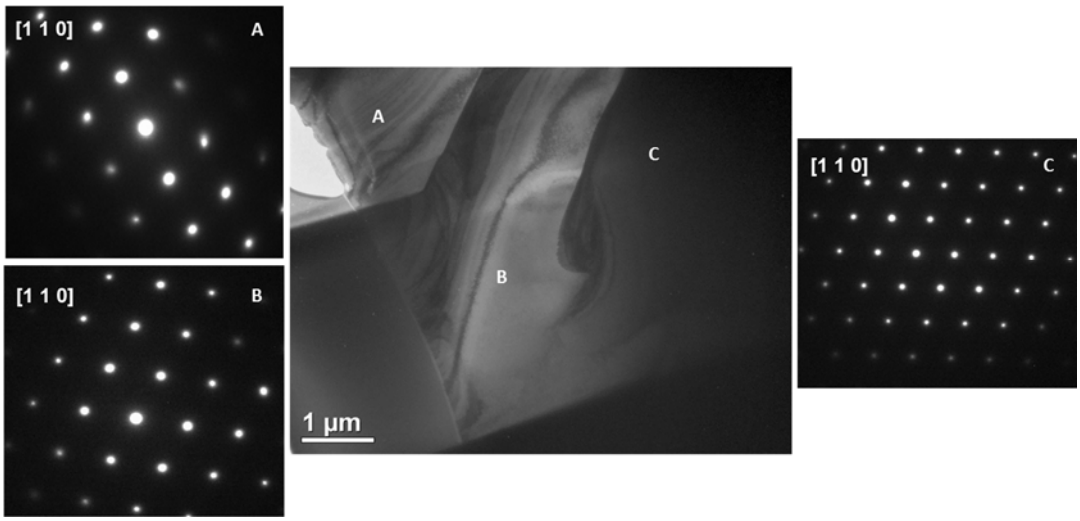

Figure 6.13 BF TEM image of a FIB section of laser melted 4TaC-1HfC and respective SAED patterns.

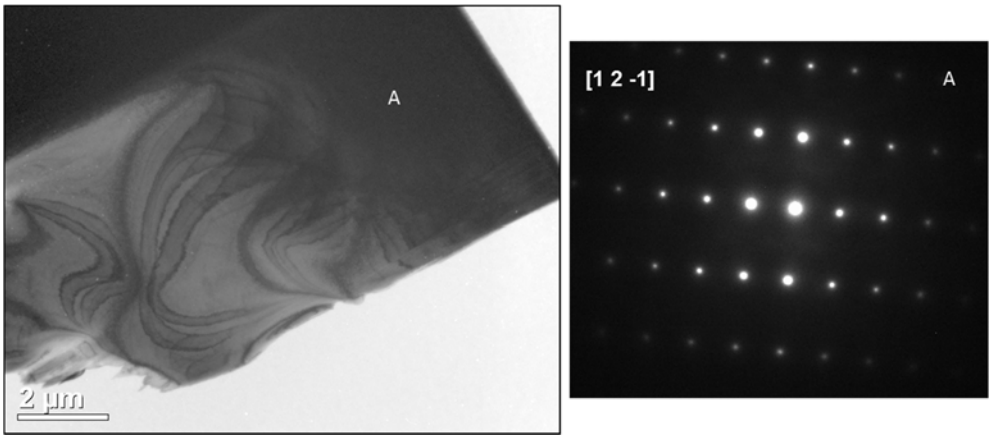

Figure 6.14 BF TEM image of a FIB section of laser melted HfC and [1 2 -1] SAED pattern.

6.4 Discussion

Figure 6.15 reveals that there is a maximum melting point of the solid solutions is at the 4TaC-1HfC composition, at 3905 °C, in fair agreement with the value suggested by Agte and Alterthum [28]. This maximum melting point is only for the solid solutions because the maximum observed melting point in the TaC-HfC system is for $HfC_{0.98}$, at 3959 ± 50 °C. However, unlike previous reports, the T_m of TaC measured in this study was the lowest in the TaC-HfC system, at 3768 ± 40 °C. Intermediate compositions between 4TaC-1HfC and $HfC_{0.98}$ have lower solid/liquid transition temperatures, although

still higher than pure TaC. The highest melting temperature measured reported for $HfC_{0.94}$ is 3928°C and the highest for any compound is 3983 °C for $TaC_{0.88}$, both temperatures determined by Rudy [1]. Gusev et al. [31] reported a similar trend to Rudy's results [1] but with slighter higher values (Table 6.4), however their values were obtained from thermodynamic calculations. The trend obtained in this work is the opposite, with HfC having the highest melting temperature and TaC the lowest.

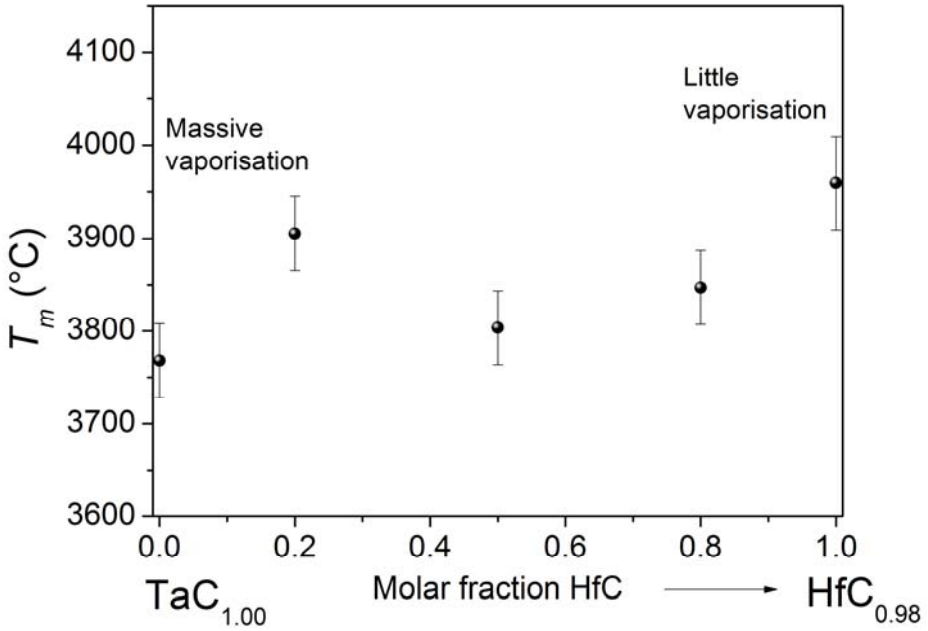

Figure 6.15 Experimental melting temperatures (T_m) in the TaC-HfC system as a function of HfC content for TaC, HfC and TaC-HfC solid solutions.

			Melting temperature T_m (°C)				
Authors	Ref.	Year	TaC (C/Ta)	4TaC-1HfC	1TaC-1HfC	1TaC-4HfC	HfC (C/Hf)
Agte and Alterthum	[28]	1930	3877	3940	3900†	3881†	3887
Rudy	[27]	1965	3983 (0.88)	3965	3945	3934	3928 (0.94)
Andrievskii et al.	[29]	1967	3840 (0.98)	3990	-	-	3750 (0.97)
Gusev et al.	[31]	1985	4002*	3960*	3917*	3937*	3948*
Okamoto	[182]	1998	3969* (0.88)				
Okamoto	[183]	2001	-	-	-	-	3942* (0.94)
This work	-	-	3768 ± 40 (1.00)	3905 ± 40	3803 ± 40	3847 ± 40	3959 ± 50 (0.98)

Table 6.4 Reported melting temperatures (T_m) in the TaC-HfC system including the results of this work. († interpolated values, * by thermodynamic calculation).

However, these data should be considered cautiously, in the light of the large, and hard to quantify, effect of the sample's emissivity. The melting point values reported in Figure 6.15 and Table 6.4 are dependent on the retained emissivity values for the various compositions measured by Deadmore [179], but these emissivity values were measured almost 1000 °C below the observed thermal arrests in this work. In the present work, NSE value as a function of wavelength and temperature can be evaluated only approximately from the thermal radiance spectra recorded by the multi-channel spectro-pyrometer. In fact, fitting of these spectra can only be performed if additional information about the ε_λ wavelength dependence is available [184]. Unfortunately, no such information is available at high temperature. Modine et al. [185] performed 0 K calculations of the optical properties of TaC, obtaining for the wavelength range covered in the current analysis, between 515 nm and 900 nm, that ε_λ decreases with wavelength, as expected for a material with a metallic-like behaviour. However, there is no meaningful reason to extrapolate this behaviour to very high temperature, especially when considering that ε_λ undergoes a sharp change of behaviour at intermediate (1800-2400 °C) temperature [180]. Moreover,

the same emissivity trend cannot be inferred for the other compositions, which also have a different temperature dependence of ε_λ, as highlighted by Deadmore [179]. Therefore, following the advice of Neuer et al. [184], in the current work radiance spectra were fitted using the rough hypothesis of wavelength-independent emissivity (grey body approximation). In this way, qualitative emissivity variation trends, with respect to ε_λ at 3000 K, have been obtained as a function of temperature. Such trends are reported in Figure 6.16.

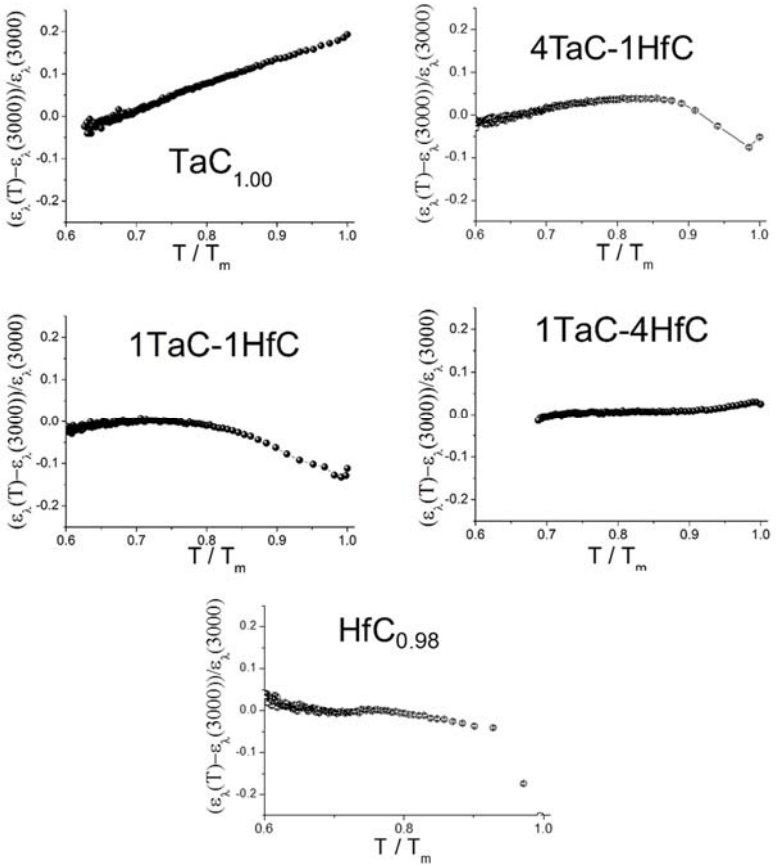

Figure 6.16 Relative normal spectral emissivity variation on data recorded in this work by fitting experimental radiance spectra within the grey body approximation. As a result of using this approximation, such data are purely qualitative.

Emissivity changes can be observed between approximately 3000 °C and 4000 °C, however the changes in emissivity are comparable with the current uncertainty on NSE estimate ($\Delta\varepsilon_\lambda/\varepsilon_\lambda \approx 0.1$). This observation partially supports the assumption that the final values measured by Deadmore [179] can be taken as a good approximation. In some cases non-negligible ε_λ discontinuity is evident at the solid-

liquid transition, reversible when the transition occurs from liquid to solid. At the transition temperature such NSE discontinuity only affects the emissivity value of the liquid carbides, it is assumed to be not relevant to the current melting point data.

It is more conservative and useful to report the current melting point data in terms of radiance temperature T_λ, i.e. assuming that all the samples behave as ideal blackbodies over the spectral range investigated. The radiance temperatures measured in the laser heating experiments are shown in Figure 6.17. True temperatures in Figure 6.15 are related to radiance temperature by Equation 3.20.

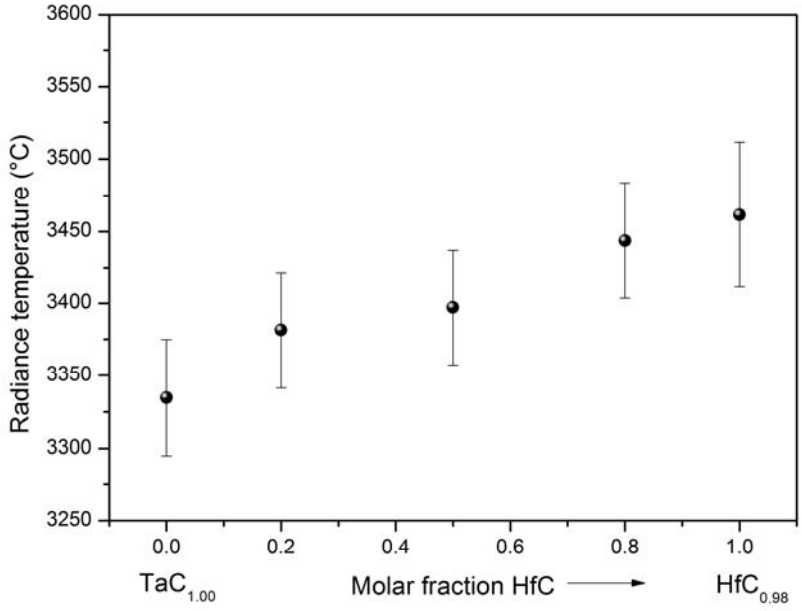

Figure 6.17 Radiance temperature of samples in the TaC-HfC system measured using laser heating experiment.

The radiance temperature at 650 nm is used as a representative point of the whole spectrum analysed here (515 nm – 900 nm). Such a spectral window covers most of the visible range, where the largest part of thermal radiation (L_{ex} in Equation 3.18) is emitted [160] at the melting/solidification temperatures investigated here (Figure 6.18).

The 650-nm radiance temperature of TaC was 3335 °C, almost 400 °C less than the true temperature. The radiance temperatures (Figure 6.17) through the TaC-HfC system hold a more uniform trend than the reported true temperatures obtained with the help of Deadmore's emissivity data. According to the thermal radiation intensity curves reported in Figure 6.18, radiance temperature increases with the HfC content, and has a maximum value of 3462 °C for HfC. HfC can therefore be retained as the compound possessing the highest radiance melting temperature. In other words, it has the top radiance emission at melting among all the compounds. This property can have interesting applications, as for example, it means that this material is the most suited to dissipate at melting its thermal energy by radiation. Of course vaporisation effects on the recorded temperature cannot be neglected in this discussion. Such effects have been observed more extensively in TaC-rich compositions, and most of all in pure TaC. The experiment geometry is conceived in such a way (sample perpendicular to the pyrometer's optical axis) that vaporisation is believed not to interfere with the temperature measurements. This is consistent with the fact that the qualitative ε_λ vs. temperature curves reported in Figure 6.16 show no sudden emissivity decrease, as would be expected with an optical effect of the occurrence of an opaque vapour plume.

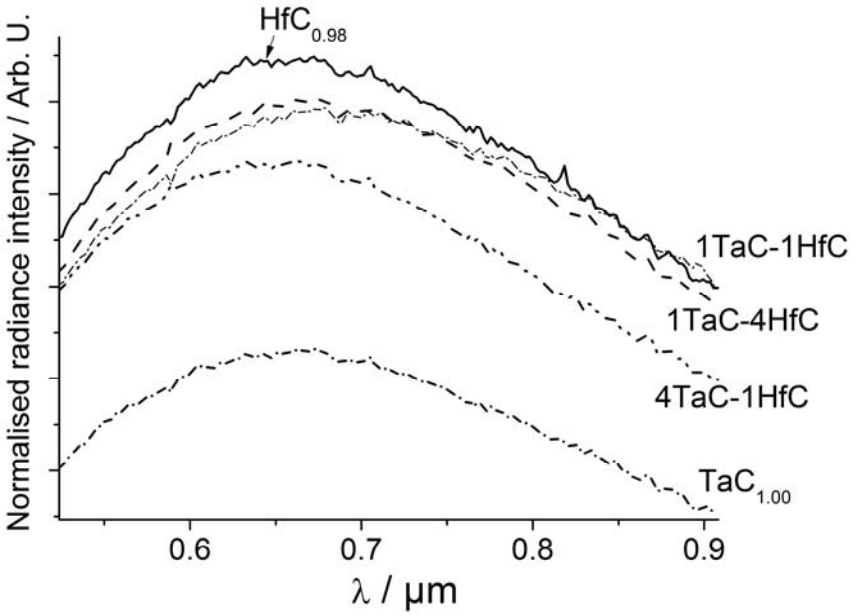

Figure 6.18 Normalised thermal radiation (radiance) intensity (L_{ex} in Equation 3.18) measured by a multi-channel spectro-pyrometer at the melting point of the five compositions studied in this work.

Table 6.4 compares the melting points of TaC-HfC ceramics reported by several authors. Agte and Alterthum in 1930 [28] reported a maximum melting temperature for the 4TaC-1HfC solid solution at 3940 °C and lower melting points of the end member carbides. This was later contradicted by Rudy [27] who reported a maximum melting point for $TaC_{0.88}$ and a decreasing melting point trend with increasing HfC content. Subsequent work by Andrievskii et al. [29] reported a melting point behaviour similar to that reported by Agte and Alterthum with 4TaC-1HfC reported as the highest melting compound at 3990 °C. Later work by Gusev et al. [31] described a calculated phase diagram (CalPhaD) determined using thermodynamic calculations in which the end members have higher melting points than the solid solution.

The results from this work show a melting point for $HfC_{0.98}$ of 3959 ± 40 °C, which would then become the highest melting point recorded for any compound, considering that the melting temperature of TaC was found here to be lower than HfC. In addition radiance melting temperature increase is observed in the solid solutions of TaC-HfC, with the solid solution radiance melting points in between the values of the single member carbides.

When these values are transformed into real temperatures by using Equation 3.20 with the emissivity data proposed by Deadmore [179], then there is a maximum melting point for the composition 4TaC-1HfC. However, even with this assumption the real melting point of HfC remains the highest of the series. Still, the main limitation of this technique is that temperature measurements rely on the emissivity data available, which is unavailable. Improvements on the current technique could be achieved by better emissivity measurements employing pyrometers with higher time-resolution [129].

7 Conclusions and future work

7.1 Conclusions

Two processing routes were proposed and conducted to synthesise and consolidate 4TaC-1HfC powders from metallic Ta and Hf and carbon using reactive routes by SHS and SPS. Using a RSPS, 4TaC-1HfC ceramics were fabricated in a single step. With the heating rates and mechanical pressures applied the SHS reaction was produced at ~1135 °C. XRD analysis showed that reflections of samples after RSPS were of TaC, HfC and HfO_2. TaC peaks show a broad left shoulder that confirmed that a single-phase solid solution was not formed. Analysis by SEM showed that microstructures consisted of core/rim structures of HfO_2 of ~15 μm surrounded by a HfC phase in a porous TaC matrix.

A second processing route consisting of SHS+SPS using an SPS furnace in both steps was conducted and 4TaC-1HfC powders were synthesised and sintered. XRD analysis showed that after SHS, the synthesised powders consisted of TaC, Ta_2C, HfC and HfO_2. Improved densification and solid state diffusion was achieved by grinding and sieving of the reacted powders, and as a result of the deaglommeration of powders. XRD analysis after SPS showed that there was more than one composition of the (Ta,Hf)C solid solution, additional EDS maps confirmed this. Microstructures consisted of matrix of (Ta,Hf)C solid solutions and a secondary phase of ~2 vol% of HfO_2. By extending the sintering times (>20 min) at similar temperatures the homogeneity of the (Ta,Hf)C solid solutions can be improved.

The results of this work shows that for the binary system of TaC-HfC a two-step reactive processing route SHS+SPS produced better results than a single-step RSPS. Samples with higher density and a refined microstructure were obtained by SHS+SPS. Also this work, also demonstrates that fabrication of UHTCs using reactive routes involving SHS are fast, economical methods to synthesise refractory carbides, with processing time in the orders of seconds, and consolidation on the order of minutes. This provides energy and cost-saving advantages over conventional processing routes and also processing can be easily upscaled.

A processing method was proposed and successfully conducted to produce single-phase solid solution TaC-HfC ceramics from commercial powders of TaC and HfC using the SPS technique. Solid solutions of 4TaC-1HfC composition were formed at sintering temperatures ≥2350 °C for 20 min and 30 MPa. Densification was nearly complete at 2250 °C, while solid solution formation and grain growth still occurred at 2350 °C. Analysis by HRTEM imaging showed the absence of liquid phase during sintering suggesting that densification occurred by solid state diffusion.

In addition a two-step sintering method was proposed to produce TaC-HfC single phase highly dense solid solution ceramics. A single phase solid solution were formed on 4TaC-1HfC, 1TaC-1Hf and 1TaC-4HfC compositions using a thermal schedule of 2100 °C/ 30 min/ 55 MPa followed by 2350 °C/ 20 min/ 30 MPa. Solid solution formation was confirmed with XRD analysis and EDS maps. As the HfC content increased the relative density dropped, this suggesting that HfC was more difficult to sinter due to oxygen impurities in the powders. This also suggest that the carbides could increase its oxygen content even by keeping the powders at room condition. The examined range of processing routes demonstrated that it is possible to make (Ta,Hf)C solid solutions from commercial powders via SPS.

Mechanical properties observed were influenced by the porosity of the samples. An increase in hardness and elastic modulus was expected since the HfC values are higher than TaC, however the highest hardness and elastic modulus were observed on 1TaC-HfC specimens. The highest thermal conductivity was observed on TaC with 52.8 W/m·K at 1950 °C, while HfC showed the lowest. Solid solution values were in between the values of the single end member carbides. CTE increased linearly by increasing HfC content to a maximum of 7.66 ± 0.11 $x10^{-6}$ /K for HfC between 25-2000 °C. The thermal and mechanical properties measured showed that these materials are suitable for UHTC applications.

Successful laser melting experiments were conducted on TaC, HfC and TaC-HfC solid solution samples using a laser heating technique developed at the Institute for Transuranium Elements (ITU) (Karlsruhe, Germany).

Thermograms of melted samples, independent of composition, showed a clear thermal arrest in the cooling section of the thermograms. A lack of an inflection point or thermal arrest during heating makes liquidus point identification difficult. Thermograms obtained do not show further inflections during heating or cooling indicating that TaC. HfC and TaC-HfC solid solutions melt congruently and do not have any phase changes below the melting temperature.

Higher power outputs were needed to melt TaC specimens, compared to other compositions, due to their higher thermal conductivity and emissivity. The measured melting temperature of TaC was 3768 ± 40 °C. The TaC thermogram showed signal noise at maximum temperatures, suggesting liquid was boiling. Significant volumes of vapour products were observed during TaC melting experiments. Less disruption on the thermogram signal and subsequent less vaporisation during melting was observed on TaC-HfC solid solutions and HfC.

Melting experiments of TaC-HfC solid solutions produced the following T_m results: 3905 ± 40 °C for 4TaC-1HfC, 3803 ± 40 °C for 1TaC-1HfC and 3847 ± 40 °C for 1TaC-4HfC. The results show a melting point of 3959 ± 50 °C for $HfC_{0.98}$, which would become the highest melting compound in the TaC-HfC system, considering that the melting temperature of TaC was found to be lower than HfC. Radiance melting temperature increase is observed in the TaC-HfC solid solutions, with the radiance melting points in between the values of the single member carbides.

Melting data should be considered cautiously due to the effect of sample emissivity. Fitting of NSE spectra can be only performed with additional ε_λ wavelength dependence information, which unfortunately is not available at high temperature.

The radiance temperature through the TaC-HfC system holds a more uniform trend than the true temperatures obtained with the help of Deadmore's emissivity data. According to thermal radiation curves it increases with the HfC content, to a maximum value of 3462 ± 50 °C for HfC. $HfC_{0.98}$ is the compound possessing the highest radiance temperature.

TEM analysis on FIB sections showed that TaC was present after melting and additional SAED patterns showed that only cubic crystals were present on the sample. No other phases or polymorphs were observed. Also indexing of SAED patterns on 4TaC-1HfC FIB sections showed that only cubic phases are present. As expected, since no higher order carbides are formed in Hf-C system, TEM analysis only showed cubic HfC crystals.

Based on results HfC was found to be better than the TaC and TaC-HfC solid solutions due to the very high melting temperature. Although in this work the mechanical properties of HfC were lower due to porosity, these are expected to be higher at full density, as reported by the literature. In addition, TaC-HfC solid solutions and more specific 1TaC-1HfC could be more useful were oxidation resistance is more important.

7.2 Future work

For the reactive processing route, specifically the SHS+SHS route it is recommended that after the powders have been synthesised further carbothermal reduction could be conducted to investigate if the oxides present after SHS can be reduced. This can enhance the formation of the solid solutions and reduction or removal of secondary phases can be achieved.

Further high temperature characterisation (>1200°C) could be conducted in TaC, HfC and TaC-HfC solid solutions. Measurement of high temperature strength and hardness could be undertaken. Knowledge of high temperature properties of these materials is limited, more investigations are required.

Further studies are required on the oxidation and nitridation of carbide powders under conditions of ambient storage over time. Composition analysis and sinterability studies could be conducted by comparison studies in powders stored in a standard cupboard with powders stored in a controlled atmosphere (glove box).

The large uncertainties affecting high temperature emissivity data of the current tantalum and hafnium carbides call for further research on this topic. Investigating laser heated samples with a blackbody hole bored in them (a sort of laser-heating Pirani-Alterthum approach) could be one possibility to study it more accurately.

References

1. E. Rudy, *Ternary phase equilibra in transition metal-boron-carbon-silicon systems. Part V. Compendium of phase diagram data*. 1969, Air Force Materials Laboratory, Wright-Patterson Air Force Base. p. 361-390.
2. C. Agte and K. Moers, *Methods for the preparation of pure high-melting carbides, nitrides and borides and a description of a few of their properties. I. The preparation of pure high-melting carbides and nitrides, as well as a few binary mixtures of these, according to the sinter method and a description of a few of their properties.* Zeitschrift fuer Anorganische und Allgemeine Chemie, 1931. **198**: p. 233-243.
3. H.O. Pierson, *Handbook of Refractory Carbides and Nitrides: Properties, Characteristics, Processing, and Applications*. 1996, Westwood, NJ, USA, Noyes Publications. p 340.
4. E.J. Wuchina and M. Opeka, *The Group IV Carbides and Nitrides*, in *Ultra-High Temperature Ceramics: Materials for Extreme Environment Applications*, W.G. Fahrenholtz, E.J. Wuchina, W.E. Lee, and Y. Zhou, Editors. 2014, John Wiley & Sons, Inc.: New York, NY, USA. p. 361-390.
5. M.J. Gasch, D.T Ellerby, and S.M. Johnson, *Ultra High Temperature Ceramic Composites*, in *Handbook of Ceramic Matrix Composites*, N. Bansal, Editor. 2005, Kluwer Academic Publishers: New York, NY, USA. p. 197-224.
6. W.G. Fahrenholtz, E.J. Wuchina, W.E. Lee, and Y. Zhou, *Introduction*, in *Ultra-High Temperature Ceramics: Materials for Extreme Environment Applications*, W.G. Fahrenholtz, E.J. Wuchina, W.E. Lee, and Y. Zhou, Editors. 2014, John Wiley and Sons, Inc: Hoboken, New, Jersey, USA. p. 1-4.
7. P. Di Mare, *Mach 20 or Bust*, in *Air & Space Magazine*. 2007, Smithsonian.
8. W.G. Fahrenholtz, *A historical perspective on research related to ultra-high temperature ceramics*, in *Ultra-High Temperature Ceramics: Materials for Extreme Environment Applications*, W.G. Fahrenholtz, E.J. Wuchina, W.E. Lee, and Y. Zhou, Editors. 2014, John Wiley and Sons, Inc: Hoboken, New, Jersey, USA. p. 6-32.
9. W.G. Fahrenholtz, G.E. Hilmas, I.G. Talmy, and J.A. Zaykoski, *Refractory diborides of zirconium and hafnium.* Journal of the American Ceramic Society, 2007. **90**(5): p. 1347-1364.
10. A. Paul, D.D. Jayaseelan, S. Venugopal, J. Binner, B. Vaidhyanathan, A. Heaton, P. Brown, and W.E. Lee, *UHTC composites for hypersonic applications*, in *American Ceramic Society Bulletin*. 2012. p. 22-29.
11. A. Paul, S. Venugopal, J. G. P. Binner, B. Vaidhyanathan, A. C. J. Heaton, and P. M. Brown, *UHTC–carbon fibre composites: Preparation, oxyacetylene torch testing and characterisation.* Journal of the European Ceramic Society, 2013. **33**(2): p. 423-432.
12. C. Carney, A. Paul, S. Venugopal, T. Parthasarathy, J. Binner, A. Katz, and P. Brown, *Qualitative analysis of hafnium diboride based ultra high temperature ceramics under oxyacetylene torch testing at temperatures above 2100°C.* Journal of the European Ceramic Society, 2014. **34**(5): p. 1045-1051.
13. J. Gonzalez-Julian, O. Cedillos-Barraza, S. Döring, S. Nolte, O. Guillon, and W.E. Lee, *Enhanced oxidation resistance of ZrB2/SiC composite through in situ reaction of gadolinium oxide in patterned surface cavities.* Journal of the European Ceramic Society, 2014. **34**(16): p. 4157-4166.
14. M.M. Opeka, I.G. Talmy, and J.A. Zaykoski, *Oxidation-based materials selection for 2000°C+ hypersonic aerosurfaces: Theoretical considerations and historical experience.* Journal of Materials Science, 2004. **39**: p. 5887-5904.

15. G.S. Upadhyaya, *G.V. Samsonov: Founder of the epoch of synthesis of new materials.* Science of Sintering, 2008. **40**: p. 99-103.

16. R.C. Evans, *An Introduction to Crystal Chemistry*. Second ed. 1966, Cambridge, UK, Cambridge University Press. p 410.

17. E.K. Storms, *The Refractory Carbides*. Refractory Materials. 1967, New York, New York, USA, Academic Press. p 285.

18. L.E. Toth, *Transition Metal Carbides and Nitrides*. Refractory Materials. 1971, New York, New York, USA, Academic Press. p 279.

19. G. Hägg, *Gezetsmässigkeiten im kristallbau bei hydriden, boriden karbiden und nitriden der übergangselemente.* Zeitschrift für Physikalische Chemie, 1931. **12**: p. 33-56.

20. A.I. Gusev, A.A. Rempel, and A.J. Magerl, *Disorder and Order in Strongly Nonstoichiometric Compounds: Transition Metal Carbides, Nitrides and Oxides*. Materials Science. 2001, Berlin, Germany, Springer-Verlag.

21. K. Yvon and E. Parthe, *On the crystal chemistry of the close-packed transition-metal carbides. I. The crystal structure of the ζ-V, Nb and Ta carbides.* Acta Crystallographica Section B, 1970. **26**(2): p. 149-153.

22. A.I. Gusev, A.S. Kurlov, and V.N. Lipatnikov, *Atomic and vacancy ordering in carbide ζ-Ta_4C_{3-x} (0.28<x<0.40) and phase equilibria in the Ta–C system.* Journal of Solid State Chemistry, 2007. **180**(11): p. 3234-3246.

23. E. Rudy, *Ternary phase equilibria in transition metal-boron-carbon-silicon systems. Part I. Related binary systems. Volume IV. Hf-C system*. 1965, Air Force Materials Laboratory, Wright-Patterson Air Force Base. p. 19.

24. A. I. Gusev, A. A. Rempel, and V. N. Lipatnikov, *Incommensurate ordered phase in non-stoichiometric tantalum carbide.* Journal of Physics: Condensed Matter, 1996. **8**(43): p. 8277.

25. E. Rudy and D.P. Harmon, *Ternary phase equilibra in transition metal-boron-carbon-silicon systems. Part I. Related binary systems. Volume V. Ta-C system. Partial investigation in the systems Nb-C and V-C*. 1965, Air Force Materials Laboratory, Wright-Patterson Air Force Base. p. 90.

26. R.V. Sara, C.E. Lowell, and R.T. Dolloff, *Research study to determine the phase equilibrium relations of selected metal carbides at high temperatures*. 1963, Union Carbide Corporation: Parma, Ohio. p. 39.

27. E. Rudy, *Ternary phase equilibria in transition metal-boron-carbon-silicon systems. Part II. Ternary systems. Vol. I. Ta-Hf-C system*. 1965, Air Force Materials Laboratory, Wright-Patterson Air Force Base. p. 84.

28. C. Agte and H. Alterthum, *Systems of high-melting carbides: Contributions to the problem carbon fusion.* Technical Physics, 1930. **11**: p. 182-191.

29. R.A. Andrievskii, N.S. Strel'nikova, N.I. Poltoratskii, E.D. Kharkhardin, and V.S. Smirnov, *Melting point in systems ZrC-HfC, TaC-ZrC, TaC-HfC.* Poroshkovaya Metallurgiya, 1967. **1**(49): p. 85-88.

30. National Institute of Standards and Technology and The American Ceramic Society, *Phase Equilibria Diagrams*. 2010.

31. A.I. Gusev, *Phase diagrams of the pseudobinary TiC-NbC, TiC-TaC, ZrC-NbC, ZrC-TaC, and HfC-TaC carbide systems.* Russian Journal of Physical Chemistry, 1985. **59**(3): p. 336-340.

32. A.L. Bowman, *The variation of lattice parameter with the carbon content of tantalum carbide.* Journal of Physical Chemistry, 1961. **65**: p. 1596-1598.

33. B.H. Eckstein and R. Forman, *Preparation and some properties of tantalum carbide.* Journal of Applied Physics, 1962. **33**(1): p. 82.

34. I. Zaplatynsky, *Observations on zeta phase in the system Ta-C.* Journal of the American Ceramic Society, 1966. **49**(2): p. 109-109.

35. W.F. Brizes, *Diffusion of carbon in the carbides of tantalum.* Journal of Nuclear Materials, 1968. **26**(2): p. 227-231.

36. T.Y. Kosolapova and G.N. Makarenko, *Methods of producing pure carbides*, in *Refractory Carbides*, G.V. Samsonov, Editor. 1974, Consulants Bureau: London, UK. p. 15-22.

37. G.V. Samsonov and V.N. Paderno, *Preparation and some properties of hafnium carbide.* Zhurnal Prikladnoi Khimii, 1961. **34**: p. 963-969.

38. J.-X. Liu, Y.-M. Kan, and G.-J. Zhang, *Synthesis of Ultra-fine Hafnium Carbide Powder and its Pressureless Sintering.* Journal of the American Ceramic Society, 2010. **93**(4): p. 980-986.

39. L. Silvestroni, A. Bellosi, C. Melandri, D. Sciti, J. X. Liu, and G. J. Zhang, *Microstructure and properties of HfC and TaC-based ceramics obtained by ultrafine powder.* Journal of the European Ceramic Society, 2011. **31**(4): p. 619-627.

40. P.H. Crayton and M.C. Gridly, *Vapour-phase synthesis of submicron tantalum carbide.* Powder Metallurgy, 1971. **14**(27): p. 78.

41. S. Venugopal, A. Paul, B. Vaidhyanathan, J. G. P. Binner, A. Heaton, and P. M. Brown, *Synthesis and spark plasma sintering of sub-micron HfB_2: Effect of various carbon sources.* Journal of the European Ceramic Society, 2014. **34**(6): p. 1471-1479.

42. N. Patra, D.D. Jayaseelan, and W.E. Lee, *Low temperature synthesis of organometallic hybrid polymer derived nanosized hafnium carbide*. 2015.

43. A.G. Merzhanov and I.P. Borovinskaya, *Self-propagating high-temperature synthesis of refractory inorganic compounds.* Dokl. Akad. Nauk USSR, 1972. **204**(2): p. 366-369.

44. H.C. Yi and J.J. Moore, *Review Self-propagating high-temperature (combustion) synthesis (SHS) of powder-compacted materials.* Journal of Materials Science, 1990. **25**: p. 1159-1168.

45. J. Subrahmanyam and M. Vijayakumar, *Self-propagating high-temperature synthesis.* Journal of Materials Science, 1992. **27**(23): p. 6249-6273.

46. B. Manley, J.B. Holt, and Z.A. Munir, *Sintering of Combustion-Synthesized Titanium Carbide*, in *Materials Science Research*. 1984, Springer US. p. 303-316.

47. J.B. Holt and Z.A. Munir, *Combustion synthesis of titanium carbide: Theory and experiment.* Journal of Materials Science, 1986. **21**(1): p. 251-259.

48. A. G. Merzhanov, *Self-propagating high-temperature synthesis.* Fiz. Khimiya. Sovrem. Probl. Ezhegod., 1983: p. 6-45.

49. V.M. Shkiro, G.A. Nersisyan, and I.P. Borovinskaya, *Principles of combustion of tantalum-carbon mixtures.* Fizika Goreniya i Vzryva, 1978. **14**(4): p. 65-68.

50. V.M. Shkiro, G.A. Nersisyan, I.P. Borovinskaya, A. G. Merzhanov, and V.S. Shekhtman, *Preparation of tantalum carbides by self-propagating high-temperature synthesis (SHS).* Poroshkovaya Metallurgiya, 1979. **4**(196): p. 14-17.

51. A.G. Merzhanov, A.S. Rogachev, A.S. Mukas'yan, B.M. Khusid, I.P. Borovinskaya, and B.B. Khina, *The role of gas-phase transport in combustion of the tantalum-carbon system.* Journal of engineering physics, 1990. **59**(1): p. 809-816.

52. R.F. Benck, L.J. Kecskes, and P.H. Netherwood, *Preparation of hafnium carbide by dynamic compaction of combustions synthesized material*. 1989, US Army Ballistic Research Laboratory: Aberdeen Proving Ground, MD, USA. p. 1-30.

53. A.G. Merzhanov, *Solid flames: discoveries, concepts, and horizons of cognition.* Combustion Science and Technology, 1994. **98**(4-6): p. 307-336.

54. C.L. Yeh and E.W. Liu, *Combustion synthesis of tantalum carbides TaC and Ta_2C.* Journal of Alloys and Compounds, 2006. **415**(1-2): p. 66-72.

55. E.A. Shtessel' and I.N. Dorozhevets, *Combustion of heterogeneous condensed systems in the presence of chemical transport reactions.* Fizika Goreniya i Vzryva, 1990. **26**(1): p. 67-73.

56. T. Kim and M.S. Wooldridge, *Catalytically assisted self-propagating high-temperature synthesis of tantalum carbide powders.* Journal of the American Ceramic Society, 2001. **84**(5): p. 976-982.

57. M.N. Rahaman, *Ceramic Processing and Sintering*. Second ed. 2003, New York, New York, USA, Marcel Dekker, Inc. p 875.

58. D.W. Richerson, *Modern Ceramic Engineering: Properties, Processing, and Use in Design*. Third ed. 2006, Boca Raton, FL, USA, CRC Press. p 707.

59. J.J. Fischer, *Hot-pressing mixed carbides of Ta, Hf, and Zr.* American Ceramic Society Bulletin, 1964. **43**(3): p. 183-185.

60. O. Gaballa, B.A. Cook, and A.M. Russell, *Reduced-temperature processing and consolidation of ultra-refractory Ta_4HfC_5.* International Journal of Refractory Metals and Hard Materials, 2013. **41**: p. 293-299.

61. S. Scholz, *Some new aspects of hot pressing of Refractories*, in *Special Ceramics 1962, Proceedings of a symposium held by the British Ceramic Research Association*, P. Popper, Editor., Academic Press Inc: New York, New York. p. 293-307.

62. E. Roeder and M. Klerk, *Studies with the electron-beam microanalyzer on hot-pressed tantalum carbide having small additions of manganese and nickel.* Zeitschrift für Metallkunde, 1963. **54**: p. 462-470.

63. L. Ramqvist, *Hot pressing of metallic carbides.* Powder Metallurgy, 1966. **9**(17): p. 26-46.

64. X. Zhang, G.E. Hilmas, W.G. Fahrenholtz, and D.M. Deason, *Hot pressing of tantalum carbide with and without sintering additives.* Journal of the American Ceramic Society, 2007. **90**(2): p. 393-401.

65. X. Zhang, G.E. Hilmas, and W.G. Fahrenholtz, *Densification and mechanical properties of TaC-based ceramics.* Materials Science and Engineering A-Structural Materials Properties Microstructure and Processing, 2009. **501**(1-2): p. 37-43.

66. X. Zhang, G.E. Hilmas, and W.G. Fahrenholtz, *Densification, mechanical properties, and oxidation resistance of TaC-TaB_2 ceramics.* Journal of the American Ceramic Society, 2008. **91**(12): p. 4129-4132.

67. D. Sciti, L. Silvestroni, S. Guicciardi, D.D. Fabbriche, and A. Bellosi, *Processing, mechanical properties and oxidation behavior of TaC and HfC composites containing 15 vol% $TaSi_2$ or $MoSi_2$.* Journal of Materials Research, 2009. **24**(06): p. 2056-2065.

68. D. Sciti, L. Silvestroni, and A. Bellosi, *High-density pressureless-sintered HfC-based composites.* Journal of the American Ceramic Society, 2006. **89**(8): p. 2668-2670.

69. J.-X. Liu, Y.-M. Kan, and G.-J. Zhang, *Pressureless sintering of tantalum carbide ceramics without additives.* Journal of the American Ceramic Society, 2010. **93**(2): p. 370-373.

70. L. Silvestroni and D. Sciti, *Sintering behavior, microstructure, and mechanical properties: A comparison among pressureless sintered ultra-refractory carbides.* Advances in Materials Science and Engineering, 2010. **2010**: p. 1-11.

71. S. A. Ghaffari, M. A. Faghihi-Sani, F. Golestani-Fard, and S. Ebrahimi, *Pressureless sintering of $Ta_{0.8}Hf_{0.2}C$ UHTC in the presence of $MoSi_2$.* Ceramics International, 2013. **39**(2): p. 1985-1989.

72. Z. A. Munir, U. Anselmi-Tamburini, and M. Ohyanagi, *The effect of electric field and pressure on the synthesis and consolidation of materials: A review of the spark plasma sintering method.* Journal of Materials Science, 2006. **41**(3): p. 763-777.

73. R. Orrù, R. Licheri, A. M. Locci, A. Cincotti, and G. Cao, *Consolidation/synthesis of materials by electric current activated/assisted sintering.* Materials Science and Engineering R, 2009. **63**: p. 127-287.

74. D.M. Hulbert, A. Anders, D.V. Dudina, J. Andersson, D. Jiang, C. Unuvar, U. Anselmi-Tamburini, E.J. Lavernia, and A.K. Mukherjee, *The absence of plasma in "spark plasma sintering".* Journal of Applied Physics, 2008. **104**(3): p. 033305.

75. D.M. Hulbert, A. Anders, J. Andersson, E.J. Lavernia, and A.K. Mukherjee, *A discussion on the absence of plasma in spark plasma sintering.* Scripta Materialia, 2009. **60**(10): p. 835-838.

76. O. Guillon, J. Gonzalez-Julian, B. Dargatz, T. Kessel, G. Schierning, J. Räthel, and M. Herrmann, *Field-assisted sintering technology/spark plasma sintering: mechanisms, materials, and technology developments.* Advanced Engineering Materials, 2014. **16**(7): p. 830-849.

77. M. Suárez, A. Fernández, J.L. Menéndez, R. Torrecillas, H.U. Kessel, J. Hennicke, R. Kirchner, and T. Kessel, *Challenges and opportunities for spark plasma sintering: A key technology for a new generation of materials*, in *Sintering Applications*, B. Ertuğ, Editor. 2013, InTech Europe: Rijeka, Croatia. p. 319-342.

78. M. Stuer, Z. Zhao, U. Aschauer, and P. Bowen, *Transparent polycrystalline alumina using spark plasma sintering: Effect of Mg, Y and La doping.* Journal of the European Ceramic Society, 2010. **30**(6): p. 1335-1343.

79. J. Langer, M.J. Hoffmann, and O. Guillon, *Electric field-assisted sintering in comparison with the hot pressing of yttria-stabilized zirconia.* Journal of the American Ceramic Society, 2011. **94**(1): p. 24-31.

80. D.V. Quach, H. Avila-Paredes, S. Kim, M. Martin, and Z.A. Munir, *Pressure effects and grain growth kinetics in the consolidation of nanostructured fully stabilized zirconia by pulsed electric current sintering.* Acta Materialia, 2010. **58**(15): p. 5022-5030.

81. Z. Shen, M. Johnsson, Z. Zhao, and M. Nygren, *Spark plasma sintering of alumina.* Journal of the American Ceramic Society, 2002. **85**(8): p. 1921-1927.

82. D. Sciti, S. Guicciardi, and M. Nygren, *Densification and mechanical behavior of HfC and HfB_2 fabricated by spark plasma sintering.* Journal of the American Ceramic Society, 2008. **91**(5): p. 1433-1440.

83. S. A. Ghaffari, M. A. Faghihi-Sani, F. Golestani-Fard, and H. Mandal, *Spark plasma sintering of TaC–HfC UHTC via disilicides sintering aids.* Journal of the European Ceramic Society, 2013. **33**(8): p. 1479-1484.

84. E. Khaleghi, Y.-S. Lin, M.A. Meyers, and E.A. Olevsky, *Spark plasma sintering of tantalum carbide.* Scripta Materialia, 2010. **63**(6): p. 577-580.

85. S.R. Bakshi, V. Musaramthota, D.A. Virzi, A.K. Keshri, D. Lahiri, V. Singh, S. Seal, and A. Agarwal, *Spark plasma sintered tantalum carbide–carbon nanotube composite: Effect of pressure, carbon nanotube length and dispersion technique on microstructure and mechanical properties.* Materials Science and Engineering: A, 2011. **528**(6): p. 2538-2547.

86. A. Nieto, D. Lahiri, and A. Agarwal, *Graphene nanoplatelets reinforced tantalum carbide consolidated by spark plasma sintering.* Materials Science and Engineering: A, 2013. **582**: p. 338-346.

87. S.R. Bakshi, V. Musaramthota, D. Lahiri, V. Singh, S. Seal, and A. Agarwal, *Spark plasma sintered tantalum carbide: Effect of pressure and nano-boron carbide addition on microstructure and mechanical properties.* Materials Science and Engineering: A, 2011. **528**(3): p. 1287-1295.

88. L. Limeng, Y. Feng, Z. Yu, and Z. Zhiguo, *Microstructure and mechanical properties of spark plasma sintered $TaC_{0.7}$ ceramics.* Journal of the American Ceramic Society, 2010. **93**(10): p. 2945-2947.

89. M.M. Opeka, I.G. Talmy, E.J. Wuchina, J.A. Zaykoski, and S.J. Causey, *Mechanical, thermal, and oxidation properties of refractory hafnium and zirconium compounds.* Journal of the European Ceramic Society, 1999. **19**(13–14): p. 2405-2414.

90. W-W. Wu, G-J. Zhang, Y-M. Kan, and P-L. Wang, *Reactive hot pressing of ZrB_2–SiC–ZrC ultra high-temperature ceramics at 1800°C.* Journal of the American Ceramic Society, 2006. **89**(9): p. 2967-2969.

91. A.M. Locci, R. Orrù, G. Cao, and Z.A. Munir, *Effect of ball milling on simultaneous spark plasma synthesis and densification of TiC–TiB_2 composites*. Materials Science and Engineering: A, 2006. **434**(1-2): p. 23-29.

92. A.M. Locci, R. Orrù, G. Cao, and Z.A. Munir, *Simultaneous spark plasma synthesis and densification of TiC-TiB_2 composites.* Journal of the American Ceramic Society, 2006. **89**(3): p. 848-855.

93. A.M. Locci, R. Orrù, and G. Cao, *Simultaneous spark plasma synthesis and consolidation of WC/Co composites.* Journal of Materials Research, 2011. **20**(03): p. 734-741.

94. R. Licheri, R. Orrù, A. M. Locci, and G. Cao, *Efficient synthesis/sintering routes to obtain fully dense ultra-high-temperature ceramics (UHTCs).* Industrial & Engineering Chemistry Research, 2007. **46**(26): p. 9087-9096.

95. R. Orrù and G. Cao, *Comparison of reactive and non-reactive spark plasma sintering routes for the fabrication of monolithic and composite ultra high temperature ceramics (UHTC) materials.* Materials, 2013. **6**(5): p. 1566-1583.

96. H. Liu, L. Liu, F. Ye, Z. Zhang, and Y. Zhou, *Microstructure and mechanical properties of the spark plasma sintered TaC/SiC composites: Effects of sintering temperatures.* Journal of the European Ceramic Society, 2012. **32**(13): p. 3617-3625.

97. X-X. Yu, G.B. Thompson, and C.R. Weinberger, *Influence of carbon vacancy formation on the elastic constants and hardening mechanisms in transition metal carbides.* Journal of the European Ceramic Society, 2015. **35**(1): p. 95-103.

98. X-X. Yu, C.R. Weinberger, and G.B. Thompson, *Ab initio investigations of the phase stability in tantalum carbides.* Acta Materialia, 2014. **80**: p. 341-349.

99. J.M. Lonergan, W.G. Fahrenholtz, and G.E. Hilmas, *Zirconium diboride with high thermal conductivity.* Journal of the American Ceramic Society, 2014. **97**(6): p. 1689-1691.

100. D.L. McClane, W.G. Fahrenholtz, G.E. Hilmas, and D. Smith, *Thermal properties of (Zr,TM)B_2 solid Solutions with TM = Hf, Nb, W, Ti, and Y.* Journal of the American Ceramic Society, 2014. **97**(5): p. 1552-1558.

101. W.S. Williams, *High-temperature thermal conductivity of transition metal carbides and nitrides.* Journal of the American Ceramic Society, 1966. **49**(3): p. 156-159.

102. A. Perecherla and W.S. Williams, *Room-temperature thermal conductivity of cemented transition-metal carbides.* Journal of the American Ceramic Society, 1988. **71**(12): p. 1130-1133.

103. I.G. Barantseva and V.N. Paderno, *Thermal expansion of solid solutions in the systems ZrC-NbC anf HfC-TaC*, in *Refractory Carbides*, G.V. Samsonov, Editor. 1974, Consultants Bureau: London, UK. p. 283-285.

104. E. Opila and N.S. Jacobson, *Oxidation and corrosion of ceramics*, in *Ceramics Science and Technology, Volume 4, Applications*, R. Riedel and I.-W. Chen, Editors. 2013, Wiley-VCH: Weinheim, Germany. p. 74-79.

105. J.B. Berkowitz-Mattuck, *High-temperature oxidation: IV. Zirconium and hafnium carbides.* Journal of The Electrochemical Society, 1967. **114**(10): p. 1030-1033.

106. S. Shimada, M. Inagaki, and K. Matsui, *Oxidation kinetics of hafnium carbide in the temperature range of 480° to 600°C.* Journal of the American Ceramic Society, 1992. **75**(10): p. 2671-2678.

107. S. Shimada, K. Nakajima, and M. Inagaki, *Oxidation of single crystals of hafnium carbide in a temperature range of 600° to 900°C.* Journal of the American Ceramic Society, 1997. **80**(7): p. 1749-1756.

108. C.B. Bargeron, R.C. Benson, A.N. Jette, and T.E. Phillips, *Oxidation of hafnium carbide in the temperature range 1400° to 2060°C.* Journal of the American Ceramic Society, 1993. **76**(4): p. 1040-1046.

109. E.L. Courtright, J.T. Prater, G.R. Holcomb, G.R. St. Pierre, and R.A. Rapp, *Oxidation of hafnium carbide and hafnium carbide with addtions of tantalum and praseodymium.* Oxidation of Metals, 1991. **36**(5/6): p. 423-437.

110. E. Wuchina, E. Opila, M. Opeka, W. Fahrenholtz, and I. Talmy, *UHTCs: Ultra high temperature ceramic materials for extreme environment applications*, in *The Electrochemical Society Interface*. 2007. p. 30-36.

111. M. Desmaison-Brut, N. Alexandre, and J. Desmaison, *Comparison of the oxidation behaviour of two dense hot isostatically pressed tantalum carbide (TaC and Ta_2C) materials.* Journal of the European Ceramic Society, 1997. **17**(11): p. 1325-1334.

112. S. Shimada, M. Johnsson, and S. Urbonaite, *Thermoanalytical study on oxidation of $TaC_{1-x}N_x$ powders by simultaneous TG-DTA-MS technique.* Thermochimica Acta, 2004. **419**(1–2): p. 143-148.

113. E. Wuchina and M. Opeka, *Oxidation of Hf-based ceramics*, in *High Temperature Corrosion and Materials Chemistry*, M. McNallan, E. Opila, T. Maruyama, and T. Narita, Editors. 1999, The Electrochemical Society, Inc.: Pennington, New Jersey, USA. p. 477-488.

114. S. Shimada, F. Yunazar, and S. Otani, *Oxidation of hafnium carbide and titanium carbide single crystals with the formation of carbon at high temperatures and low oxygen pressures.* Journal of the American Ceramic Society, 2000. **83**(4): p. 721-728.

115. M.M. Opeka, *Thermodynamics-based materials selection for corrosion-resistant performance in high-temperature missile propulsion systems*, in *High Temperature Corrosion and Materials Chemistry V*, E. Opila, J. Fergus, T. Maruyama, J. Misuzaki, T. Narita, D. Shifler, and E. Wuchina, Editors. 2004, The Electrochemical Society: Pennington, New Jersey, USA. p. 420-430.

116. E. Eakins, D.D. Jayaseelan, and W.E. Lee, *Toward oxidation-resistant ZrB_2-SiC ultra high temperature ceramics.* Metallurgical and Materials Transactions A, 2010. **42**(4): p. 878-887.

117. E. Rudy and G. Progulski, *Ternary phase equilibra in transition metal-boron-carbon-silicon systems. Part III. Special experimental techniques. Volume II. A Pirani-furnace for the precision determination of the melting temperature of refractory metallic substances*. 1967, Aerojet-General Corporation: Sacramento, California, USA. p. 53.

118. D. Manara, M. Sheindlin, W. Heinz, and C. Ronchi, *New techniques for high-temperature melting measurements in volatile refractory materials via laser surface heating.* Rev Sci Instrum, 2008. **79**(11): p. 113901.

119. M. Pirani and H. Alterthum, *Method for the determination of the melting point of metals which fuse at high temperatures.* Zeitschrift fuer Elektrochemie und Angewandte Physikalische Chemie, 1923. **29**: p. 5-8.

120. R. Kieffer, F. Benesovsky, and E.R. Honak, *A new method for the preparation of the metal borides of the transition metals.* Zeitschrift für anorganische und allgemeine Chemie, 1952. **268**(3): p. 191-200.

121. R.V. Sara, *Phase equilibria in the system tungsten-carbon.* Journal of the American Ceramic Society, 1965. **48**(5): p. 251-257.

122. R.V. Sara, *The hafnium-carbon system.* Transactions of the American Institute of Mining, Metallurgical and Petroleum Engineers, 1965. **233**(9): p. 1683-1691.

123. G.V. Samsonov and E.V. Petrash, *Various physicochemical properties of alloys of titanium boride and nitride.* Metallovedenie i Obrabotka Metallov, 1955(No. 4): p. 19-24.

124. G.V. Samsonov, V.S. Neshpor, and V.A. Ermakova, *Properties of alloys of the niobium-silicon system.* Zhurnal Neorganicheskoi Khimii, 1958. **3**: p. 868-78.

125. V Nerses, E.J. Rapperport, J.L. Klein, L.F. Pease, and S.J. Michalik, *Refractory metal constitution diagrams*. 1964, Nuclear Metals Divirions, Textron Inc: West Concord, Mass, USA. p. 300.

126. R.F. Domagala and E. Heckenbach, *High temperature furnace for melting point determination.* Review of Scientific Instruments, 1964. **35**(12): p. 1663-1664.

127. R.L. Bickerdike and G. Hughes, *An examination of part of the titanium-carbon system.* Journal of the Less Common Metals, 1959. **1**(1): p. 42-49.

128. G. Wille, F. Millot, and J. C. Rifflet, *Thermophysical properties of containerless liquid iron up to 2500 K.* International Journal of Thermophysics, 2002. **23**(5): p. 1197-1206.

129. D. Manara, M. Sheindlin, and M. Lewis, *Advances in measurements of the melting transition in non-stoichiometric UO_2.* International Journal of Thermophysics, 2004. **25**(2): p. 533-545.

130. C. A. Utton, F. De Bruycker, K. Boboridis, R. Jardin, H. Noel, C. Guéneau, and D. Manara, *Laser melting of uranium carbides.* Journal of Nuclear Materials, 2009. **385**(2): p. 443-448.

131. D. Manara, C. Ronchi, M. Sheindlin, M. Lewis, and M. Brykin, *Melting of stoichiometric and hyperstoichiometric uranium dioxide.* Journal of Nuclear Materials, 2005. **342**(1-3): p. 148-163.

132. F. De Bruycker, K. Boboridis, D. Manara, P. Pöml, M. Rini, and R.J.M. Konings, *Reassessing the melting temperature of PuO_2.* Materials Today, 2010. **13**(11): p. 52-55.

133. F. De Bruycker, K. Boboridis, P. Pöml, R. Eloirdi, R.J.M. Konings, and D. Manara, *The melting behaviour of plutonium dioxide: A laser-heating study.* Journal of Nuclear Materials, 2011. **416**(1-2): p. 166-172.

134. U. Carvajal Nuñez, D. Prieur, R. Bohler, and D. Manara, *Melting point determination of uranium nitride and uranium plutonium nitride: A laser heating study.* Journal of Nuclear Materials, 2014. **449**(1-3): p. 1-8.

135. H.F. Jackson, D.D. Jayaseelan, W.E. Lee, M.J. Reece, F. Inam, D. Manara, C.P. Casoni, F. De Bruycker, and K. Boboridis, *Laser melting of spark plasma-sintered zirconium carbide: Thermophysical properties of a generation IV very high-temperature reactor material.* International Journal of Applied Ceramic Technology, 2009. **7**(3): p. 316-326.

136. H.F. Jackson, D.D. Jayaseelan, D. Manara, C.P. Casoni, and W.E. Lee, *Laser melting of zirconium carbide: Determination of phase transitions in refractory ceramic systems.* Journal of the American Ceramic Society, 2011. **94**(10): p. 3561-3569.

137. G. Mie, *Contributions on the optics of turbid media, particularly colloidal metal solutions.* Annalen der Physik, Series IV, 1908. **25**: p. 377-445.

138. A. Rawle, *Basic principles of particle size analysis*. 2014, Malvern Instruments, UK.: Worchestershire, UK. p. 8.

139. E. Giorgi, R. Harrison, and O. Cedillos-Barraza, *Horiba Analysers - Experimental Results*. 2013, Centre for Nuclear Engineering, Imperial College London: London, UK.

140. W. E. Lee and W.M. Rainforth, *Ceramic Microstructures*. 1994, Chapman & Hall. p 590.

141. D. Brandon and W.D. Kaplan, *Microstructural Characterization of Materials*. 2nd ed. 2008, Chichester, West Sussex, England, John Wiley & Sons Ltd. p 536.

142. B.D. Cullity and S.R. Stock, *Elements of X-Ray Diffraction*. Third ed. 2001, Upper Saddle River, NJ, USA, Prentice Hall. p 664.

143. C.B. Carter and M.G. Norton, *Ceramic Materials: Science and Engineering*. Second ed. 2013, New York, USA, Springer. p 766.

144. J. Goldstein, D. Newbury, D. Joy, C. Lyman, P. Echlin, E. Lifshin, L. Sawyer, and J. Michael, *Scanning Electron Microscopy and X-Ray Microanalysis*. Third ed. 2003, New York, NY, USA, Springer.

145. ASTM International, *E112 Standard Test Methods for Determining Average Grain Size*. 2012, ASTM International: West Conshohocken, PA, USA.

146. ASTM International, *E1382 Standard Test Methods for Determining Average Grain Size Using Semiautomatic and Automatic Image Analysis*. 2010, ASTM International: West Conshohocken, PA, USA.

147. D.B. Williams and C.B. Carter, *Transmission Electron Microscopy*. Second ed. 2009, New York, New York, Springer. p 760.

148. ASTM International, *C1327 Standard Test Method for Vickers Indentation Hardness of Advanced Ceramics*. 2008, ASTM International: West Conshohocken, PA, USA.

149. A.C. Fischer-Cripps, *Nanoindentation*. Third ed. Mechanical Engineering. 2011, New York, NY, USA, Springer. p 279.

150. W.C. Oliver and G.M. Pharr, *An improved technique for determining hardness and elastic modulus using load and displacement sensing indentation experiments.* Journal of Materials Research, 1992. **7**(6): p. 1564-1582.

151. W.C. Oliver and G.M. Pharr, *Measurement of hardness and elastic modulus by intrumented indentation: advances in understanding and refinements to methodology.* Journla of Materials Research, 2004. **19**(1): p. 3-20.

152. J.B. Wachtman, W.R. Cannon, and M.J. Matthewson, *Mechanical Properties of Ceramics*. Second ed. 2009, Hoboken, NJ, USA., John Wiley & Sons, Inc. p 479.

153. S. Timoshenko and J.N. Goodier, *Theory of Elasticity*. Second ed. 1951, New York, NY, USA, McGraw-Hill.

154. G. Simmons and H. Wang, *Single Crystal Elastic Constants and Calculated Aggregate Properties: a Handbook*. 1971, Cambridge, MA, USA, MIT Press.

155. G.R. Anstis, P. Chantikul, B.R. Lawn, and D.B. Marshall, *A critical evaluation of indentation techniques for measuring fracture toughness: I, direct crack measurements.* Journal of the American Ceramic Society, 1981. **64**(1981): p. 533-538.

156. ASTM International, *E831 Standard Test Method for Linear Thermal Expansion of Solid Materials by Thermomechanical Analysis*. 2013, ASTM International: West Conshohocken, PA, USA.

157. ASTM International, *E228 Standard Test Method for Linear Thermal Expansion of Solid Materials with a Push-Rod Dilatometer*. 2011, ASTM International: West Conshohocken, PA, USA.

158. W.J. Parker, R.J. Jenkins, C.P. Butler, and G.L. Abbott, *Flash method of determining thermal diffusivity, heat capacity and thermal conductivity.* Journal of Applied Physics, 1961. **32**: p. 1679-1684.

159. ASTM International, *E1461 Standard Test Method for Thermal Diffusivity by the Flash Method*. 2013, ASTM International: West Conshohocken, PA, USA.

160. D.P. DeWitt and J.C. Richmond, *Thermal Radiative Properties of Materials*, in *Theory and Practice of Radiation Thermometry*. 2007, John Wiley & Sons, Inc. p. 91-187.

161. J.L. Engelke, F.A. Halden, and E.P. Earley, *Synthesis of new high temperature materials*. 1960, Stanford Research Institute: Menlo Park, CA, USA. p. 45.

162. R. Licheri, R. Orrù, C. Musa, and G. Cao, *Combination of SHS and SPS techniques for fabrication of fully dense ZrB_2-ZrC-SiC composites.* Materials Letters, 2008. **62**(3): p. 432-435.

163. R. Licheri, R. Orrù, C. Musa, A.M. Locci, and G. Cao, *Spark plasma sintering of UHTC powders obtained by self-propagating high-temperature synthesis.* Journal of Materials Science, 2008. **43**(19): p. 6406-6413.

164. E. Rudy, H. Nowotny, F. Benesovsky, R. Kieffer, and A. Neckel, *Über hafniumkarbid enthaltende karbidsysteme.* Monatshefte für Chemie, 1960. **91**(1): p. 176-187.

165. A.R. West, *Solid State Chemistry and its Applications*. Second ed. 2013, Chichester, West Sussex, UK, John Wiley and Sons, Ltd. p 584.

166. A. Denton and N. Ashcroft, *Vegard's law.* Physical Review A, 1991. **43**(6): p. 3161-3164.

167. S. A. Ghaffari, M. A. Faghihi-Sani, F. Golestani-Fard, and M. Nojabayy, *Diffusion and solid solution formation between the binary carbides of TaC, HfC and ZrC.* International Journal of Refractory Metals and Hard Materials, 2013. **41**: p. 180-184.

168. R.W. Rice, *Porosity of Ceramics*. First ed. 1998, New York, NY, USA, Marcel Dekker, Inc. p 539.

169. Y. Arai, Y. Okamoto, and Y. Suzuki, *Thermal conductivity of neptunium mononitride from 740 to 1600 K.* Journal of Nuclear Materials, 1994. **211**: p. 248-250.

170. B.C. Schulz, B. Wang, R.A. Morris, D. Butts, and G.B. Thompson, *Influence of hafnium carbide on vacuum plasma spray processed tantalum carbide microstructures.* Journal of the European Ceramic Society, 2013. **33**(6): p. 1219-1224.

171. D.L. Deadmore and I. Zlapatynsky, *The ternary system tantalum-hafnium-carbon at 2050°C*. 1965, National Aeronautics and Space Administration: Washington, D.C. p. 14.

172. J. Sautereau and A. Mocellin, *Sintering behavior of ultrafine niobium monocarbide and tantalum monocarbide powders.* Journal of Materials Science, 1974. **9**: p. 761-771.

173. D. Sciti, L. Silvestroni, V. Medri, and F. Monteverde, *Sintering and densification mechanisms of ultra-high temperature ceramics*, in *Ultra-High Temperature Ceramics: Materials for Extreme Environment Applications*, W.G. Fahrenholtz, E.J. Wuchina, W.E. Lee, and Y. Zhou, Editors. 2014, John Wiley and Sons, Inc: Hoboken, New, Jersey, USA. p. 112-143.

174. S. Baik and P.F. Becher, *Effect of oxygen contamination on densification of TiB_2.* Journal of the American Ceramic Society, 1987. **70**(8): p. 527-530.

175. W.J. Clegg, *Role of carbon in the sintering of boron-doped silicon carbide.* Journal of the American Ceramic Society, 2000. **83**(5): p. 1039-1043.

176. H.E. Exner, *Physical and chemical nature of cemented carbides.* International Metals Reviews, 1979. **24**(1): p. 149-173.

177. M. C. L. Patterson, S. He, L. L. Fehrenbacher, J. Hanigofsky, and B. D. Reed, *Advanced HfC-TaC oxidation resistant composite rocket thruster.* Materials and Manufacturing Processes, 1996. **11**(3): p. 367-379.

178. E.L Courtright, H.C. Graham, A.P. Katz, and R.J. Kerans, *Ultrahigh Temperature Assessment Study - Ceramic Matrix Composites*. 1992, Wright Laboratory: Wright-Patterson AFB, Ohio, USA. p. 144.

179. D.L. Deadmore, *Normal spectral emittance (0.65μ) of TaC-HfC solid solutions and tungsten above 1600°C.* Journal of the American Ceramic Society, 1964. **47**(12): p. 649-650.

180. P.T.B. Shaffer, *Evidence for high-temperature forms of zirconium and tantalum monocarbides.* Journal of the American Ceramic Society, 1963. **46**(6): p. 177-179.

181. J.A. Coffman, G.M. Kibler, T.R. Riethof, and A.A. Watts, *Carbonization of Plastics and Refractory Materials Research, Part I*. 1960, General Electric Company: Wright-Patterson Air Force Base, OH, USA. p. 89.

182. H. Okamoto, *C-Ta (Carbon-Tantalum).* Journal of Phase Equilibria, 1998. **19**(1): p. 88-88.

183. H. Okamoto, *C-Hf (Carbon-Hafnium).* Journal of Phase Equilibria, 2001. **22**(4): p. 510-510.

184. G. Neuer, L. Fiessler, M. Groll, and E. Schreiber. *Critical analysis of the different methods of multiwavelength pyrometry*. in *Temperature: its measurement and control in science and industry*. 1992. AIP Publishing.

185. F. Modine, R. Major, T. Haywood, G. Gruzalski, and D. Smith, *Optical properties of tantalum carbide from the infrared to the near ultraviolet.* Physical Review B, 1984. **29**(2): p. 836-841.